

Understanding and Engineering Interfacial Charge Transfer of Carbon Nanotubes and Graphene for Energy and Sensing Applications

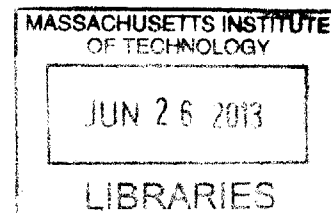
by

Geraldine L.C. Paulus

Ir., Chemical Engineering
University of Leuven (KUL), 2007

M.Sc., Safety Engineering
University of Leuven (KUL), 2008

ARCHIVES



Submitted to the Department of Chemical Engineering
in Partial Fulfillment of the Requirements for the Degree of

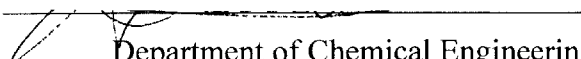
Doctor of Philosophy in Chemical Engineering
at the

MASSACHUSETTS INSTITUTE OF TECHNOLOGY


JUNE 2013

© 2013 Massachusetts Institute of Technology. All rights reserved.

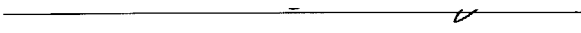
Signature of Author:


Department of Chemical Engineering
May 15, 2013

Certified by:


Michael S. Strano
Professor of Chemical Engineering
Thesis Supervisor

Accepted by:


Patrick S. Doyle
Professor of Chemical Engineering
Chairman, Committee for Graduate Students

Understanding and Engineering Interfacial Charge Transfer of Carbon Nanotubes and Graphene for Energy and Sensing Applications

by

Geraldine L.C. Paulus

Submitted to the Department of Chemical Engineering
on May 15, 2013 in Partial Fulfillment of the
Requirements for the Degree of Doctor of Philosophy in Chemical Engineering

ABSTRACT

Graphene is a one-atom thick planar monolayer of sp^2 -bonded carbon atoms organized in a hexagonal crystal lattice. A single walled carbon nanotube (SWCNT) can be thought of as a graphene sheet rolled up into a seamless hollow cylinder with extremely high length-to-diameter ratio. Their large surface area, and exceptional optical, mechanical and electronic properties make these low-dimensional carbon materials ideal candidates for (opto-)electronic and sensing applications. In this thesis I studied the charge transfer processes that occur at their interface, and developed applications based on the discovered properties.

When light is incident on a semiconducting SWCNT, it can excite an electron from the valence band to the conduction band, thereby creating a Coulombically bound electron-hole pair, also known as an exciton. Excitons can decay via radiative or non-radiative recombination or by colliding with other excitons. They can diffuse along the length of a SWCNT or hop from larger band gap SWCNTs to smaller band gap SWCNTs, a process known as exciton energy transfer (EET). We studied their behavior as a function of temperature in SWCNT fibers and showed that at room temperature the rate constant for EET is more than two orders of magnitude larger than that of each of the different recombination processes. This led us to construct a core-shell SWCNT fiber, which consists of a core of smaller band gap SWCNTs, surrounded by a shell of larger band gap SWCNTs, essentially forming what is known as a type I heterojunction. In agreement with a model that describes exciton behavior in the SWCNT fibers, we found that upon illumination all the energy (in the form of excitons) was quickly transferred from the shell to the core, faster than the excitons would otherwise recombine. The SWCNT fiber proved to be an efficient optical and energetic concentrator.

We showed that SWCNTs and poly(3-hexylthiophene) (P3HT) form a type II heterojunction, which implies that excitons generated in the P3HT can easily dissociate into free charge carriers at the interface with the SWCNTs. Despite this, the efficiency of a P3HT/SWCNT bulk heterojunction (BHJ) photovoltaic is subpar. We developed a P3HT/SWCNT planar heterojunction (PHJ) and achieved efficiencies that were 30 times higher, which showed that the formation of bundled aggregates in BHJs was the cause: metallic SWCNTs can quench the excitons in an entire bundle.

Another interesting feature of our SWCNT/P3HT PHJ is that a maximum efficiency was reached when ~60 nm of P3HT was used, which is surprising since in a planar photovoltaic a

maximum is expected for ~ 8.5 nm of P3HT, the value of the exciton diffusion length. A Kinetic Monte Carlo simulation revealed that bulk exciton dissociation was responsible for the lower efficiencies observed in devices with low P3HT thickness.

Next we created and studied a junction between SWCNTs and a monolayer of graphene, an ideal one-dimensional/two-dimensional carbon interface. We used Raman spectroscopy to probe the degree of charge transfer at the interface and based on a shift in the G peak position of the graphene Raman signal at the junction deduced that a typical metallic (semiconducting) SWCNT dopes the graphene with $1.12 \times 10^{13} \text{ cm}^{-2}$ ($0.325 \times 10^{13} \text{ cm}^{-2}$) electrons upon contact, in agreement with the fact that the Fermi level of the SWCNTs is more shallow than that of the graphene. A molecular dynamics simulation ruled out that the observed Raman peak shifts are due to strain, although it did show that SWCNTs are being compressed radially by the graphene sheet, resulting in a widening of their Raman peaks.

We studied charge transfer between diazonium molecules and graphene, to better inform transistor and sensor design. The reaction rate depends on the degree of overlap between the filled energy levels in graphene and the unoccupied ones in the diazonium molecule. We showed that with increasing degree of functionalization the charge transfer characteristics of a graphene field effect transistor (FET) alter in the following ways: the minimum conductivity decreases, the Dirac point upshifts, the conductivity plateau at high carrier density decreases and the electron-hole conduction asymmetry increases. We developed a theoretical model of charge transport in graphene FETs that takes into account the effect of both short-range and long-range scatterers. Fitting it to the charge-transport data reveals quantitative information about the number of impurities in the substrate supporting the graphene, about the number of defects created as a result of the reaction, and about the degree of electron-hole conduction asymmetry.

Graphene functionalization also affects the graphene Raman signal. After reaction, the D to G intensity ratio increases, which is a sign of covalent modification of the graphene lattice. Additionally, the G peak and 2D peak positions increase while the 2D/G intensity ratio decreases, which are signs of hole-doping.

Based on a Raman analysis, we were also able to show that the end group of the diazonium salt can affect both the degree of chemisorption (covalent modification) as well as the degree of physisorption (doping).

Finally, we studied the effects of charge transfer between graphene and biological cells on the graphene Raman signal and designed a fundamentally new type of biosensor. Graphene can be thought of as a continuous array of information units (sensor units). The Raman signal collected in each unit can report on its local environment. In contrast to graphene FET biosensors, the graphene Raman biosensor offers subcellular spatial resolution.

The graphene Raman signal was shown to display a strong dependence on pH. Metabolically active cells acidify their local environment; therefore, pH is a proxy for cellular metabolism. We placed both human embryonic kidney (HEK) cells that were genetically engineered to produce mouse antibodies and control HEK cells that were not genetically modified onto the graphene. Based on the change in the graphene Raman signal we deduced the former have a metabolic rate that is four times higher than that of the control cells. Increased cellular adhesion allows the cells to interact more closely with the graphene monolayer and intensifies the observed Raman effects.

Thesis Supervisor: Michael S. Strano
Title: Professor of Chemical Engineering

Acknowledgements

Foremost, I would like to express my sincere appreciation to my advisor, Professor Michael Strano, without whose experience and knowledge this thesis would not have been possible. His unwavering enthusiasm and passion for science is what convinced me to join his research group five years ago and what motivated me to keep going when faced with the difficult challenges that are invariably linked with the pursuit of this degree. His sense of wonder and his curiosity are truly contagious. In guiding me he has always kept my own interests in mind and has always supported interdisciplinary exploration in my work. His continuous guidance, encouragement and mentorship have made me a confident researcher, unafraid to tackle new territory, which will undoubtedly benefit my career and for which I will forever be grateful.

Just like my thesis, my committee members represent a myriad of fields. I am very lucky to have been advised by this multidisciplinary team: Professor Tonio Buonassisi, from mechanical engineering, who is an esteemed expert in the field of photovoltaics; Professor Karen Gleason, from chemical engineering, polymer expert and pioneer of their synthesis via chemical vapor deposition and Professor Jing Kong, from electrical engineering, who spearheaded the chemical synthesis of graphene. They have always supported my scientific road of discovery and passed on so much advice pertaining to their own field but also to the other fields I was exploring. All of my committee members have provided me with useful scientific recommendations and feedback to my work and kept me on the right track towards obtaining my PhD.

In addition to my committee members, I want to acknowledge Professor Dane Wittrup, Dr. Cary Opel, Dr. Jeon Woong Kang, Dr. Ramachandra R. Dasari, Dr. Ki Kang Kim, Professor Thomas Palacios, Professor Pablo Jarillo-Herrero and Professor Milly Dresselhaus for fruitful collaborations and/or stimulating and intellectual discussions about my work.

I genuinely want to thank the entire Strano Research Group; the road towards a PhD is one with many ups and downs and the environment you work in on a daily basis can make all the difference. I have had the pleasure of working with and learning from a group of incredibly talented and intelligent people, including Qing Hua Wang, Chih-Jen Shih, Moon-Ho Ham, Jae-Hee Han, Aravind Vijayaraghavan, Kourosh Kalantar-zadeh, Zachary Ulissi, Tom McNicholas, Steven Shimizu, Zhong Jin, Justin Nelson, Nigel Reuel, Markita Landry and Sebastian Kruss. I am also indebted to Katie Lee, Chris Kevin Ong, Evan Piephoff, Brittany Grassbaugh, and Abdullah Alsaeed, undergraduate students who have given me the extra hands and eyes that make this thesis more complete. With many of my colleagues – to name just a few: Qing Hua Wang, Jingqing Zhang, Ardemis Boghossian, Darin Bellisario, Joel Abrahamson, Tom McNicholas, Andrew Hilmer, and Sayalee Mahajan, I have formed lasting friendships, which I have no doubt will outlast the duration of my or their stay at MIT. They have all been a sounding board to me, both on a scientific and a personal level.

I am fortunate and thankful to be surrounded by a group of amazing and supporting friends: Elif Yavuz, Annouck Luyten, Stephanie Byttebier, Charlotte Dekeersmaeker, Robrecht Thoonen, Kimberley Dong, Sarah Miller, Roel Sterken, Katya Rablova, Jil Ulrich, Mandana Manzari, Sven Reynaert, Eve Monseur, Arne Devriendt and so many others!

I owe my deepest gratitude to my family: my mom Jackie, my dad Walter and my sister Ellen. They are my home basis, the ground in which I am rooted. Without them I would not have grown into the person I am today, both from a scientific and a personal perspective. I have been blessed with an amazing education. I look up to each of them and I know they are my biggest fans. I wish to thank them from the bottom of my heart for all they have done and continue to do for me, and above all for their unconditional love, patience and support.

Finally I want to thank the love of my life, my husband Dirk. He is my partner and teammate in life. I thank him for sharing in my struggles and in my success, for sharing his experiences, for lifting my spirits, for reassuring me, for cheering me on, for listening to me, for helping me find my way, for being so kindhearted and caring, for knowing me so well and for simply loving me so much!

Table of contents

1. Introduction	12
1.1. Low dimensional materials	12
1.2. Exciton engineering: the next frontier of chemical reaction engineering	19
1.3. References	28
2. Study and manipulation of SWCNT-SWCNT interactions	31
2.1. Background and motivation	31
2.2. Materials and methods	34
2.2.1. Preparation of the SWCNT solution	34
2.2.2. Preparation of the SWCNT fibers	36
2.3. Results and discussion	37
2.3.1. Optical properties of a (6,5) enriched SWCNT solid-state fiber	37
2.3.2. Temperature-dependent photophysics of a (6,5) enriched SWCNT solid-state fiber	40
2.3.3. Observation of spatial inhomogeneities in PL of (6,5) enriched SWCNT fiber	52
2.3.4. The exciton antenna: spatial and energetic concentration of the incident light	61
2.4. Conclusions	63
2.5. Ongoing work	65
2.6. References	68
3. Study and manipulation of SWCNT-P3HT interactions	72
3.1. Background and motivation	72
3.2. Materials and methods	76
3.2.1. Experimental materials and methods	76
3.2.2. Methodological and computational approach	77
3.3. Results and discussion	93
3.3.1. Optical T-matrix model	93
3.3.2. Kinetic Monte Carlo Simulation	100
3.4. Conclusions	108
3.5. Ongoing work	109
3.6. References	113
4. Study and manipulation of SWCNT-graphene interactions	121

4.1.	Background and motivation	121
4.2.	Materials and methods	123
4.2.1.	SWCNT synthesis	123
4.2.2.	Graphene synthesis and transfer	124
4.2.3.	Raman spectroscopy	125
4.2.4.	Statistics	125
4.2.5.	Molecular dynamics simulation	126
4.3.	Results and discussion	127
4.3.1.	Doping effect investigated by Raman spectroscopy	127
4.3.2.	Strain effect investigated by molecular dynamics	147
4.4.	Conclusions	155
4.5.	Ongoing work	156
4.6.	References	158
5. Study and manipulation of covalent electron transfer chemistry of graphene with diazonium salts		162
5.1.	Background and motivation	162
5.1.1.	Overview of typical experimental conditions	163
5.1.2.	Reaction mechanism: theoretical predictions and experimental findings	164
5.1.3.	Rate of covalent attachment	167
5.2.	Materials and methods	169
5.2.1.	Graphene synthesis and transfer	169
5.2.2.	Raman spectroscopy	170
5.2.3.	Graphene functionalization	170
5.2.4.	Graphene FET design	170
5.3.	Results and discussion	172
5.3.1.	Effect of degree of functionalization	172
5.3.2.	Effect of different diazonium end-groups	185
5.3.3.	Effect of other reaction conditions	188
5.4.	Conclusions	190
5.5.	Ongoing work	191
5.6.	References	192
6. Study and manipulation of graphene-cell doping interactions		197
6.1.	Background and motivation	197
6.2.	Materials and methods	199
6.2.1.	Graphene synthesis and transfer	199
6.2.2.	Raman spectroscopy and mapping	200
6.2.3.	Cell line generation	201
6.2.4.	Cell passaging	201
6.2.5.	IgG expression and purification	202

6.2.6.	UV-VIS spectroscopy	203
6.2.7.	Statistics	203
6.3.	Results and discussion	203
6.3.1.	Graphene pH response investigated by Raman spectroscopy	203
6.3.2.	Graphene as an array of addressable pH sensors: a single cell physiometer	213
6.3.3.	Graphene as a cytometer based on cell-induced graphene doping	217
6.3.4.	A graphene cell physiometer as a tool to measure cellular metabolic rate	222
6.4.	Conclusions	231
6.5.	Ongoing work	231
6.6.	References	240
7.	Conclusions and outlook	244

List of figures

Figure 1.1	Carbon low dimensional materials	15
Figure 1.2	SWCNT physical structure	17
Figure 1.3	Exciton engineering	21
Figure 2.1	SWCNT photophysics	32
Figure 2.2	SWCNT separation via density ultracentrifugation	35
Figure 2.3	Dielectrophoretic assembly of SWCNT fibers	37
Figure 2.4	Optical properties of a (6,5) enriched SWCNT fiber	38
Figure 2.5	EEP and reversible PL change as a function of temperature	41
Figure 2.6	Theoretical prediction of the PL and QY of pure SWCNT fibers	47
Figure 2.7	Temperature dependent exciton-energy transfer efficiency	47
Figure 2.8	Analysis of average dataset of repeatedly temperature-cycled fiber	51
Figure 2.9	Spatially resolved, temperature-dependent PL behavior observed in an in-house built dual-channel microscope	54
Figure 2.10	Schematic of an in-house built dual-channel microscope setup	55
Figure 2.11	Spatial inhomogeneities in fiber PL explained by SWCNT density and alignment	59
Figure 2.12	Development of an exciton antenna from a core-shell carbon nanotube structure	62
Figure 2.13	Possible configurations for polymer-free SWCNT-based photovoltaics	66
Figure 3.1	Schematics of hybrid planar nano-heterojunction solar cells based on conjugated polymers and carbon nanotubes or PCBM	77
Figure 3.2	Lattice structure of P3HT employed in the Monte Carlo simulation	81
Figure 3.3	Bulk exciton dissociation efficiency	89
Figure 3.4	Schematic summary of the Kinetic Monte Carlo simulation	91
Figure 3.5	Optical constants as a function of wavelength	93
Figure 3.6	Optical modeling of the active layer in the P3HT/SWCNT device	96
Figure 3.7	Results of the optical transfer-matrix model for the most efficient P3HT-SWCNT structure (i.e. with 60nm of P3HT)	97
Figure 3.8	Optical modeling of the active layer in the P3HT/PCBM device	99
Figure 3.9	Short-circuit current per nanotube as a function of P3HT thickness	103
Figure 3.10	Short-circuit current density of the P3HT-Br/PCBM photovoltaic	106
Figure 3.11	Increasing SWCNT density in the P3HT/SWCNT PV	110
Figure 4.1	Sample setup and characterization	129
Figure 4.2	Representative Raman spectra of the relevant regions of the sample	131
Figure 4.3	Influence of half-wave retardation plate on the G-band Raman signal of a SWCNT and graphene	133
Figure 4.4	Statistical plots showing the influence of the m-SWCNT on graphene	134
Figure 4.5	Doping trajectories showing the influence of the m-SWCNT on graphene	135
Figure 4.6	Representative intensity loss (~8.5%) of graphene G peak signal upon insertion of the half wave plate ($\alpha=90^\circ$)	137
Figure 4.7	Statistical plots showing the influence of graphene on the m-SWCNT	138
Figure 4.8	Influence of doping at a sc-SWCNT/graphene junction	140
Figure 4.9	Influence of strain on the m-SWCNT	149
Figure 4.10	Influence of strain on the graphene, caused by the underlying	

	m-SWCNT	152
Figure 4.11	Influence of strain the sc-SWCNT/graphene junction	154
Figure 5.1.	Schematic illustration of grafting of a diazonium salt with functional group R and counterion X to the graphene lattice	165
Figure 5.2	Schematic representation of the $DOS(E)$ of graphene and the unoccupied $DOS(E)$ of a typical diazonium salt	169
Figure 5.3	Experimental setup	171
Figure 5.4	Effect of degree of functionalization on graphene Raman peak parameters	173
Figure 5.5	Effect of degree of functionalization on graphene charge transport characteristics	176
Figure 5.6	Effect of diazonium end-group on functionalized graphene Raman signal	185
Figure 5.7	Effect of chemi- and physisorption on functionalized bilayer graphene Raman signal	188
Figure 5.8	Effect of reaction conditions on the charge transport characteristics of graphene FETs	189
Figure 6.1	Experimental setup	204
Figure 6.2	pH dependence of graphene Raman signal	205
Figure 6.3	Graphene, a tool for subcellular mapping of cellular metabolism	214
Figure 6.4	Additional examples of Raman footprints for different cells	216
Figure 6.5	Graphene, a tool for mapping phenotypic diversity in cell populations	218
Figure 6.6	Scatter plots of 2D peak position vs. G peak position of graphene covered in growth medium (black dots) and cells (red squares) for IgG-producing cells (top panels) and non-IgG-producing control cells (bottom panels)	220
Figure 6.7	Scatter plots of 2D peak position vs. G peak position of graphene covered in growth medium (black dots) and cells (red squares) for IgG-producing cells (top panels) and non-IgG-producing control cells (bottom panels)	221
Figure 6.8	Absorption spectra of growth medium (blue), growth medium that has been centrifuged (red), and medium+IgG (green)	226
Figure 6.9	Raman data of graphene exposed to air (blue), growth medium (red) and both growth medium and IgG (green), without incubation	228
Figure 6.10	Raman data of graphene exposed to air (blue), growth medium (red) and both growth medium and IgG (green), after incubation	229
Figure 6.11	Effect of non-stimulated neural progenitor cells on the graphene Raman signal	234
Figure 6.12	Effect of stimulated neural progenitor cells on the graphene Raman signal	235
Figure 6.13	Raman data of graphene exposed to medium vs. medium containing dopamine	238
Figure 7.1.	Overview of the different mechanisms for charge transfer at the interface of carbon nanotubes and graphene	245

List of tables

Table 1.1	Calculation of the Thiele modulus for a 13 nm thin film of MDMO-PPV	24
Table 4.1	Key parameters of the bond length distribution of the m-SWCNT in our system (with 95% confidence intervals)	150
Table 4.2	Key parameters of the bond length distribution of the graphene in our system (with 95% confidence intervals)	153
Table 6.1.	Summary of doping effects of different chemical environments on graphene	230

1. Introduction

Some of the work, text and figures presented in this chapter are reprinted or adapted with permission from reference [1] (Copyright © 2011, American Institute of Chemical Engineers (AIChE)).

1.1. Low dimensional materials

Low dimensional materials (LDMs) are a new class of materials, which have one or more physical dimensions constrained to the nanometer scale. This constraint implies that the electrons within them are confined to less than three dimensions, a property that imparts such materials with new and unusual properties, as well as new opportunities for novel engineering applications. The properties of low-dimensional materials are substantially different from those of their bulk counterparts, and their understanding requires the application of fundamental chemical engineering concepts. In studying such materials, the central focus has been on understanding their physical and chemical properties, and their potential technological applications. Examples of LDM include two dimensional nanosheets (2D), one-dimensional nanowires, nanotubes and nanorods (1D), and zero-dimensional quantum dots (0D), all of which showcase a whole new range of properties when compared to their three-dimensional bulk equivalents, with the change in properties arising from quantum confinement and/or surface and interfacial effects [2].

Quantum confinement effects appear when the confining dimension(s) is (are) on the order of the wavelength of the electron wave function. This implies that when

electrons or holes (the absence of electrons) are moving, their mean free path is larger than the dimension of the quantum structure, which typically happens at the nanoscale. In general, solids have a defined spectrum of allowable electronic states, called the electronic density of states (DOS). The nanoscale confinement in LDMs brings about a transition from a continuous to a discontinuous DOS which results in a whole new set of physical, optical and chemical properties. For example, as a result of quantum confinement the electronic band gap of 0D and 1D semiconductors becomes size dependent, leading to their use in many interesting photo-electronic applications, such as solar cells, light emitting diodes (LED) and diode lasers [3-6]. Electrical conductivity is typically expected to be lower for LDMs than for their bulk equivalents due to scattering from e.g. wire boundaries, edge effects, and quantization of conductivity [7].

As dimensions of electronics keep getting smaller though, it is likely to encounter ballistic transport of electrons, meaning there is negligible resistivity in the medium due to scattering. It can be observed when the mean free path of the electron is much bigger than the dimensions of the medium it travels through. This phenomenon occurs at the nanoscale and is thus more likely to be observed in LDMs than in their bulk equivalents. InAs nanowires with a diameter of 50nm have shown ballistic transport over a length scale of about 200nm at room temperature [8]. However, it is generally hard to observe ballistic conduction in nanowires at room temperature due to edge effects: the dangling bonds present defects and act as scattering sites for the electrons.

Thermal energy is another area where LDMs have unique properties. It is stored and transmitted in nanostructures using electrons and particularly phonons – quantized units of solid lattice vibration. Like electrons, phonons have allowable energy levels in

the solid and a density of phonon states. Quantum confinement generally lowers the values of thermal properties such as thermal conductivity, but can increase the specific heat of LDMs compared to their bulk counter-parts, due to increased boundary scattering and quantization of the phonon DOS. For example, Si nanowires compared to bulk Si have a reduced thermal conductivity χ due to quantification of the DOS, a development important for thermoelectric applications [9]. Nanowires are also great candidates for temperature sensors, as their conductance increases with increasing temperatures [10].

Other shape, surface and interfacial effects characteristic of LDMs are very beneficial. A large surface-to-volume ratio is a big advantage that can be exploited for example in excitonic solar cells, where it's important to have large interfacial contact area between the p-type and the n-type material. Other examples are size-, shape- and or facet-controlled catalytic nanoparticles: their high surface-to-volume ratios, inherent energy of exposed atoms and surface-specific binding can lead to a high reactivity and selectivity [11].

Carbon LDMs

In my thesis I have focused on carbon as a unique precursor for low dimensional materials. Graphene is a one-atom thick planar monolayer of sp^2 -bonded carbon atoms organized in a hexagonal crystal lattice (Fig. 1.1). It can be thought of as the building block for carbon materials of all other dimensionalities (Fig. 1.1). 3D graphite for example is essentially composed of stacked sheets of 2D graphene with weak interplane bonding; the distance between the sheets is 0.34 nm [12]. It was shown that the electronic structure of stacked graphene already approaches that of graphite at 10 layers [13]. This

trend can also be observed by monitoring the DOS of graphene, bilayer graphene, trilayer graphene and graphite, schematically drawn in Figure 1.1. Figure 1.1 also illustrates that graphene can be wrapped to form a 0D bucky ball with a completely discrete DOS or rolled up to form a 1D single walled carbon nanotube (SWCNT) with discontinuous spikes in its DOS, known as Van Hove singularities (Fig. 1.1). Graphene and SWCNTs have unique and remarkable mechanical, electrical and optical properties.

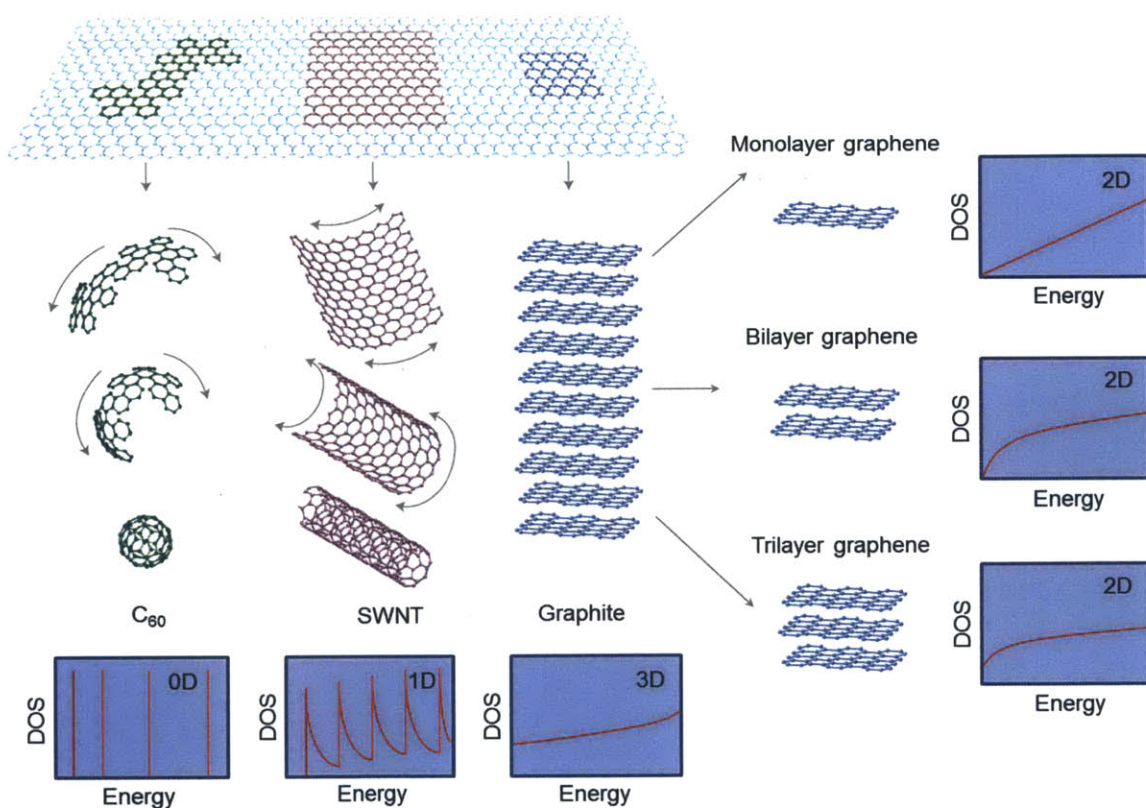


Figure 1.1. Carbon low dimensional materials. 2D Graphene (top panel) can be thought of as the building block of carbon materials of all other dimensionalities: 0D buckyballs, 1D carbon nanotubes and 3D graphite. Reprinted in part with permission [14]. A qualitative Density Of States (DOS) of each material is included.

Graphene

Graphene has been studied theoretically for more than sixty years [15,16], but was never believed to exist in reality since all two-dimensional crystal structures were considered to be thermodynamically unstable [17,18]. Interest in graphene has exploded since the discovery of free-standing graphene and the demonstration that quasiparticles in graphene are massless Dirac fermions [14,19]. Andre Geim and Konstantin Novoselov were awarded the 2010 Nobel Prize in Physics for this work.

Graphene can be mechanically exfoliated from highly ordered pyrolytic graphite (HOPG), synthesized on metal catalyst substrates via chemical vapor deposition, grown epitaxially on silicon carbide, or obtained via the reduction of graphene oxide [20].

The valence and conduction band of graphene touch at 6 corners of the two-dimensional hexagonal Brillouin zone, making it a semimetal. The energy-momentum ($E-k$) dispersion relationship is linear for low energies near these 6 corners (see DOS of graphene in inset Figure 1.1). The electron mobility (which represents how fast an electron can propagate through a materials when pulled by an electric field) of graphene can reach up to $25000 \text{ cm}^2/(\text{V.s})$ for graphene supported on SiO_2 (with carrier density $n = 5 \times 10^{12} \text{ cm}^{-2}$), and can reach values up to $230000 \text{ cm}^2/(\text{V.s})$ for suspended graphene (with carrier density $n = 2 \times 10^{11} \text{ cm}^{-2}$) [21]. This can be put in perspective by realizing the electron mobility of p-doped silicon (phosphorus density $= 10^{13} \text{ cm}^{-3}$) is $\sim 1400 \text{ cm}^2/(\text{V.s})$. Note that because graphene is a semimetal, it can be reduced to nanoscale dimensions without becoming an insulator, as is the case for many doped semiconductors.

Graphene is optically transparent (just 2.3% of white light is absorbed [22]). It is both flexible and strong; it has a breaking strength of 42 N/m, a Young's modulus of 1 TPa [23]. It has a specific surface area of $2630 \text{ m}^2/\text{g}$. Suspended graphene has a room

temperature thermal conductivity of $\sim 5000 \text{ W}/(\text{m}\cdot\text{K})$ [24]; this is quite remarkable, as it is 2.5 times higher than the room-temperature thermal conductivity of graphite (its bulk equivalent).

SWCNT

SWCNTs are synthesized via arc discharge [25], laser ablation [26], high-pressure carbon monoxide disproportionation [27], and chemical vapor deposition [28]. Length to diameter ratios of 132000000:1 have been achieved (length 18.5cm, diameter 1.4nm) [29]. Conceptually, a SWCNT can be thought of as a rolled up sheet of graphene. The vector along which the graphene sheet is rolled up (called chiral vector \mathbf{C}) and the tube diameter (nanometer-scale) determine the exact form of the DOS of the resulting SWCNT, whether it is metallic, semi-metallic or semiconducting, and the size of its band gap. The chiral vector \mathbf{C} can be written as $\mathbf{C} = n\mathbf{a}_1 + m\mathbf{a}_2$, where \mathbf{a}_1 and \mathbf{a}_2 are the graphene lattice vectors (Fig. 1.2.). The pair (n,m) is called the chiral index or the SWCNT chirality.

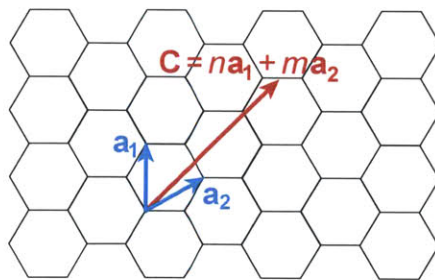


Figure 1.2. SWCNT physical structure. \mathbf{a}_1 and \mathbf{a}_2 are graphene's basic lattice vectors. A SWCNT can be thought of as rolled of graphene sheet along the chiral vector \mathbf{C} . This determines the physical and electronic structure of the resulting SWCNT.

The chirality of the SWCNT thus uniquely defines its electronic density of states. The occurrence of the Van Hove singularities in the SWCNTs electronic DOS (inset Fig.

1.1), as well as the presence of a band gap for semiconducting (sc-) SWCNTs is the reason for sc-SWCNT near-infrared (nIR) fluorescence [30], which is stable and without photobleaching [31].

It is important to note that SWCNTs differ from nanowires in the sense that they are flexible, seamless hollow cylinders, whereas nanowires are solid cylinders, often with a larger diameter with many dangling bonds on their surface.

Room temperature electron mobilities of up to $79000 \text{ cm}^2/(\text{V}\cdot\text{s})$ have been achieved for sc-SWCNTs [32] and metallic (m-) SWCNTs have a reported current density of $4 \times 10^9 \text{ A/cm}^2$, roughly 1000 times higher than that in copper [33]. The absence of dangling bonds on their surface also results in greatly enhanced electric ballistic transport in SWCNTs compared to nanowires: ballistic length scales of up to 0.5mm have been measured in SWCNTs at room temperature [34], making them ideal candidates for nano-electronic applications such as field-effect transistors [35].

Like graphene, SWCNTs have a flexibility and transparency (SWCNT-films have a reported optical transparency of $>80\%$ [36]) implying they can be used as thin transparent flexible conductive electrodes [37-39].

SWCNTs have tensile strength of $\sim 100 \text{ GPa}$ [40], a Young's modulus of up to $\sim 2 \text{ TPa}$ [41] and due to their low density (2.1 g/cm^3) this amounts to an impressive specific strength of 47619 kNm/kg , compared to 154 kNm/kg for high-carbon steel.

Unlike most LDMs carbon nanotubes exhibit a larger value of the room-temperature thermal conductivity χ ($3000\text{-}35000 \text{ W/mK}$ [24]) in comparison to that of their already very conductive bulk equivalent graphite, since the inter-layer interactions in graphite quench the conductivity by nearly an order of magnitude [42].

1.2. Exciton engineering: the next frontier of chemical reaction engineering [1]

Excitons are electron-hole quasiparticles that are central to the operation of most photovoltaics and certainly many photocatalytic processes [43]. They form when an electromagnetic wave interacts with many types of matter; in my work specifically, I'm interested in excitons formed in semiconductors. A photon with an energy greater than the semiconductor's band gap can be absorbed by it. In this process, the photon excites an electron from the valence band to the conduction band, leaving behind a positively-charged hole (the absence of an electron) in the valence band. The electron and hole are bound together by a Coulombic force, creating a localized neutral particle, the exciton. The separation of excitons into electrons and holes is the source of usable electrical energy in a polymer heterojunction photovoltaic cell for example, or a dye sensitized solar cell. The diffusion of excitons to an engineered interface that can subsequently split them into electrons and holes remains a central challenge in many polymer and nano-composite photovoltaic cells.

But while one may find many chemical engineers making significant contributions to the materials for solar energy systems, quite curiously, one notices little conceptual usage of the exciton in the work of a chemical engineer. This is unusual, because unlike electrons or holes moving throughout a photovoltaic device, excitons are largely neutral. We relegate the former particles to the electrical engineers and physicists for description, since an explicit accounting of charge is central to their modeling. The exciton, however, can be described using the same population balances, mass transfer and chemical kinetics approaches that chemical engineers know well and practice extensively.

In materials with a low dielectric constant (e.g. π -conjugated polymers) or materials with constrained physical dimensions the Coulomb interaction between the electron and the hole may be significantly strong, and this leads to relatively small excitons, on the order as the size of a unit cell, with a typical binding energy of 0.1 to 1 eV. This type of exciton is called a Frenkel exciton and is relevant in organic photovoltaics and nanomaterials [44]. A good conceptual model for the Frenkel exciton is a hydrogen atom with a positively charged electron vacancy (i.e. a hole) as the nucleus and an orbiting electron (Fig. 1.3a and 1.3b), although the latter is roughly an order of magnitude smaller (diameter = 1.1 Å) and an order of magnitude more tightly bound (binding energy = 13.6eV). Because a Frenkel exciton is small enough, it can be treated as a delocalized particle: it has a diffusivity as it ‘hops’ from lattice site to lattice site (Fig. 1.3c), and can “react” to yield electrons and holes as important products. Excitons also “react” in the bulk in many first and second order reaction pathways. They can radiatively recombine, producing a photon. Many optically active nanostructures and polymeric materials will fluoresce and this process can be considered to have first order kinetics. Excitons can non-radiatively recombine to produce lattice vibrations or phonons in a similar but distinct first order process. Auger recombination, also referred to as exciton-exciton annihilation (EEA) involves second order and higher kinetics since it involves two excitons: upon collision, one exciton is annihilated whereas the other is briefly excited to a higher energy level by the energy released in the collision, after which it decays back to first excited state. These reaction pathways are schematically presented in Fig. 1.3d-f.

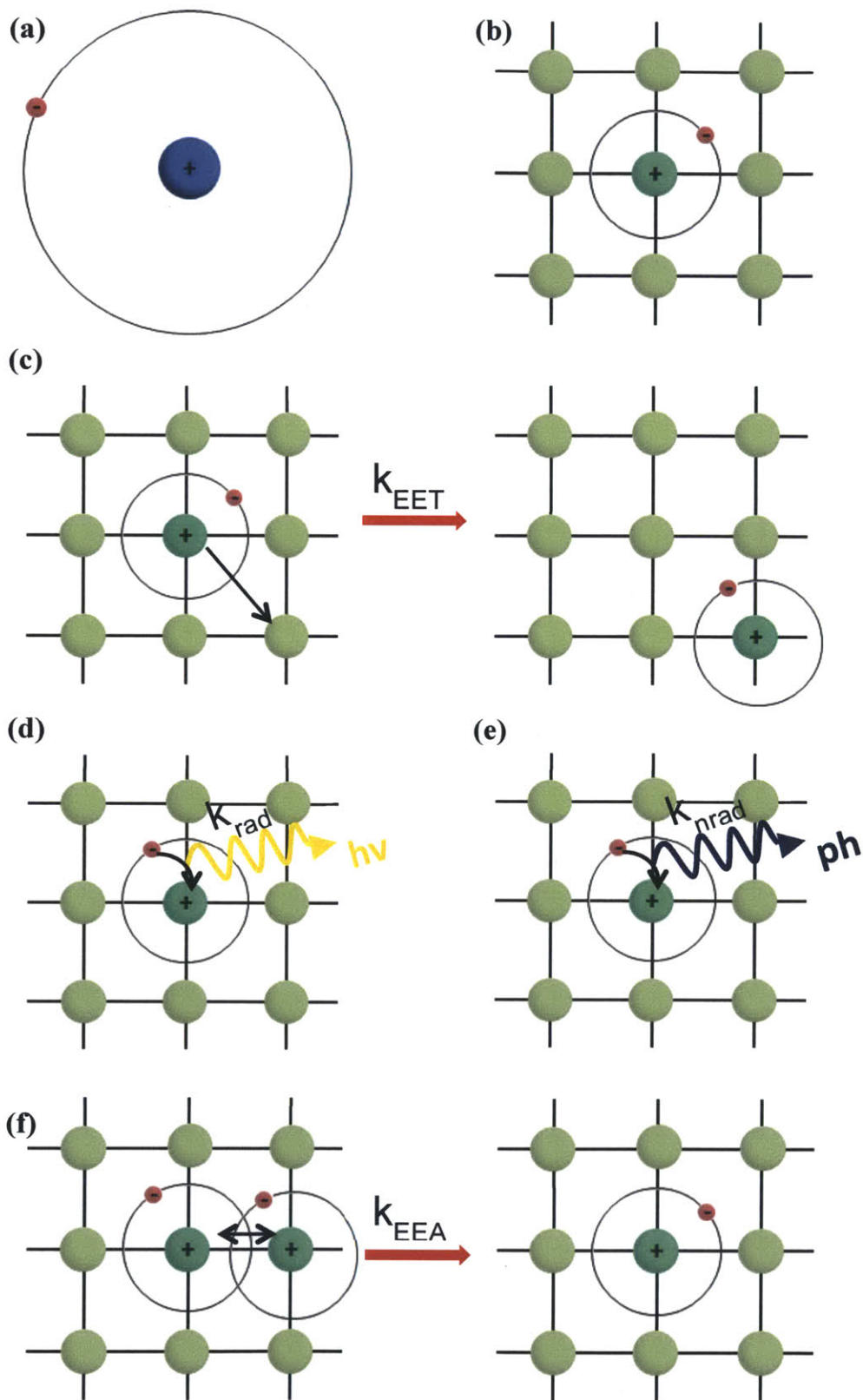


Figure 1.3. Exciton engineering. **(a)** Schematic representation of a hydrogen atom: one electron orbiting one proton, bound together by Coulomb interactions. **(b)** Frenkel exciton in a lattice: one electron was promoted from the valence band to the conduction band leaving behind a localized positively-charged hole. Coulomb interactions are relatively strong in low-dielectric materials. However, the binding energy is smaller and the particle size is larger than that of a hydrogen atom due to dielectric screening. **(c)** Exciton energy transfer, which can be thought of as a form of diffusion. **(d)** Radiative recombination of an exciton, giving rise to photoluminescence. **(e)** Defect-mediated non-radiative decay giving rise to a phonon. **(f)** Exciton-exciton annihilation where upon the collision of two excitons one is annihilated whereas the other used the energy from the collision to be promoted to a higher energy level.

There are two ways in which engineers can simulate the behavior of excitons as conserved particles: via deterministic and stochastic models.

A deterministic reaction-diffusion model for a system where an electromagnetic source is incident onto a film of an excitonic material can be represented by the following partial differential equation (PDE):

$$\frac{\partial N(y,t)}{\partial t} = G(y,t) + \frac{\partial^2 (D \cdot N(y,t))}{\partial y^2} - \frac{N(y,t)}{\tau} \quad (1.1),$$

where N represents the population of excitons in the film, which is a function of time t and depth y in the film. The one-dimensionality implied by equation (1.1) is typical for symmetric domains. The term $G(y,t)$ represents the bulk generation rate of excitons as in the case of a continuous light source (e.g. the sun for solar cell applications). This term can be absent and replaced by an initial condition if the film is excited at time $t=0$ with a short laser pulse in a pump-probe experiment for example. The diffusion coefficient D is defined conventionally for excitons in the domain. Diffusion has been reported to be thermally activated with reported values of 40 to 60 meV (*i.e.* 0.92 to 1.38 kcal/mol) for the activation barrier in π -conjugated polymer films [45,46]. The third term on the right hand side of eq. (1.1) lumps all excitonic decay channels and is characterized by the

exciton lifetime t in the material. For π -conjugated polymers the exciton lifetime is typically on the order of 100ps [47]. This lifetime is dominated by non-radiative decay (the radiative exciton lifetime is only on the order of ~ 1 ns) [46]. The excitonic decay shows Arrhenius decay with activation energies reported from 15 to 120meV (*i.e.* 0.35 to 2.77 kcal/mol) [44,45,48-50]. Depending on the boundary conditions (e.g. quenching of excitons at interfaces with other materials) the solution to eq. (1.1) will be of a different form.

We can define a diffusion length L_D for the excitons in the film:

$$L_D = \sqrt{D\tau} \tag{1.2}$$

This value represents the average distance an exciton can ‘travel’ in the material within its lifetime t and is typically measured in different materials and at different temperatures by monitoring the decay of photoluminescence (PL) after excitation at $t=0s$ using time-resolved spectroscopy.

Another typical chemical engineering parameter that is amenable to the system of reacting and diffusing excitons is the Thiele Modulus, which can be compared across several materials and systems. This parameter arises from the nondimensionalization of eq. (1.1) and considers the length scale of the domain L , in which the exciton is free to diffuse. This can be the thickness of the polymer film, a polymer domain in which the exciton resides, or the length of a nanotube along which the exciton migrates in 1D. The Thiele modulus ϕ of excitons can be defined as the square root of the ratio of the reaction rate to the diffusion rate:

$$\phi = \sqrt{\frac{kL^2}{D}} = \sqrt{\frac{L^2}{\tau D}} \quad (1.3).$$

As an example I calculated the Thiele modulus as a function of temperature for a system described in literature. Mikhnenko *et al.* extracted the exciton lifetime t in a thin film (13nm) of MDMO-PPV ((poly[2-methyl-5-(3',7'-dimethyloctyloxy)-p-phenylenevinylene]) at different temperatures by performing PL decay experiments as described above [51]. By solving eq. (1.1) they obtain a value of the diffusion coefficient. This diffusion coefficient is related to the exciton diffusion length via eq. (1.2). Table 1.1 shows the main parameters as a function of temperature. In the last column I calculated the Thiele modulus. It is clear that as the temperature increases the Thiele modulus becomes smaller and the system evolves from diffusion-controlled toward reaction-controlled, although the modulus remains of order 1.

Temperature T (K)	Lifetime t (ns)	Diffusion Coefficient D ($10^{-4}\text{cm}^2/\text{s}$)	Exciton Diffusion Length L_D (nm)	Thiele modulus ϕ
4	0.60	1.4	2.9	4.5
50	0.62	1.5	3.05	4.3
100	0.59	1.6	3.1	4.2
150	0.65	1.6	3.24	4.0
200	0.63	2.0	3.55	3.7
250	0.69	2.3	4.0	3.3
293	0.63	3.2	4.5	2.9

Table 1.1. Calculation of the Thiele modulus for a 13 nm thin film of MDMO-PPV. The MDMO-PPV is spun from solution on top of a cross-linked fullerene layer, called poly(F2D) that serves as the exciton quenching wall. In order to measure the PL decay, samples were excited by a 100fs pulsed Kerr mode locked Ti-sapphire laser, frequency doubled at about 400nm [51].

In reality, reaction and diffusion of excitons happen on a molecular level and are

stochastic in nature. Therefore, excitonic systems can often be represented by a Kinetic Monte Carlo (KMC) simulation, where the probability of an event occurring is calculated within a certain time span. Stochastic models are usually adopted when there is a small number N of excitons in the system and fluctuation is unavoidable. In the limit of large values of N , the average result of the stochastic simulation will converge to the deterministic result.

In these Monte Carlo simulations excitons are generated at the different lattice sites at rates determined by the incident light intensity and spectrum as well as by the optical properties of the excitonic material itself. Once an exciton is generated, the simulation tracks its path. Each different event described above (radiative combination, non-radiative recombination or diffusion) can be characterized by a waiting time t_w that depends on its actual rate constant k :

$$\tau_w = -\frac{1}{k} \ln(X) \quad (1.4),$$

where X represents a random number in the interval $[0,1]$. For each exciton generated, the waiting time for all different events is calculated and the event with the smallest waiting time is selected to occur.

Although the migration of excitons in solids and nanoparticles is often described by Fickian diffusion in the deterministic approach, formally, an exciton “hops” to another point in space because the local oscillation of its electric field creates a new exciton at some other point in the matrix. This exchange, called exciton energy transfer (EET, Fig. 1.3c), is stochastic in nature, and hence is easily amenable to description by Kinetic Monte Carlo simulation. The transfer is biased towards portions of the material that have

decreased energy states. Typically a hopping rate k_{ij} constant is defined:

$$k_{ij} = k_0 f(r_{ij}) \begin{cases} 1 & \text{if } E_i - E_j > 0 \\ \exp\left(\frac{-\Delta E_{ij}}{k_B T}\right) & \text{if } E_i - E_j \leq 0 \end{cases} \quad (1.5),$$

where k_0 is the attempt-to-escape frequency, E_i and E_j are the energies of site i and site j , respectively, ΔE_{ij} is their difference, r_{ij} is the distance between the sites involved, k_B is the Boltzmann constant and T is the temperature. Hopping is considered within the intrinsic density of states of the excitonic material. The functional form of $f(r_{ij})$ depends on the system under consideration. For bulk heterojunction (BHJ) solar cells for example, the hopping of excitons can be described by Förster resonance energy transfer (FRET) [52].

In this case $f(r_{ij})$ takes the following form

$$f(r_{ij}) = \frac{1}{1 + \left(\frac{r_{ij}}{a}\right)^6} \approx \left(\frac{a}{r_{ij}}\right)^6 \quad (1.6),$$

where a is the Förster radius, defined as the value of the distance at which the hopping rate is equal to the decay rate (the energy transfer efficiency is 50%). This value depends on the overlap between the emission spectrum of the donor material and the absorption spectrum of the acceptor material. A donor chromophore, initially in its electronic excited state, can transfer energy to an acceptor chromophore (in proximity, typically less than 1 nm) through nonradiative dipole-dipole coupling. This expression is valid in bulk heterojunctions where the donor and the acceptor molecules are blended on a nanometer length scale. However in a planar heterojunction the donor and acceptor molecules are typically separated by much larger distances and the hopping trajectory of excitons

between different sites of one material is better described by a random walk. In this case, $f(r_{ij})$ is best described with a Miller-Abrahams expression [53]:

$$f(r_{ij}) = \exp\left(-2 \times \frac{r_{ij}}{\alpha}\right) \quad (1.7),$$

where α is the localization length of excitons in the excitonic material.

The macroscopically defined diffusion coefficient D can also be related to what happens at the molecular level:

$$D = \frac{\langle r^2 \rangle}{2d t} \quad (1.8).$$

In this equation $\langle r^2 \rangle$ represents the mean-square displacement of the exciton during the time-interval t , two parameters which can easily be predicted by the Kinetic Monte Carlo simulation. Note that d represents the dimensionality of the system ($d = 1, 2$ or 3).

There are many reaction engineering applications of exciton transport and reaction, and these concepts have driven and guided key aspects of the work by the authors, as is demonstrated in my work.

1.3. References

- 1 Paulus, G. L. C., Shimizu, S., Abrahamson, J. T., Zhang, J., Hilmer, A. J. & Strano, M. S. The chemical engineering of low-dimensional materials. *AIChE Journal* **57**, 1104-1118 (2011).
- 2 Davies, J. H. *The Physics of Low-Dimensional Semiconductors*, sixth edition. *Cambridge University Press*, 1-438 (2006).
- 3 Weisman, R. B. & Bachilo, S. M. Dependence of optical transition energies on structure for single-walled carbon nanotubes in aqueous suspension: An empirical Kataura plot. *Nano Letters* **3**, 1235-1238 (2003).
- 4 Yu, H., Li, J. B., Loomis, R. A., Gibbons, P. C., Wang, L. W. & Buhro, W. E. Cadmium selenide quantum wires and the transition from 3D to 2D confinement. *Journal of the American Chemical Society* **125**, 16168-16169 (2003).
- 5 Li, L. S., Hu, J. T., Yang, W. D. & Alivisatos, A. P. Band gap variation of size- and shape-controlled colloidal CdSe quantum rods. *Nano Letters* **1**, 349-351 (2001).
- 6 Soloviev, V. N., Eichhofer, A., Fenske, D. & Banin, U. Molecular limit of a bulk semiconductor: Size dependence of the "band gap" in CdSe cluster molecules. *Journal of the American Chemical Society* **122**, 2673-2674 (2000).
- 7 Cahay, M. L., J.P.; Lockwood, D.J.; Bandyopadhyay, S.; Harris, J.S. Quantum confinement VI: nanostructured materials and devices. *Electrochemical Society*, 1-398 (2001).
- 8 Zhou, X., Dayeh, S. A., Aplin, D., Wang, D. & Yu, E. T. Direct observation of ballistic and drift carrier transport regimes in InAs nanowires. *Applied Physics Letters* **89**, 053113-1:3 (2006).
- 9 Li, D. Y., Wu, Y. Y., Kim, P., Shi, L., Yang, P. D. & Majumdar, A. Thermal conductivity of individual silicon nanowires. *Applied Physics Letters* **83**, 2934-1:3 (2003).
- 10 Lu, X. & Chu, J. H. Phonon heat transport in silicon nanowires. *European Physical Journal B* **26**, 375-378 (2002).
- 11 Lee, K., Kim, M. & Kim, H. Catalytic nanoparticles being facet-controlled. *Journal of Materials Chemistry* **20**, 3791-3798 (2010).
- 12 Bacon, G. The interlayer spacing of graphite. *Acta Crystallographica* **4**, 558-561 (1951).
- 13 Partoens, B. & Peeters, F. M. From graphene to graphite: Electronic structure around the K point. *Physical Review B* **74**, 075404-1:3 (2006).
- 14 Geim, A. K. & Novoselov, K. S. The rise of graphene. *Nature Materials* **6**, 183-191 (2007).
- 15 Wallace, P. R. The band theory of graphite. *Physical Review* **71**, 622-634 (1947).
- 16 Slonczewski, J. C. & Weiss, P. R. Band structure of graphite. *Physical Review* **109**, 272-279 (1958).
- 17 Peierls, R. E. Quelques proprietes typiques des corps solides. *Ann. IH Poincare* **5**, 177-122 (1935).
- 18 Landau, L. Zur theorie der phasenumwandlungen II. *Phys. Z. Sowjetunion* **11**, 26-35 (1937).
- 19 Novoselov, K., Geim, A. K., Morozov, S., Jiang, D., Grigorieva, M. K. I., Dubonos, S. & Firsov, A. Two-dimensional gas of massless Dirac fermions in graphene. *Nature* **438**, 197-200 (2005).

- 20 Soldano, C., Mahmood, A. & Dujardin, E. Production, properties and potential of graphene. *Carbon* **48**, 2127-2150 (2010).
- 21 Bolotin, K. I., Sikes, K., Jiang, Z., Klima, M., Fudenberg, G., Hone, J., Kim, P. & Stormer, H. Ultrahigh electron mobility in suspended graphene. *Solid State Communications* **146**, 351-355 (2008).
- 22 Nair, R., Blake, P., Grigorenko, A., Novoselov, K., Booth, T., Stauber, T., Peres, N. & Geim, A. Fine structure constant defines visual transparency of graphene. *Science* **320**, 1308-1308 (2008).
- 23 Lee, C., Wei, X., Kysar, J. W. & Hone, J. Measurement of the elastic properties and intrinsic strength of monolayer graphene. *Science* **321**, 385-388 (2008).
- 24 Balandin, A. A. Thermal properties of graphene and nanostructured carbon materials. *Nature Materials* **10**, 569-581 (2011).
- 25 Ebbesen, T. & Ajayan, P. Large-scale synthesis of carbon nanotubes. *Nature* **358**, 220-222 (1992).
- 26 Guo, T., Nikolaev, P., Rinzler, A. G., Tomanek, D., Colbert, D. T. & Smalley, R. E. Self-assembly of tubular fullerenes. *The Journal of Physical Chemistry* **99**, 10694-10697 (1995).
- 27 Nikolaev, P., Bronikowski, M., Bradley, R., Rohmund, F., Colbert, D., Smith, K. & Smalley, R. Gas-phase catalytic growth of single-walled carbon nanotubes from carbon monoxide. *Chemical Physics Letters* **313**, 91-97 (1999).
- 28 José Yacamán, M., Miki-Yoshida, M., Rendón, L. & Santiesteban, J. Catalytic growth of carbon microtubules with fullerene structure. *Applied Physics Letters* **62**, 202-204 (1993).
- 29 Wang, X., Li, Q., Xie, J., Jin, Z., Wang, J., Li, Y., Jiang, K. & Fan, S. Fabrication of ultralong and electrically uniform single-walled carbon nanotubes on clean substrates. *Nano Letters* **9**, 3137-3141 (2009).
- 30 Bachilo, S. M., Strano, M. S., Kittrell, C., Hauge, R. H., Smalley, R. E. & Weisman, R. B. Structure-assigned optical spectra of single-walled carbon nanotubes. *Science* **298**, 2361-2366 (2002).
- 31 Carlson, L. J. & Krauss, T. D. Photophysics of individual single-walled carbon nanotubes. *Accounts of chemical research* **41**, 235-243 (2008).
- 32 Dürkop, T., Getty, S., Cobas, E. & Fuhrer, M. Extraordinary mobility in semiconducting carbon nanotubes. *Nano Letters* **4**, 35-39 (2004).
- 33 Hong, S. & Myung, S. A flexible approach to mobility. *Nature Nanotechnology* **2**, 207-208 (2007).
- 34 Purewal, M. S., Hong, B. H., Ravi, A., Chandra, B., Hone, J. & Kim, P. Scaling of resistance and electron mean free path of single-walled carbon nanotubes. *Physical Review Letters* **98**, 186808-1:4 (2007).
- 35 Martel, R., Schmidt, T., Shea, H. R., Hertel, T. & Avouris, P. Single- and multi-wall carbon nanotube field-effect transistors. *Applied Physics Letters* **73**, 2447-2449 (1998).
- 36 Saran, N., Parikh, K., Suh, D.-S., Munoz, E., Kolla, H. & Manohar, S. K. Fabrication and characterization of thin films of single-walled carbon nanotube bundles on flexible plastic substrates. *Journal of the American Chemical Society* **126**, 4462-4463 (2004).
- 37 Pasquier, A. D., Unalan, H. E., Kanwal, A., Miller, S. & Chhowalla, M. Conducting and transparent single-wall carbon nanotube electrodes for polymer-fullerene solar cells. *Applied Physics Letters* **87**, 203511-1:3 (2005).

- 38 Wu, J. B., Becerril, H. A., Bao, Z. N., Liu, Z. F., Chen, Y. S. & Peumans, P. Organic solar cells with solution-processed graphene transparent electrodes. *Applied Physics Letters* **92**, 263302-1:3 (2008).
- 39 Park, H., Rowehl, J. A., Kim, K. K., Bulovic, V. & Kong, J. Doped graphene electrodes for organic solar cells. *Nanotechnology* **21**, 505204-1:6 (2010).
- 40 Wang, M. Å., Golberg, D. & Bando, Y. Tensile tests on individual single-walled carbon nanotubes: linking nanotube strength with its defects. *Advanced Materials* **22**, 4071-4075 (2010).
- 41 Salvétat, J.-P., Bonard, J.-M., Thomson, N., Kulik, A., Forro, L., Benoit, W. & Zuppiroli, L. Mechanical properties of carbon nanotubes. *Applied Physics A: Materials Science & Processing* **69**, 255-260 (1999).
- 42 Berber, S., Kwon, Y. K. & Tomanek, D. Unusually high thermal conductivity of carbon nanotubes. *Physical Review Letters* **84**, 4613-4616 (2000).
- 43 Liang, W. Y. Excitons. *Physics Education* **5**, 226-228 (1970).
- 44 Frenkel, J. On the Transformation of light into Heat in Solids. I. *Physical Review* **37**, 17-44 (1931).
- 45 Devi, L. S., Al-Suti, M. K., Dosche, C., Khan, M. S., Friend, R. H. & Kohler, A. Triplet energy transfer in conjugated polymers. I. Experimental investigation of a weakly disordered compound. *Physical Review B* **78**, 045210-1:8 (2008).
- 46 Lutich, A. A., Poschl, A., Jiang, G. X., Stefani, F. D., Susa, A. S., Rogach, A. L. & Feldmann, J. Efficient energy transfer in layered hybrid organic/inorganic nanocomposites: A dual function of semiconductor nanocrystals. *Applied Physics Letters* **96**, 083109-1: 3 (2010).
- 47 Skotheim, T. A. R., J.R. Handbook of Conducting Polymers, Third Edition. *CRC Press, Taylor & Francis Group, LLC.*, 1-1024 (2007).
- 48 Xu, B., Lowe, J. & Holdcroft, S. Non-radiative decay channels in poly(3-hexylthiophene) and poly(3-dodecylthiophene) and how to control them by molecular engineering. *Thin Solid Films* **243**, 638-642 (1994).
- 49 Ohkita, H., Cook, S., Ford, T. A., Greenham, N. C. & Durrant, J. R. Monomolecular triplet decay dynamics in fluorene-based conjugated polymer films studied by transient absorption spectroscopy. *Journal of Photochemistry and Photobiology A: Chemistry* **182**, 225-230 (2006).
- 50 Bjorklund, T. G., Lim, S. H. & Bardeen, C. J. Use of picosecond fluorescence dynamics as an indicator of exciton motion in conjugated polymers: Dependence on chemical structure and temperature. *Journal of Physical Chemistry B* **105**, 11970-11977 (2001).
- 51 Mikhnenko, O. V., Cordella, F., Sieval, A. B., Hummelen, J. C., Blom, P. W. M. & Loi, M. A. Temperature dependence of exciton diffusion in conjugated polymers. *Journal of Physical Chemistry B* **112**, 11601-11604 (2008).
- 52 Förster, T. Zwischenmolekulare energiewanderung und fluoreszenz. *Annalen Der Physik* **2**, 55-75 (1948).
- 53 Miller, A. & Abrahams, E. Impurity conduction at low concentrations. *Physical Review* **120**, 745-755 (1960).

2. Study and manipulation of SWCNT-SWCNT interactions

Some of the work, text and figures presented in this chapter are reprinted or adapted with permission from reference [1] (Copyright © 2010, Nature Publishing Group).

2.1. Background and motivation

There has been renewed interest in developing photonic materials for optical concentration [2,3] and photon collection [4,5] for applications such as higher efficiency photovoltaic cells [6] and infrared photo emitters/photodetectors [7]. One dimensional (1D) materials, such as inorganic nanowires [4] and carbon nanotubes [8-14] are promising candidates for this due to their aligned axial transition dipoles [8-10], large absorption cross sections and high quantum efficiencies [11-13]. In the case of single-walled carbon nanotubes (SWCNTs), photonic applications have been hampered by an inability to separate and sort them as optically distinct species [10,15-17]. Recent advances in our laboratory [16] and elsewhere [17] have enabled this separation on preparative scales. While the photophysics of isolated, single carbon nanotubes and heterogeneous aggregates have been extensively studied [8-14], these new separation methods allow us to construct optically homogenous materials of dimensions much larger than typical excitation wavelengths of interest, enabling new photonic structures.

Optical properties of SWCNT bundles have been studied abundantly using Rayleigh and Raman scattering [8-10] and photoluminescence (PL) excitation (PLE) and absorption spectroscopy [11-14]. Each type of SWCNT (classified by its (n,m) chirality)

has a unique electronic band structure. An example is shown in Figure 2.1a for a semiconducting SWCNT, characterized by the typical Van Hove Singularities and a band gap. E_{ii} represents the optical transition energy between the i^{th} valence (v_i) and conduction (c_i) band. In nanotube fluorescence, light absorption at E_{22} excites an electron from v_2 to c_2 , forming an exciton. The exciton then non-radiatively decays to the first excited state (v_1, c_1) and finally recombines radiatively giving rise to fluorescent emission at E_{11} , usually in the near-infrared (NIR). The exciton lifetime is about 100 ns [18].

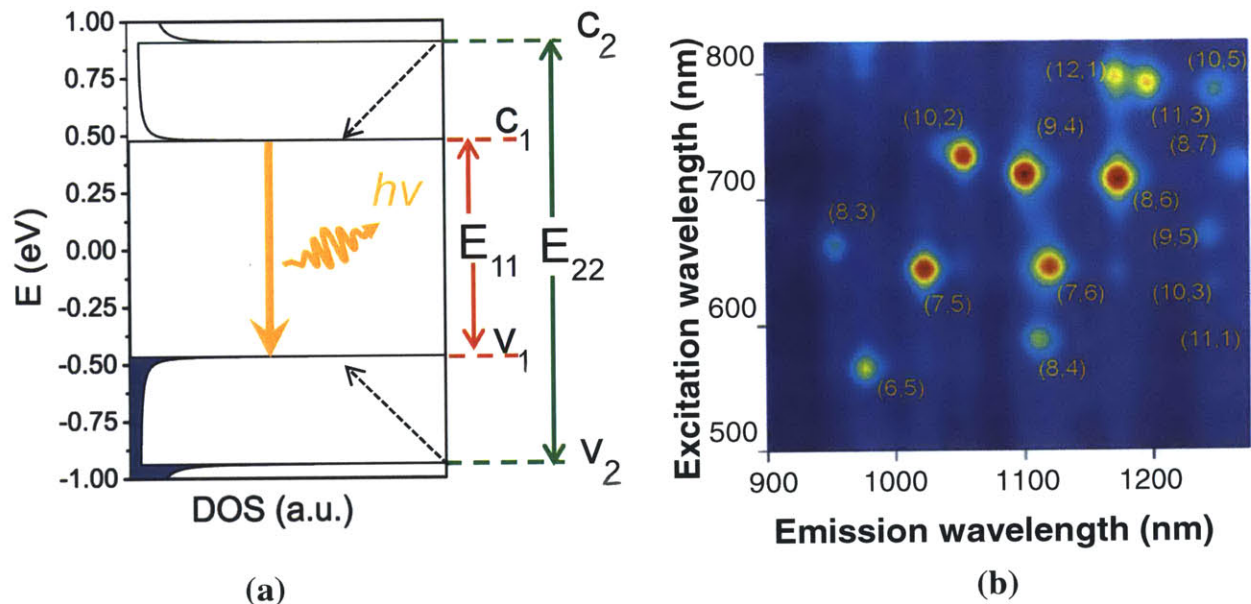


Figure 2.1. SWCNT photophysics. **(a)** Schematic electronic density of states of a sc-SWCNT. Solid arrows denote optical excitation and emission transitions; dashed lines denote non-radiative relaxation paths for electrons (in the conduction bands, denoted by c_i) and holes (in the valence bands, denoted by v_i) Adapted with permission from reference [19]. **(b)** Excitation-emission profile: contour plot of fluorescence intensities for a solution of HiPco SWCNTs as a function of the excitation wavelength (corresponding to E_{22}) and the resulting emission wavelength (corresponding to E_{11}). Adapted with permission from [20] (©IOP Publishing Ltd and Deutsche Physikalische Gesellschaft. Published under a CC BY-NC-SA license).

As a result of the unique SWCNT band structure one can assemble an excitation-emission profile (EEP) where upon broad range excitation of a sample containing various

chiral SWCNT types the resulting fluorescence is recorded. Each type of chirality SWCNT is characterized by a unique (E_{11} , E_{22}) pair and thus causes a single fluorescence peak in the EEP. Combining these fluorimetric results with resonance Raman data allows each peak to be assigned to a specific SWCNT chirality. An example of an EEP is shown in Figure 2.1b.

Diameter- and distance-dependent exciton energy transfer (EET) (also referred to as Förster resonance energy transfer (FRET) [21]) from larger band gap semiconducting SWCNT to smaller band gap ones within bundles in solution has been illustrated [11-14]. Recently, Lefebvre *et al.* have elegantly examined EET within a single pair of SWCNTs, highlighting the potential for such species to form more complex solid state antenna structures, and concentrators [14]. The systems described in this Chapter create such structures for the first time. Time-resolved spectroscopy of SWCNT bundles reveals extremely rapid excited-state relaxation (1 picosecond) compared to isolated SWCNTs [22]. This behavior has been attributed to energy transfer from the semiconducting to the metallic SWCNTs within each bundle [23], followed by rapid non-radiative carrier cooling in the metallic nanotubes [24]. SWCNT bundles have also found applications in the solar energy field; they can, for example, be used to replace the transparent electrode in organic solar cells [6]. However, none of these applications to date has considered optically homogeneous SWCNT bundles, which have only recently become available in preparative quantities [16] [17] for photonic applications.

The improvement of photonic devices by increases in quantum efficiency as well as power conversion efficiency has been an important research focus for many decades. For example, EET between shorter- and longer-wavelength dyes was utilized to develop

tandem organic solar concentrators with high efficiency [2]. Micro-concentrator photovoltaics using soft-lithographically molded replicas of commercially available lens arrays were demonstrated to increase total output power [3]. In the field of nano-optics, engineering of the nanostructure plays a critical role in the control of propagating light in photonic applications such as optical antennae structures [4,5,7].

In this work, (6,5) semiconducting sc-SWCNTs were isolated and dielectrophoretically spun into largely homogeneous solid filaments. A small residual amount of (7,6) SWCNT leads to a surprisingly large amount of EET in the (6,5)-enriched fiber. We also find that the photoluminescence (PL) quantum yield of these fibers unexpectedly decay sharply as they are heated to only 357 K with recovery upon cooling them back to room temperature. This behavior is attributed to Auger recombination. We then construct core-shell structures where the SWCNT composition determines the absorption bandwidth and where EET is controlled through gradients in the optical band gap of the different SWCNT making up the shell and the core. These structures form antennae that funnel excitons to their core and emit in the nIR regime, creating unique photonic devices, and optical concentrators.

2.2. Experimental Methods and Materials

2.2.1. Preparation of the SWCNT solution

In order to obtain a solution of electronically homogeneous, semiconducting (6,5)-enriched SWCNTs, density gradient centrifugation was used [16,25], originally developed by Arnold *et al.* [17]. We started from a HiPco SWCNT mixture (HPR162.3,

Rice University) and added either sodium cholate (SC) and sodium dodecyl sulfate (SDS) (SC:SDS = 4:1 by weight ratio) or 2 wt% SC alone to suspend the hydrophobic SWCNTs. A density gradient was established using a non-ionic medium, iodixanol (OptiPrep, 60 w/v% iodixanol, Sigma-Aldrich). Three different concentrations for the initial gradient were tested (20, 22.5, and 25 w/v% with a volume of 6 ml), as shown in Figure 2.2a. Upon centrifugation SWCNTs will sediment at the isopycnic point that matches its chirality (where their density matches that of the gradient).

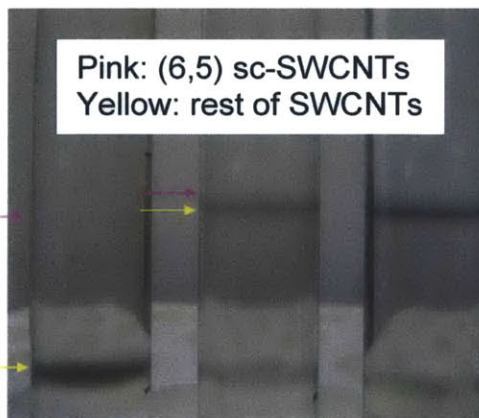
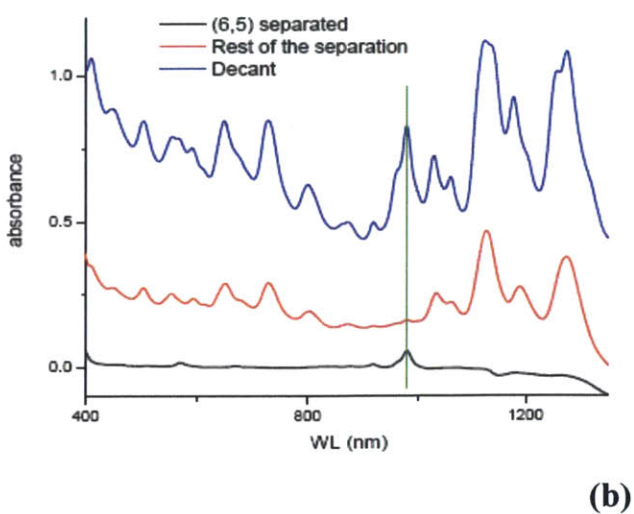
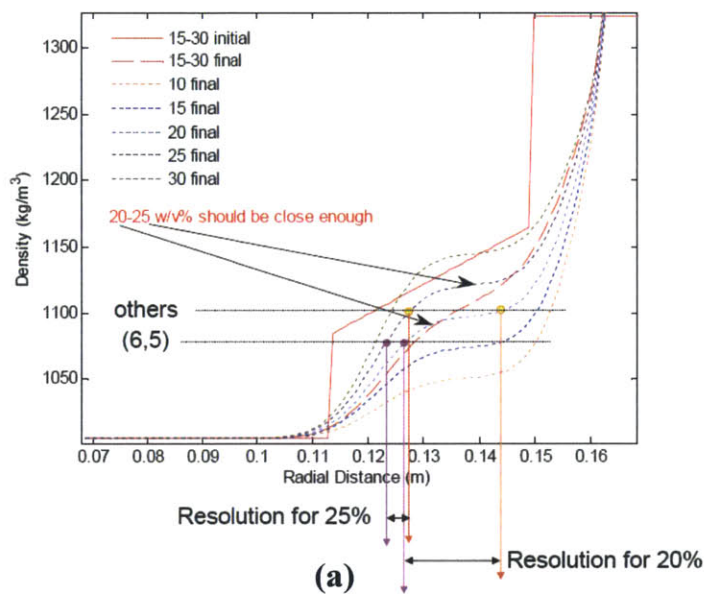


Figure 2.2. SWCNT separation via density ultracentrifugation. **(a)**, Density measurement of the SWCNT separated along the centrifuge tubes. The concentration of the initial gradient was adjusted to be 20, 22.5, and 25 w/v% with a volume of 6 ml. **(b)**, (Left panel) UV-vis-nIR absorption spectra of the SWCNT before and after separation, where a vertical green line positions at the (6,5) E_{11} wavelength. (Right panel) Among these conditions, 20 w/v% of density gradient showed the highest resolution for sorting predominant (6,5) SWCNT (the most left centrifuge tube). Pink and yellow arrows indicate (6,5) and other tubes, respectively.

Among these conditions, the 20 w/v% of density gradient showed the highest resolution for sorting predominant large band gap (6,5) chirality SWCNT (Fig. 2.2a-b). The metallic (m-) SWCNT fraction is unwanted since it has been shown that in nanotube bundles energy is rapidly transferred to m-SWCNTs followed by rapid nonradiative carrier cooling in the m-SWCNTs [23] [24]. Therefore, after the separation of the (6,5) sc-SWCNTs, 4-nitrobenzene diazonium tetrafluoroborate (4-NBD) was added to the remaining solution to selectively react with m-SWCNTs. They were then removed with a density-induced separation technique, leaving a solution of pure sc-SWCNTs with smaller band gaps (larger diameters) compared to the (6,5) fraction. This process is similar to what has been reported in literature [16,17,25,26].

2.2.2. Preparation of the SWCNT fibers

Electronically homogenous fibers of diameters up to 4 μm were created using a mechanically automated dielectrophoresis (DEP) drawing apparatus (Fig. 2.3a). The DEP process is a simple and well-known route to manipulate, align, and assemble one-dimensional nanostructures using an alternating current (AC) electric field [27,28]. In short, an object in solution in which an AC external electric field induces a dipole, experiences a force proportional to the field intensity gradient. In a non-uniform field, the

electric field will be stronger on one side of the object and weaker on the other side of the object. Therefore, there will be a net force on the object. This is the DEP force, which is the driving force for the object to move along. The DEP technique assembles an aligned fiber of a controlled length and diameter from the previously purified and separated (6,5) SWCNT solution (with 2% sodium cholate surfactant) on top of a chemically pre-etched, microscopically sharpened tungsten (W) tip (Fig. 2.3b).

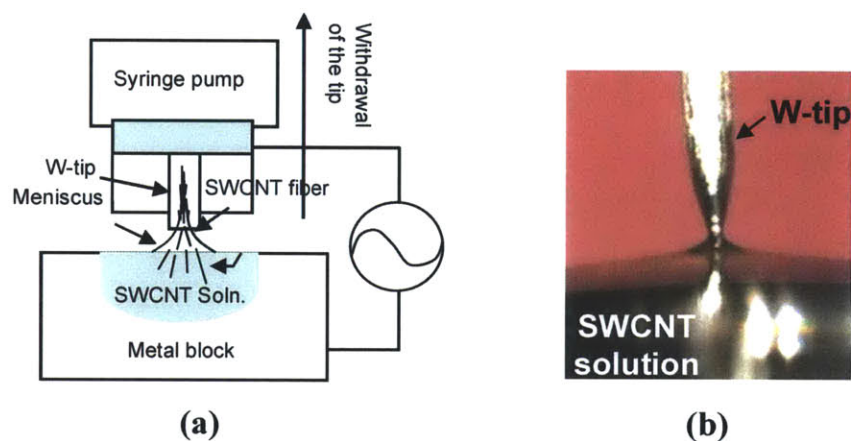


Figure 2.3. Dielectrophoretic assembly of SWCNT fibers. **(a)** Schematic of the dielectrophoretic drawing apparatus. **(b)** Digital micrograph of tungsten tip pulling SWCNT fiber from the purified (6,5) solution.

2.3. Results and discussion

2.3.1. Optical properties of a (6,5) enriched SWCNT solid-state fiber

Figure 2.4a is an optical micrograph of a typical (6,5) enriched SWCNT fiber, which shows bright photoluminescence (PL) upon excitation (at 658 nm and mW). The PL is imaged with a nIR InGaAs array with 1 sec exposure. Both an absorption spectrum

(Fig. 2.4b) and a EEP (Fig. 2.4c) performed directly on the fiber confirm that it contains mostly (6,5) SWCNT (~ 99 mol%) with minority compositions of (7,6) SWCNT ($\sim 1\%$).

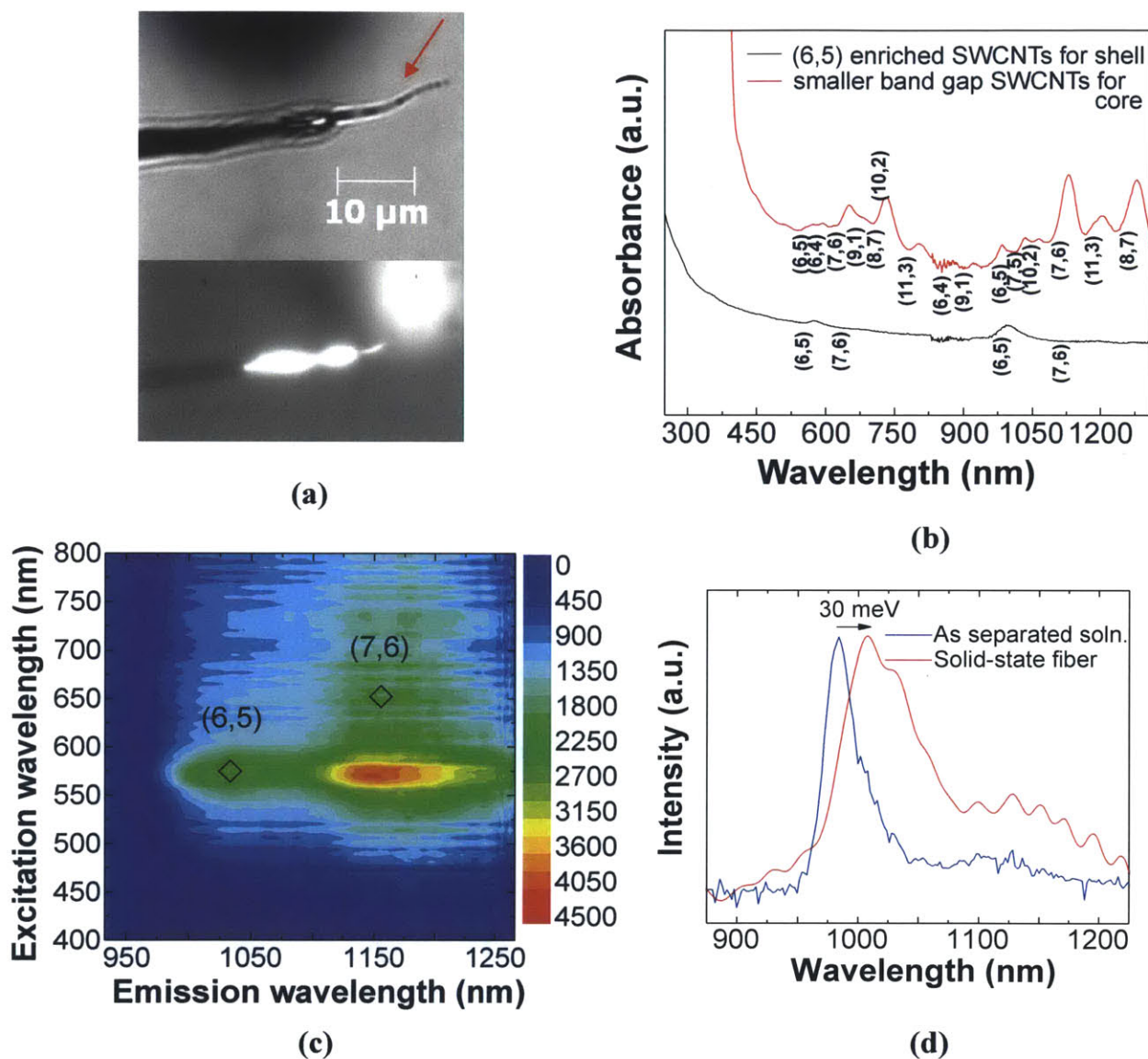


Figure 2.4. Optical properties of a (6,5)-enriched SWCNT fiber. **(a)** Upper panel: An optical image of a SWCNT fiber supported on a tungsten tip; lower panel: a corresponding two dimensional (2D) nIR InGaAs PL image (with 658 nm wavelength excitation, 1 mW), showing a bright PL from the very end of the fiber in a solid-state, confirming a high degree of semiconductor purity. Note that the emission at the upper-right corner is due to a halogen lamp source. **(b)** UV-vis-nIR absorption spectrum of the (6,5) enriched SWCNT solution and of the smaller band gap SWCNT solution **(c)** A corresponding excitation-emission profile demonstrating EET from the majority fraction

of larger band gap (6,5) SWCNTs to the minority fraction of smaller band gap (7,6) SWCNTs. **(d)** The PL spectra of both as-separated solution and a solid-state fiber taken at 570 nm wavelength monochromatic light excitation, corresponding to the E_{22} transition of individual (6,5) SWCNT in an aqueous solution. Note that the peak of the fiber (solid red line, ~1008 nm) is red-shifted (by about 30 meV) from that of individual SWCNT in an aqueous solution (solid blue line, ~984 nm).

Evidence for EET (or FRET) is found in the EEP (Fig. 2.4c). Besides the (E_{11} , E_{22}) peaks of the (6,5) and the (7,6) SWCNTs there is a third peak (with the highest intensity of all) that corresponds to the E_{22} excitation of (6,5) SWCNTs but the E_{11} emission of (7,6) SWCNTs indicating that upon excitation of the fiber (containing 99% (6,5) SWCNTs), energy is transferred via EET to the smaller band gap (7,6) SWCNTs in the fiber, where the excitons recombine radiatively, giving rise to PL corresponding to the E_{11} band gap of the (7,6) SWCNTs.

Fiber formation is known to perturb the electronic and exciton transport properties for SWCNT through inter-tube coupling [15,18,29]. The (6,5) SWCNT have an emission maximum that is 30 meV red-shifted from its value of 1.26 eV in the starting solution, shown in Figure 2.4d. The result for this fiber containing 3.3×10^7 SWCNTs is consistent with that of Wang *et al.* [18], who utilized Rayleigh scattering spectroscopy to measure E_{11} red-shifts in the range of tens of meV upon bundling. This energy shift in the fiber states is understood to be a result of mutual dielectric screening of the excitons by neighboring SWCNTs. In summary, our fibers are analogous to several recently investigated bundled systems, including SWCNT dimers [14] and surface grown bundles [13] with the key exception that they contain 10^7 times as many SWCNTs, in structures that are larger than the wavelength of the absorbing light.

2.3.2. Temperature-dependent photophysics of a (6,5) enriched SWCNT solid-state fiber

We study the temperature-dependence of the fiber photophysics. Figure 2.5a-b show typical nIR EEPs of a fiber (inset, Fig. 2.5a) taken at temperatures of 298 K and 347 K, respectively. Peaks are assigned to the PL of the (6,5) and (7,6) SWCNTs. The fiber was suspended under a blanket of ultra-high purity nitrogen (>99.999%) (3 L/min) and its temperature was controlled (between 298 K to 357 K) using a thermal isolation microscope stage (Linkam Co.). Although the fiber is irradiated with a 570 nm light source (the wavelength corresponding to the E_{22} of (6,5) SWCNTs) and contains only ~1% (7,6) SWCNTs, the resulting PL from the latter is most significant. In fact, a calculation of the quantum yield (defined as the ratio of photons emitted to photons absorbed), shows that it is about two orders of magnitude larger for the (7,6) SWCNT than for the (6,5) SWCNT (Fig. 2.5c). This effect is due to the EET between the two types of SWCNTs, as described above. Another interesting phenomenon is the evolution of the spectral intensity with temperature: the PL intensity data (Fig. 2.5d) show a decrease in PL of both the (6,5) and (7,6) SWCNTs with increasing temperature. The decrease becomes more significant at higher temperatures. The quantum yield of the whole fiber itself, shown in Figure 2.5e, indicates a similar decay.

A theoretical deterministic model is developed to provide a plausible explanation for this trend. Taking into account the different pathways for exciton generation and decay the following system of ordinary differential equations (ODE's) is set up:

$$\frac{dN_{1(6,5)}}{dt} = G_{(6,5)} - k_{EET}N_{1(6,5)} - k_rN_{1(6,5)} - k_dN_{1(6,5)} - k_aN_{1(6,5)}(N_{1(6,5)} - 1) + k_{2-1}N_{2(6,5)} \quad (2.1),$$

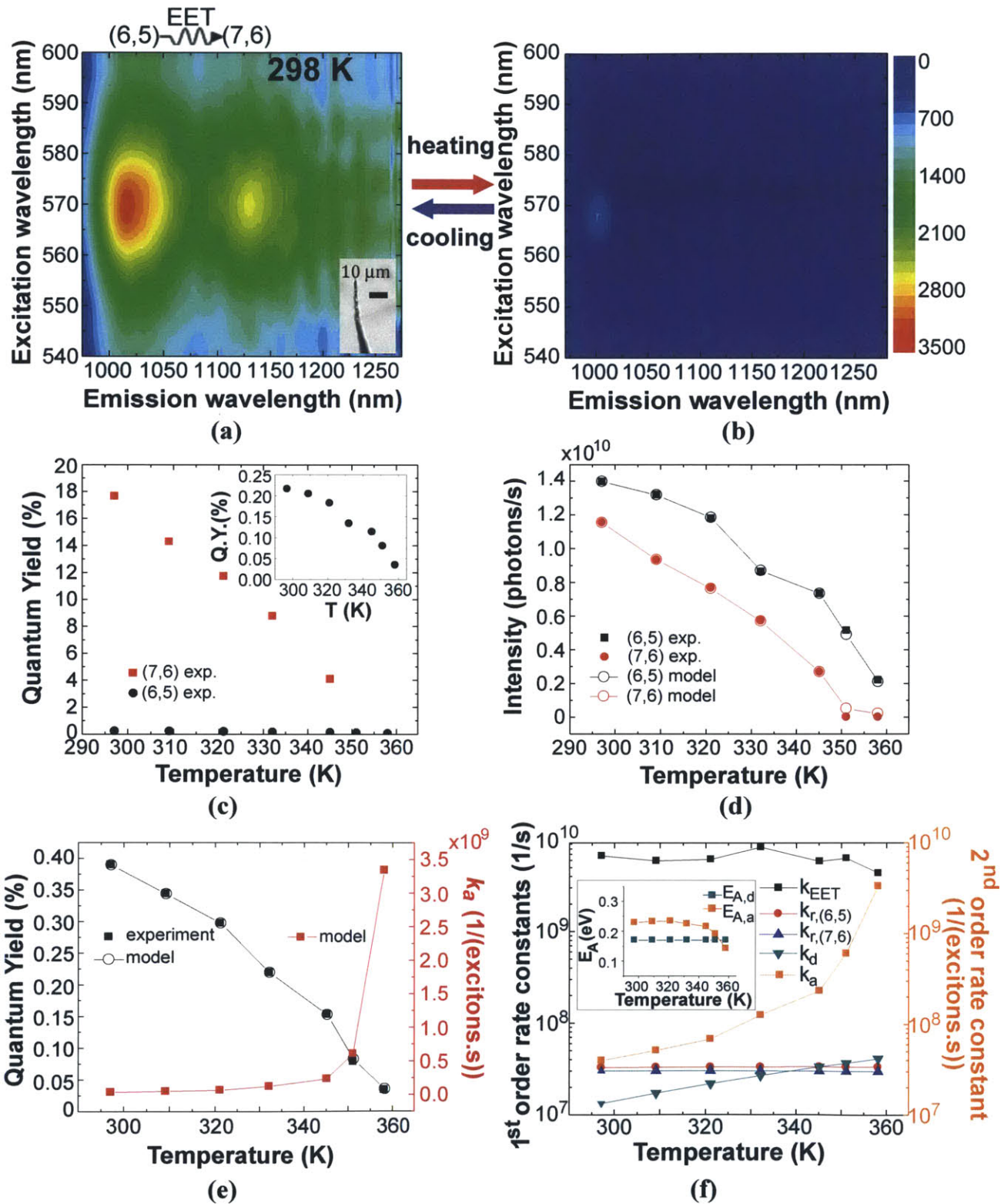


Figure 2.5. EEP and reversible PL change as a function of temperature. (a),(b), Typical nIR (970–1280 nm) EEPs of a fiber (inset of Fig. 2.5a) taken at temperatures of 298 K and 357 K, respectively. (c) Quantum yield of both types of SWCNTs present in the fiber vs.

temperature (the quantum yield is defined as the ratio of photons emitted to photons absorbed). Inset shows the quantum yield of the (6,5) tube on a different scale. **(d)** Plots of the PL intensities of both (6,5) and (7,6) emission vs. temperature (both experimental data and model fit). **(e)** A plot of the quantum yield of the fiber (both experimental data and its fit) vs. temperature, demonstrating a monotonic decrease with increasing temperature. The exciton-exciton annihilation constant k_a is largely responsible for the strong decrease in the quantum yield with temperature. **(f)** A plot showing the temperature-dependence of all of the first and second order rate constants in the system, calculated from theory ($k_{r,(6,5)}$, $k_{r,(7,6)}$) or from numerical simulations based on the model developed (k_{EET} , k_d , k_a). Inset shows the dependence of the activation barrier of both k_d and k_a on temperature.

$$\frac{dN_{2(6,5)}}{dt} = \frac{1}{2}k_a N_{1(6,5)}(N_{1(6,5)} - 1) - k_{2-1}N_{2(6,5)} \quad (2.2),$$

$$\frac{dN_{1(7,6)}}{dt} = G_{(7,6)} + k_{EET}N_{1(6,5)} - k_r N_{1(7,6)} - k_d N_{1(7,6)} - k_a N_{1(7,6)}(N_{1(7,6)} - 1) + k_{2-1}N_{2(7,6)} \quad (2.3),$$

$$\frac{dN_{2(7,6)}}{dt} = \frac{1}{2}k_a N_{1(7,6)}(N_{1(7,6)} - 1) - k_{2-1}N_{2(7,6)} \quad (2.4).$$

In this scheme, N denotes the total amount of excitons in the system, with subscript 1 (2) referring to excitons where the energy-difference between the electron and the hole equals to E_{11} (E_{22}), and subscript (6,5) or (7,6) denotes the chirality of the nanotubes. Here, G is the exciton generation rate calculated based on the extinction coefficient of the fiber (estimated using Beer's law (taking into account scattering) to be $5.07 \times 10^5 \text{ m}^{-1}$), the incident power density of the light ($4.1 \text{ } \mu\text{W}$), the spot size of the incident light ($1.69 \times 10^{-13} \text{ m}^2$), and the illuminated area of the fiber ($1.11 \times 10^{-12} \text{ m}^2$). For the (6,5) SWCNTs, this leads to an estimated exciton generation rate $G_{(6,5)}$ of 6.47×10^{12} excitons/s. The amount of excitons generated on the (7,6) tubes is considerably smaller (6.53×10^{10} excitons/s). As discussed earlier, in bundles, excitons on 'donor' (6,5) nanotubes can transfer to 'acceptor' (7,6) nanotubes *via* EET [11-14], and this is represented by a first-order reaction with rate constant k_{EET} . Excitons can decay through

radiative relaxation, resulting in the formation of photons detected as photoluminescence. It is expected that k_{EET} is several orders greater than the radiative rate constant k_r [11,18]. The temperature-dependent reaction rate constant k_r for this first order reaction is governed by a simple interpolation formula, as proposed by Perebeinos *et al.* [30]:

$$\frac{1}{k_r} = \tau_r = \tau_{\min} \times \frac{T}{T_{\min}} \exp\left(\frac{T_{\min} - T}{T}\right) \quad (2.5),$$

where τ_{\min} , T_{\min} , and T are the minimum radiative lifetime, its corresponding temperature, and the environmental temperature, respectively. Both τ_{\min} and T_{\min} show a diameter-dependence:

$$\tau_{\min} \approx \tau_0 + \alpha d \quad (2.6),$$

$$T_{\min} \approx \frac{\beta}{d} \quad (2.7),$$

where both α and β are the proportionality factors in the correlation, and d is the tube-diameter. The best-fit values for the three parameters are: $\tau_0 = 12$ ns, $\alpha = 24$ ns/nm, $\beta = 272$ K nm [30]. As shown in Figure 2.5f the temperature-dependence of k_r is rather weak in the temperature range considered in this experiment. For both types of SWCNTs k_r is of the order of magnitude of 10^7 per second. The excited excitons can also recombine non-radiatively (thus giving rise to lattice vibrations), mediated by defects along the nanotubes length or by the nanotubes ends [31]. The defect-mediated decay rate constant k_d is well described with classical Arrhenius kinetics [32,33]:

$$k_d = k_{d,0} \exp\left(-\frac{E_{A,d}}{k_B T}\right) \quad (2.8),$$

with $k_{a,0}$ the pre-exponential factor, $E_{A,a}$ the activation energy, k_B the Boltzmann constant, and T the temperature of the fiber. A final possible excitonic decay channel in the SWCNT fiber is exciton-exciton annihilation (otherwise known as the ‘Auger’ process). In this case, the bimolecular reaction $2N_1 \xrightarrow{k_a} N_2 + GS$ describes how upon the collision of two excitons at the E_{11} level, one is annihilated (decays to the ground state GS) while the energy that is being released in the collision is used to promote the other exciton to the E_{22} level. Given the nature of this exciton-exciton annihilation (EEA) mechanism, we propose to describe the temperature-dependence *via* collision theory [34], which results in a modified Arrhenius expression where the prefactor shows a \sqrt{T} dependence:

$$k_a = k_{a,0} \sqrt{T} \exp\left(\frac{-E_{A,a}}{k_B T}\right) \quad (2.9),$$

with $k_{a,0}$ the pre-exponential factor and $E_{A,a}$ the activation energy. The N_2 exciton quasi-immediately relaxes back to the E_{11} level with a rate constant $k_{21} = 2.3 \times 10^{13} s^{-1}$ [35]. Since the excitons on the E_{22} level are very short-lived intermediates, one can employ the pseudo-steady-state-approximation to equations (2.2) and (2.4), leading to an expression for $N_{2(6,5)}$ and $N_{2(7,6)}$, which can then be plugged into equations (2.1) and (2.3) respectively. The final system of ODE’s to be solved numerically is then reduced to

$$\frac{dN_{1(6,5)}}{dt} = G_{(6,5)} - k_{FFT} N_{1(6,5)} - k_r N_{1(6,5)} - k_d N_{1(6,5)} - \frac{1}{2} k_a N_{1(6,5)} (N_{1(6,5)} - 1) \quad (2.10),$$

$$\frac{dN_{1(7,6)}}{dt} = G_{(7,6)} + k_{FFT} N_{1(6,5)} - k_r N_{1(7,6)} - k_d N_{1(7,6)} - \frac{1}{2} k_a N_{1(7,6)} (N_{1(7,6)} - 1) \quad (2.11).$$

With knowledge of G and k_r a fit of the model to the data (Fig. 2.5d), results in values for both k_{EET} , k_d , and k_a for every data point (Fig. 2.5f). The value of k_{EET} is found to be reasonably invariant with temperature at $6.24 \pm 1.19 \times 10^9 \text{ s}^{-1}$, as expected [21].

It is possible to calculate the exciton energy transfer (EET) efficiency η_{EET} in the fiber. Tan *et al.* reported, as an example, a value of $\eta_{EET} \sim 75$ under resonant excitation of the (5,4) SWCNTs [11]. In their work, the EET efficiency was considered to be equivalent to the ratio of photoluminescence (PL) intensities of acceptor to donor tubes (I_A/I_D) at a given excitation energy for the latter. They finally approximated the efficiency as $I_A/I_D \approx \tau_{nrA}/\tau_{EET}$, where τ_{nrA} and τ_{EET} are the lifetime of non-radiative decay of acceptor tube and that of EET between donor and acceptor tubes, respectively. In this work, a mean value of I_A/I_D (from five different fibers) is calculated to be 1.54 ± 0.81 , when excited at 570 nm (corresponding to the E_{22} transition of (6,5) SWCNTs) at room temperature. An important feature of the work of Tan *et al.* is that the overall concentration of the acceptor tubes (e.g. (6,5), (7,5), (8,4) and (7,6)) is much larger than that of the donor (5,4) tubes, whereas in this work, the acceptor SWCNTs make up only $\sim 1\%$ of the total bundle (as seen in the absorption spectra (compare Figure 3c in reference [11], and Figure 2.4b in this work respectively). Moreover, when Tan *et al.* approximate the value of I_A/I_D by τ_{nrA}/τ_{EET} (a ratio of *rate constants*, not *rates*), they eliminate the fact that the nanotubes can be present in different concentrations from their calculation. Since there are so few acceptors SWCNTs in our fibers, it makes more sense in this case to think of the EET efficiency η_{EET} as the ratio of quantum yields (QYs) instead of ratio of lifetimes

$$\eta_{EET} \neq \frac{I_A}{I_D} @ \text{donor excitation (Tan et al.)} \quad (2.12),$$

$$\eta_{EET} = \frac{QY_A}{QY_D} @ \text{donor excitation}$$

with

$$QY_A = QY_{(7,6)} = \frac{PL_{(7,6)}}{G_{(7,6)} @ 570nm} \quad (2.13),$$

$$QY_D = QY_{(6,5)} = \frac{PL_{(6,5)}}{G_{(6,5)} @ 570nm}$$

and in this work

$$G_{(7,6)} = 0.01 * G = 6.53 \times 10^{11} \text{ excitons/s} \quad (2.14).$$

$$G_{(6,5)} = 0.99 * G = 6.47 \times 10^{12} \text{ excitons/s}$$

From Figure 2.5c, this leads to $\eta_{EET} = 81.7$ at room temperature, comparable to the value found by Tan *et al.* [11].

Another way to investigate the effect of EET in our fibers is to consider two separate fibers, one consisting of 100% (7,6) SWCNTs and the other of 100% (6,5) SWCNTs. When both fibers are excited at their respective E_{22} wavelength, with monochromatic light of the same intensity, our model predicts the PL intensity and quantum yield for both types of fibers to be similar, as indicated in Figure 2.6. It should be noted this time the EET contribution is absent in the model, since it considers pure fibers.

The values for k_r are taken from literature as before [30], and for k_d and k_a the values from Figure 2.5f are used as an approximation.

Comparing the QY of the (7,6) SWCNTs in the fibers used in this work consisting of ~99% (6,5) tubes and ~1% (7,6) tubes (Fig. 2.5c) to the QY of the (7,6) tubes in a pure fiber (Fig. 2.6b), is also a measure of the EET efficiency η_{EET} . This is shown in Figure 2.7. Only at high temperatures this ratio goes down substantially, due to the increased effect of the non-radiative EEA process.

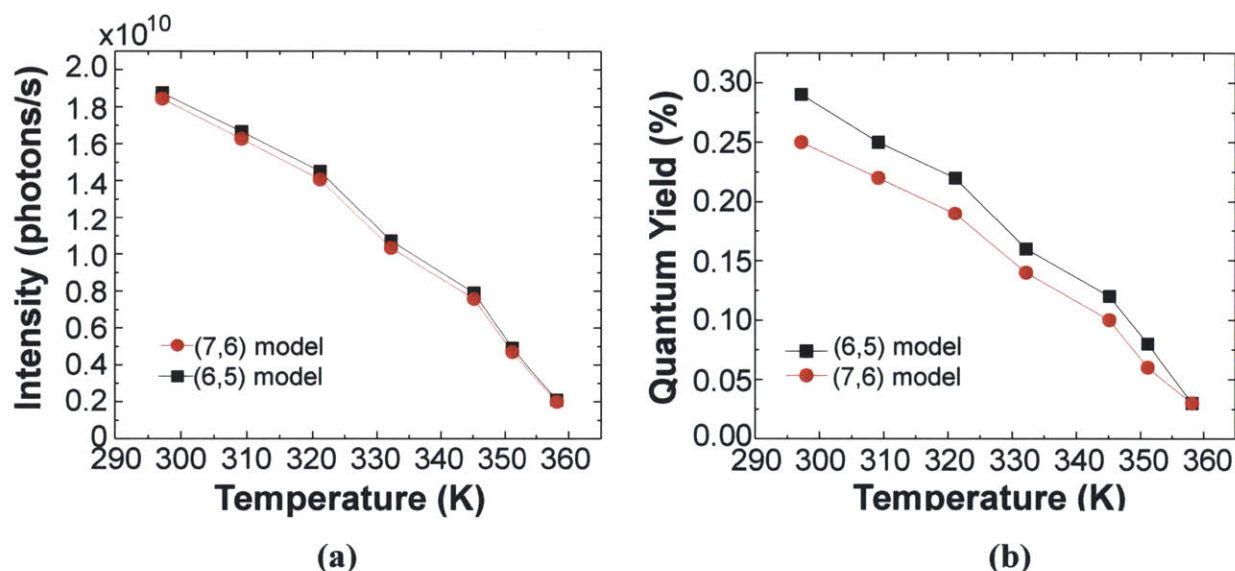


Figure 2.6. Theoretical prediction of the PL (a), and QY, (b), of pure SWCNT fibers.

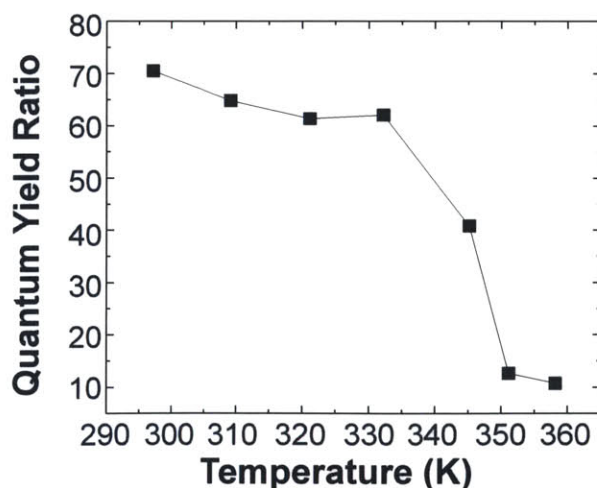


Figure 2.7. Temperature dependent exciton-energy transfer efficiency. The ratio of the theoretically calculated quantum yield of the (7,6) SWCNTs in the (6,5) enriched fiber

(containing 1% (7,6) SWCNTs and 99% (6,5) SWCNTs) to the quantum yield of the (7,6) SWCNTs in a pure fiber (100% (7,6) SWCNTs).

The defect-related rate constant equals $k_d = 10^{10} \exp\left(-\frac{0.17eV}{k_B T}\right)$, where the value

for the activation barrier is in agreement with values found elsewhere in literature [33].

The second order exciton-exciton annihilation rate constant becomes

$k_a = 10^{10} \sqrt{T} \exp\left(\frac{-0.1937eV \pm 0.028494eV}{k_B T}\right)$. It is interesting to compare the value of k_a

found here to values reported in literature. Generally, exciton-exciton annihilation (EEA)

is demonstrated (in transient pump-probe experiments) to occur only at higher pump-

fluences than the one in our experiments [36-39]. In our experiments however, a

monochromatic light source instead of a laser is used and they are carried out at steady-

state, where continuously 6.53×10^{12} excitons per second (G) are being generated in the

fiber. Considering the fiber contains $\sim 3.3 \times 10^7$ SWCNTs this implies the creation of

$\sim 1.99 \times 10^5$ excitons per second per nanotube. The EEA rate constant deduced from the

transient experiments is usually on the order of $10^{12}/(\text{excitons sec})$ [38,39], which is a

factor of 10^4 higher than the room temperature value of the Auger rate constant k_a

deduced from the model presented here (see Fig. 2.5f). This apparent discrepancy can be

explained by the fact that EEA does not occur continuously on every single nanotube in

our fibers. The model does assume, for the sake of simplicity, that the excitons are

generated uniformly throughout the bundle. In reality however, it is likely that more

excitons are generated on the tubes located close to the surface facing the excitation

source, and fewer excitons are generated on the tubes at the other end of the bundle. For

the first order rate processes in this system, this does not matter, since these rates only

depend on the total number of excitons present in the system, not on the vicinity of other excitons. However, for the second order rate process (Auger recombination or EEA), the vicinity of other excitons matters (two excitons need to be generated within approximately 90 nm of each other, for exciton-exciton annihilation to occur, where 90 nm is twice the diffusion length of excitons along the length of a nanotubes [40]. In reality, it is likely that the Auger process occurs significantly on the nanotubes located closest to the incoming light and not so much on the nanotubes furthest away from the excitation source. We can thus state that

$$\text{Auger rate} = k_{a, \text{as in literature}} * N_{\text{close to light}}^2 + 0 * N_{\text{far from light}}^2 \quad \text{where } k_{a, \text{as in literature}} \approx 10^{12} \text{ ps}^{-1} \quad (2.15).$$

However in our model N represents the total amount of excitons present in the system:

$$N = N_{\text{total}} = N_{\text{close to light}} + N_{\text{far from light}} \quad (2.16).$$

This leads to:

$$\text{Auger rate} = k_{a, \text{as in literature}} * N_{\text{close to light}}^2 + 0 * N_{\text{far from light}}^2 = k_{a, \text{as in our work}} * N_{\text{total}}^2 \quad (2.17),$$

$$k_{a, \text{as in literature}} * N_{\text{close to light}}^2 = k_{a, \text{as in our work}} * N_{\text{total}}^2 \quad (2.18),$$

$$\frac{k_{a, \text{as in literature}}}{k_{a, \text{as in our work}}} = 10^4 = \frac{N_{\text{total}}^2}{N_{\text{close to light}}^2} \quad (2.19),$$

or

$$100 = \frac{N_{\text{total}}}{N_{\text{close to light}}} \quad (2.20).$$

From equation (2.19) and (2.20) one can see the discrepancy between the value of k_a in literature ($k_{a, \text{as in literature}} \sim 10^{12}/(\text{exciton.s})$) and the value of k_a in our model (

$k_{a, \text{as in our work}} \sim 10^8 / (\text{excitons.s})$). This indicates that in about 1% of the tubes excitons are generated close enough to each other for the Auger process to occur. The total Auger rate constant for the whole system is still high enough to cause the PL to be quenched at high temperature, as indicated by the data. The k_a of our model can therefore in hindsight be written as an effective rate constant $k_{a, \text{eff}}$:

$$\text{Auger rate} = k_{a, \text{eff}} * N_{\text{total}}^2 = k_a * \left(\frac{1}{100} * N_{\text{total}} \right)^2 \quad (2.21),$$

where $k_{a, \text{eff}} = 10^8 \text{ s}^{-1}$ and $k_a = 10^{12} \text{ s}^{-1}$.

It is worth mentioning that the activation energy for this Auger process shows a small variation with temperature (see inset of Figure 2.5f). This is not uncommon for multistep reactions in solids [41-43]. The Auger process is a combination of a diffusion step and a reaction step (one exciton gets promoted to the E_{22} level, the other one is demoted to the GS). Therefore the effective Auger rate constant k_a used in the model can be written as

$$\frac{1}{k_a} = \frac{1}{k_D} + \frac{1}{k_R} \quad (2.22),$$

where k_D and k_R are the rate constants for the diffusive and the reaction step respectively. From equation (2.22), one can easily deduce the effective activation energy of the Auger process to be

$$E_{A,a} = \frac{E_{A,D} k_R + E_{A,R} k_D}{k_D + k_R} \quad (2.23).$$

Because both k_D and k_R vary with temperature, $E_{A,a}$ is also temperature-dependent. Taking into account that k_a is a second order rate constant, it is clear that exciton-exciton annihilation (or the Auger process) is the most efficient decay channel in the fiber. The non-radiative decay channel is much more efficient than its radiative counterpart and is responsible for the low PL quantum yields of the fibers in this work, 10^{-3} to 10^{-4} (Figure 2e), values that are similar to those reported in literature for much smaller bundle systems [18,44].

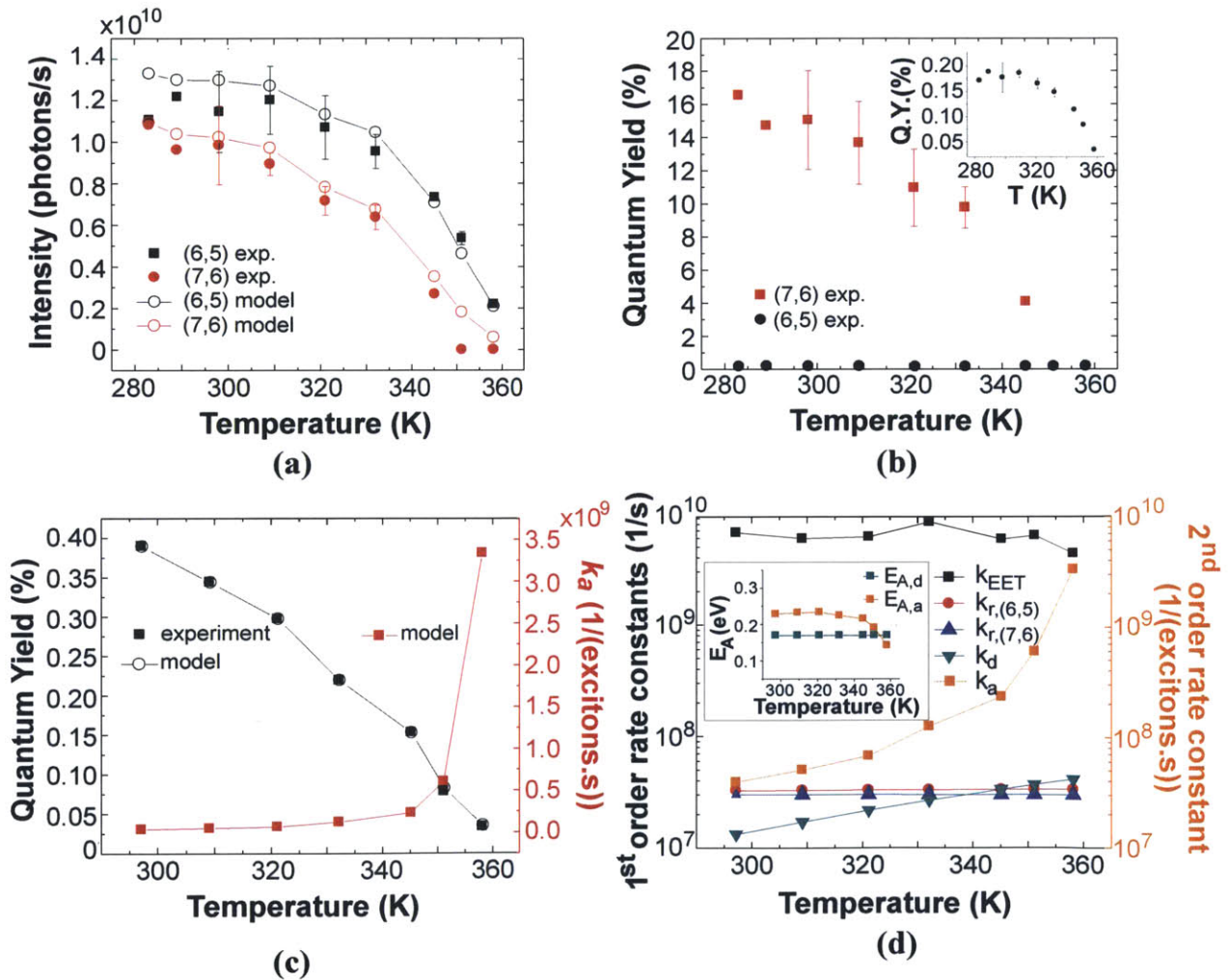


Figure 2.8. Analysis of average dataset of repeatedly temperature-cycled fiber. **(a)** Plots of the PL intensities of both (6,5) and (7,6) emission vs. the temperature. **(b)** Quantum yield of both types of SWCNT present in the fiber vs. the temperature (the quantum yield

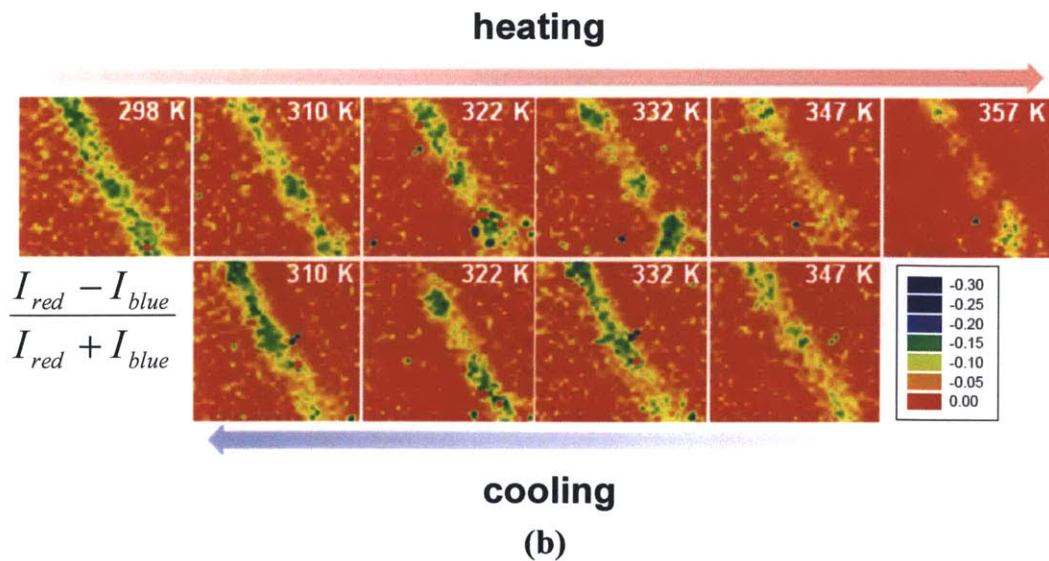
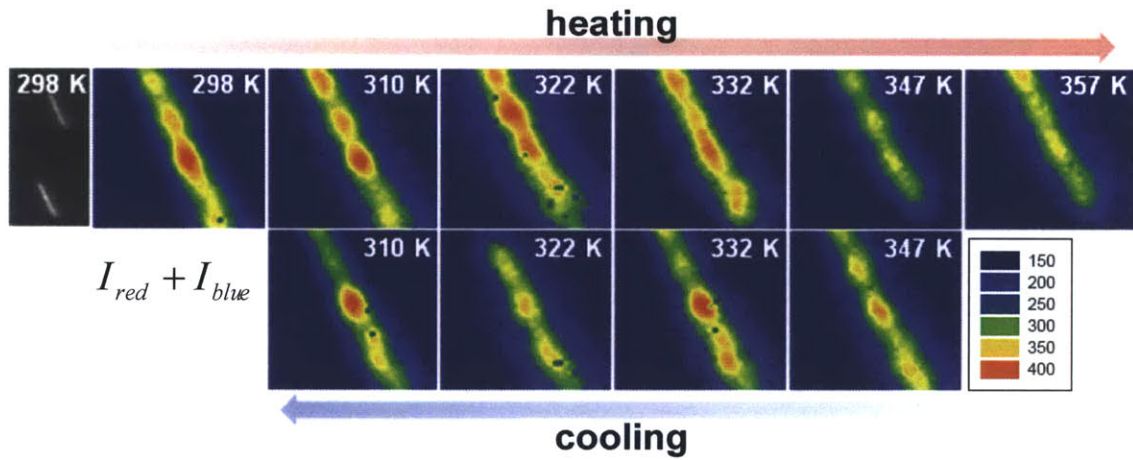
is defined as the ratio of photons emitted to photons absorbed). Inset shows the quantum yield of the (6,5) tube on a different scale. **(c)** A plot of the quantum yield of the whole fiber (both experimental data and its fit) vs. the temperature, demonstrating overall monotonic decreases with increasing temperature. The Auger rate constant k_a is responsible for the strong decrease in the quantum yield with temperature. **(d)** A plot showing the temperature-dependence of all of the first and second order rate constants in the system, calculated from theory ($k_{r,(6,5)}$, $k_{r,(7,6)}$) or from numerical simulations based on the model developed (k_{EET} , k_d , k_a). Inset shows the dependence of the activation barrier of both k_d and k_a on temperature.

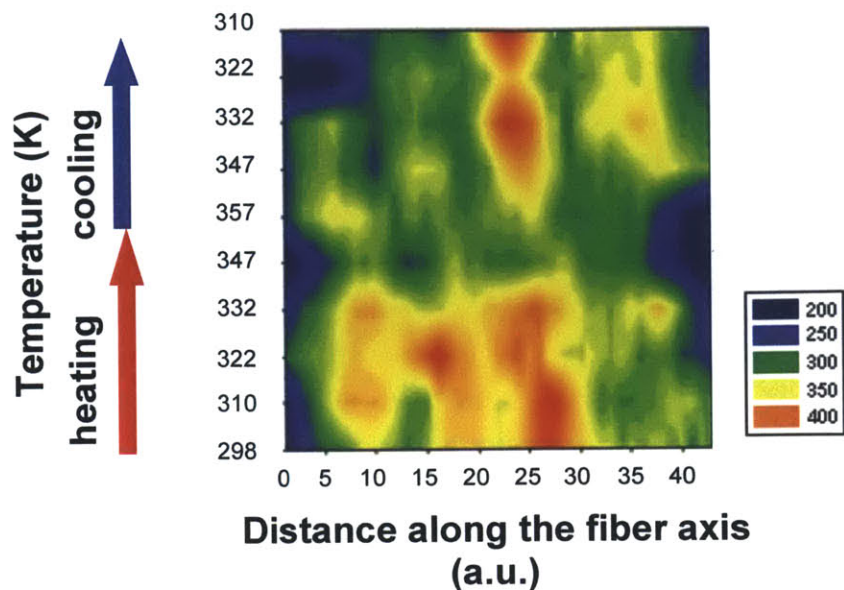
A similar analysis has been performed on an average dataset, containing data taken while heating the sample, while subsequently cooling the sample and during a repeat of this hysteresis experiment six days later (Figure 2.8). The fact that the results are similar to the ones described earlier shows that the transition in PL upon temperature cycling is reversible, repeatable, and not related to environmental or morphological changes.

2.3.3. Observation of spatial inhomogeneities in PL of (6,5) enriched SWCNT fiber

As suggested by the nIR micrograph in Figure 2.9, we find considerable spatial heterogeneity in the emission density along the length of such fibers. This spatial variation also undergoes a remarkable transition with temperature, and again in an approximately reversible manner. Figure 2.9a shows a higher resolution nIR intensity map of the total relative density around a fiber of 1.6 μm diameter suspended on a N_2 blanketed thermal isolation microscopy stage. Localized regions of high emission intensity are clearly visible along the length of the fiber. Upon progressive heating from 298 K to 357 K, these regions broaden and become delocalized. Cycling the system back to 298 K repeatedly confirms that this delocalization is reversible and not associated with

thermal annealing or impurity desorption. While the images resemble the spatial heterogeneity observed in near-field investigations of single carbon nanotubes, invariably created by lattice defects, it is important to note that the images in Figure 2.9a arise from an ensemble collection of approximately 2.4×10^8 SWCNT, so sidewall defects cannot explain the phenomena. Also, the localization lengths (2 to 5 μm) are longer than the range of nanotube lengths (100 to 1000 nm); therefore nanotube ends, which are known to be strong centers of irradiative recombination [12,31], cannot be responsible.





(c)

Figure 2.9. Spatially resolved, temperature-dependent PL behavior under an in-house built dual-channel microscope. **(a)** Temperature-evolutional, high-resolution nIR PL intensity maps of the total relative density around a fiber suspended on a thermal isolation microscope stage blanketed with continuous, ultra-high purity N_2 (>99.999%) with a flow rate of 3 L/min. **(b)** Normalized differential intensity contour plots of the same fiber mapping spatial variations with temperature in the local emission energy (see main text and S.I.6 for details). **(c)** A detailed close-up of the PL intensity along the fiber axis showing a reversible recovery of the energy with temperature.

The phenomenon was further investigated by adapting the nIR PL microscope to split the collection image in photon energy using a pass filter with wavelength centered at 1090 nm, yielding a pair of images, named ‘red’ and ‘blue’, corresponding to long and short pass wavelengths respectively.

In-house dual channel microscope

PL three-dimensional (3D) profiles were acquired with an in-house built spectrofluorometer incorporating a xenon arc lamp, Kratos GM-252 monochromators and an E1-L Germanium Detector (Edinburgh Instruments). To obtain splitting nIR PL images with respect to a relative wavelength of outgoing photons, we employed an in-

house built dual-channel microscope (Fig. 2.10a) with a 568 nm laser excitation and a pass filter with wavelength centered at 1090 nm. This produces a pair of upper and lower images (upper-left image of Fig. 2.9a in the main text), corresponding to short and long pass wavelengths, respectively.

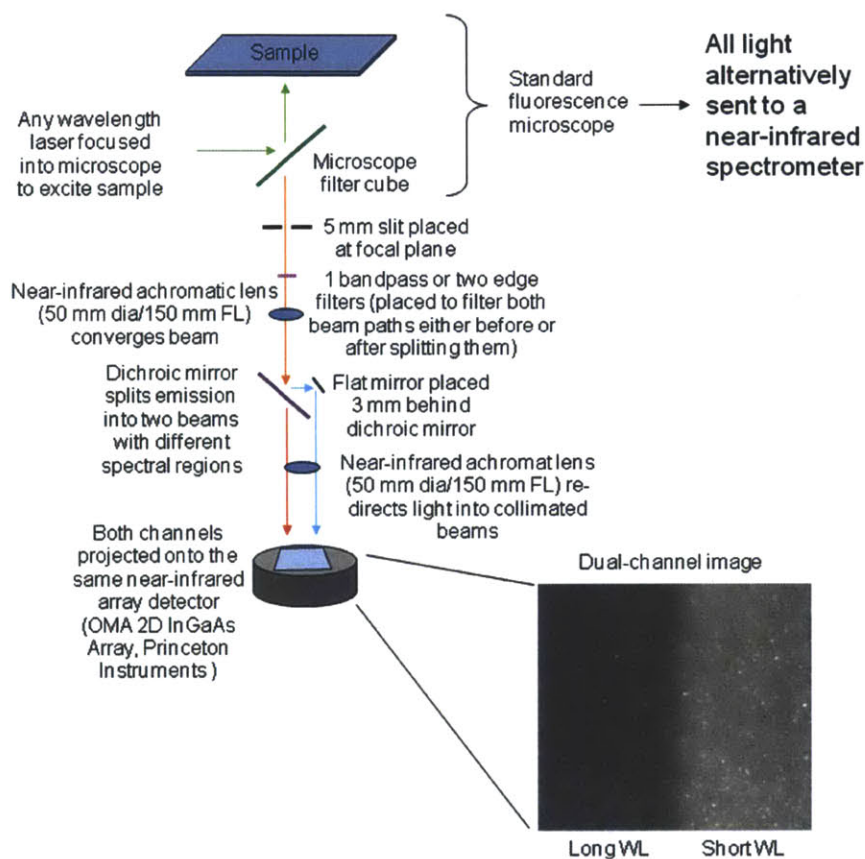


Figure 2.10. Schematic of an in-house built dual-channel microscope setup. Light leaving the sample which is nearly collimated passes through a 5 mm aperture (slit) at the focal plane (approximately 60 mm from the microscope output port), then through a bandpass or two edgepass filters to spectroscopically isolate one fluorescence band. This light passes through a plano-convex achromat lens to converge it. It is then split by a dichroic mirror into long and short wavelength portions and again through a plano-convex achromatic lens to collimate the two beams which are captured by two different regions of a nIR array detector.

To map the spatial variations in the local emission energy (Fig. 2.9b) the normalized intensity difference between both images is calculated: $(I_{red} - I_{blue}) / (I_{red} +$

I_{blue}). The resulting mapping reveals that the localized regions of high intensity seen in Fig. 3a are blue-shifted relative to the mean value for the whole fiber (Fig. 2.9b). With increasing temperature, there is a net emission energy loss that recovers with cycling back to 298 K (Fig. 2.9c). Because the relative variation in red-shift is of the same order observed between bundled and isolated SWCNTs (30 meV), we hypothesize that the relatively blue-shifted regions are associated with increased inter-tube spacing or decreased physical density along the fiber length. This is supported by the fact that the regions are spatially of order of the persistence length of a SWCNT bundle [45]. The fact that these blue-shifted regions have higher intensities (as indicated by Fig. 2.9a), could be because they contain more nanotubes, although packed in a less dense manner. The larger volume of these regions is also visible in a scanning electron microscope image (Fig. 2.11a).

Origin and description of the bead-bar phenomenon

The middle/lower panels of Figure 2.11 show images of typical fibers obtained using a high-resolution optical scanning electron microscope (SEM), respectively. Close inspection of this type of optical micrograph reveals regions of decreased physical density as “beads” along the fiber length, alternated with denser “bar’-like regions. This structure is likely formed during the DEP process in a self-limiting process, since incomplete nanotube alignment during formation promotes outward or splayed growth, while van der Waals attraction of the bare tubes acts to densify nanotube segments [27]. The high resolution SEM image revealed that the bead-like structures have fewer secondary electrons than bar-like regions (Fig. 2.11a, lower panel). The regions with

fewer secondary electrons correspond to those with a lower SWCNT density. It is hypothesized that the bead-like structures with lower SWCNT density also have a smaller degree of the alignment. In order to confirm this, we investigated the polarizability of the fiber by investigating the Raman G-band of the same fiber seen in the SEM image using a Jobin Yvon LabRam HR 800 micro-Raman with 633 nm laser excitation (Fig. 2.11a, upper panel). Note that the incident laser used for the measurement was vertically (V) polarized to the detector with the same direction. A stronger polarizability implies a higher degree of the alignment of nanotubes within the fiber. As seen in the optical image (Fig. 2.11, middle panel), the large bead at the very left end is found to have the lowest polarizability. This end is the last region that is pulled out from the as-separated solution during the DEP process, and has a significant loss of the alignment. Comparing the overall polarizability with morphology of the fiber, it is apparently found that the relationship between the polarizability and the alignment in the bead-like structures is consistent along the fiber. It is possible to compute more quantitative values to describe the orientational order of SWCNT in “beads” and “bars”. The nematic order parameter $S = \langle P_2(\cos\beta) \rangle$ is calculated, which quantifies the degree of the nanotube alignment of those regions along the fiber [46,47]. Here β is the angle a SWCNT makes with the V direction, $P_2(x)$ is the second Legendre polynomial, and $\langle \dots \rangle$ denotes an average over the orientation distribution $p(\beta)$, S being 0 for an isotropic distribution and 1 for perfect alignment.

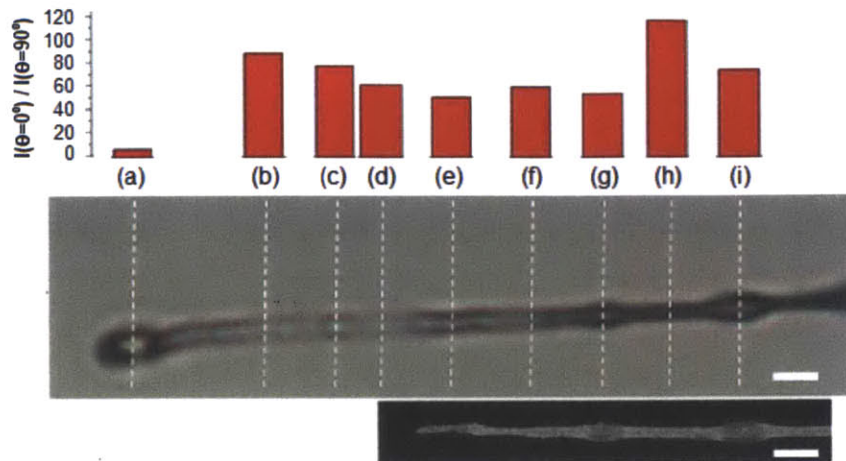
$$I_{vv}(\theta) \propto A \cos^4 \theta + B \cos^2 \theta \sin^2 \theta + C \sin^4 \theta \quad (2.24),$$

where $A = \langle \cos^4 \beta \rangle$, $B = 3 \langle \cos^2 \beta \sin^2 \beta \rangle$, $C = 3 \langle \sin^4 \beta \rangle / 8$, and θ represents the angle between the V direction and the fiber alignment axis.

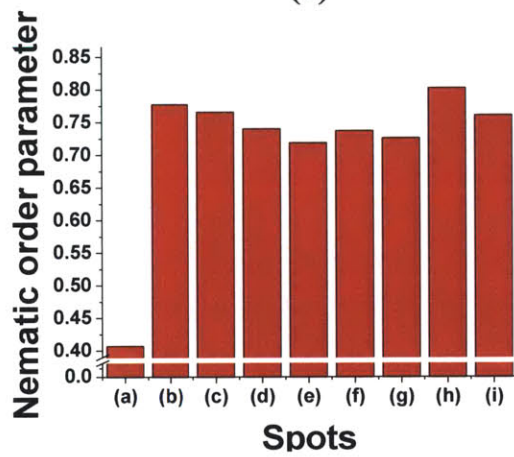
Using the Raman G-band polarizability (Fig. 2.11a, upper panel) and Eqn. (2.24), a value for S is extracted which is shown in Fig. 2.11b. The order of the extent of the nematic order parameters along the fiber exactly follows the result of the polarizability of Raman G-band intensity (Fig. 2.11a, upper panel). It should be noted though that the nematic order parameters calculated here reflect that a higher degree of the alignment in the bars results in a higher probability of nanotube bundling, which implies a stronger red-shift of the E_{11} transition compared to the beads [10]. As a consequence, the regions of the bundle with lower degree of bundling (beads) are expected to show a *relative* blue-shift of λ_{em} corresponding to the E_{11} transition than the others, due to the a smaller degree of dielectric screening.

It should be noted that Figure 2.11a,b clearly corroborate the morphology-dependent spatial variation of the wavelength shift along the fiber (observed in Fig. 2.9b of the main text). The beads are also visible as regions of reduced electron scattering cross section in SEM, where denser segments are clearly observed to connect with more loosely defined beads. In summary, all these results illustrate that the bead-like structures have a lower density of nanotubes as well as a smaller degree of the alignment, as is schematically shown in Figure 2.11c.

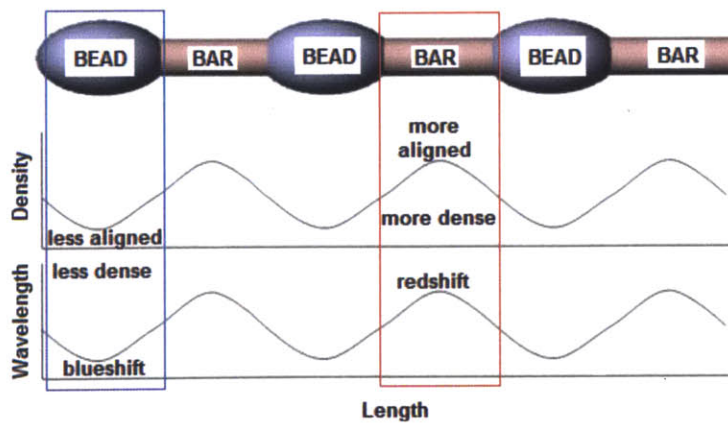
Figure 2.9a,c clearly illustrate a disproportionate diminution of the PL intensity of the least dense regions (the 'beads') with increasing temperature. There are two plausible explanations for this observation. It has been shown in the main text (Fig. 2.5f) that the exciton-exciton annihilation (EEA) is the most efficient decay channel and that it shows the strongest temperature-dependence. This Auger process is a second-order rate process (with the Auger rate = $-k_a N_{1(6,5)} (N_{1(6,5)} - 1)$).



(a)



(b)



(c)

Figure 2.11. Spatial inhomogeneities in fiber PL explained by SWCNT density and alignment. (a) An optical (middle panel)/SEM (lower panel) image of different fibers

with the result of polarizability of Raman G-band along the fiber (upper panel). The same scale bar ($2\ \mu\text{m}$) is applied to both images. **(b)** The nematic order parameters calculated from the polarizability of Raman G-band. **(c)** A schematic illustration of the fiber with the bead-like structures, showing structural correlation with spatial variation of the wavelength shift along the fiber.

Therefore, if there is a larger exciton population in the “beads” of the fiber than in the “bars”, this would result in a much larger contribution of the Auger decay in the “beads”. Though the beads are less dense and aligned (as is indicated by the polarization experiments (Fig. 2.11a,b) and the relative blue-shift in their emission (Fig. 2.9b in the main text), more excitons are generated in them (as indicated by the brighter emission of the beads compared to the bars at room temperature in Fig. 2.9a).

A second possible reason for a faster PL decay in “beads” is that the non-radiative decay channels depend upon SWCNT density and inter-tube spacing. Hirori *et al.* found that SWCNTs with a more red-shifted λ_{em} (corresponding to E_{11}) showed a weaker PL decay [48], suggesting the activation energy of the potential fluctuations in these SWCNT is relatively higher. This facilitates the exciton relaxation process, since the decay rate of localized excitons is smaller than that of free excitons [48]. As shown in Figure 2.11, the “bar”-like structures in the fiber are found to be the more-aligned state and to have a higher density of SWCNT population. Thus in the context of the results of Hirori *et al.* [48] discussed above, such “bars” with their relative red-shifts, are expected to show a slower decay of PL with increase in temperature than “beads”. Consequently, this would give rise to a slower PL delocalization with temperature in the regions of “bars” than in the “beads”, likely due to more localized excitons resulting from the higher density of SWCNT in the structure. A detailed quantitative study on PL delocalization in the semiconducting SWCNT fiber is beyond the scope of the current manuscript.

However it could be performed by using an advanced technique, such as tip-enhanced near-field optical microscopy as a future work [31].

2.3.4. The exciton antenna: spatial and energetic concentration of the incident light

A carbon nanotube fiber can potentially form unique types of optical antenna structures, distinct from porphyrin systems [49], photosynthetic proteins [50], in that the excitons are one-dimensionally quantum confined, but can successively transfer energy to a central concentrator element *via* EET. This possibility was explored by forming a fiber consisting of successive shells with larger band gap SWCNTs radiating outward. The effect is to transfer excitons *via* an efficient EET pathway to a central core, thereby realizing a concentration effect. To this end, our SWCNT separation procedure, published elsewhere [16], was used to create a solution of primarily small band gap SWCNTs, from which a fiber was drawn on a tungsten tip (as described in 2.2), forming the collector core. A (6,5)-enriched SWCNT solution was then successively deposited creating an absorbing shell (Figure 2.12a,b). The multistep DEP fiber formation creates the desired core-shell structure, but the tip contains solely (6,5) SWCNTs (Fig. 2.12a). The distribution of chiralities and their concentrations for the core is found to be: [(8,7), 28.4%], [(11,3), 10.5%], [(7,6), (26.3%)], [(10,2), 5.26%], [(6,5), 8.42%], [(7,5), 8.42%], [(9,1), 6.32%], and [(6,4), 6.32%]; a derivative method has been used to estimate these values [17].

Figure 2.12c is the resulting excitation-emission profile, and it is clear that the dominant emission is produced by the smallest band gap (8,7) SWCNTs, when the fiber

itself is excited over a broad range extending from the ultraviolet (UV) to nIR wavelengths. Figure 2.12d shows the resulting PL from the nanotubes as a function of their diameters (inversely proportional to their band gaps).

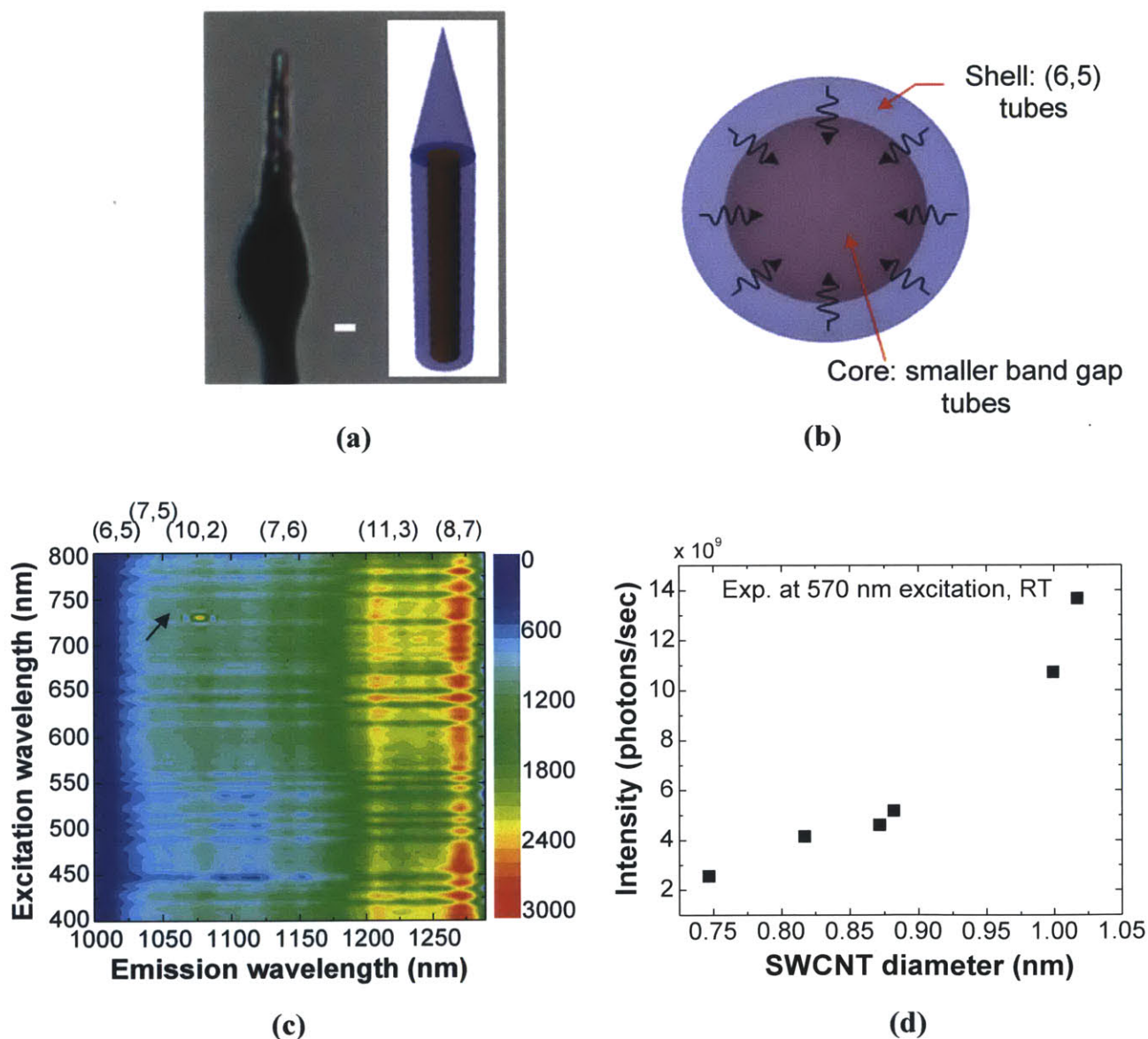


Figure 2.12. Development of an exciton antenna from a core-shell carbon nanotube structure. (a) An optical image of the exciton antenna (scale bar, 2 μm) with a schematic illustration. (b) A top view of the antenna structure where curved black arrows indicate the inward EET upon photoexcitation. (c) The resulting excitation profile, demonstrating the dominant emission produced from the smallest band gap element (8,7) upon

photoexcitation over a broad range extending from the UV to nIR wavelengths. **(d)** Experimental data showing the PL intensity for each type of SWCNT in the exciton antenna for excitation at 570 nm and at room temperature.

Because the excitons are funneled to the central core of the fiber, a spatial concentration is realized. The transfer is shown to be extensive, with most species showing no radiative recombination within our detection limits. However, curiously some residual emission is detected from the larger band gap (10,2) (marked by an arrow in Fig. 2.12c). Because this component is present only as a minority, and it is unlikely that it is preferentially enriched at the core-shell interface, this may be evidence for an anomalously low EET efficiency for the (10,2) species. The EET efficiencies depend linearly on the energy-difference between the donor and the acceptor [14] (and thus their chiralities). However, EET also depends on the fractions of every type of nanotube in the fiber as well as their spatial distribution in the core-shell structure.

We note that there is the potential to enhance existing single nanowire or carbon nanotube photovoltaic devices, particularly if one creates an axial conductive core along which excitons can be split and harvested, as in the case where the core is one terminal of a p-n junction [51]. The concept of successive annular shells that behave as exciton concentrators has yet to be extended to inorganic nanowire devices [49].

2.4. Conclusions

There has been renewed interest in solar concentrators and optical antennae for improvements in photovoltaic energy harvesting and new opto-electronic devices. In this

work, we dielectrophoretically assembled single-walled carbon nanotubes (SWCNTs) of homogeneous composition into aligned filaments that can exchange excitation energy, concentrating it to the center of core-shell structures with radial gradients in the optical band gap. An unusually sharp, reversible decay in photoemission occurs as such filaments were cycled from ambient temperature to only 357 K, attributed to the strongly temperature-dependent second order exciton-exciton annihilation process. Core-shell structures consisting of annular shells of mostly (6,5) SWCNTs ($E_g = 1.21$ eV) and cores with band gaps smaller than those of the shell ($E_g = 1.17$ eV (7,5) to 0.98 eV (8,7)) demonstrate the concentration concept: broadband absorption in the ultraviolet (UV)–near-infrared (nIR) wavelength regime provides quasi-singular photoemission at the (8,7) SWCNTs. This approach demonstrates the potential of specifically designed collections of nanotubes to manipulate and concentrate excitons in unique ways.

The optical antenna approach in this work is similar to biological methods of photon concentration that have been studied extensively [50],[52,53]. Photosynthetic reaction centers in plant photosynthesis, for example, contain light-harvesting antennae that funnel excitation to a specific location, such as the P680 site in photosystem II where the excitons are split into electrons and holes. Although the nanotube concentrator in this work focuses the light into the nIR upon spatial concentration, there are applications where the benefits associated with this concentration make up for this energy loss. Many 1D nanostructures have narrow absorption cross sections, for example, and our antenna concept can be used to systematically increase the absorption bandwidth over a desired window, while concentrating the output in space and energy, potentially leading to new photovoltaics and photodetectors. Future efforts should therefore focus on interfacing

such antenna structures with various opto-electronic devices, including photodiodes, photovoltaics, and bolometers.

2.5. Ongoing work

In May 2011 Liu *et al.* published a method for large-scale single chirality separation based on simple size exclusion chromatography, using a commercially available Sephacryl gel [54]. This has catapulted the nanotube separation field forward, since it has made large-scale separation easy and cheap. Tvrdy *et al.* have recently developed a kinetic model that describes this separation based on the chirality-selective adsorption to specific hydrogels [55]. With respect to the exciton antenna work this means we are no longer limited to using the few chiralities of SWCNTs that were easily separated with density gradient centrifugation methods.

Ongoing work focuses on using and optimizing the new separation techniques and make large quantities of single-chirality SWCNTs.

We plan to study the EET between layers of homogeneous SWCNT chiralities with ultrafast spectroscopy. Based on the results we aim to create photovoltaic planar heterojunctions with the SWCNT-films as the active light-absorbing material. The idea here is that excitons will be generated in all the single-chirality films. Each film will preferentially absorb a different part of the solar spectrum. This way light absorption can be optimized. Moreover, by placing the layers in order of decreasing band gap (Figure 2.13a-b) the excitons will be funneled very efficiently from the top layer to the bottom

layer. The model described in this Chapter (eqn. 2.10, 2.11) shows that in the SWCNT fibers the rate of diffusion of excitons from larger band gap SWCNT to lower band gap SWCNT via EET was larger than any of their recombination rates (Fig. 2.5f, Fig. 2.8d). We will optimize the SWCNT film morphology and thickness in order to achieve optimal light absorption and energy funneling. SWCNTs are typically p-doped so the bottom SWCNT film would be contacted with an n-dope acceptor (such as e.g. PCBM or C60 molecules). This way polymer-free organic photovoltaics can be made, either in an a cylindrical form (Figure 2.13a) or a planar form (2.13b). Jain and Howden *et al.* have already developed a polymer-free all-carbon planar photovoltaic which relies on exciton dissociation at the (6,5) SWCNT/C60 interface (Figure 2.13c) [56]. Following this effort where a single chirality film is in contact with the n-doped substrate (Figure 2.13c), we will create a multilayered planar structure where homogenous films of different SWCNT chirality are used (Figure (2.13a-b)).

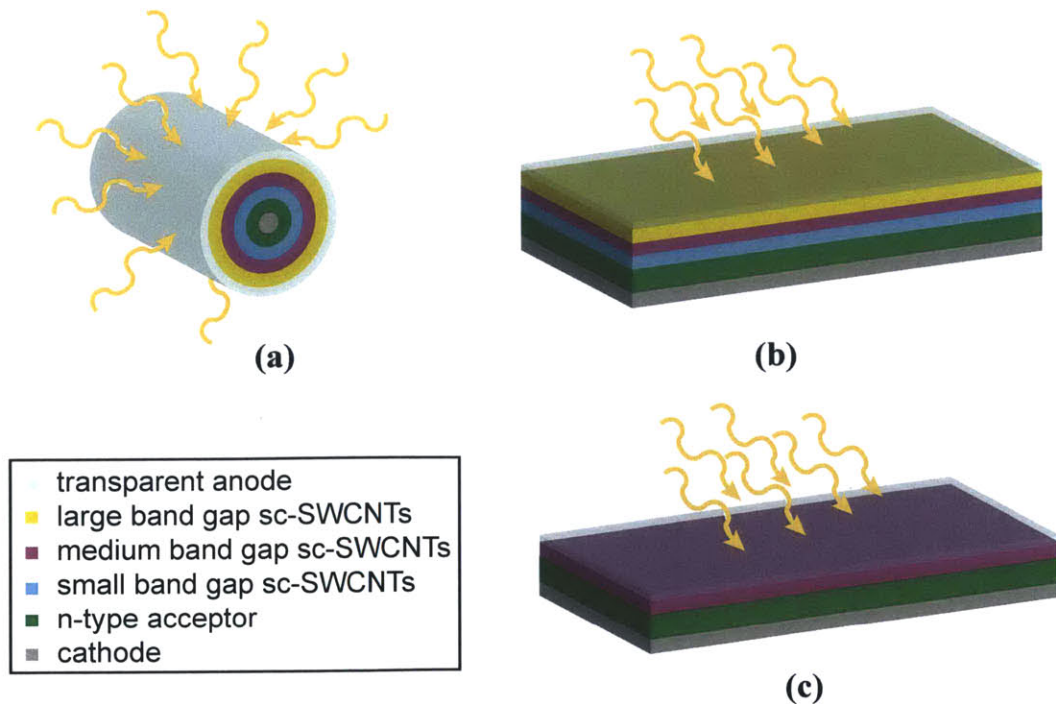


Figure 2.13. Possible configurations of polymer-free SWCNT-based photovoltaics. Yellow arrows represent (sun)light. One or more SWCNT layers constitute the electron-donating part of the photovoltaic, whereas as an n-type material such as PCBM functions as the electron acceptor. The p-type SWCNTs are contacted with a transparent anode, whereas the n-type acceptor is connected to a cathode. If multiple films of different SWCNT chirality are used, the larger band gap ones are located closest to the anode, the smaller band gap ones closest to the cathode. **(a)** Cylindrical photovoltaic with multiple SWCNTs layers. **(b)** Planar photovoltaic with multiple SWCNTs layers. **(c)** First realized polymer-free organic photovoltaic with homogenous (6,5) SWCNT-film as the electron donor and C60 as the electron acceptor.

2.6 References

- 1 Han, J. H., Paulus, G. L. C., Maruyama, R., Heller, D. A., Kim, W. J., Barone, P. W., Lee, C. Y., Choi, J. H., Ham, M. H., Song, C., Fantini, C. & Strano, M. S. Exciton antennas and concentrators from core-shell and corrugated carbon nanotube filaments of homogeneous composition. *Nature Materials* **9**, 833-839 (2010).
- 2 Currie, M. J., Mapel, J. K., Heidel, T. D., Goffri, S. & Baldo, M. A. High-efficiency organic solar concentrators for photovoltaics. *Science* **321**, 226-228 (2008).
- 3 Yoon, J., Baca, A. J., Park, S.-I., Elvikis, P., Geddes, J. B., Li, L., Kim, R. H., Xiao, J., Wang, S. & Kim, T.-H. Ultrathin silicon solar microcells for semitransparent, mechanically flexible and microconcentrator module designs. *Nature Materials* **7**, 907-915 (2008).
- 4 Mühlischlegel, P., Eisler, H.-J., Martin, O., Hecht, B. & Pohl, D. Resonant optical antennas. *Science* **308**, 1607-1609 (2005).
- 5 Taminiou, T., Stefani, F., Segerink, F. & Van Hulst, N. Optical antennas direct single-molecule emission. *Nature Photonics* **2**, 234-237 (2008).
- 6 Van De Lagemaat, J., Barnes, T. M., Rumbles, G., Shaheen, S. E., Coutts, T. J., Weeks, C., Levitsky, I., Peltola, J. & Glatkowski, P. Organic solar cells with carbon nanotubes replacing InO: Sn as the transparent electrode. *Applied Physics Letters* **88**, 233503-1:3 (2006).
- 7 Schuller, J. A., Taubner, T. & Brongersma, M. L. Optical antenna thermal emitters. *Nature Photonics* **3**, 658-661 (2009).
- 8 Lin, M. F. Optical spectra of single-wall carbon nanotube bundles. *Physical Review B* **62**, 13153-13159 (2000).
- 9 Yu, Z. H. & Brus, L. Rayleigh and Raman scattering from individual carbon nanotube bundles. *Journal of Physical Chemistry B* **105**, 1123-1134 (2001).
- 10 Wang, F., Sfeir, M. Y., Huang, L. M., Huang, X. M. H., Wu, Y., Kim, J. H., Hone, J., O'Brien, S., Brus, L. E. & Heinz, T. F. Interactions between individual carbon nanotubes studied by Rayleigh scattering spectroscopy. *Physical Review Letters* **96**, 167401-1:4 (2006).
- 11 Tan, P. H., Rozhin, A. G., Hasan, T., Hu, P., Scardaci, V., Milne, W. I. & Ferrari, A. C. Photoluminescence spectroscopy of carbon nanotube bundles: Evidence for exciton energy transfer. *Physical Review Letters* **99**, 137402-1:4 (2007).
- 12 Qian, H., Georgi, C., Anderson, N., Green, A. A., Hersam, M. C., Novotny, L. & Hartschuh, A. Exciton transfer and propagation in carbon nanotubes studied by near-field optical microscopy. *Physica Status Solidi B-Basic Solid State Physics* **245**, 2243-2246 (2008).
- 13 Kato, T. & Hatakeyama, R. Exciton energy transfer-assisted photoluminescence brightening from freestanding single-walled carbon nanotube bundles. *Journal of the American Chemical Society* **130**, 8101-8107 (2008).
- 14 Lefebvre, J. & Finnie, P. Photoluminescence and Forster Resonance Energy Transfer in Elemental Bundles of Single-Walled Carbon Nanotubes. *Journal of Physical Chemistry C* **113**, 7536-7540 (2009).
- 15 Delaney, P., Choi, H. J., Ihm, J., Louie, S. G. & Cohen, M. L. Broken symmetry and pseudogaps in ropes of carbon nanotubes. *Physical Review B* **60**, 7899-7904 (1999).

- 16 Kim, W.-J., Nair, N., Lee, C. Y. & Strano, M. S. Covalent functionalization of single-walled carbon nanotubes alters their densities allowing electronic and other types of separation. *Journal of Physical Chemistry C* **112**, 7326-7331 (2008).
- 17 Arnold, M. S., Green, A. A., Hulvat, J. F., Stupp, S. I. & Hersam, M. C. Sorting carbon nanotubes by electronic structure using density differentiation. *Nature Nanotechnology* **1**, 60-65 (2006).
- 18 Wang, F., Dukovic, G., Brus, L. E. & Heinz, T. F. Time-resolved fluorescence of carbon nanotubes and its implication for radiative lifetimes. *Physical Review Letters* **92**, 177401-1:4 (2004).
- 19 Bachilo, S. M., Strano, M. S., Kittrell, C., Hauge, R. H., Smalley, R. E. & Weisman, R. B. Structure-assigned optical spectra of single-walled carbon nanotubes. *Science* **298**, 2361-2366 (2002).
- 20 Maruyama, S., Miyauchi, Y., Murakami, Y. & Chiashi, S. Optical characterization of single-walled carbon nanotubes synthesized by catalytic decomposition of alcohol. *New Journal of Physics* **5**, 149-1:12 (2003).
- 21 Förster, T. 10th Spiers Memorial Lecture. Transfer mechanisms of electronic excitation. *Discussions of the Faraday Society*, 7-17 (1959).
- 22 Scardaci, V., Rozhin, A. G., Tan, P. H., Wang, F., White, I. H., Milne, W. I. & Ferrari, A. C. Carbon nanotubes for ultrafast photonics. *Physica Status Solidi B-Basic Solid State Physics* **244**, 4303-4307 (2007).
- 23 Hertel, T., Fasel, R. & Moos, G. Charge-carrier dynamics in single-wall carbon nanotube bundles: a time-domain study. *Applied Physics A - Materials Science & Processing* **75**, 449-465 (2002).
- 24 Lauret, J. S., Voisin, C., Cassabois, G., Delalande, C., Roussignol, P., Jost, O. & Capes, L. Ultrafast carrier dynamics in single-wall carbon nanotubes. *Physical Review Letters* **90**, 057404-1:4 (2003).
- 25 Nair, N., Kim, W.-J., Braatz, R. D. & Strano, M. S. Dynamics of surfactant-suspended single-walled carbon nanotubes in a centrifugal field. *Langmuir* **24**, 1790-1795 (2008).
- 26 Nair, N., Kim, W.-J., Usrey, M. L. & Strano, M. S. A structure-reactivity relationship for single walled carbon nanotubes reacting with 4-hydroxybenzene diazonium salt. *Journal of the American Chemical Society* **129**, 3946-3954 (2007).
- 27 Tang, J., Gao, B., Geng, H. Z., Velev, O. D., Qin, L. C. & Zhou, O. Assembly of 1D nanostructures into sub-micrometer diameter fibrils with controlled and variable length by dielectrophoresis. *Advanced Materials* **15**, 1352-1355 (2003).
- 28 Li, J. Q., Zhang, Q., Peng, N. & Zhu, Q. Manipulation of carbon nanotubes using AC dielectrophoresis. *Applied Physics Letters* **86**, 153116-1:3 (2005).
- 29 Walsh, A. G., Vamivakas, A. N., Yin, Y., Cronin, S. B., Unlu, M. S., Goldberg, B. B. & Swan, A. K. Screening of excitons in single, suspended carbon nanotubes. *Nano Letters* **7**, 1485-1488 (2007).
- 30 Perebeinos, V., Tersoff, J. & Avouris, P. Radiative lifetime of excitons in carbon nanotubes. *Nano Letters* **5**, 2495-2499 (2005).
- 31 Qian, H., Georgi, C., Anderson, N., Green, A. A., Hersam, M. C., Novotny, L. & Hartschuh, A. Exciton energy transfer in pairs of single-walled carbon nanotubes. *Nano Letters* **8**, 1363-1367 (2008).
- 32 Uchida, T., Tachibana, M. & Kojima, K. Thermal relaxation kinetics of defects in single-wall carbon nanotubes. *Journal of Applied Physics* **101**, 084313-1:4 (2007).

- 33 Hagen, A., Steiner, M., Raschke, M. B., Lienau, C., Hertel, T., Qian, H. H., Meixner, A. J. & Hartschuh, A. Exponential decay lifetimes of excitons in individual single-walled carbon nanotubes. *Physical Review Letters* **95**, 197401-1:4 (2005).
- 34 Trautz, M. Das Gesetz der Reaktionsgeschwindigkeit und der Gleichgewichte in Gasen. Bestätigung der Additivität von $Cv-3/2R$. Neue Bestimmung der Integrationskonstanten und der Moleküldurchmesser. *Zeitschrift für anorganische und allgemeine Chemie* **96**, 1-28 (1916).
- 35 Manzoni, C., Gambetta, A., Menna, E., Meneghetti, M., Lanzani, G. & Cerullo, G. Intersubband exciton relaxation dynamics in single-walled carbon nanotubes. *Physical Review Letters* **94**, 207401-1:4 (2005).
- 36 Murakami, Y. & Kono, J. Existence of an upper limit on the density of excitons in carbon nanotubes by diffusion-limited exciton-exciton annihilation: Experiment and theory. *Physical Review B* **80**, 035432-1:10 (2009).
- 37 Lueer, L., Hoseinkhani, S., Polli, D., Crochet, J., Hertel, T. & Lanzani, G. Size and mobility of excitons in (6,5) carbon nanotubes. *Nature Physics* **5**, 54-58 (2009).
- 38 Valkunas, L., Ma, Y. Z. & Fleming, G. R. Exciton-exciton annihilation in single-walled carbon nanotubes. *Physical Review B* **73**, 115432-1:12 (2006).
- 39 Wang, F., Dukovic, G., Knoesel, E., Brus, L. E. & Heinz, T. F. Observation of rapid Auger recombination in optically excited semiconducting carbon nanotubes. *Physical Review B* **70**, 241403-1:4 (2004).
- 40 Cagnet, L., Tsyboulski, D. A., Rocha, J.-D. R., Doyle, C. D., Tour, J. M. & Weisman, R. B. Stepwise quenching of exciton fluorescence in carbon nanotubes by single-molecule reactions. *Science* **316**, 1465-1468 (2007).
- 41 Vyazovkin, S. Kinetic concepts of thermally stimulated reactions in solids: a view from a historical perspective. *International Reviews in Physical Chemistry* **19**, 45-60 (2000).
- 42 Jost, W. The theory of electrolytical charge and diffusion in crystals. II. *Zeitschrift Fur Physikalische Chemie-Abteilung a-Chemische Thermodynamik Kinetik Elektrochemie Eigenschaftslehre* **169**, 129-134 (1934).
- 43 Zeldowitsch, J. B. On the theory of reactions on powders and porous substances. *Acta Physicochimica Urss* **10**, 583-592 (1939).
- 44 O'Connell, M. J., Bachilo, S. M., Huffman, C. B., Moore, V. C., Strano, M. S., Haroz, E. H., Rialon, K. L., Boul, P. J., Noon, W. H., Kittrell, C., Ma, J. P., Hauge, R. H., Weisman, R. B. & Smalley, R. E. Band gap fluorescence from individual single-walled carbon nanotubes. *Science* **297**, 593-596 (2002).
- 45 Buehler, M. J. Mesoscale modeling of mechanics of carbon nanotubes: Self-assembly, self-folding, and fracture. *Journal of Materials Research* **21**, 2855-2869 (2006).
- 46 Chaikin, P. & Lubensky, T. Principles of condensed matter physics *Science* **273**, 1348-1348 (1996).
- 47 Fagan, J. A., Simpson, J. R., Landi, B. J., Richter, L. J., Mandelbaum, I., Bajpai, V., Ho, D. L., Raffaele, R., Walker, A. R. H., Bauer, B. J. & Hobbie, E. K. Dielectric response of aligned semiconducting single-wall nanotubes. *Physical Review Letters* **98**, 147402-1:4 (2007).
- 48 Hirori, H., Matsuda, K., Miyauchi, Y., Maruyama, S. & Kanemitsu, Y. Exciton localization of single-walled carbon nanotubes revealed by femtosecond excitation correlation spectroscopy. *Physical Review Letters* **97**, 257401-1:4 (2006).

- 49 Kroeze, J. E., Koehorst, R. B. M. & Savenije, T. J. Singlet and triplet exciton diffusion in a self-organizing porphyrin antenna layer. *Advanced Functional Materials* **14**, 992-998 (2004).
- 50 Gottfried, D. S., Steffen, M. A. & Boxer, S. G. Large protein-induced dipoles for a symmetric carotenoid in a photosynthetic antenna complex. *Science* **251**, 662-665 (1991).
- 51 Abdula, D. & Shim, M. Performance and Photovoltaic Response of Polymer-Doped Carbon Nanotube p-n Diodes. *Acs Nano* **2**, 2154-2159 (2008).
- 52 Bibby, T. S., Nield, J., Partensky, F. & Barber, J. Oxyphotobacteria - Antenna ring around photosystem I. *Nature* **413**, 590-590 (2001).
- 53 Green, B. R. & Parson, W. W. *Light-harvesting antennas in photosynthesis*. Vol. 13 (Springer, 2003).
- 54 Liu, H., Nishide, D., Tanaka, T. & Kataura, H. Large-scale single-chirality separation of single-wall carbon nanotubes by simple gel chromatography. *Nature Communications* **2**, 309-1:8 (2011).
- 55 Tvrdy, K., Jain, R. M., Han, R., Hilmer, A. J., McNicholas, T. P. & Strano, M. S. A Kinetic Model for the Deterministic Prediction of Gel-Based Single-Chirality Single-Walled Carbon Nanotube Separation. *Acs Nano* **7**, 1779-1789 (2013).
- 56 Jain, R. M., Howden, R., Tvrdy, K., Shimizu, S., Hilmer, A. J., McNicholas, T. P., Gleason, K. K. & Strano, M. S. Polymer-Free Near-Infrared Photovoltaics with Single Chirality (6,5) Semiconducting Carbon Nanotube Active Layers. *Advanced Materials* **24**, 4436-4439 (2012).

3. Study and manipulation of SWCNT-P3HT interactions

Some of the work, text and figures presented in this chapter are reprinted or adapted with permission from reference [1] (Copyright © 2010, American Chemical Society) and reference [2] (Copyright © 2012, Institute of Physics (IOP Science)).

3.1. Background and motivation

As alternatives to silicon solar cells, conjugated polymer-based organic solar cells are inexpensive, easily fabricated, thin, low-weight and flexible [3-5]. Recent efforts to increase their efficiency have largely focused on the development of new low band gap polymers with a high hole mobility and a deep highest occupied molecular orbital (HOMO) level, and of acceptor molecules with a high lowest unoccupied molecular orbital (LUMO) level. These advances have led to power conversion efficiencies (PCEs) of up to 7.4% [6-15]. Design rules have been formulated for tandem solar cells to even reach an efficiency of 15% [16]. The conjugated semiconducting polymers used in photovoltaics typically have low dielectric constants, which causes Frenkel excitons to be created upon light absorption [17]. These Coulombically bound electron-hole pairs have a binding energy of approximately 0.5 eV [18]. The best device architectures are donor-acceptor (D/A) heterojunctions, in which an electron-accepting material forms an interface with the light-absorbing polymer [19]. Due to the offset in band energies between the donor and the acceptor material, the interface between both provides a force that is strong enough to dissociate the excitons and generate free charge carriers. After an

exciton is split, the hole remains in the polymer (the donor material), whereas the electron is transferred to the acceptor material and both free charge carriers are transported to their respective electrodes. P3HT attracted a lot of attention as a donor material due to its good solubility, processability, thermal stability, mechanical strength, broadband absorption [20], and hole mobility exceeding $0.1 \text{ cm}^2/\text{V}\cdot\text{s}$ [21]. Examples of typical electron acceptors are dyes (e.g. CuPc) [22], inorganic semiconductors (e.g. TiO_2 [23], ZnO [24], CdSe [25]), fullerenes (e.g. C_{60} [26]) and their derivatives (e.g. PCBM [3]). More recently SWCNTs have been employed because their one-dimensional structure serves as an efficient electron-transport pathway [1,27-30]; moreover the SWCNTs are characterized by high carrier mobility ($>10^4 \text{ cm}^2/\text{s}$, [31]).

In the most efficient solar cells the donor and acceptor materials are blended together to form an interpenetrating network, known as a bulk heterojunction (BHJ) [32]. Here, the donor and the acceptor materials phase-segregate on a nanometer length scale, such that essentially every exciton can reach a D/A interface within its lifetime, increasing the total amount of excitons dissociating into free charge carriers in comparison to a planar (bilayer) heterojunction (PHJ) solar cell. Power conversion efficiencies of 5% have been achieved this way for the ‘workhorse’ P3HT/PCBM solar cells [33]. However, both multi-walled carbon nanotubes (MWCNT) [27] and single-walled carbon nanotubes (SWCNT) [28-30] BHJ photovoltaic cells have suffered from much lower efficiencies compared to conjugated polymer/fullerene BHJ photovoltaic cells [34,35].

To address this, we fabricated a highly idealized interface consisting of single, electronically contacted millimeter-long, chemical vapor deposition (CVD)-grown

SWCNTs contacting a spin-coated *p*-type P3HT layer, creating a PHJ photovoltaic [1] (Fig.3.1a). Prior to contacting the SWCNTs with the P3HT, they were converted from *p*-type to *n*-type by drop-casting them with polyethylene imine (PEI) solution, followed by rinsing with methanol [1,36,37]. This planar nano-heterojunction device provides a simpler and better-defined substrate for exciton dissociation than typical bulk junctions, and is therefore ideal for answering these questions. The SWCNT/P3HT PHJ displayed a short-current density of $20\text{mA}/\text{cm}^2$ and a per-tube efficiencies of $\sim 3\%$ [1], compared to $0.5\text{mA}/\text{cm}^2$ and 0.09% for the best SWCNT/polymer BHJ [29]. It is clear from the results in [1] that the polymer/nanotube interface itself is responsible for exciton dissociation. Typical open-circuit voltages are near 0.5V with fill factors of $0.25\text{--}0.3$, which are largely invariant with the number of nanotubes per device and P3HT thickness. This work showed that the primary reasons for low energy conversion efficiency in BHJ devices incorporating SWCNTs are (1) the formation of bundled aggregates as a consequence of incomplete polymer dispersion and (2) the presence of tube-tube junctions created for the same reason. The clustering of SWCNTs can be detrimental in case a metallic-SWCNT is part of bundle of SWCNTs: the *m*-SWCNT can quench all the excitons that reach the cluster of SWCNTs [38] [39].

Other disadvantages of BHJs are: the interpenetration of the two phases makes charge extraction more difficult: a continuous pathway must exist between the hole (electron)-collecting electrode and the donor (acceptor) material, and even then, there is ample opportunity for electron-hole recombination. Moreover, the ideal nanoscale morphology of a BHJ is hard to achieve and control, and it is difficult to characterize and model the actually realized structure. This had led to the recent reappraisal of the need for

planar heterojunctions [40-43].

Where for BHJs the ideal thickness of the active layers is determined by a trade-off between increasing light absorption and reducing electron-hole recombination [44-46], for a PHJ the maximum photocurrent is expected to be obtained for a device where the thickness of the light-absorbing material is equal to the exciton diffusion length of that material, ranging from 5 to 14nm for most conjugated polymers [47-51]. The reasoning is that devices with a smaller active thickness do not absorb enough of the light whereas a larger active thickness (typically ~100nm is required to absorb most of the light [52,53]) is of no use in a PHJ since any excitons generated at a distance larger than the exciton diffusion length from the heterojunction would recombine before reaching the junction. Note that this limited exciton diffusion length was the main argument for creating bulk heterojunction solar cells. However, in our earlier work (SWCNT/P3HT PHJ described in [1]) a maximum in both the power conversion efficiency (*PCE*) as well as in the short-circuit current (I_{SC}) is obtained for a thickness of 60-65 nm of P3HT, far higher than the exciton diffusion length in P3HT (8.5nm) [51]. Another state-of-the-art organic PHJ (where P3HT was the donor and PCBM molecules the acceptor [43], Fig. 3.1b) displayed very similar behavior. It is this peculiarity that we are able to describe with a simple model.

We simulate the photon absorption in the P3HT, by calculating the optical electric field distribution in the device, thereby taking into account optical interference effects. The resulting distribution of excitons in the P3HT serves as an input to a kinetic Monte Carlo simulation, which tracks exciton diffusion, recombination and dissociation. We find that bulk exciton dissociation is mainly responsible for the maximum photocurrent at

60nm for the P3HT/SWCNT-based PHJ. In the P3HT/PCBM bilayer it is revealed that the main factor contributing to the maximum is the (mobile) PCBM molecules diffusing into the P3HT upon annealing, changing the total device thickness and morphology.

3.2. Materials and methods

3.2.1. Experimental materials and methods

A device schematic of the ITO/P3HT/SWCNTs/Al planar heterojunction photovoltaic [1] is shown in Figure 3.1a. CVD-growth of the SWCNTs onto the Si/SiO₂ substrate resulted in millimeter-long well-isolated and aligned SWCNTs. It was shown that ~90% of the SWCNT are semiconducting and the average tube diameter is 2nm. Regioregular (RR) P3HT was spincoated from solution on top of the SWCNTs, after which the structure was annealed, and finally ITO was sputtered on top of the P3HT. The Al electrode was deposited on the other end of the SWCNT via e-beam evaporation and serves as the cathode [1].

The device-schematic of the ITO/PEDOT-PSS/P3HT-Br/PCBM/Al PHJ is shown in Figure 3.1b. A PEDOT:PSS dispersion was spuncast onto an ITO-coated glass substrate. The P3HT-Br solution was spun on top, irradiated with UV-light and annealed at 150°C for 15 minutes. Then the PCBM solution was spuncast on top. Subsequently the entire structure is annealed again under the same conditions. Finally a 100nm Al cathode was deposited by thermal evaporation under vacuum [43]. The experimental methods and results of the SWCNT-P3HT and PCBM-P3HT PHJs described in 3.1 can be found in [1] and [43] respectively.

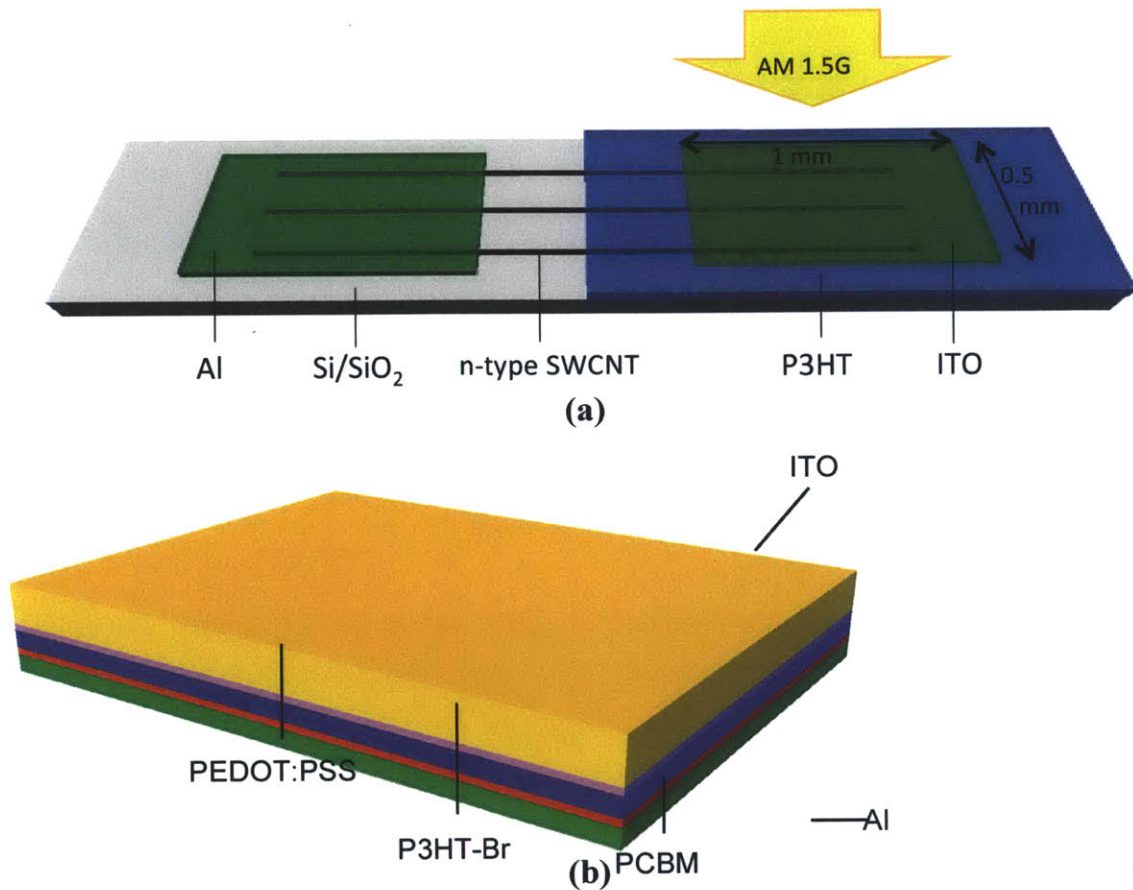


Figure 3.1. Schematics of hybrid planar nano-heterojunction solar cells based on conjugated polymers and carbon nanotubes or PCBM. **(a)** Schematic of PHJ solar cell based on a P3HT film on laterally aligned SWCNTs. More experimental details on the device fabrication can be found in ref. [1] **(b)** Schematic of P3HT-Br/PHJ solar cell described in ref. [43].

3.2.2. Methodological and computational approach

Kinetic Monte Carlo Simulation

In semiconducting polymers, transport of excitons, electrons and holes occurs by short-range hopping between localized states. Therefore, a natural way to model these polymeric devices is to track the movement of an ensemble of these particles using a Kinetic Monte Carlo (KMC) simulation based on a ‘first reaction method’ (FRM)

algorithm [54].

An alternative method to simulate organic solar cells is a drift-diffusion model [55-60]. However, often these models reduce complex three-dimensional morphologies to homogeneous, one-dimensional structures. As we will show later on, non-homogeneities in the active layer are key to explaining the anomalous thickness-dependence of the photocurrent observed in PHJs.

Watkins *et al.* were the first to examine the influence of the polymeric solar cell morphology on the internal quantum efficiency (*IQE*) with a KMC simulation [61]. Later more sophisticated models have been created that also predict other important figures of merit of organic solar cells (such as the short-circuit current I_{SC} , the open-circuit voltage V_{OC} , the fill factor FF and the *PCE*) by taking into account all or a subset of the following aspects: exciton creation, exciton diffusion, exciton dissociation, dark injection at the electrodes, charge transport, charge recombination, charge extraction, electrostatic interactions, space-charge effects, energetic disorder, polaronic effects and device morphology [62-69].

The optical-to-electrical conversion process in an excitonic solar cell can be broken up into four steps [63], each associated with their own efficiency η : (1) the absorption of a photon and generation of an exciton (η_{abs}), (2) exciton diffusion (η_{diff}), (3) exciton dissociation into free carriers (η_{diss}) and (4) charge collection at the electrodes (η_{cc}). The external quantum efficiency η_{EQE} can be written as:

$$\eta_{EQE} = \eta_{abs} \eta_{diff} \eta_{diss} \eta_{cc} \quad (3.1).$$

For planar heterojunction donor-acceptor solar cells, it is common practice to assume the

third and the fourth steps to be 100% efficient [63]: exciton dissociation happens extremely fast (10–100 fs) [61,63] and free electrons (holes) can move rapidly towards the cathode (anode) through an n-type (p-type) material where no significant carrier recombination occurs, at least for values of the mobility $\mu_{holes/electrons} > 2 \times 10^{-4} \text{ cm}^2/\text{V.s}$, as shown by Yang *et al.* [63]. The active materials utilized in the two PHJs studied in this work [1,43] do fall in this high-mobility category: $\mu_{holes \text{ in P3HT}} \sim 3 \times 10^{-4} \text{ cm}^2/\text{V.s}$ [70], $\mu_{electrons \text{ in SWCNT}} \sim 10^4 \text{ cm}^2/\text{V.s}$ [71] and $\mu_{electrons \text{ in PCBM}} \sim 10^{-3} \text{ cm}^2/\text{V.s}$ [72]. Therefore, to a first order approximation, the current output in planar heterojunction solar cells is determined by the amount of light absorbed by the solar cell and by the ability of the excitons to reach the heterojunction [63]. The absence of the need to track charge transport in PHJs and to focus primarily on excitons strongly reduces the computational time of the model while not affecting its validity. Before the way the model approaches the different events that excitons undergo is addressed in more detail, we introduce the lattice in which these events will take place.

KMC lattice setup

1. P3HT/SWCNT device

Since there are so few SWCNTs in the simulated devices (5-10 per device), we assume that excitons are generated solely in the P3HT. The polymer slab is modeled as a lattice of 60 nm in length (*x*-axis), 12nm in width (*z*-axis) and a variable height (*y*-axis) to explore the thickness-dependence. The lattice is defined by three lattice constants (Fig. 3.2) based on a grazing incidence XRD study performed by Erb *et al.* [73]. They showed that in annealed semi-crystalline P3HT the backbone of the polymer is oriented parallel

to the substrate and the alkyl sidechains perpendicular. They determine the interchain distances as 1.61 nm in the y -axis and 0.39 nm (*i.e.* the π - π stacking distance of P3HT) in the z -axis. These two characteristic distances make up two of the lattice constants ($a_y = 1.61$ nm, $a_z = 0.39$ nm). Since conjugated polymers can be regarded as arrays of chromophores that are identified as fully conjugated segments of the polymer [20,74], the remaining lattice constant is the π -conjugation length along the backbone of the P3HT ($a_x = 3.9$ nm which is ~ 10 repeat units of the polymer) [75]. In order to account for the spatial disorder in the P3HT, each lattice site is shifted by a random vector creating an off-lattice representation, that never exceeds $0.4 \times a$, where a represents the lattice constant [74]. Periodic boundary conditions in the x - and z - directions (where the xz -plane lies parallel to the PHJ interface) are employed to prevent finite-size effects. In the y -direction excitons are quenched at the P3HT/ITO ($y=0$) interface and dissociate into free charge carriers at the P3HT/SWCNT interface.

2. P3HT/PCBM device

The P3HT that Kim *et al.* use has been chemically modified: 5mol% 3-bromothiophene was added to the P3HT to create a bromine-functionalized P3HT (P3HT-Br5) that shows higher thermal stability [43]. No absorption spectrum of this modified structure is available, but the authors confirm that the π - π stacking feature is not affected (by investigating 2D GIWAXS patterns). Moreover, since bromine is a small molecule that attaches to the alkyl-sidechains of the polymer [43], and the backbone of the polymer is responsible for photo-absorption [74], we assume as a first order approximation that the exciton generation and diffusion in the P3HT-Br5 copolymer is no

different than in normal RR-P3HT. We therefore use the same P3HT-lattice as the one developed for the P3HT/SWCNT case described in the previous section.

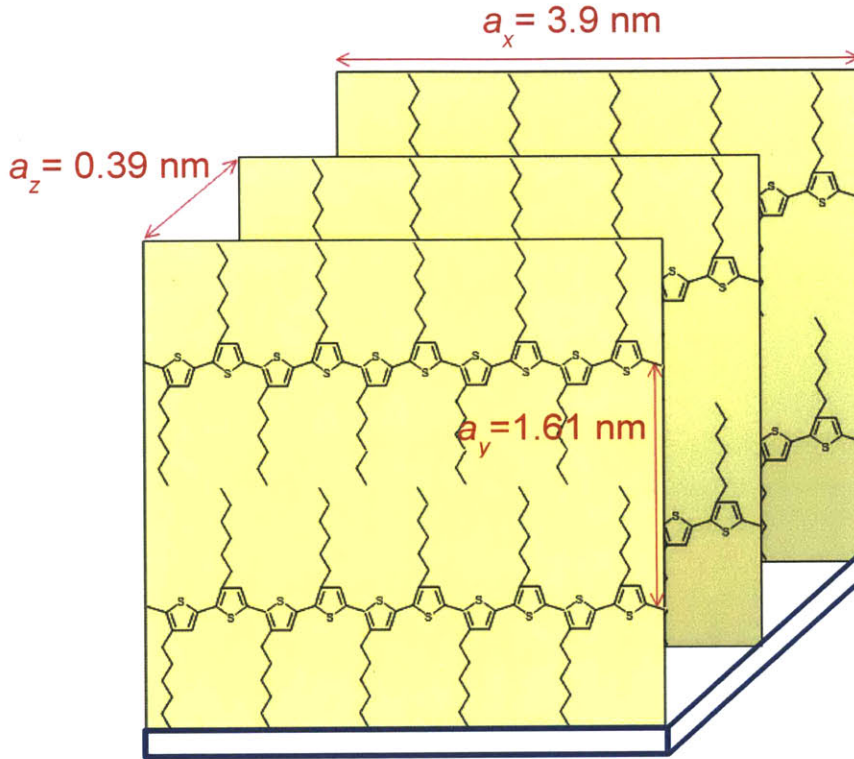


Figure 3.2. Lattice structure of P3HT employed in the Monte Carlo simulation. Lattice constants $a_x = 3.9 \text{ nm}$, $a_y = 1.61 \text{ nm}$, $a_z = 0.39 \text{ nm}$.

Similarly to the P3HT/SWCNT case the model states that excitons get quenched at $y=0$ (i.e. the P3HT/PEDOT:PSS interface) [76] and that each exciton that reaches the hetero-interface (in this case with PCBM) contributes to the generated photocurrent. The exciton diffusion length of PCBM has never been measured experimentally, but PCBM is shown to have a very crystalline FCC lattice structure, much like C60 [77]. Therefore we approximate the exciton diffusion length in PCBM by the one in C60, i.e. 40nm [78,79]. Since the thickness of PCBM in this device is only 25nm [43], we can assume that all the excitons generated in the PCBM contribute to the photocurrent. In fact, ballistic

conduction of excitons in PCBM has been previously suggested [79]. This assumption also reduces the computational time, as hopping of excitons only needs to be considered in the P3HT-lattice.

Exciton events

1. Exciton generation

It is assumed that each photon absorbed in the photoactive part of the device generates one exciton. Due to the fact that the solar cells described consist of multiple layers and that each layer has a different dielectric constant, light may be reflected at each interface and interfere with the incoming light. An elegant way to calculate the generation of excitons in such a multilayered structure is to employ the T-matrix method. The full details of this theory are discussed elsewhere in the literature [80-83]. Although using this method of determining the exciton generation profile in organic solar cells to examine their performance is not novel in and of itself, the resulting photocurrent is mostly calculated with a drift-diffusion model [46,57,58,82] or with the rudimentary assumption that every absorbed photon contributes to the photocurrent (i.e. the internal quantum efficiency IQE is 100%) [45,83,84].

Most KMC simulations of organic solar cells in the literature focus on charge transport and the influence of morphology on the performance of BHJs and assume a uniform [62,64,65,67-69] or Gaussian [61] distribution of excitons in the device.

Since it has been shown that optical interference is the major factor influencing thickness-dependence of the photocurrent and efficiency in BHJs [45,46], we deem it most accurate to use the optical T-matrix method (with AM1.5G illumination of the

devices) to determine the exciton generation profile that will subsequently serve as the ‘input’ for the KMC simulation where the generated excitons can hop around in the P3HT lattice.

It is important to note that the T-matrix theory assumes (1) parallelism and planarity of all interfaces with respect to the incoming light, (2) the absence of scattering, (3) homogeneous and isotropic layers (such that the linear optical response can be described by a scalar complex index of refraction and (4) a well-defined uniform thickness of each layer. Knowing the complex index of refraction $\tilde{n} = n + ik$, where n is the real part and k the imaginary part, interface-matrices can be set up that take into account reflection and transmission at each interface. For every layer j a phase matrix then describes the propagation through that particular layer. Combining these matrices, for each layer j , the total optical electric field $E_j(y, \lambda)$ can be calculated at every point y and for each wavelength λ , where $0 \leq y \leq d_j$, with d_j the thickness of layer j .

Based on the concept of the Poynting vector the time average of energy dissipation per unit time at point y is

$$Q_j(y, \lambda) = \frac{1}{2} c_0 \varepsilon_0 \alpha_j(\lambda) n_j(\lambda) |E_j(y, \lambda)|^2 \quad (3.2),$$

with c_0 is the speed of light in vacuum, ε_0 the permittivity of vacuum and the absorption

coefficient $\alpha_j(\lambda) = \frac{4\pi k_j(\lambda)}{\lambda}$. Based on the relationship between intensity I and the

amplitude E of a monochromatic propagating wave, Equation (3.2) can be written as:

$$Q_j(y, \lambda) = \frac{n_j(\lambda)}{n_{air}(\lambda)} \alpha_j(\lambda) I_0(\lambda) \left| \frac{E_j(y, \lambda)}{E_0(\lambda)} \right|^2 \quad (3.3),$$

where the subscript 0 refers to a property of the incoming wave (light).

Often a glass substrate is used (e.g. in the P3HT/PCBM solar cell we discuss [43]). Because this substrate typically is orders of magnitude thicker (~1mm) than the rest of the multilayered stack, coherence is lost between the glass substrate and the neighboring films and Equation (3.3) cannot be used. Adding intensities rather than amplitudes is required for the air/glass reflection terms, which ultimately results in Equation (3.4):

$$Q_j(y, \lambda) = \frac{n_j(\lambda)}{n_g(\lambda)} \alpha_j(\lambda) I_0(\lambda) \left(\frac{1-R^*}{1-RR^*} \right) \left| \frac{E_j(y, \lambda)}{E_g(\lambda)} \right|^2 \quad (3.4),$$

where subscript g refers to a property of the glass substrate, R^* is the reflectance between air and the glass substrate and R is the reflectance between the glass substrate and the rest of the multilayered stack.

Dividing the dissipated energy $Q_j(y, \lambda)$ (in units of $W.m^{-2}.nm^{-1}$) by the incoming energy results in the number of photons dissipated per second as a function of depth and wavelength:

$$G_j(y, \lambda) = \frac{Q_j(y, \lambda)}{h\nu} = \frac{Q_j(y, \lambda)}{hc_0/\lambda} \quad (3.5),$$

Finally, the sum of $G_j(y, \lambda)$ for all wavelengths in the solar spectrum results in the photon generation rate at depth y in layer j .

2. Exciton diffusion

Once it is determined where in the lattice and at what rate excitons are generated, the KMC simulation allows these excitons to start hopping around in the lattice. In literature many different expressions can be found that describe the hopping of the excitons from site to site within a polymer slab [54,63,74,85]. In general, the hopping rates take the form,

$$v_{ij} = v_0 f(r_{ij}) \begin{cases} 1 & \text{if } E_i - E_j > 0 \\ \exp\left(\frac{-\Delta E_{ij}}{k_B T}\right) & \text{if } E_i - E_j \leq 0 \end{cases} \quad (3.6),$$

where v_0 is the attempt-to-escape frequency, E_i and E_j are the energies of site i and site j , respectively, ΔE_{ij} is their difference, r_{ij} is the distance between the sites involved, k_B is the Boltzmann constant and T is the temperature. Hopping is considered within the intrinsic density of states of the polymer. The energy disorder in the lattice is simulated by assigning each lattice site a random energy that follows a Gaussian distribution; for P3HT the center energy and Gaussian width of this distribution are 1.9 eV and 0.08 eV respectively [74].

For BHJ solar cells, where the donor-acceptor separation is generally limited to the exciton diffusion length, the hopping of excitons between donor molecule i and acceptor molecule j can be described by Förster resonance energy transfer (FRET) [54,61,63], where

$$f(r_{ij}) = \left(\frac{a}{r_{ij}}\right)^6 \quad (3.7),$$

with a the Förster radius, defined as the value of the distance at which the hopping rate is

equal to the decay rate (the energy transfer efficiency is 50%). A donor chromophore, initially in its electronic excited state, can transfer energy to an acceptor chromophore (in proximity, typically *less than 1 nm*) through nonradiative dipole–dipole coupling [86]. This expression is valid in bulk heterojunctions where the donor and the acceptor molecules are *blended on a nanometer* length scale.

However, in PHJs the donor and acceptor molecules are separated by much larger distances. When an exciton is generated on a chromophore in the bulk of the P3HT, it will either recombine (non-) radiatively, dissociate, OR, transfer its energy *to another P3HT* chromophore molecule in its immediate surroundings. Therefore one could think of the one P3HT chromophore as the donor molecule *i* and another P3HT molecule as the acceptor molecule *j*. Since the Förster distance r_{ij} depends on the overlap integral of the donor emission spectrum with the acceptor absorption spectrum, this implies that in our own P3HT/SWCNT system it depends on the overlap between the emission spectrum and the absorption spectrum of P3HT. There is close to no overlap between the emission and absorption spectrum of P3HT though: P3HT emits most between 600 and 800 nm [87], whereas it absorbs most between 400 and 600nm [88]. Hence *FRET* (Förster Resonance Energy Transfer) is not a good way to describe the energy transfer of excitons *in a bulk of a homogeneous material*.

Rather, it has been shown excitons hop from site *i* to site *j* within the same material via the Miller-Abraham rate process [74,85,89,90].

$$f(r_{ij}) = \exp\left(-2 \times \frac{r_{ij}}{\alpha}\right) \quad (3.8),$$

with α the localization length of excitons in P3HT which takes on a value of 6.7 nm [20,91]. We note that there is confusion in the literature on this point. For example, certain papers that discuss the effect of morphology on the efficiency of polymeric solar cells, go from bulk heterojunction all the way to planar heterojunctions, without changing their expression for exciton motion in the polymers [63]. Apart from the above theoretical argument, there is also experimental evidence that the Miller-Abraham expression (Eq. (3.8) substituted in Eq. (3.6)) is more correct to describe the motion of excitons in a bulk (relatively homogeneous) material. Scheidler *et al.* studied the migration and relaxation of excitons in poly(phenylenevinylene) by describing the results of photoluminescence quenching experiments in PPV with a Monte Carlo simulation [74]. They run their simulation both with the Miller-Abrahams expression and with the Förster-expression for exciton migration and find that their quenching data at several temperatures are consistently better predicted when using the Miller-Abrahams expression (see Figure 5 of ref. [74]).

It should be noted that the excitons that find themselves within a few nanometers from the heterojunction do experience the influence of an acceptor molecule (to borrow from FRET-terminology). This is taken into account in the model. If an exciton residing on donor molecule i ‘sees’ in its immediate surroundings an acceptor molecule j (where there is significant overlap between the emission spectrum of molecule i with the absorption spectrum of molecule j), it will preferentially migrate there (e.g. at the interface between P3HT and SWCNT or between P3HT and PCBM). Whereas if molecule i is surrounded by other molecules of the same material (e.g. in the bulk of P3HT), its migration path will look more like a random walk (conform the Miller-

Abrahams process). To simulate this effect in a simple way the model assigns a lower energy to molecules of the acceptor material (SWCNT or PCBM). Thus once excitons reach the vicinity of the interface (i.e. find themselves within the exciton diffusion length of the hetero-interface) in the simulation, they are more ‘drawn’ to the interface than to surrounding molecules of the same type, as the hopping probability between molecule i and j depends on the energy difference between the two molecules (Eq. 3.6).

3. Exciton recombination

Excitons can recombine, either radiatively or non-radiatively. The radiative rate constant for excitons in pristine P3HT thin films has a reported value of 10^8 /s [87]. Non-radiative recombination is modeled through the random insertion of ‘trap-sites’ in the polymer slab [74,92,93]; these represent non-radiative quenching sites in the polymer, often caused by defects. If an exciton hops into a trap, it is irreversibly immobilized. The non-radiative rate constant has not been measured for P3HT and therefore the degree of traps is an adjustable parameter in the model. It should be noted that for the P3HT-SWCNT case, the degree of traps is presumably much higher since sputtering of ITO on top of the polymer is known to provide additional defects (quenching sites) in the polymer near the ITO/polymer boundary [94-96]. This introduces a non-homogeneity in the trap-site distribution.

4. Exciton dissociation

It has been previously suggested that excitons, which are generated in conjugated polymer solar cells, only dissociate at the heterojunction that the polymer forms with the

acceptor material [97]. Recently however, several ultrafast spectroscopy investigations [20,98-100] have shown that excitons dissociate within the P3HT bulk as well and form free polarons. Guo *et al.* [20] employed the Onsager-Braun model [101,102] to show how the dissociation yield of excitons in RR-P3HT in the bulk becomes increasingly significant with increasing strength of the electric field E . They show that there exists a relationship between the bulk exciton dissociation yield ($BEDY$) and the electric field E present in a material:

$$BEDY = \frac{k_D(E)}{k_V + k_D(E)} \quad (3.9),$$

where k_D is the field-dependent dissociation rate constant and k_V is the field-independent vibrational relaxation rate constant [20].

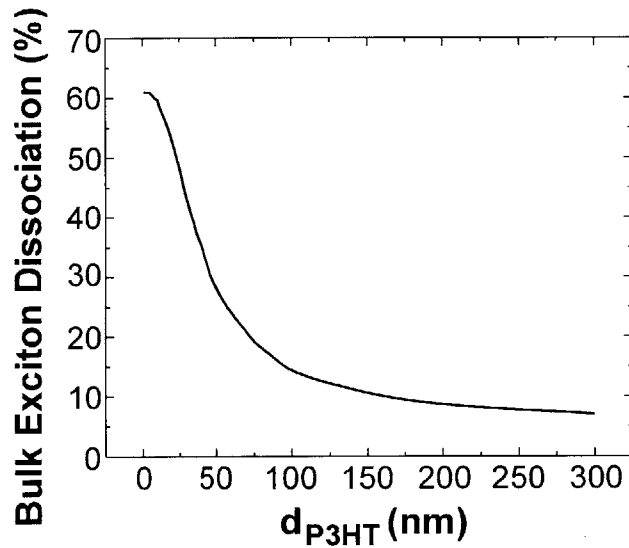


Figure 3.3. Bulk exciton dissociation efficiency. Percentage of generated excitons that dissociate in the bulk, as a function of P3HT thickness, when $V_{bi} = 0.5V$.

Based on this equation, Guo *et al.*, plot the evolution of the $BEDY$ as a function of the electric field E for RR-P3HT films with a typical crystallinity of 61%, as shown in Figure

4 of the Supporting Information of reference [20]. The degree of crystallinity was determined based on the measurement of a typical RR-P3HT film, a completely amorphous RRa-P3HT film and the theoretical density of a 100% crystalline RR-P3HT film [20]. The value is consistent with another recent report of 60% for a RR-P3HT film [103]. It should be noted that Guo's calculations are done for room temperature conditions.

Our model aims to calculate the short-circuit current; at short-circuit conditions, the electric field E in a planar heterojunction can be estimated as V_{bi}/d , where V_{bi} represents the built-in potential of the solar cell, determined by the work function of the two electrodes, and d represents the thickness of the material to which the electric field is applied. Based on Guo's analysis and the relationship between the electric field E and the P3HT thickness d_{P3HT} , we plot the trend of $BEDY$ as a function of d_{P3HT} , as shown in Figure 1(d). From Figure 1(d), we can conclude that at $V_{bi} \sim 0.5$ V up to 60% of the excitons dissociate in the bulk for P3HT thicknesses up to 10–15 nm, whereas less than 10% dissociate for thicknesses larger than ~ 150 nm.

In PHJs, it can be assumed that an electron generated by bulk exciton dissociation has little chance of contributing to the photocurrent since it is generated far from the electron-accepting phase. Most likely, it will recombine quickly, in a non-radiative way, either with an intrinsic hole from the naturally p -doped P3HT [21], with a photo-induced hole that was generated at the interface with the SWCNT and is diffusing back to the ITO or with a hole that exists as the result of bulk dissociation itself. Thus in our model we state that after their generation, only the excitons that do not dissociate in the bulk can hop around in the lattice.

Summary of the model

The optical T-matrix procedure results in the rate of excitons generated at each point in the lattice. The KMC model is then applied to each exciton, generated in each lattice site, as is schematically shown in Figure 3.4.

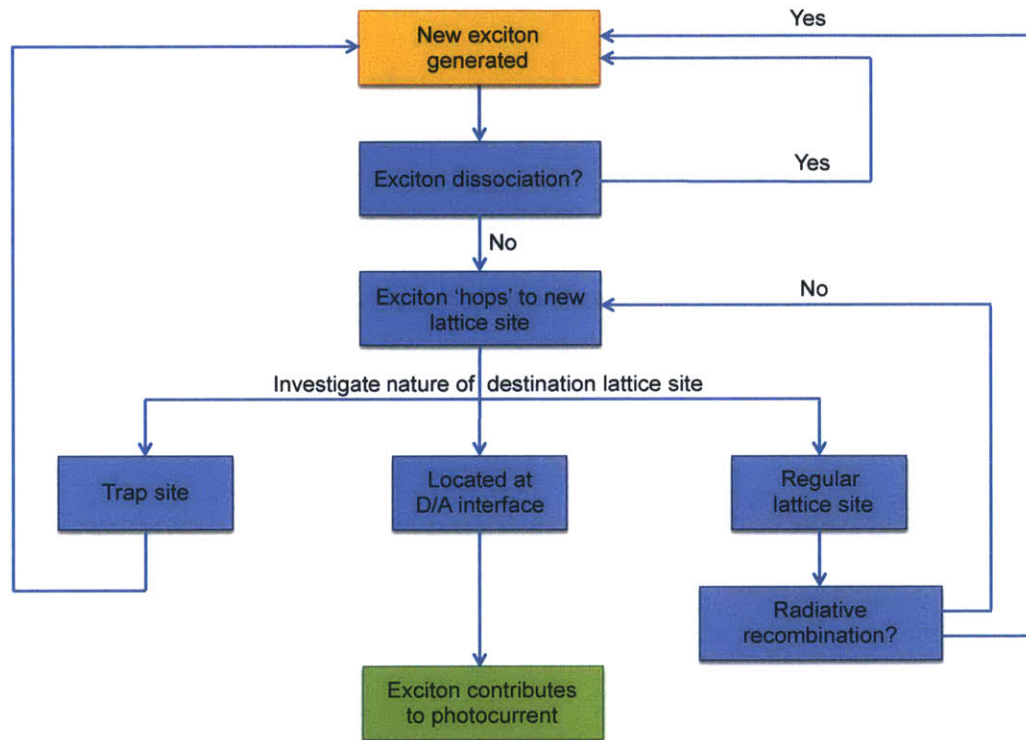


Figure 3.4. Schematic summary of the Kinetic Monte Carlo simulation. The optical T-matrix procedure determines the rate of excitons generated at each lattice site. The above KMC scheme is applied to each of them.

Once an exciton is generated in a specific lattice site, the model checks what the chance is this exciton will dissociate within its lifetime, based on Figure 1(d). If it will dissociate at some point, the model exits the current loop and start investigating the path of another exciton. If it does not, then the exciton is allowed to diffuse/'hop' to another

lattice site. In order to determine what happens next, the nature of this lattice site is investigated. There are several possibilities:

- The destination site is a trap (which represent an exciton quenching event). In this case the exciton gets quenched, and can no longer contribute to the current; the model moves on to investigate the next exciton.
- The destination site is located at the donor/accepter (D/A) interface. As explained above, in this case the exciton can contribute to the photocurrent.
- The destination site is neither a trap-site nor located at the D/A interface, rather it is a regular lattice site. Before the model allows for the exciton to hop to the next lattice site, it determines whether or not the exciton recombines radiatively. In case radiative recombination occurs, the exciton decays and the model moves on to the next exciton. In case it does not, the exciton hops to a new lattice site, whose nature is again investigated.

Computational details

The simulation codes for both the optical T-matrix model and the Kinetic Monte Carlo Simulation were written in Matlab. The codes were run on a quad core computer (Intel i7 975x, 3.33 GHz). Depending on the thickness of P3HT, the code simulating the photocurrent in a P3HT/SWCNT device ran for 2 to 48 hours. This long runtime is due to the fact that the simulations were each run 400 times. This is required because charge is only generated when the exciton reaches a nanotube and since the surface coverage of nanotubes is very small, there is a large stochastic variance and the codes need to be run 400 times to get a meaningful average: the remaining fluctuations are smaller than the

standard deviation of the experimental data points. For the P3HT/PCBM devices, the codes ran for a couple of hours. For every value of d_{P3HT} , the codes only needed to be run 10 times to get a meaningful average, since the interfacial area between P3HT and PCBM is substantially larger than between P3HT and SWCNT. For all simulations a steady-state time of 0.1 second is imposed to allow fluctuations to be dampened (this is a greater than or equal value compared to other steady-state times reported [61,63]).

3.3. Results and discussion

3.3.1. Optical T-matrix model

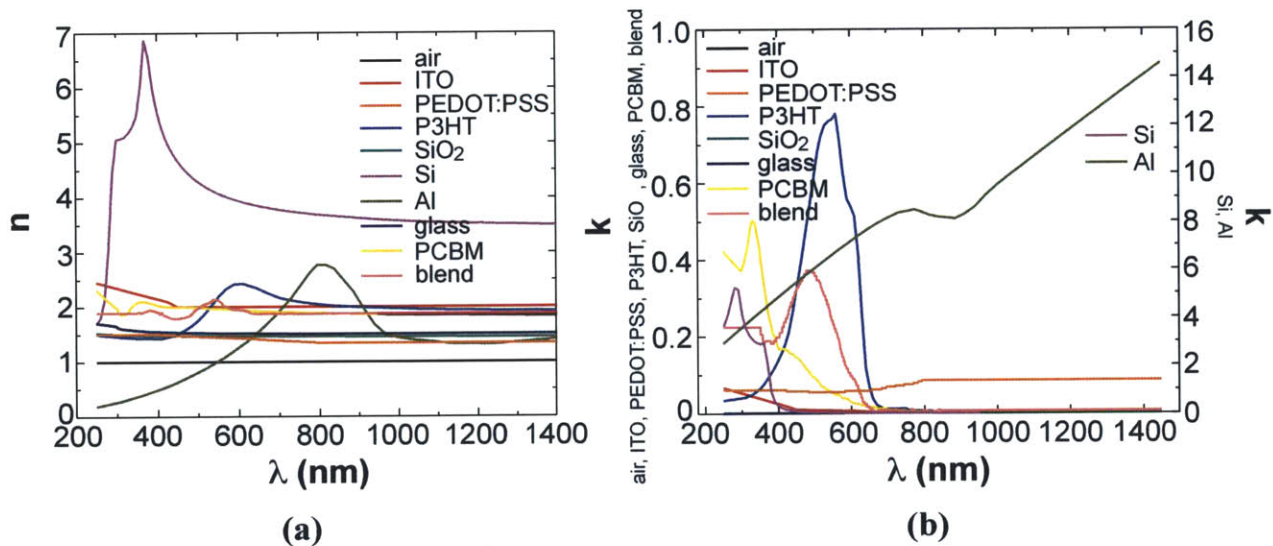


Figure 3.5. Optical constants as a function of wavelength. (a) real part of the complex index of refraction, n . (b) imaginary part of the complex index of refraction, k .

P3HT/SWCNT device

Figure 3.6a shows the device structure to which the T-matrix method is applied. Note that since the nanotubes are so sparsely divided across the SiO₂ surface (several

microns apart) [1], it is assumed they do not contribute substantially to the optical electric field in the device and they are omitted from the optical intensity model. It is easy to demonstrate the validity of this assumption. The dimensions of the P3HT covered by ITO are 1mm x 0.5mm x (5nm - 300 nm), depending on the thickness of the P3HT layer, which results in a volume of $2.5 \times 10^{-6} \text{ mm}^3$ to $1.5 \times 10^{-4} \text{ mm}^3$. The volume of a single SWCNT covered by ITO is $\pi \times r^2 \times l$, where on average the radius r is 1nm and $l = 1\text{mm}$ [1]. With the number of SWCNT per device ranging from 5 to 10 [1], the total volume taking in by the SWCNT falls between $5 \times \pi \times 10^{-12} \text{ mm}^3$ to $\pi \times 10^{-11} \text{ mm}^3$. For the case of a maximum amount of SWCNTs in a device with only 5nm of P3HT the volume ratio of P3HT to SWCNT is still approximately $8 \times 10^4 : 1$. For the case of a minimum amount of SWCNTs with the thickest layer of P3HT the volume ratio is $\sim 9.6 \times 10^6 : 1$. A typical SWCNT film has an absorption coefficient of $3 \times 10^4 - 3 \times 10^5 \text{ cm}^{-1}$ throughout the solar spectrum. [Supporting Information of [104]]. The absorption coefficient of a material is

related to its imaginary part k of its index of refraction via $\alpha_j(\lambda) = \frac{4\pi k_j(\lambda)}{\lambda}$. $k_j(\lambda)$ for

P3HT is plotted in Figure 3.5b. The peak of the P3HT absorption spectrum largely coincides with the solar AM1.5 spectrum. At the peak of the solar spectrum ($\lambda=495\text{nm}$), the absorption coefficient of P3HT is 14856 cm^{-1} , whereas the maximum absorption coefficient of a SWCNT at this wavelength is $\sim 225000 \text{ cm}^{-1}$, about a factor 15 higher than the P3HT absorption. This higher absorption coefficient is not sufficient to overcome the massive difference in volume that can absorb light. Moreover, the SWCNTs are located underneath the P3HT, which means a lot of the sunlight is already absorbed by the P3HT the time it reaches the SWCNTs, decreasing the amount of light absorbed by SWCNTs

compared to by P3HT even more. Finally it should be noted that this calculation assumed that the SWCNTs were in resonance with the peak of the solar spectrum. The absorption coefficients mentioned are for a film of SWCNTs of all types of chiralities, whereas in the devices described in our manuscript, 1-10 individual SWCNTs are used per device. Each SWCNT is characterized by its own chirality and Van Hove singularities in its Density of States. Only at these Van Hove singularities – very narrow regions in the wavelength spectrum, does the SWCNT absorb strongly. Each SWCNT will thus only absorb very strongly over a small part of the wavelength spectrum, whereas the P3HT will absorb strongly in a much broader spectrum (see Fig.3.5b).

The thickness of P3HT is varied to investigate its influence on the absorption efficiency and ultimately the photocurrent. The values of real and complex index of refraction for all the different materials are taken from spectroscopic data, available in literature [105-110]. Their value as a function of wavelength is plotted in Figure 3.5a and b respectively. Due to the absence of a thick glass substrate in the device fabrication, Equation (3.3) can be used. A plot of $\left| \frac{E}{E_0} \right|^2$ allows one to see where and to what extent interference plays a role in the device. If the value is greater than 1, optical enhancement occurs.

Figure 3.6b shows this intensity ratio at 495nm, the wavelength corresponding to the peak of the solar spectrum (AM1.5). Fig. 3.6c shows the value of $\left| \frac{E}{E_0} \right|^2$, averaged out over all wavelengths of the solar spectrum.

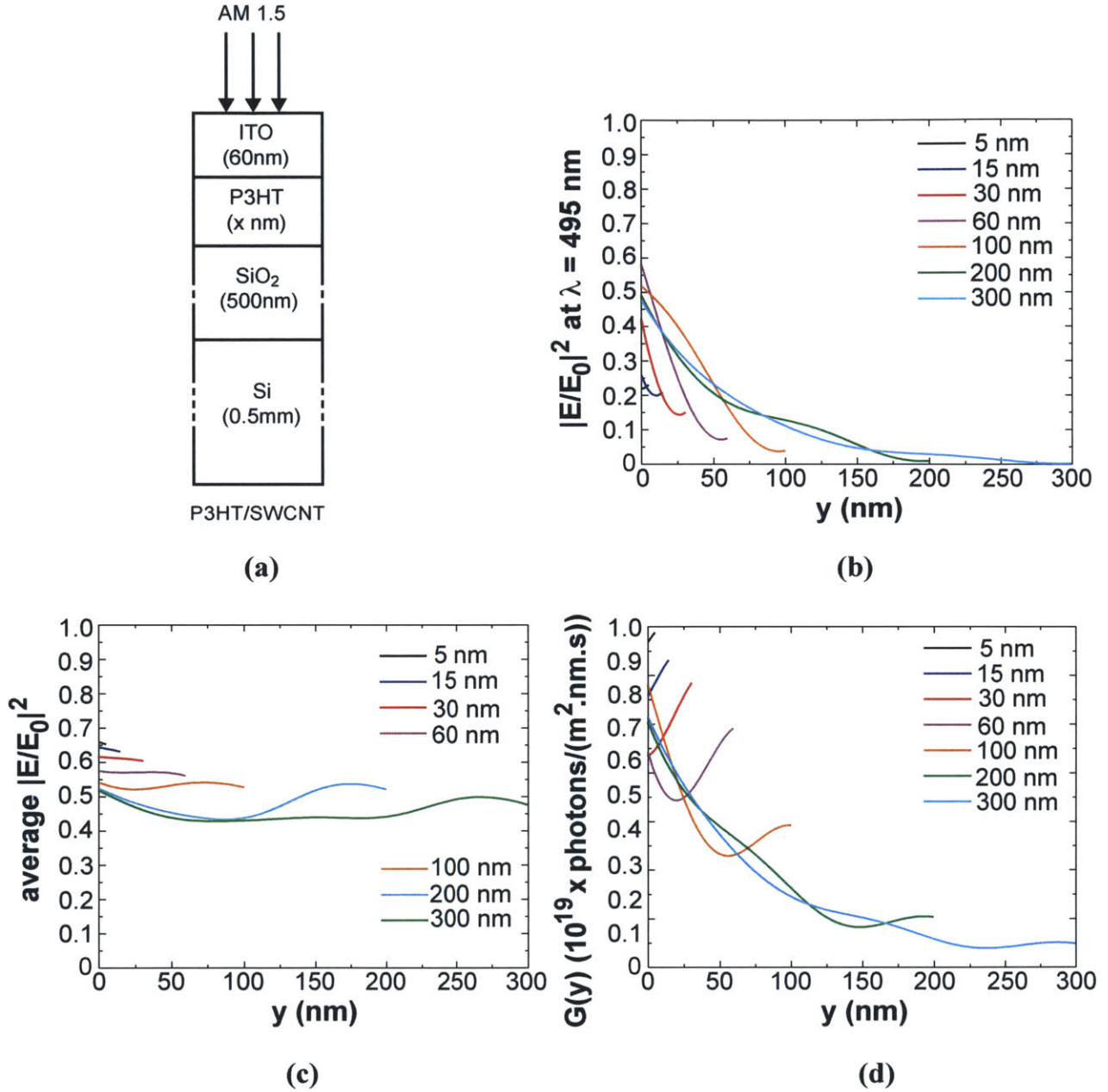


Figure 3.6. Optical modeling of the active layer in the P3HT/SWCNT device. **(a)** Geometry of the P3HT/SWCNT device. Note that the P3HT has a variable thickness, and that SWCNTs are excluded from the optical model, since they are so sparsely divided across the SiO₂ interface. **(b)** Ratio of the optical intensity in P3HT to the optical intensity of the incoming light $\left| \frac{E}{E_0} \right|^2$, at 495nm (the peak of the solar spectrum) as a function of penetration depth in the active part of the device, for different values of d_{P3HT} . **(c)** $\left| \frac{E}{E_0} \right|^2$ averaged out over all wavelengths in the solar spectrum, as a function of

penetration depth in the active part of the device and for different values of d_{P3HT} . **(d)** Generation rate of excitons $G(y)$ as a function of depth in the optically active part of the device, for different values of d_{P3HT} .

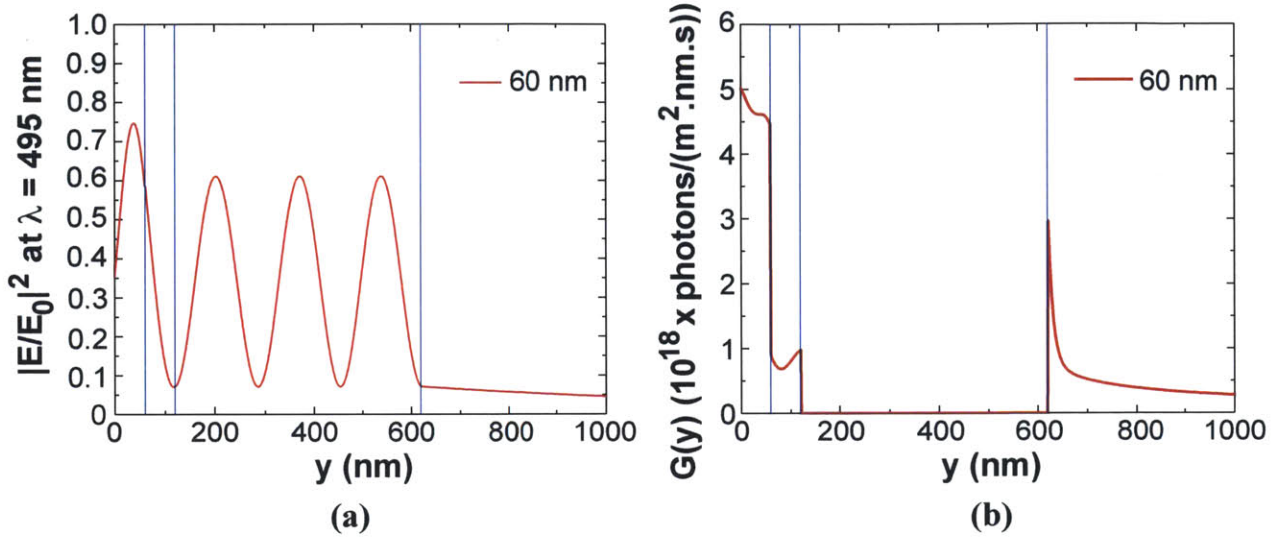


Figure 3.7. Results of the optical transfer-matrix model for the most efficient P3HT-SWCNT structure (i.e. with 60nm of P3HT). Blue lines indicate an interface in the layered device: 60nm ITO / 60nm P3HT/ 500nm SiO₂ / 1mm Si. Note that only the first 200nm of the Si is shown (the optical intensity eventually decays to zero in the mm thick Si). **(a)** Ratio of the optical intensity in the device to the optical intensity of the incoming light $\left|\frac{E}{E_0}\right|^2$, at 495 nm (the peak of the solar spectrum) as a function of penetration depth in the device. **(b)** Generation rate of excitons $G(y)$ as a function of penetration depth in the device.

Figure 3.6d shows the generation rate of excitons $G(y)$ as a function of distance penetrated by the light in the active part of the device ($0 \leq y \leq (d_{P3HT} + d_{PCBM})$), and this for different values of the total P3HT thickness. The overall trend does not deviate all too far from exponential decay, as predicted by Beer-Lambert (which neglects reflection at interfaces), especially for high values of d_{P3HT} . This is mainly due to the fact that the strongly reflecting Al is not located directly underneath the active layer (Fig. 3.1a). From $G(y)$, the exciton generation rate per lattice site (occupying a volume of 2.45 nm^3) can be

easily calculated as a function of polymer depth for devices with different P3HT thicknesses. This will serve as the input in the Kinetic Monte Carlo simulation. Note that Figures 3.6b-d only show how the optical intensity and the generation rate vary in the optically active part of the device, since it is only the excitons generated in this part of the device that can possibly contribute to the current. The trend of the optical intensity and the generation rate throughout the entire device, the interested reader is referred to Figure 3.7.

P3HT/PCBM device

The device structure used as a basis for the optical T-matrix model is shown in Figure 3.8a. Because a thick glass substrate is used in the experimental setup, Equation (3.4) must be used when calculating the exciton generation rate $G(y)$. Excitons can be generated in both the P3HT and the PCBM. Optical constants for PEDOT:PSS, PCBM, glass and Al are available in literature [107,111,112] and are plotted as a function of

wavelength in Figure 3.5. A plot of $\left| \frac{E}{E_g} \right|^2$ as a function of penetration depth of the light in

the optically active materials (P3HT and PCBM) is shown in Figure 3.8b for $\lambda=495$ nm.

There is clearly more optical enhancement than in the P3HT/SWCNT case as indicated

by the larger values of $\left| \frac{E}{E_g} \right|^2$; this is largely due to the fact that the reflecting Al cathode

is positioned directly beneath the active materials. The resulting generation rate $G(y)$ is shown in Figure 3.8c. Note that $G(y)$ shows a discontinuity at the interface between P3HT and PCBM. A comparison of the percentage of incoming photons absorbed

between the P3HT/SWCNT bilayer device and the P3HT/PCBM bilayer device shows that the absorption efficiency is higher in the latter (Fig.3.8d).

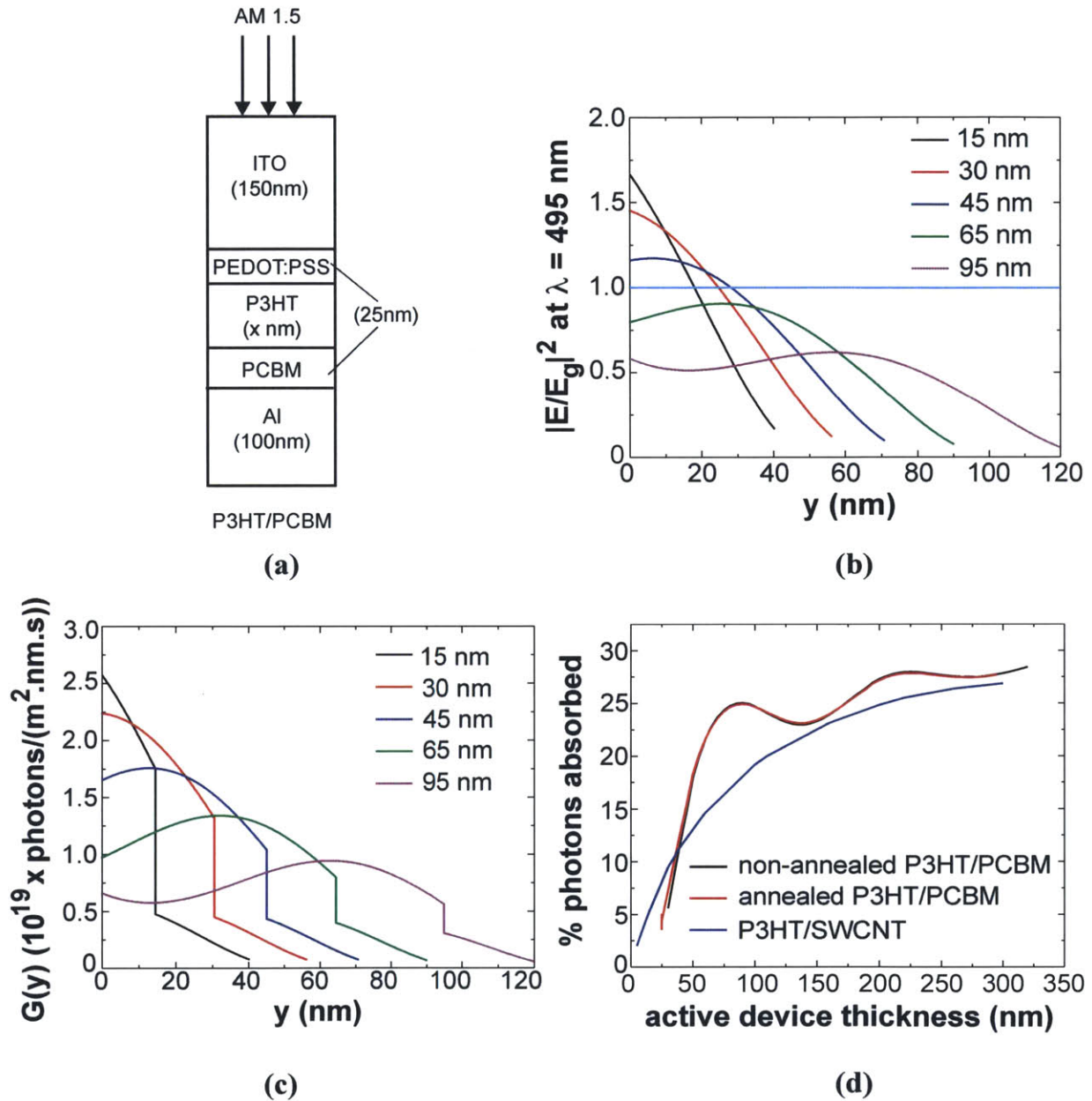


Figure 3.8. Optical modeling of the active layer in the P3HT/PCBM device. (a) Geometry of the P3HT/PCBM device. Note that P3HT has a variable thickness. (b) Ratio of the optical intensity in P3HT to the optical intensity of the light in the substrate $\left| \frac{E}{E_g} \right|^2$, at 495nm (the peak of the solar spectrum) as a function of penetration depth in optically active part of the device, for different values of d_{P3HT} . A perfect planar heterojunction is

assumed. The orange horizontal line at $\left| \frac{E}{E_g} \right|^2 = 1$ is a reference: a value greater than 1 implies optical enhancement of the incoming light. **(c)** Generation rate of excitons $G(y)$ as a function of depth in the active part of the device, for different values of d_{P3HT} . A perfect planar heterojunction is assumed. **(d)** Comparison of the percentage of incoming photons absorbed for the different devices studied in this work.

3.3.2. Kinetic Monte Carlo Simulation

P3HT/SWCNT device

The attempt-to-escape frequency of Equation (3.6) is an unknown in the model but a sensitivity analysis revealed that the model is fairly robust with respect to this parameter (it does not show significant changes in its output for different values of v_0 between 10^{-12} sec and 10^{-14} sec). Non-radiative recombination of excitons is modeled through the insertion of traps in the P3HT lattice. The **trap density** is unknown a priori. A value of 20% has been successfully used in describing the non-radiative recombination in PPV [74], but using this value leads to an underestimation of the photocurrent of the P3HT device in the current model. A value of 10%, however, leads to a good agreement between data and model. This implies one defect for every 100 monomer units [75]. Though Athanasopoulos *et al.* cite much lower percentages of trapsites in conjugated polymers, their work does not necessarily contradict our value. In several of their papers they describe the influence of trap-percentage on the exciton diffusion length [92,93]. The authors mention that the magnitude of the diffusion length L_D for molecular materials is about an order of magnitude higher than values found for conjugated polymers (typically below 10nm). The authors next go on to showing that the limited

exciton diffusion length in polymers is simply due to a high amount of trapsites and due to disorder in the polymer. For very low values of the trap-percentage the diffusion length for an example polymer is predicted to be ~45nm. A higher degree of traps significantly reduces this exciton diffusion length. The exciton diffusion length of P3HT has been measured many times in literature, with a maximum reported value of 8.5nm [113]. Other reported values [114-116] are:

- 3-8.5 nm by Goh et al. (ref. [114])
- 5.3 nm by Kroeze et al. (ref. [115])
- 4 nm by Luer et al. (ref. [116])

It makes sense that a higher degree of trap sites is responsible for these much lower values of the diffusion length. One could still argue that Athanasopoulos *et al.* find that 1.5% of traps is already enough to reduce the exciton diffusion length in PIF from 45 nm to 10nm. There is however considerable difference between the lattice structure of PIF (considered in Athanasopoulos' work) and P3HT (considered in our work) and the way it was simulated in their work vs. ours. Conjugated polymers can be regarded as arrays of chromophores that can be identified as fully conjugated segments of the polymer chain (ref. 5 of the Supporting Information and references herein). Since excitons hop from chromophore to chromophore it makes most sense to construct the lattice like we did in our manuscript: based on 3 lattice constants: $a_x = 3.9\text{nm}$ (the length of a conjugated segment of P3HT), $a_y = 1.61\text{nm}$ (the interchain distance in P3HT) and $a_z = 0.39\text{nm}$ (the π - π stacking distance in P3HT). Our value of 10% trapsites implies **one defect for every 100 monomer units** (one monomer unit is 0.39nm long in P3HT). In the work of Athanasopoulos *et al.* [92,93] the lattice in which the excitons hop around is simulated in

the KMC as a cubic lattice with a lattice constant of 1 nm. We calculate the monomer unit length of PIF as approximately 1.01 nm (based on dimensions given in [117]). Athanasopoulos *et al.* thus constructed their lattice based on the monomer unit dimension, rather than on the length of a conjugated segment of the polymer. With this in mind, the calculated value of 1.5% trapsites in their KMC model (based on their lattice structure) implies about **1.5 defects per 100 monomer units**, a value that's even slightly higher than ours.

Finally, the trap density in our model is not a very sensitive parameter: a sensitivity analysis revealed that values of 10 +/-2% give very similar results for the P3HT/SWCNT case.

As explained in the methodology section, the upper two layers of lattice sites (~top 3nm of the P3HT) are assumed to contain a much higher percentage of traps; since sputtering of ITO on top of the polymer is known to provide many additional defects (quenching sites) in the polymer near the ITO/polymer boundary [94-96]. We find that setting the trap density to 75% for the top two layers leads to a good fit with the experimental data. Since the exciton dissociation efficiency η_{diss} and the carrier collection efficiency η_{cc} are 100% in planar heterojunction devices [63], the photocurrent is determined entirely by the amount of excitons that reach the SWCNTs.

The experiments show that in contrast to the photocurrent I_{SC} , the open-circuit voltage V_{OC} (~0.46 V) and the fill factor FF (~0.28) don't show a meaningful variation with P3HT-thickness [1]. Therefore the reported maximum efficiency at a value of $d_{P3HT} = 60\text{nm}$ is entirely due to a maximum in the photocurrent.

The result of the simulation is shown in Figure 3.9 (blue curve). The model

predicts the experimentally observed photocurrent. Without taking into account bulk exciton dissociation the maximum is reached for a value close to the exciton diffusion length (Fig. 3.9, green curve).

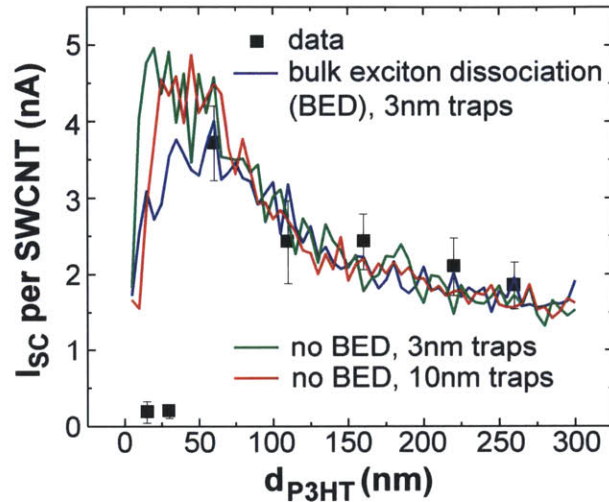


Figure 3.9. Short-circuit current per nanotube as a function of P3HT thickness. The black squares are the experimental results [1], and the blue line represents the results from the KMC model assuming bulk exciton dissociation. The green curve shows the result without making this assumption. The red curve shows the result for a higher extent of defects in the P3HT due to ITO sputtering. Error bars for the experimental data indicate one standard deviation for 4 to 15 devices. A KMC simulation was run at 60 data points, each 5nm apart. Due to the stochastic nature of KMC, each simulation (at every value of d_{P3HT}) was run 400 times to get a meaningful average.

An alternative explanation for the shifted maximum is that the extent of sputtering damage on the P3HT is more significant, and a high percentage of defects (~75%) is found in the top 10 nm of the P3HT rather than only in the top 3nm (Fig. 3.9, red curve). However, this hypothesis has recently been rejected in experimental work [1]. Either way, the fact that a maximum photocurrent and efficiency is reached at $d_{P3HT} = 60$ nm and not 8.5nm is due to the fact that there is a bulk exciton sink. More experimental work is needed to determine the exact physical nature of this sink. It should be noted that all versions of the model systematically overestimate the value of the first two experimental

data points. Most likely, the layer of P3HT is insufficiently uniform and thick (thickness on the nm-scale is hard to control when spincoating), such that it is likely that the device is shunt.

P3HT/PCBM device

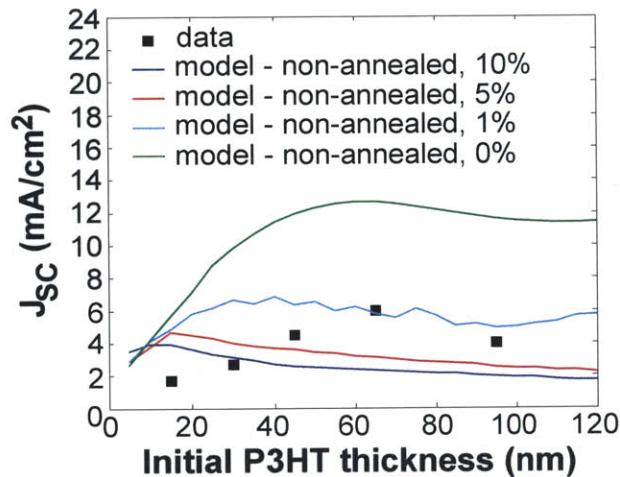
The KMC simulated total photocurrent (composed of excitons reaching the P3HT/PCBM interface that were generated in both the P3HT and the PCBM) does not show a maximum at 65nm but rather shows a monotonic decay with increasing P3HT thickness, when assuming a trap-site concentration of 10% (Fig. 3.10a, dark blue curve). Moreover the model underestimates the generated photocurrent density. Decreasing the amount of trap-sites might increase the fidelity between the model and the data. Plots for 5%, 1% and 0% trap-sites are also included in Figure 3.10a. While the predicted photocurrent density increases (due to fewer non-radiative recombination centers), the trend does not follow the data well. It is interesting to note that in the case of 0% traps for a non-annealed device the curve follows the trend of Figure 3.8d which shows the total amount of photons absorbed as a function of the active device thickness. At 0% traps, virtually every exciton that is generated reaches the donor/acceptor interface since radiative recombination is a rare event.

We argue that upon annealing of the structure (the device is annealed at 150°C for 15 minutes [43]), the small PCBM molecules are able to diffuse into P3HT-Br. It should be noted that experimentally, precautions were taken that the PCBM did not dissolve into the P3HT directly upon spincoating. This is likely to happen in spincoated bilayer devices, as most conjugated organic molecules are soluble in similar solvents, such that

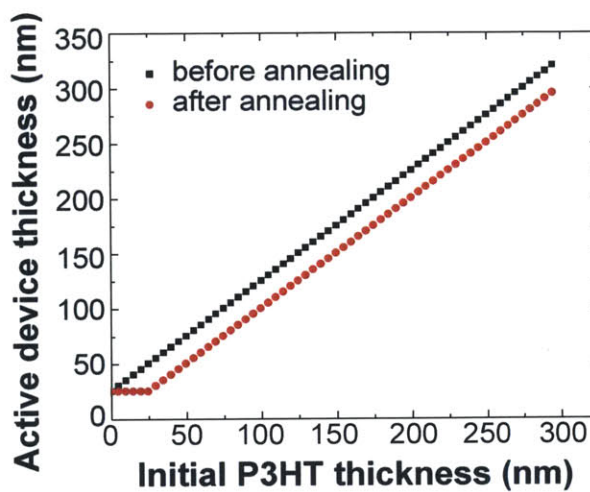
spincoating e.g. the PCBM onto the underlayer of P3HT results in re-dissolution of the bottom layer and thus substantial mixing of the PCBM and the P3HT occurs and one can no longer speak of a real PHJ. However, Kim *et al.* cross-linked their P3HT-Br layer (via UV irradiation), making sure that the initially formed bilayer consists of a sharp interface [40,43]. In our model we hypothesize that only upon annealing the mobile PCBM molecules diffuse into the P3HT. It has been shown before that upon annealing the short-circuit current increased substantially for a (90nm MEH-PPV)/(100nm C60) bilayer [118] and for a (80nm P3HT)/(22nm PCBM) bilayer device [40], and our hypothesis was recently confirmed experimentally by several groups [41,119,120].

The effect of thermal annealing on the photocurrent as a function of polymer thickness has not yet been investigated. Ferenczi *et al.* however show that upon similar annealing conditions about 35nm of the original PCBM film diffused into the P3HT and that the total device thickness decreased by 30nm [41]. Hence it is postulated that the PCBM fills up the voids in the P3HT. This introduces a non-homogeneity in the system, particularly, a mixed region emerges in the middle of the device, characterized by a 45wt% PCBM/P3HT concentration [41]. Since the device studied in this work only has 25 nm of PCBM [43], we will assume that all of it is able to diffuse into the P3HT and the total device thickness thus decreases by 25 nm. The optical constants of a 45wt% PCBM/P3HT blend are taken from literature [121] and plotted in Figure 3.5. An analysis of the optical absorption in the annealed device shows that for the same active device thickness the percentage of photons absorbed barely changes upon annealing (Fig. 3.8d). However, as mentioned above, the active device thickness does decrease upon annealing, leading to a smaller number of photons absorbed (Fig. 3.10b). It has been shown that in a

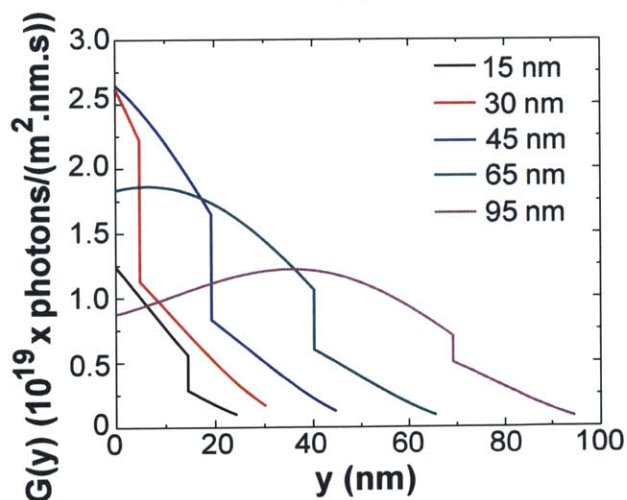
45wt% PCBM/P3HT blend all the generated excitons dissociate into free charge carriers but that about 40% of these charges never reach their respective electrode due to recombination or traps [41,122]. Taken this into account the total photocurrent for the annealed device is calculated as a function of the initial P3HT thickness (i.e. prior to annealing). The results of the optical model and the subsequent KMC simulation for the annealed P3HT/PCBM PHJ are shown in Figure 3.10c and d respectively. Note that the results of the optical model are again only shown for the optically active part of the device.



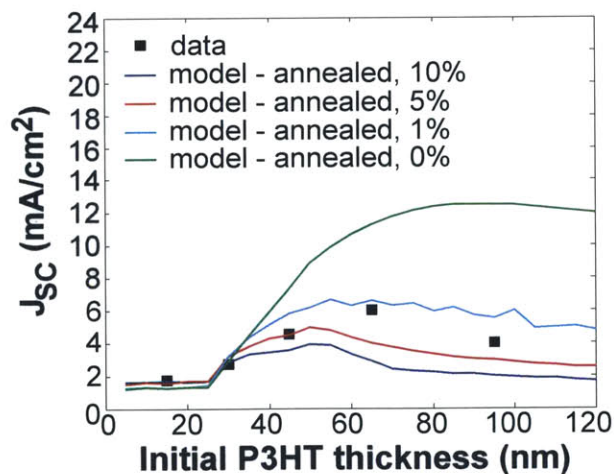
(a)



(b)



(c)



(d)

Figure 3.10. Short-circuit current density of the P3HT-Br/PCBM photovoltaic. Black dots represent experimental data [43], the solid lines represent the results of the model with 10% traps (blue), 5% traps (red), 1% traps (cyan), and 0% traps (green). **(a)** Results for the non-annealed device. **(b)** Plot of the final device thickness versus the original device thickness prior to annealing. **(c)** Results of the optical model for the annealed P3HT/PCBM bilayer solar cell. Generation rate of excitons $G(y)$ as a function of the active part of the device, for different values of d_{P3HT} . **(d)** Results for the annealed device, where PCBM molecules diffuse into the P3HT-Br matrix.

The trend predicted by the model for the annealed device with 10% trap-sites in the bulk of P3HT clearly shows how the position of maximum current is shifted to larger values of the P3HT thickness, but still underestimates the magnitude of the current density found experimentally. Model predictions for lower trap concentration (5%, 1% and 0%) are included in Figure 3.10d. At 1% the model predicts the data fairly accurately. It is possible that that due to the use of a slightly different P3HT polymer, or merely due to different processing and post-treatment conditions for the data in Figure 4 (taken from ref. [1]) compared to the data in Figure 3.10 (taken from ref. [43]), the percentage of traps in the model is different for the two sets of experimental data. However, this would imply only one defect per 1000 monomer units, a value much lower than those typically reported in literature (as discussed earlier). This leads us to assume the discrepancy is largely due to an underestimation of the absorption coefficient of P3HT-Br. Since experimental data were not available, we assumed the same absorption characteristics for the modified P3HT-Br5 as for regular P3HT. The Br-unit attached to the end of the hexyl-chain of P3HT is light sensitive and thus it is possible that the P3HT-Br polymer is able to absorb more light than the regular P3HT. An increased light-absorption of the modified polymer could also explain the underestimation of the generated short-circuit current density. Future experiments will reveal this.

Finally it should be noted that expanding the KMC simulation to include charge transport as well would not improve the results of the model. First of all charge transport in PHJs is commonly assumed to be 100% efficient ($\eta_{cc}=100\%$) as explained in the methodology section. Secondly, even if $\eta_{cc}<100\%$, this would only result in a stronger underestimation of the experimentally observed current. Abandoning the assumption that all of the excitons generated in the PCBM can contribute to the current would also decrease our simulated photocurrent.

It should be clear that taking into account the interdiffusion of PCBM into P3HT predicts the correct trend and that annealing can be beneficial for the device characteristics, depending on the thicknesses of the active areas. Finally it should be noted that experiments showed that annealing did not alter the device characteristics of the P3HT/SWCNT device, since the nanotubes are long one-dimensional structures that are grown attached to the SiO₂ substrate and hence cannot diffuse into the P3HT, even upon annealing.

3.4. Conclusions

Due to their simple geometry and design, planar heterojunction (PHJ) solar cells have advantages both as potential photovoltaics with more efficient charge extraction than their bulk heterojunction (BHJ) counterparts, and as idealized interfaces to study basic device operation. The main reason for creating BHJs was the limited exciton diffusion length in the active materials of the PHJ: if an exciton is generated at a distance greater than its diffusion length from the hetero-interface of the PHJ, it would be very unlikely to be able to contribute to the photocurrent. Based on this argument one expects

a maximum in the photocurrent of PHJs for a thickness of the active layer equal to the exciton diffusion length ($\sim 10\text{nm}$). However in two recently developed PHJs that have appeared in the literature, a maximum photocurrent is observed for 60-65nm of poly(3-hexylthiophene) (P3HT).

Optical modeling reveals that interference plays a much bigger role in the P3HT/PCBM device since the reflecting electrode is positioned underneath the active layer. A Kinetic Monte Carlo simulation tracking the path of the generated excitons reveals that for the P3HT/SWCNT device the maximum occurs mainly due to a bulk exciton sink, presumably the dissociation of excitons in the bulk of P3HT for small values of d_{P3HT} . In the P3HT/PCBM device the maximum arises mainly due to the diffusion of PCBM into P3HT upon annealing, which can be beneficial for the output current, depending on the thickness of the active layer. It is clear that planar heterojunctions are not just governed by the exciton diffusion length of the donor material, as was previously thought, but that optical interference effects, bulk dissociation, defects in the polymer (e.g. due to sputtering damage), and diffusion of small molecules into the polymer upon annealing all play a role in the eventual photocurrent.

Based upon the results of this model it will be possible to more intelligently design nanostructured photovoltaics and optimize them towards higher efficiencies.

3.5. Ongoing work

Ongoing and future work will focus on increasing the efficiency of P3HT/SWCNT based devices. Several avenues can be pursued.

Previous work showed that device efficiency increases with the number of SWCNTs [1], implying an increase of SWCNT density while still ensuring every SWCNT has a clear path to the electrode (as opposed to the SWCNTs in the earlier described BHJs [28-30]) is an obvious next step. We made the cross-bar structure shown in Figure 3.11.

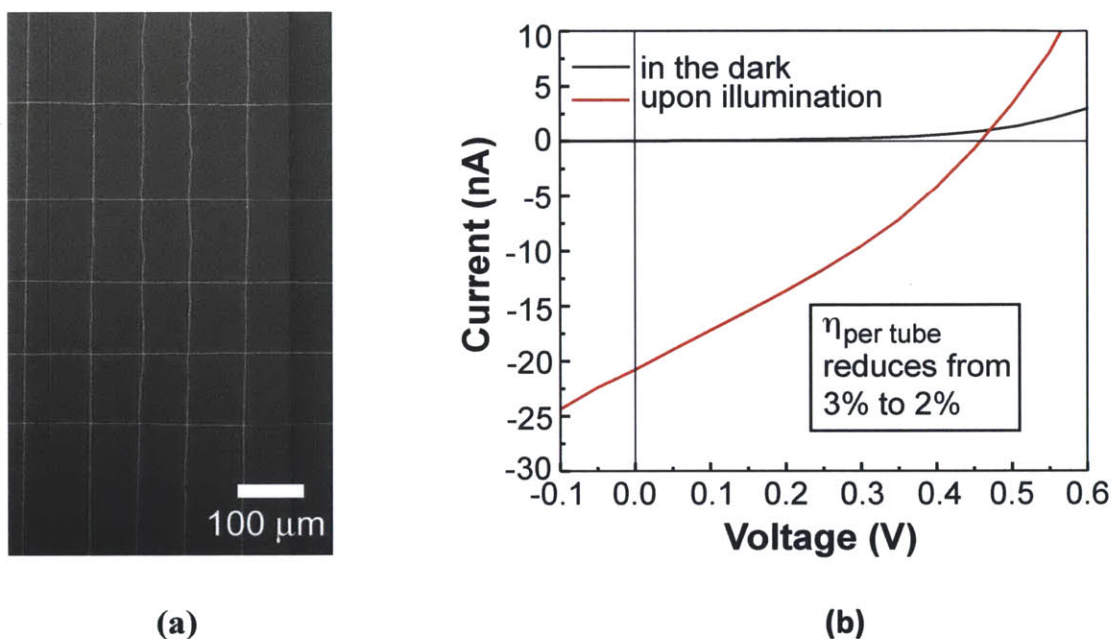


Figure 3.11. Increasing SWCNT density in the P3HT/SWCNT PV. **(a)** SEM image of the cross-bar SWCNTs: after one set of SWCNTs is grown, the wafer is rotated by 90 degrees and a second set of SWCNTs is grown via CVD. **(b)** Total photocurrent increases, but efficiency per SWCNT decreases in the cross-bar structure.

The cross-bar structure was achieved by growing aligned CVD-SWCNTs in one direction, flip the wafer by 90 degrees, and grow another set of aligned CVD-SWCNTs perpendicular to the first set of SWCNTs. The total short circuit current increased compared to our earlier devices but the per-tube efficiency decreased, confirming that SWCNT-SWCNT junctions are detrimental for the solar cell's performance.

Based on our previous work [1,2] it is clear that mostly the excitons generated within the diffusion distance away from the P3HT/SWCNT junction are able to contribute to the photocurrent. This means there is a lot of excess P3HT in our devices. The Gleason group developed an oxidative CVD (oCVD) process that allows the conformal deposition of different polymers [123]. By growing the SWCNTs on top of a trenched wafer, converting them to n-type SWCNTs by coating them with PEI, and then conformally coating them with a p-type polymer we use very little material to create an equally efficient photovoltaic device with less material.

A problem with our previous P3HT/ SWCNT devices was a fairly low fill factor (FF) [1]. In order to determine whether a series resistance is responsible, we can compare our currents measured with a solar simulator to those obtained with a technique called SunsVoc, which basically measures the open circuit voltage V_{OC} of the device under different light intensities. This V_{OC} is related to current via the ideal diode equation. Since no current flows through the device (open circuit conditions), the effect of series resistance is less pronounced. A quick estimate for the series resistance is the slope of the IV -curve at the open circuit voltage V_{OC} . Since the total current in our devices can also be improved, parallel resistance may be an issue as well; it can be estimated as the slope of the IV -curve at the short-circuit current I_{SC} . The series resistance (which should be minimized) and the parallel resistance (which should be maximized) of the devices reported on in reference [1] are $33\text{M}\Omega$ and $36\text{M}\Omega$ respectively. Clearly the main issue with the devices is the large series resistance. Contact resistances at each interface can contribute significantly. Choosing to abandon sputtering to deposit the ITO in favor of electron-beam deposition should cause less damage to the P3HT at the ITO/P3HT

interface. The sputtered ITO itself also has a limited conductivity ($\sim 10^4 \text{S/m}$, [124124]). Replacing it by a more conductive, flexible, transparent electrode (potentially graphene) can significantly help reduce the series resistance. Finally the resistance of the P3HT can also add to the series resistance; eliminating the excess P3HT as proposed above will help in this regard.

3.6. References

- 1 Ham, M. H., Paulus, G. L. C., Lee, C. Y., Song, C., Kalantar-zadeh, K., Choi, W., Han, J. H. & Strano, M. S. Evidence for High-Efficiency Exciton Dissociation at Polymer/Single-Walled Carbon Nanotube Interfaces in Planar Nano-heterojunction Photovoltaics. *Acs Nano* **4**, 6251-6259 (2010).
- 2 Paulus, G. L. C. H., M.-H. & Strano, M.S. Anomalous thickness-dependence of photocurrent explained for state-of-the-art planar nano-heterojunction organic solar cells. *Nanotechnology* **23**, 095402-1:14 (2012).
- 3 Dennler, G., Scharber, M. C. & Brabec, C. J. Polymer-Fullerene Bulk-Heterojunction Solar Cells. *Advanced Materials* **21**, 1323-1338 (2009).
- 4 Yao, Y., Hou, J., Xu, Z., Li, G. & Yang, Y. Effects of solvent mixtures on the nanoscale phase separation in polymer solar cells. *Advanced Functional Materials* **18**, 1783-1789 (2008).
- 5 Hwang, I. W., Cho, S., Kim, J. Y., Lee, K., Coates, N. E., Moses, D. & Heeger, A. J. Carrier generation and transport in bulk heterojunction films processed with 1,8-octanedithiol as a processing additive. *Journal of Applied Physics* **104**, 033706-1:9 (2008).
- 6 Park, S. H., Roy, A., Beaupré, S., Cho, S., Coates, N., Moon, J. S., Moses, D., Leclerc, M., Lee, K. & Heeger, A. J. Bulk heterojunction solar cells with internal quantum efficiency approaching 100&percent. *Nature Photonics* **3**, 297-302 (2009).
- 7 Liang, Y. & Yu, L. A New Class of Semiconducting Polymers for Bulk Heterojunction Solar Cells with Exceptionally High Performance. *Accounts of Chemical Research* **43**, 1227-1236 (2010).
- 8 Piliago, C., Holcombe, T. W., Douglas, J. D., Woo, C. H., Beaujuge, P. M. & Frechet, J. M. J. Synthetic control of structural order in N-alkylthieno [3, 4-c] pyrrole-4, 6-dione-based polymers for efficient solar cells. *Journal of the American Chemical Society* **132**, 7595-7597 (2010).
- 9 Wang, E., Hou, L., Wang, Z., Hellström, S., Zhang, F., Inganäs, O. & Andersson, M. R. An Easily Synthesized Blue Polymer for High-Performance Polymer Solar Cells. *Advanced Materials* **22**, 5240-5244 (2010).
- 10 Zhou, H., Yang, L., Price, S. C., Knight, K. J. & You, W. Enhanced Photovoltaic Performance of Low-Bandgap Polymers with Deep LUMO Levels. *Angewandte Chemie International Edition* **49**, 7992-7995 (2010).
- 11 Chen, Y. C., Yu, C. Y., Fan, Y. L., Hung, L. I., Chen, C. P. & Ting, C. Low-bandgap conjugated polymer for high efficient photovoltaic applications. *Chemical Communications* **46**, 6503-6505 (2010).
- 12 Chen, H. Y., Hou, J., Zhang, S., Liang, Y., Yang, G., Yang, Y., Yu, L., Wu, Y. & Li, G. Polymer solar cells with enhanced open-circuit voltage and efficiency. *Nature Photonics* **3**, 649-653 (2009).
- 13 Price, S. C., Stuart, A. C., Yang, L., Zhou, H. & You, W. Fluorine Substituted Conjugated Polymer of Medium Band Gap Yields 7% Efficiency in Polymer-Fullerene Solar Cells. *Journal of the American Chemical Society* **133**, 4625-4631 (2011).

- 14 Liang, Y., Xu, Z., Xia, J., Tsai, S. T., Wu, Y., Li, G., Ray, C. & Yu, L. For the bright future—bulk heterojunction polymer solar cells with power conversion efficiency of 7.4%. *Advanced Materials* **22**, E135-E138 (2010).
- 15 Zhao, G., He, Y. & Li, Y. 6.5% Efficiency of Polymer Solar Cells Based on poly(3-hexylthiophene) and Indene-C60 Bisadduct by Device Optimization. *Advanced Materials* **22**, 4355-4358 (2010).
- 16 Dennler, G., Scharber, M. C., Ameri, T., Denk, P., Forberich, K., Waldauf, C. & Brabec, C. J. Design Rules for Donors in Bulk-Heterojunction Tandem Solar Cells - Towards 15 % Energy-Conversion Efficiency. *Advanced Materials* **20**, 579-583 (2008).
- 17 Frenkel, J. On the Transformation of light into Heat in Solids. I. *Physical Review* **37**, 17-44 (1931).
- 18 Arkhipov, V. I. & Bassler, H. Exciton dissociation and charge photogeneration in pristine and doped conjugated polymers. *Physica Status Solidi a-Applied Research* **201**, 1152-1187 (2004).
- 19 Tang, C. W. 2-layer organic photovoltaics cell. *Applied Physics Letters* **48**, 183-185 (1986).
- 20 Guo, J. M., Ohkita, H., Benten, H. & Ito, S. Near-IR Femtosecond Transient Absorption Spectroscopy of Ultrafast Polaron and Triplet Exciton Formation in Polythiophene Films with Different Regioregularities. *Journal of the American Chemical Society* **131**, 16869-16880 (2009).
- 21 Yang, K., Wang, Y., Jain, A., Samulson, L. & Kumar, J. Determination of electron and hole mobility of regioregular poly(3-hexylthiophene) by the time of flight method. *Journal of Macromolecular Science Part a-Pure and Applied Chemistry* **44**, 1261-1264 (2007).
- 22 Chen, L. L., Li, W. L., Wei, H. Z., Chu, B. & Li, B. Organic ultraviolet photovoltaic diodes based on copper phthalocyanine as an electron acceptor. *Solar Energy Materials and Solar Cells* **90**, 1788-1796 (2006).
- 23 van Hal, P. A., Christiaans, M. P. T., Wienk, M. M., Kroon, J. M. & Janssen, R. A. J. Photoinduced electron transfer from conjugated polymers to TiO₂. *Journal of Physical Chemistry B* **103**, 4352-4359 (1999).
- 24 Ravirajan, P., Peiro, A. M., Nazeeruddin, M. K., Graetzel, M., Bradley, D. D. C., Durrant, J. R. & Nelson, J. Hybrid polymer/zinc oxide photovoltaic devices with vertically oriented ZnO nanorods and an amphiphilic molecular interface layer. *Journal of Physical Chemistry B* **110**, 7635-7639 (2006).
- 25 Sun, B. Q., Marx, E. & Greenham, N. C. Photovoltaic devices using blends of branched CdSe nanoparticles and conjugated polymers. *Nano Letters* **3**, 961-963 (2003).
- 26 Sariciftci, N. S., Smilowitz, L., Heeger, A. J. & Wudl, F. Photoinduced electron-transfer from a conducting polymer to buckminsterfullerene. *Science* **258**, 1474-1476 (1992).
- 27 Ago, H., Petritsch, K., Shaffer, M. S. P., Windle, A. H. & Friend, R. H. Composites of carbon nanotubes and conjugated polymers for photovoltaic devices. *Advanced Materials* **11**, 1281-1285 (1999).
- 28 Kymakis, E. & Amaratunga, G. A. J. Single-wall carbon nanotube/conjugated polymer photovoltaic devices. *Applied Physics Letters* **80**, 112-114 (2002).
- 29 Kymakis, E., Koudoumas, E., Franghiadakis, I. & Amaratunga, G. A. J. Post-fabrication annealing effects in polymer-nanotube photovoltaic cells. *Journal of Physics D-Applied Physics* **39**, 1058-1062 (2006).

- 30 Geng, J. & Zeng, T. Influence of single-walled carbon nanotubes induced crystallinity enhancement and morphology change on polymer photovoltaic devices. *Journal of the American Chemical Society* **128**, 16827-16833 (2006).
- 31 Dürkop, T., Getty, S., Cobas, E. & Fuhrer, M. Extraordinary mobility in semiconducting carbon nanotubes. *Nano Letters* **4**, 35-39 (2004).
- 32 Gunes, S., Neugebauer, H. & Sariciftci, N. S. Conjugated polymer-based organic solar cells. *Chemical Reviews* **107**, 1324-1338 (2007).
- 33 Reyes-Reyes, M., Kim, K. & Carroll, D. L. High-efficiency photovoltaic devices based on annealed poly(3-hexylthiophene) and 1-(3-methoxycarbonyl)-propyl-1-phenyl-(6,6)C-61 blends. *Applied Physics Letters* **87**, 083506-1:3 (2005).
- 34 Kim, J. Y., Lee, K., Coates, N. E., Moses, D., Nguyen, T.-Q., Dante, M. & Heeger, A. J. Efficient tandem polymer solar cells fabricated by all-solution processing. *Science* **317**, 222-225 (2007).
- 35 Li, G., Shrotriya, V., Huang, J. S., Yao, Y., Moriarty, T., Emery, K. & Yang, Y. High-efficiency solution processable polymer photovoltaic cells by self-organization of polymer blends. *Nature Materials* **4**, 864-868 (2005).
- 36 Shim, M., Javey, A., Kam, N. W. S. & Dai, H. J. Polymer functionalization for air-stable n-type carbon nanotube field-effect transistors. *Journal of the American Chemical Society* **123**, 11512-11513 (2001).
- 37 Li, Z., Saini, V., Dervishi, E., Kunets, V. P., Zhang, J., Xu, Y., Biris, A. R., Salamo, G. J. & Biris, A. S. Polymer functionalized n-type single wall carbon nanotube photovoltaic devices. *Applied Physics Letters* **96**, 033110-1:3 (2010).
- 38 Hertel, T., Fasel, R. & Moos, G. Charge-carrier dynamics in single-wall carbon nanotube bundles: a time-domain study. *Applied Physics A - Materials Science & Processing* **75**, 449-465 (2002).
- 39 Lauret, J. S., Voisin, C., Cassabois, G., Delalande, C., Roussignol, P., Jost, O. & Capes, L. Ultrafast carrier dynamics in single-wall carbon nanotubes. *Physical Review Letters* **90**, 057404-1:4 (2003).
- 40 Ayzner, A. L., Tassone, C. J., Tolbert, S. H. & Schwartz, B. J. Reappraising the Need for Bulk Heterojunctions in Polymer-Fullerene Photovoltaics: The Role of Carrier Transport in All-Solution-Processed P3HT/PCBM Bilayer Solar Cells. *Journal of Physical Chemistry C* **113**, 20050-20060 (2009).
- 41 Ferenczi, T. A. M., Nelson, J., Belton, C., Ballantyne, A. M., Campoy-Quiles, M., Braun, F. M. & Bradley, D. D. C. Planar heterojunction organic photovoltaic diodes via a novel stamp transfer process. *Journal of Physics-Condensed Matter* **20**, 475203-1:8 (2008).
- 42 Xue, J. G., Rand, B. P., Uchida, S. & Forrest, S. R. A hybrid planar-mixed molecular heterojunction photovoltaic cell. *Advanced Materials* **17**, 66-71 (2005).
- 43 Kim, B. J., Miyamoto, Y., Ma, B. W. & Frechet, J. M. J. Photocrosslinkable Polythiophenes for Efficient, Thermally Stable, Organic Photovoltaics. *Advanced Functional Materials* **19**, 2273-2281 (2009).
- 44 Li, G., Shrotriya, V., Yao, Y. & Yang, Y. Investigation of annealing effects and film thickness dependence of polymer solar cells based on poly (3-hexylthiophene). *Journal of Applied Physics* **98**, 043704-1:5 (2005).
- 45 Moulé, A. J., Bonekamp, J. B. & Meerholz, K. The effect of active layer thickness and composition on the performance of bulk-heterojunction solar cells. *Journal of Applied Physics* **100**, 094503-1:7 (2006).

- 46 Sievers, D. W., Shrotriya, V. & Yang, Y. Modeling optical effects and thickness dependent current in polymer bulk-heterojunction solar cells. *Journal of Applied Physics* **100**, 114509-1:7 (2006).
- 47 Theander, M., Yartsev, A., Zigmantas, D., Sundström, V., Mammo, W., Andersson, M. & Inganäs, O. Photoluminescence quenching at a polythiophene/C₆₀ heterojunction. *Physical Review B* **61**, 12957-12963 (2000).
- 48 Haugeneder, A., Neges, M., Kallinger, C., Spirkl, W., Lemmer, U., Feldmann, J., Scherf, U., Harth, E., Gügel, A. & Müllen, K. Exciton diffusion and dissociation in conjugated polymer/fullerene blends and heterostructures. *Physical Review B* **59**, 15346-15351 (1999).
- 49 Halls, J., Pichler, K., Friend, R., Moratti, S. & Holmes, A. Exciton diffusion and dissociation in a poly (p phenylenevinylene)/C heterojunction photovoltaic cell. *Applied Physics Letters* **68**, 3120-1:3 (1996).
- 50 Stübinger, T. & Brütting, W. Exciton diffusion and optical interference in organic donor-acceptor photovoltaic cells. *Journal of Applied Physics* **90**, 3632-3641 (2001).
- 51 Shaw, P. E., Ruseckas, A. & Samuel, I. D. W. Exciton Diffusion Measurements in Poly(3-hexylthiophene). *Advanced Materials* **20**, 3516-3520 (2008).
- 52 Nunzi, J. M. Organic photovoltaic materials and devices. *Comptes Rendus Physique* **3**, 523-542 (2002).
- 53 Günes, S., Neugebauer, H. & Sariciftci, N. S. Conjugated polymer-based organic solar cells. *Chemical Reviews* **107**, 1324-1338 (2007).
- 54 Lukkien, J. J., Segers, J. P. L., Hilbers, P. A. J., Gelten, R. J. & Jansen, A. P. J. Efficient Monte Carlo methods for the simulation of catalytic surface reactions. *Physical Review E* **58**, 2598-2610 (1998).
- 55 Buxton, G. A. & Clarke, N. Predicting structure and property relations in polymeric photovoltaic devices. *Physical Review B* **74**, 085207-1:5 (2006).
- 56 Martin, C., Burlakov, V., Assender, H. & Barkhouse, D. A numerical model for explaining the role of the interface morphology in composite solar cells. *Journal of Applied Physics* **102**, 104506-1:9 (2007).
- 57 Williams, J. & Walker, A. B. Two-dimensional simulations of bulk heterojunction solar cell characteristics. *Nanotechnology* **19**, 424011-1:6 (2008).
- 58 Monestier, F., Simon, J.-J., Torchio, P., Escoubas, L., Ratier, B., Hojeij, W., Lucas, B., Moliton, A., Cathelinaud, M., Defranoux, C. & Flory, F. Optical modeling of organic solar cells based on CuPc and C60. *Appl. Opt.* **47**, C251-C256 (2008).
- 59 Koster, L., Smits, E., Mihailetschi, V. & Blom, P. W. M. Device model for the operation of polymer/fullerene bulk heterojunction solar cells. *Physical Review B* **72**, 085205-1:9 (2005).
- 60 Lacic, S. & Inganäs, O. Modeling electrical transport in blend heterojunction organic solar cells. *Journal of Applied Physics* **97**, 124901-1:7 (2005).
- 61 Watkins, P. K., Walker, A. B. & Verschoor, G. L. B. Dynamical Monte Carlo modelling of organic solar cells: The dependence of internal quantum efficiency on morphology. *Nano Letters* **5**, 1814-1818 (2005).
- 62 Marsh, R., Groves, C. & Greenham, N. A microscopic model for the behavior of nanostructured organic photovoltaic devices. *Journal of Applied Physics* **101**, 083509-1:7 (2007).
- 63 Yang, F. & Forrest, S. R. Photocurrent generation in nanostructured organic solar cells. *Acs Nano* **2**, 1022-1032 (2008).

- 64 Meng, L., Shang, Y., Li, Q., Li, Y., Zhan, X., Shuai, Z., Kimber, R. G. E. & Walker, A. B. Dynamic Monte Carlo Simulation for Highly Efficient Polymer Blend Photovoltaics. *The Journal of Physical Chemistry B* **114**, 36-41 (2009).
- 65 Kimber, R. G. E., Walker, A. B., Schröder-Turk, G. E. & Cleaver, D. J. Bicontinuous minimal surface nanostructures for polymer blend solar cells. *Phys. Chem. Chem. Phys.* **12**, 844-851 (2009).
- 66 Nelson, J., Kwiatkowski, J. J., Kirkpatrick, J. & Frost, J. M. Modeling Charge Transport in Organic Photovoltaic Materials. *Accounts of Chemical Research* **42**, 1768-1778 (2009).
- 67 Casalegno, M., Raos, G. & Po, R. Methodological assessment of kinetic Monte Carlo simulations of organic photovoltaic devices: The treatment of electrostatic interactions. *The Journal of chemical physics* **132**, 094705-1:14 (2010).
- 68 Groves, C., Kimber, R. G. E. & Walker, A. B. Simulation of loss mechanisms in organic solar cells: A description of the mesoscopic Monte Carlo technique and an evaluation of the first reaction method. *The Journal of chemical physics* **133**, 144110-1:7 (2010).
- 69 Meng, L., Wang, D., Li, Q., Yi, Y., Brédas, J. L. & Shuai, Z. An improved dynamic Monte Carlo model coupled with Poisson equation to simulate the performance of organic photovoltaic devices. *The Journal of chemical physics* **134**, 124102-1:7 (2011).
- 70 Choulis, S. A., Kim, Y., Nelson, J., Bradley, D. D. C., Giles, M., Shkunov, M. & McCulloch, I. High ambipolar and balanced carrier mobility in regioregular poly(3-hexylthiophene). *Applied Physics Letters* **85**, 3890-3892 (2004).
- 71 Saito, R., Dresselhaus, G., Dresselhaus, M. S. & Knovel. *Physical properties of carbon nanotubes*. Vol. 4 (1998).
- 72 von Hauff, E., Dyakonov, V. & Parisi, J. Study of field effect mobility in PCBM films and P3HT: PCBM blends. *Solar Energy Materials and Solar Cells* **87**, 149-156 (2005).
- 73 Erb, T., Zhokhavets, U., Gobsch, G., Raleva, S., Stühn, B., Schilinsky, P., Waldauf, C. & Brabec, C. J. Correlation between structural and optical properties of composite polymer/fullerene films for organic solar cells. *Advanced Functional Materials* **15**, 1193-1196 (2005).
- 74 Scheidler, M., Lemmer, U., Kersting, R., Karg, S., Riess, W., Cleve, B., Mahrt, R., Kurz, H., Bäessler, H. & Göbel, E. Monte Carlo study of picosecond exciton relaxation and dissociation in poly (phenylenevinylene). *Physical Review B* **54**, 5536-5544 (1996).
- 75 Holdcroft, S. A photochemical study of poly (3-hexylthiophene). *Macromolecules* **24**, 4834-4838 (1991).
- 76 Moulé, A. & Meerholz, K. Intensity-dependent photocurrent generation at the anode in bulk-heterojunction solar cells. *Applied Physics B: Lasers and Optics* **92**, 209-218 (2008).
- 77 Hoppe, H. & Sariciftci, N. S. Morphology of polymer/fullerene bulk heterojunction solar cells. *Journal of Materials Chemistry* **16**, 45-61 (2006).
- 78 Peumans, P., Yakimov, A. & Forrest, S. R. Small molecular weight organic thin-film photodetectors and solar cells. *Journal of Applied Physics* **93**, 3693-3723 (2003).
- 79 Bakulin, A. A., Hummelen, J. C., Pshenichnikov, M. S. & van Loosdrecht, P. H. M. Ultrafast Hole-Transfer Dynamics in Polymer/PCBM Bulk Heterojunctions. *Advanced Functional Materials* **20**, 1653-1660 (2010).
- 80 Gerrard, A. & Burch, J. M. *Introduction to matrix methods in optics*. (1994).

- 81 Heavens, O. S. *Optical properties of thin solid films*. (1991).
- 82 Pettersson, L. A. A., Roman, L. S. & Inganas, O. Modeling photocurrent action spectra of photovoltaic devices based on organic thin films. *Journal of Applied Physics* **86**, 487-496 (1999).
- 83 Moule, A. J. & Meerholz, K. Minimizing optical losses in bulk heterojunction polymer solar cells. *Applied Physics B-Lasers and Optics* **86**, 721-727 (2007).
- 84 Hoppe, H., Arnold, N., Saricifci, N. & Meissner, D. Modeling the optical absorption within conjugated polymer/fullerene-based bulk-heterojunction organic solar cells. *Solar Energy Materials and Solar Cells* **80**, 105-113 (2003).
- 85 Nelson, J. Diffusion-limited recombination in polymer-fullerene blends and its influence on photocurrent collection. *Physical Review B* **67**, 155209-1:10 (2003).
- 86 Förster, T. Zwischenmolekulare energiewanderung und fluoreszenz. *Annalen Der Physik* **2**, 55-75 (1948).
- 87 Magnani, L., Rumbles, G., Samuel, I. D. W., Murray, K., Moratti, S. C., Holmes, A. B. & Friend, R. H. Photoluminescence studies of chain interactions in electroluminescent polymers. *Synthetic Metals* **84**, 899-900 (1997).
- 88 Shrotriya, V., Ouyang, J., Tseng, R. J., Li, G. & Yang, Y. Absorption spectra modification in poly(3-hexylthiophene): methanofullerene blend thin films. *Chemical Physics Letters* **411**, 138-143 (2005).
- 89 Miller, A. & Abrahams, E. Impurity conduction at low concentrations. *Physical Review* **120**, 745-755 (1960).
- 90 Fishchuk, I., Kadashchuk, A. & Bäessler, H. Theory of hopping charge carrier transport at large carrier concentrations in disordered organic solids: Polarons versus bare charge carriers. *physica status solidi (C)* **5**, 746-749 (2008).
- 91 Barford, W. & Trembath, D. Exciton localization in polymers with static disorder. *Physical Review B* **80**, 165418-1:12 (2009).
- 92 Athanasopoulos, S., Hennebicq, E., Beljonne, D. & Walker, A. B. Trap limited exciton transport in conjugated polymers. *The Journal of Physical Chemistry C* **112**, 11532-11538 (2008).
- 93 Athanasopoulos, S., Emelianova, E. V., Walker, A. B. & Beljonne, D. Modelling exciton diffusion in disordered conjugated polymers. *Proceedings of SPIE* **7722**, 772214-1:8 (2010).
- 94 Ahlswede, E., Hanisch, J. & Powalla, M. Influence of cathode sputter deposition on organic solar cells. *Applied Physics Letters* **90**, 063513-1:3 (2007).
- 95 Gu, G., Bulovic, V., Burrows, P. E., Forrest, S. R. & Thompson, M. E. Transparent organic light emitting devices. *Applied Physics Letters* **68**, 2606-2608 (1996).
- 96 Isomura, N., Satoh, T., Suzuki, M., Ohwaki, T. & Taga, Y. Photoemission spectroscopy of the interface between indium-tin-oxide and copper phthalocyanine for transparent organic light-emitting devices. *Japanese Journal of Applied Physics Part 2-Letters* **40**, L1038-L1039 (2001).
- 97 Thompson, B. C. & Frechet, J. M. J. Organic photovoltaics - Polymer-fullerene composite solar cells. *Angewandte Chemie-International Edition* **47**, 58-77 (2008).
- 98 Sheng, C. X., Tong, M., Singh, S. & Vardeny, Z. V. Experimental determination of the charge/neutral branching ratio η in the photoexcitation of pi-conjugated polymers by broadband ultrafast spectroscopy. *Physical Review B* **75**, 1-7 (2007).
- 99 Cook, S., Furube, A. & Katoh, R. Analysis of the excited states of regioregular polythiophene P3HT. *Energy & Environmental Science* **1**, 294-299 (2008).
- 100 Piris, J., Dykstra, T. E., Bakulin, A. A., van Loosdrecht, P. H. M., Knulst, W., Trinh, M. T., Schins, J. M. & Siebbeles, L. D. A. Photogeneration and Ultrafast Dynamics

- of Excitons and Charges in P3HT/PCBM Blends. *Journal of Physical Chemistry C* **113**, 14500-14506 (2009).
- 101 Onsager, L. Initial recombination of ions. *Physical Review* **54**, 554-557 (1938).
- 102 Braun, C. L. Electric-field assisted dissociation of charge-transfer states as a mechanism of photocarrier production. *Journal of Chemical Physics* **80**, 4157-4161 (1984).
- 103 van Bavel, S., Sourty, E., de With, G., Frolic, K. & Loos, J. Relation between Photoactive Layer Thickness, 3D Morphology, and Device Performance in P3HT/PCBM Bulk-Heterojunction Solar Cells. *Macromolecules* **42**, 7396-7403 (2009).
- 104 Itkis, M. E., Borondics, F., Yu, A. & Haddon, R. C. Bolometric Infrared Photoresponse of Suspended Single-Walled Carbon Nanotube Films. *Science* **312**, 413-416 (2006).
- 105 Kim, Y., Cook, S., Tuladhar, S. M., Choulis, S. A., Nelson, J., Durrant, J. R., Bradley, D. D. C., Giles, M., McCulloch, I., Ha, C. S. & Ree, M. A strong regioregularity effect in self-organizing conjugated polymer films and high-efficiency polythiophene: fullerene solar cells. *Nature Materials* **5**, 197-203 (2006).
- 106 Philipp, H. & Taft, E. Optical constants of silicon in the region 1 to 10 eV. *Physical Review* **120**, 37-38 (1960).
- 107 Palik, E. D. & Ghosh, G. *Handbook of optical constants of solids: five-volume set.* (1998).
- 108 Rivnay, J., Jimison, L. H., Toney, M. F., Preiner, M., Melosh, N. A. & Salleo, A. Interfacial effects in thin films of polymeric semiconductors. *Journal of Vacuum Science & Technology B* **26**, 1454-1460 (2008).
- 109 Jung, Y. S. Spectroscopic ellipsometry studies on the optical constants of indium tin oxide films deposited under various sputtering conditions. *Thin Solid Films* **467**, 36-42 (2004).
- 110 Edlén, B. The refractive index of air. *Metrologia* **2**, 71 (1966).
- 111 Pettersson, L. A. A., Ghosh, S. & Inganas, O. Optical anisotropy in thin films of poly(3,4-ethylenedioxythiophene)-poly(4-styrenesulfonate). *Organic Electronics* **3**, 143-148 (2002).
- 112 Hoppe, H., Sariciftci, N. S. & Meissner, D. Optical constants of conjugated polymer/fullerene based bulk-heterojunction organic solar cells. *Molecular Crystals and Liquid Crystals* **385**, 233-239 (2002).
- 113 Shaw, P. E., Ruseckas, A. & Samuel, I. D. W. Exciton diffusion measurements in poly(3-hexylthiophene). *Advanced Materials* **20**, 3516-3520 (2008).
- 114 Goh, C., Scully, S. R. & McGehee, M. D. Effects of molecular interface modification in hybrid organic-inorganic photovoltaic cells. *Journal of Applied Physics* **101**, 114503 (2007).
- 115 Kroeze, J. E., Savenije, T. J., Vermeulen, M. J. W. & Warman, J. M. Contactless determination of the photoconductivity action spectrum, exciton diffusion length, and charge separation efficiency in polythiophene-sensitized TiO₂ bilayers. *Journal of Physical Chemistry B* **107**, 7696-7705 (2003).
- 116 Luer, L., Egelhaaf, H. J., Oelkrug, D., Cerullo, G., Lanzani, G., Huisman, B. H. & de Leeuw, D. Oxygen-induced quenching of photoexcited states in polythiophene films. *Organic Electronics* **5**, 83-89 (2004).
- 117 Reisch, H., Wiesler, U., Scherf, U. & Tuytuytkov, N. Poly(indenofluorene) (PIF), a novel low band gap polyhydrocarbon. *Macromolecules* **29**, 8204-8210 (1996).

- 118 Drees, M., Premaratne, K., Graupner, W., Heflin, J. R., Davis, R. M., Marciu, D. & Miller, M. Creation of a gradient polymer-fullerene interface in photovoltaic devices by thermally controlled interdiffusion. *Applied Physics Letters* **81**, 4607-4609 (2002).
- 119 Chen, D., Liu, F., Wang, C., Nakahara, A. & Russell, T. P. Bulk Heterojunction Photovoltaic Active Layers via Bilayer Interdiffusion. *Nano Letters* **11**, 2071-2078 (2011).
- 120 Treat, N. D., Brady, M. A., Smith, G., Toney, M. F., Kramer, E. J., Hawker, C. J. & Chabynyc, M. L. Interdiffusion of PCBM and P3HT Reveals Miscibility in a Photovoltaically Active Blend. *Advanced Energy Materials* **1**, 82-89 (2011).
- 121 Huang, Y. C., Chuang, S. Y., Wu, M. C., Chen, H. L., Chen, C. W. & Su, W. F. Quantitative nanoscale monitoring the effect of annealing process on the morphology and optical properties of poly(3-hexylthiophene)/ [6,6] -phenyl C₆₁-butyric acid methyl ester thin film used in photovoltaic devices. *Journal of Applied Physics* **106**, 034506-1:6 (2009).
- 122 Hwang, I. W., Moses, D. & Heeger, A. J. Photoinduced carrier generation in P3HT/PCBM bulk heterojunction materials. *Journal of Physical Chemistry C* **112**, 4350-4354 (2008).
- 123 Asatekin, A., Barr, M. C., Baxamusa, S. H., Lau, K. K. S., Tenhaeff, W., Xu, J. & Gleason, K. K. Designing polymer surfaces via vapor deposition. *Materials Today* **13**, 26-33 (2010).
- 124 Granqvist, C. G. & Hultaker, A. Transparent and conducting ITO films: new developments and applications. *Thin Solid Films* **411**, 1-5 (2002).

4. Study and manipulation of SWCNT-graphene interactions

Some of the work, text and figures presented in this Chapter are reprinted or adapted with permission from reference [1] (Copyright © 2012, WILEY-VCH Verlag GmbH & Co.).

4.1. Background and motivation

Both single layer graphene (SLG) and single walled carbon nanotubes (SWCNTs) have exceptional optical, mechanical, thermal and electronic properties [2-7], as described in Chapter 1.

Although electronic transport in graphene as well as in SWCNTs has been extensively explored [8-11], very few studies have investigated transport through the interface formed between a carbon nanotube and graphene or graphite, and in fact no study to date has investigated a junction between SWCNTs and SLG. Paulson *et al.* used conductive atomic force microscopy (AFM) to measure the contact resistance between a multi-walled carbon nanotube (MWCNT) and highly ordered pyrolytic graphite (HOPG) and found that the resistance varies significantly (between ~ 5 and $\sim 75\text{k}\Omega$) based on the orientation of the MWCNT lattice with respect to the graphite lattice [12]. Both HOPG and MWCNTs are considered to be zero-gap metals. Pei *et al.* grew both semiconducting (sc-) and metallic (m-) SWCNTs on top of exfoliated few-layer-graphene (FLG) and designed bottom-gated field-effect transistor by contacting the SWCNTs and the graphene with palladium electrodes [13]. They found fairly symmetric I - V curves for a

junction between a m-SWCNT and FLG, suggesting no obvious potential barrier between the m-SWCNT and graphene. For a sc-SWCNT/FLG junction they observed rectifying behavior, characterized by a small positive threshold voltage of 0.1 V, indicating the existence of a Schottky barrier.

In this part of my thesis, I describe the creation and study of a junction between SWCNTs and a monolayer of graphene, an ideal one-dimensional / two-dimensional carbon-allotrope conductive interface, for the first time. My interest is in the degree of charge transfer (or doping) between the two materials. The ability to controllably dope graphene and change its work function is key to its implementation in devices such as (opto-) electronics and biosensors, and interconnects [14-18]. Additionally, there is a strong preference to dope graphene without covalently functionalizing it or substituting carbon atoms, such that graphene's outstanding electronic properties are preserved [19,20]. Finally the transition from 2D to 1D electronic conduction may lead to new physics that could be of interest for engineering novel electronic junctions, including rectifiers, transistors and sensors.

The interactions between a single m-SWCNT and a single layer graphene sheet that covers the SWCNT are studied using Raman spectroscopy, a technique that relies on the inelastic scattering of monochromatic laser photons with molecular vibrations (phonons), resulting in an energy shift of the laser photons. Comparing the Raman data of the SWCNT/graphene junction with those of bare graphene and bare SWCNTs reveals that the SWCNT locally dopes the graphene at the junction formed between them. Similar results were obtained for a sc-SWCNT/graphene junction. We demonstrate polarized spectral deconvolution of the Raman spectra as a technique to enable the study

of these carbon junctions. A molecular dynamics simulation rules out strain as the cause of the observed Raman peak shifts. Since the SWCNT is able to dope the graphene in a spatially controlled way without affecting its sp^2 -lattice structure, we do not expect a significant mobility loss in the graphene.

4.2. Materials and methods

4.2.1. SWCNT synthesis

Aligned SWCNTs were grown via atmospheric CVD on a SiO_2/Si (300nm of SiO_2) wafer. The SiO_2/Si wafers were cut with a die-saw (9x14mm sample dimensions) and cleaned by ultrasonically cleaning them for 10 min in acetone and for 10 minutes in IPA, after which they were dried with a stream of N_2 .

The catalyst for growth is based on solution-dispersed SWCNTs from Nano-C, grown with a pyrolysis method (Nano-CAPT). 2mg/ml of the Nano-CAPT SWCNTs were weighed out and added to a 2wt% sodium cholate hydrate aqueous solution; the SWCNTs were dispersed in the surfactant by homogenizing and tip-sonicating the mixture for 1 hour each.

The solution typically contains about 30wt% of Fe or Fe oxide nanoparticles. These Fe particles serve as the catalyst for the aligned SWCNT growth, and the SWCNTs already present in the catalyst disperse the particles such that many individual catalytic sites are present and such that the Fe-particles are now not necessarily stuck to the substrate, enabling lift-off from the surface during growth. The SWCNTs ‘float’ along with the gas flow during growth; this mechanism is known as kite-growth [21].

Using a syringe, a ~1mm wide strip of SWCNT/Fe catalyst solution was deposited along the bottom width of the SiO₂/Si wafer and the wafer was placed inside the quartz tube of the CVD furnace. The temperature is ramped up to 900°C in 20 minutes under stable flow of 100sccm ultrahigh-purity hydrogen (H₂), kept constant at 900°C for 10 min, ramped up to 970°C while flowing 3.4 sccm of H₂. At this point a stable flow of 2sccm ultrahigh-purity methane (CH₄) was added for the next 45 minutes during which the SWCNTs grow.

After growth, the wafers with the SWCNTs were annealed in air at 350°C for 1.5 hour to remove any possible amorphous carbon via oxidation.

Scanning electron microscopy imaging (SEM, model JEOL 6060) was used to verify SWCNT growth and to identify the locations of suitably long SWCNTs for detailed Raman characterization.

4.2.2. Graphene synthesis and transfer

SLG was synthesized by low-pressure CVD on a copper foil substrate (25 μm, 99.8%, Alfa Aesar) that acts as the catalyst. The Cu foil was cut (~3/4" x 2") and cleaned by submerging in a 1:1 HCl:DI H₂O solution for 5 minutes, followed by rinsing it with DI H₂O, acetone and IPA. The film was then blow-dried with a N₂-gun and placed on a hotplate (85°C) for 5 minutes. Under a stable H₂ flow (30sccm), the Cu sheet was heated to 1000°C in 20 minutes, and kept at 1000°C for another 20 minutes to anneal it. Next, 3sccm of CH₄ was added and graphene was synthesized for 35 minutes.

The graphene on Cu was covered in poly(methyl methacrylate) (950PMMA, A4, MicroChem) by spin coating (3000 rpm, 1 min) and dried in air (~15 min). Graphene on

the reverse side of the Cu sheet was removed by reactive ion etching (Plasmatherm RIE, 100 W, 7 mtorr oxygen, 5 min). The Cu-graphene-PMMA stack was placed on the surface of Cu etchant (6 M HCl and 1 M CuCl₂ in water). After complete Cu etching (~30 minutes), the graphene-PMMA layer was scooped out with a clean wafer into several sequential baths of ultrapure water for rinsing. Finally it was scooped out with the target substrate (wafer with aligned SWCNTs as described above) and dried in air overnight before immersion in several baths of clean acetone to dissolve the PMMA, followed by rinsing in isopropanol and drying with ultrapure nitrogen.

4.2.3. Raman Spectroscopy

Raman spectroscopic measurements were performed on a Horiba Jobin Yvon LabRAM HR800 system using a 633 nm excitation laser, 100X objective lens with ~1 μm diameter spot size, and 600 lines/mm grating with ~3-4 cm⁻¹ spectral resolution. The Raman peaks were fit to Lorentzians.

It is crucial for the experiments to calibrate the Raman spectrometer prior to collecting data. Cyclohexane was used as a reference. Moreover, the calibration may shift over time or with temperature changes; therefore we collected the Raman signal of cyclohexane right before and after collecting graphene Raman data and adjusted the data accordingly.

4.2.4. Statistics

For each two distributions compared in this Chapter, we tested whether they are statistically significantly different from one another. First, for each dataset a Shapiro-Wilks test was performed, with the null hypothesis being that the data is normally distributed. The significance level was set at 0.05. For p-values less than 0.05 the null hypothesis was rejected, and vice versa. If two distributions being compared are both normal, an independent two-sample t-test was performed where the null-hypothesis states that the data in both datasets comes from normal distributions with equal means but unknown variances. If on the other hand, one or both of the distributions compared are not normally distributed, a two-sample Kolmogorov-Smirnov test was performed; the null hypothesis is that both datasets come from the same continuous distribution.

For either test, the null hypothesis was rejected for p-values <0.01 , in which case the difference between both datasets was declared statistically significant. Where appropriated, the p-value of either the t-test or the Kolmogorov-Smirnov test was reported in the figure caption.

4.2.5. Molecular dynamics simulation

For the MD simulations VMD was used in combination with the NAMD package. For the SWCNTs and graphene the CHARMM27 force field was used [22,23], and the VMD inorganic builder plugin was used to determine the SiO_2 force field [24].

The SiO_2 in the simulation is 50 unit cells long and wide ($\sim 25\text{nm}$), and 10 unit cells deep ($\sim 7\text{nm}$). The (13,7) SWCNT (diameter $\sim 1.35\text{nm}$) is 22nm long. The graphene sheet covering the SWCNT is 20nm long and wide. The results of the simulation did not change significantly if we change the size of the simulation.

In the initial condition for the simulation the graphene sheet was bent into a Gaussian shape over the SWCNT; the FWHM and height of the Gaussian were varied in several simulations to verify that the final equilibrated structure is independent of the initial conditions. It should be noted that when the graphene sheet was located too far from the SWCNT at time 0, the structure did not converge to the same solution since in the simulation the VDW interactions were truncated after 12 Å. During the simulation the graphene and SWCNT atoms were allowed to equilibrate and move, whereas the SiO₂ atoms remained fixed.

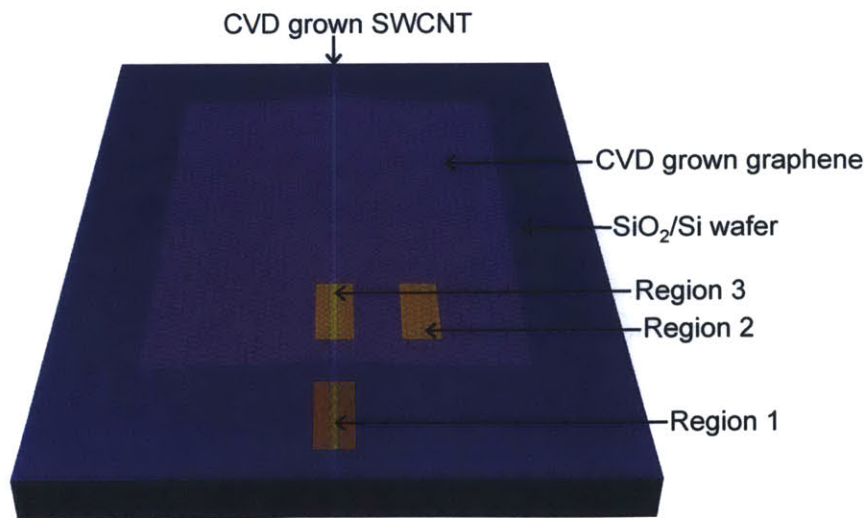
The simulations were run at 300K (controlled via Langevin dynamics) in the NVT ensemble, assuming a vacuum and typically reach an equilibrium state after ~ 500 time steps (= 1 ps). At first, each simulation was run for 15000 time steps. Then, the output coordinate file served as the initial condition for the next simulation and thermal velocities were redistributed. This was repeated 4 times. Out of each of those 4 simulations 500 time points were taken (in total 2000), which were then averaged.

4.3. Results and discussion

4.3.1. Doping effect investigated by Raman spectroscopy

Aligned SWCNTs were grown on a SiO₂/Si wafer via chemical vapor deposition (CVD). A monolayer of graphene was also synthesized via CVD and transferred on top of the wafer with SWCNTs as described in Chapter 4.2.

Figure 4.1a shows a schematic of the SWCNT/graphene junction. Figure 4.1b shows an array of SEM images of the entire wafer and indicates the particular metallic-SWCNT/graphene junction being investigated, and Figure 4.1c is an atomic force microscopy (AFM) image of a representative SWCNT. The way the sample is made allows for direct comparison between different regions of the same sample. Raman spectroscopic maps were taken at 3 different regions in the same sample (Fig.4.1a). In Region 1, 75 spatially distinct Raman spectra were taken along $\sim 100\mu\text{m}$ of the bare SWCNT. In Region 2 ($\sim 20 \times 100\mu\text{m}$), 75 spatially distinct Raman spectra are taken of the graphene alone. Finally we were able to gauge the influence of the SWCNT on the graphene and vice versa by collecting 75 Raman spectra in distinct locations in Region 3 where the graphene covers the SWCNT (spectra of the junction were taken for $\sim 100\mu\text{m}$ along the length of the SWCNT). This allows for direct internal controls. The reason for collecting this many spectra in each region is the ability to take into account any possible spatial inhomogeneity of the graphene, SWCNT and the substrate and to make meaningful statistical comparisons between the different regions.



(a)

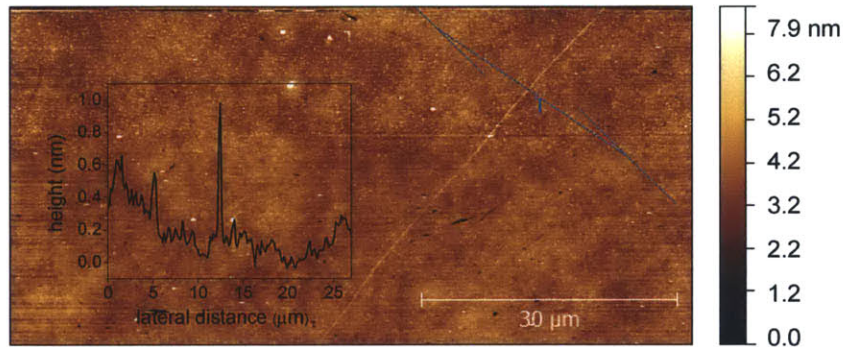
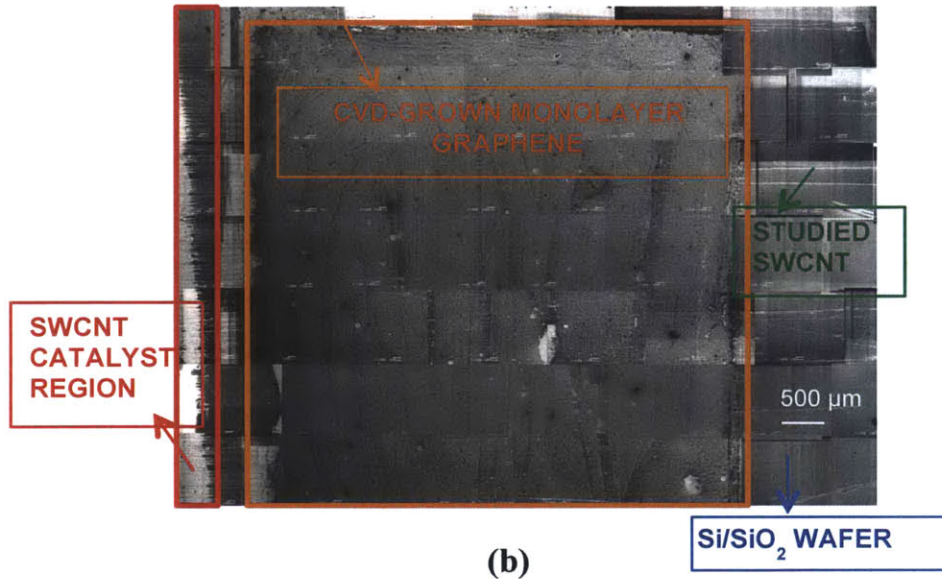


Figure 4.1. Sample setup and characterization. (a) Schematic of the SWCNT-CVD graphene junction (not to scale). Region 1 indicates a part of the SWCNT where it is not covered by graphene (Raman spectra taken along $\sim 100\mu\text{m}$ of the SWCNT). Region 2 indicates a ($\sim 100\mu\text{m}$ by $20\mu\text{m}$) region of graphene away from the junction. Region 3 indicates a region where the graphene is directly on top of the SWCNT (Raman spectra taken along $\sim 100\mu\text{m}$ of the SWCNT). In order to obtain statistically relevant data, in each region 75 distinct Raman spectra were taken at different spots. Given a laser spot size of $1\mu\text{m}$, the spectra were taken at least $1.25\mu\text{m}$ apart from one another, thereby avoiding overlap. (b) Stitched together SEM images of the entire wafer, showing the SWCNT catalyst region, the graphene sheet ($\sim 1/4''$ x $1/4''$) covering the SWCNTs. The green arrow indicates the m-SWCNT that is the subject of the current study. (c) AFM image of a typical CVD-grown SWCNT. Inset shows the height profile, indicating the SWCNT diameter is ~ 0.8 nm.

m-SWCNT/graphene junction: results

Figure 4.2 shows representative Raman spectra from each of the different regions, specifically for the m-SWCNT/graphene junction studied here. Figure 4.2a is the spectrum of the m-SWCNT in Region 1. The characteristic Raman modes of SWCNTs are the RBM (radial breathing mode), which typically occurs between 100-300 cm^{-1} ; the G band at $\sim 1580\text{cm}^{-1}$; the D peak (1300-1400 cm^{-1}) and the 2D peak (2600-2800 cm^{-1}) [25]. The D-peak, which originates from double resonant Raman scattering from a phonon and a defect, is absent in our data (Fig. 4.2a), indicating we have a virtually defect-free SWCNT. The 2D peak (also due to double scattering but from two phonons) is typically very weak in SWCNTs. The RBM is caused by out-of-plane vibrations: it corresponds to the radial expansion and contraction of the tube. Therefore it is possible to relate the RBM frequency ω_{RBM} (in cm^{-1}) to the diameter d (in nm) of the SWCNT via

$$\omega_{RBM} = \frac{227}{d} \sqrt{1 + 0.05786 d^2} \quad [26].$$

The RBM, in combination with the resonant excitation wavelength of the SWCNT allows a SWCNT to be determined as metallic (m-SWCNT) or semiconducting (sc-SWCNT). By locating the RBM of the investigated SWCNT (177 cm^{-1}) and the laser energy (2.33 eV) on a Kataura plot ([27]), we assign the SWCNT in Fig. 4.2a as metallic, and most likely a (13,7) chirality SWCNT, with a diameter of $\sim 1.35\text{nm}$. The G band is a signature of in-plane vibrations and (due to the SWCNT curvature) consists of several peaks, the most important ones being G^- (caused by a longitudinal optical phonon (LO) in m-SWCNTs) and G^+ (caused by a transverse optical phonon (TO) for m-SWCNTs). For sc-SWCNTs the G^- peak corresponds to transverse phonon and the G^+ peak to the longitudinal one. For the m-SWCNT under investigation the G^- and G^+ peaks are situated at 1572 and 1592 cm^{-1} respectively.

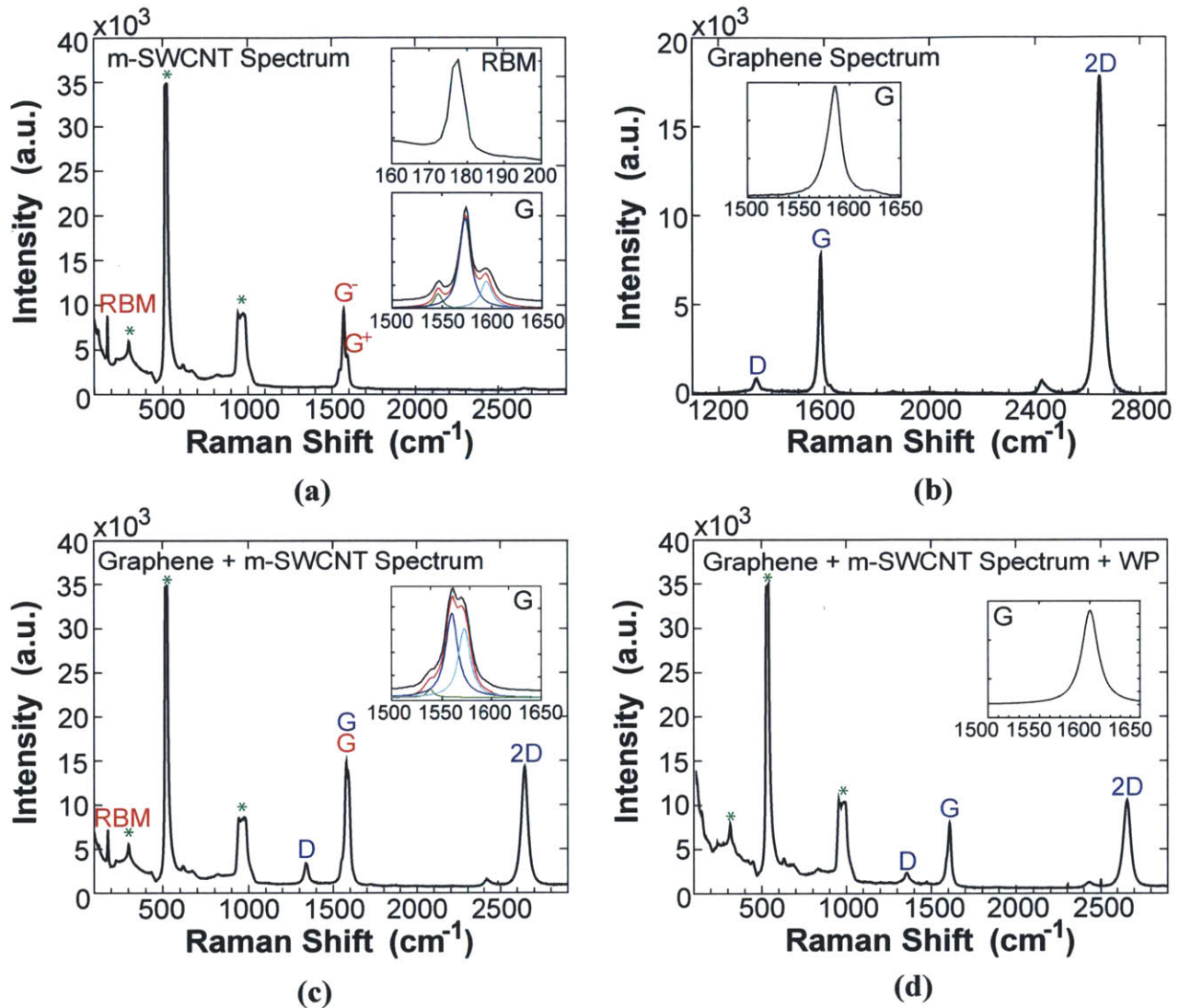


Figure 4.2. Representative Raman spectra of the relevant regions of the sample. The spectra were collected at 633nm laser excitation. Characteristic peaks are assigned (SWCNT peaks denoted in red, graphene peaks in blue and substrate peaks with green asterisks). **(a)** Spectrum taken in Region 1 (SWCNT exposed to air). The 2 insets show the RBM and the G peak. **(b)** Spectrum taken in Region 2 (Graphene exposed to air). Inset shows the G-peak. **(c)** Spectrum taken in Region 3 (Graphene covering SWCNT). Inset shows the G-peaks. **(d)** Spectrum taken in Region 3 with a half-wave plate that ensures the laser polarization is perpendicular to the SWCNT. Inset shows the G-peak.

Figure 4.2b shows the graphene Raman spectrum. A monolayer of graphene is typically characterized by a D-peak near 1300-1350 cm^{-1} , a G-peak near 1580 cm^{-1} and a

2D peak near 2600-2700cm⁻¹[28,29]. The relative intensities and the widths of the G and 2D peaks as well as the color contrast in the microscope confirm we have grown monolayer graphene (SLG) [28,29].

Figure 4.2c shows a representative spectrum of graphene covering the m-SWCNT. The RBM feature of the SWCNT and the 2D feature of graphene are clearly distinguishable; however, the G-bands of the m-SWCNT and the graphene overlap, making it difficult to tell which of the G-peaks is characteristic of the m-SWCNT and which of the graphene. Because the Raman signal of a SWCNT depends on the laser-polarization, mainly due to its anisotropic shape [30-32], it can be blocked while keeping the signal from the graphene by rotating the polarization angle of the incident laser beam.

Figure 4.3 shows the laser-polarization-dependence of the Raman signal of a SWCNT (a) and of graphene (b), obtained by using a half-wave plate to rotate the incident polarization of the laser excitation. The intensity of the Raman signal is the largest when the polarization of the incident light is parallel to the nanotube axis ($\alpha=0^\circ$ and $\alpha=180^\circ$) and disappears completely when it is perpendicular to the nanotube axis ($\alpha=90^\circ$) (Fig.

4.3a). For the SWCNT the polarization difference ratio $\Pi = \frac{I_{0^\circ} - I_{90^\circ}}{I_{0^\circ} + I_{90^\circ}}$ (where I represents

the intensity of the signal, measured as the area under the curve), equals 0.98. It is important to verify the effect of the half-wave plate on the Raman signal of graphene, shown in Figure 4.3b; the half-wave plate has no influence on the G-peak position and very little on the G-peak intensity ($\Pi = -0.04$). This result is expected, since graphene is largely isotropic. Figure 4.2d shows the spectrum taken at the exact same location as the

one in Figure 4.2c but with the insertion of the half-wave plate at $\alpha=90^\circ$. The RBM and G-band signal of the SWCNT disappear whereas the graphene peaks are still present.

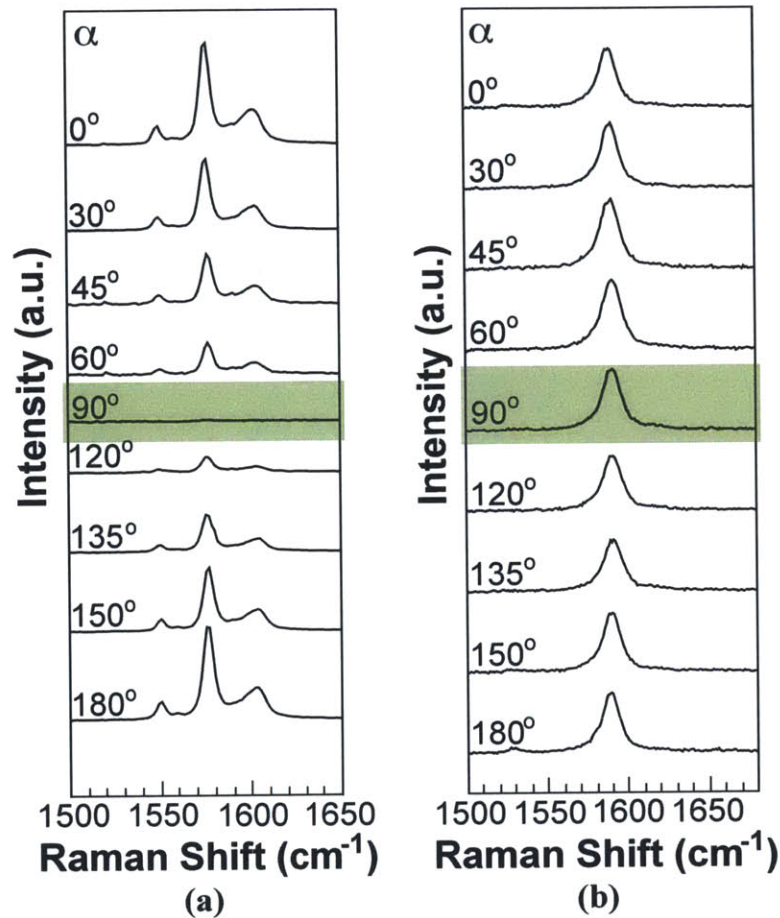


Figure 4.3. Influence of a half-wave retardation plate on the G-band Raman signal of (a) a SWCNT, and (b) graphene.

Figure 4.4 and 4.5 show the influence of the m-SWCNT on the CVD-graphene. Figure 4.4 compares the different statistical distributions of the relevant graphene Raman peak parameters extracted from all 75 spatially distinct Raman spectra collected in Region 2 (graphene alone) vs. Region 3 (graphene covering SWCNT). Figure 4.5 presents the same dataset in a different light: scatterplots of relevant peak parameters in

each region are compared and superposed to ‘doping trajectories’ (the dashed lines in Figure 4.5).

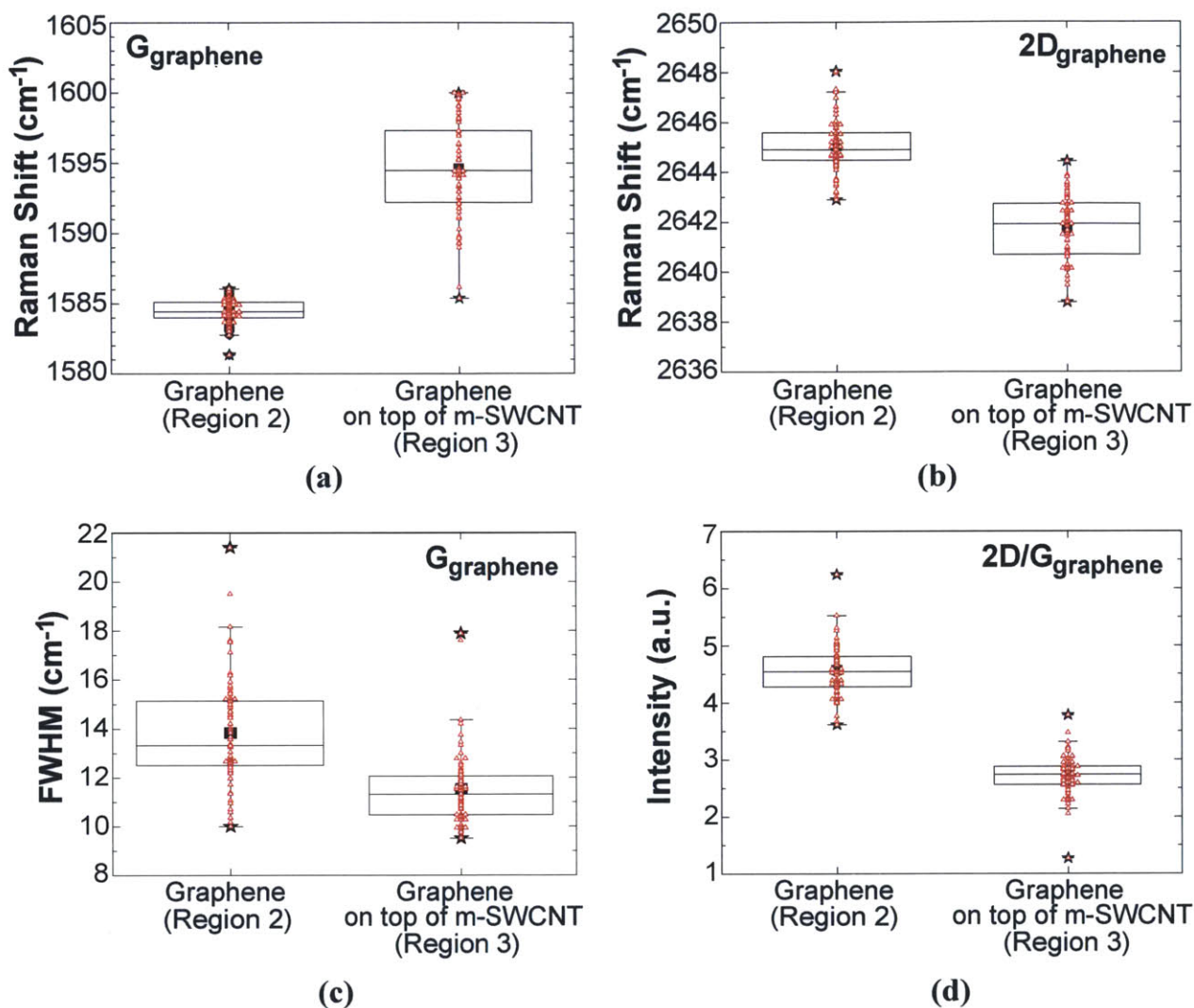


Figure 4.4. Statistical plots showing the influence of the m-SWCNT on graphene. The lower and higher ends of the boxplots represent the 25 and 75 percentile marks of the distributions respectively, and the middle line is the median value. Minimum and maximum values are represented by black stars, and the average is the black square. The red triangles represent the complete dataset superimposed on the boxplots. **(a)** G peak position of intrinsic graphene (Region 2) vs. graphene on top of the m-SWCNT (Region 3); $p < 0.01$ (see Chapter 4.2.4). The increase in position is consistent with doping. **(b)** 2D peak position of intrinsic graphene (Region 2) vs. graphene on top of the m-SWCNT (Region 3); $p < 0.01$ (see Chapter 4.2.4). The decrease in position is consistent with n-doping. **(c)** Full width at half maximum (FWHM) of intrinsic graphene (Region 2) vs. graphene on top of the m-SWCNT (Region 3); $p < 0.01$ (see Chapter 4.2.4). The decrease in width is consistent with doping. **(d)** 2D/G intensity ratio of intrinsic graphene (Region

2) vs. graphene on top of the m-SWCNT (Region 3); $p < 0.01$ (see Chapter 4.2.4). The decrease is consistent with doping.

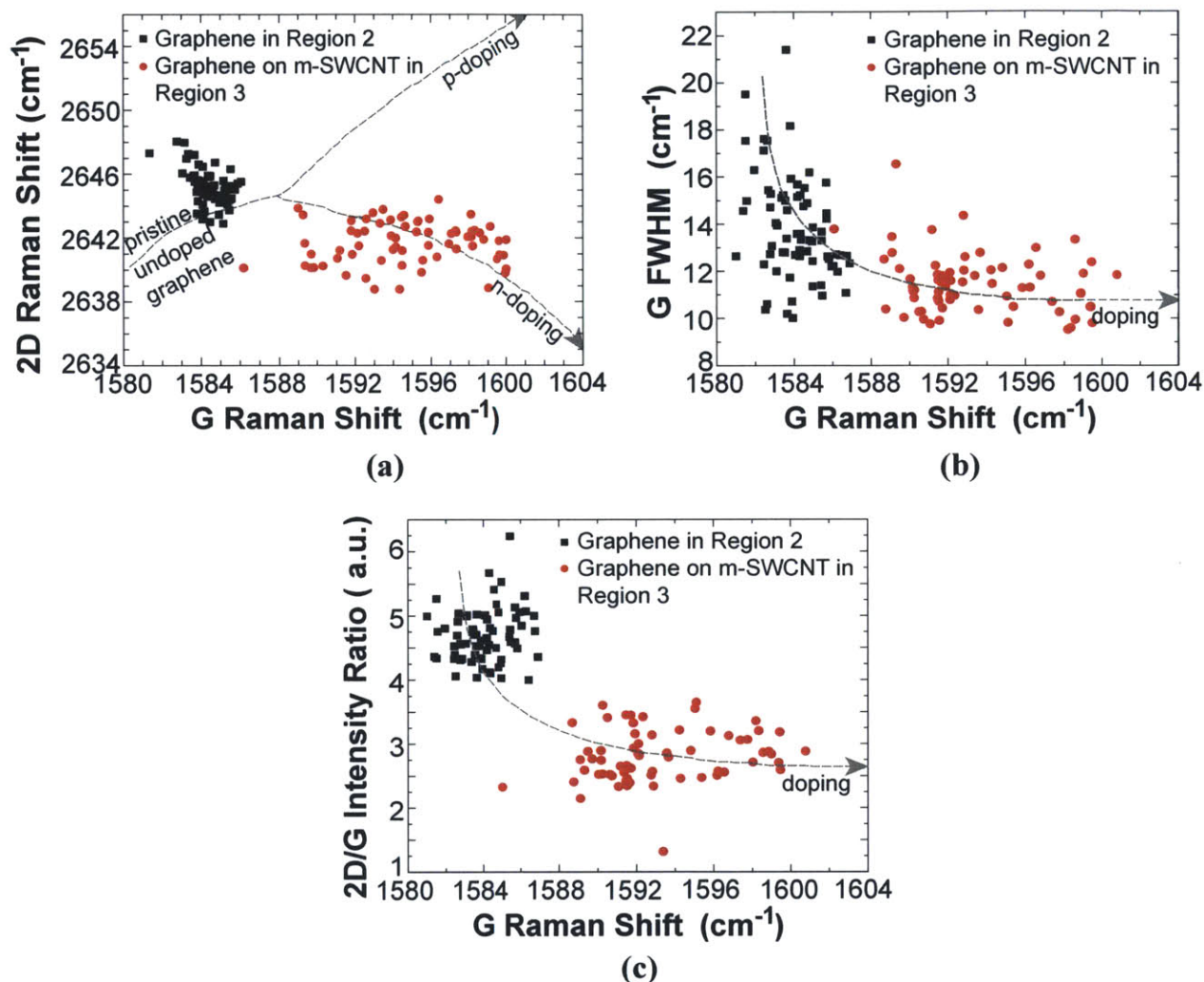


Figure 4.5. Doping trajectories showing the influence of the m-SWCNT on the graphene. Comparison of some characteristic Raman signals of the graphene in Region 2 (on the substrate, black squares) and Region 3 (on top of the SWCNT, red dots). **(a)** Effect of SWCNT on the G and 2D-peak position of graphene. **(b)** Effect of the SWCNT on the G peak position and width of the graphene. **(c)** Effect of the SWCNT on the 2D/G intensity ratio and the G position of graphene. Dashed lines represent doping trajectories adapted from [33] and [34].

Das *et al.* changed the number of charge carriers in graphene by tuning the gate voltage of a graphene field-effect transistor (FET) while simultaneously monitoring the

evolution of the relevant graphene Raman peak parameters [33]. Based on their dataset, we were able to establish the above-mentioned doping *doping trajectories*.

The G and 2D peaks contain information about the level of doping and strain in graphene [28,29,33,35,36]. Figure 4.4a shows how the G-peak position of graphene upshifts by about 10 cm^{-1} when it covers the m-SWCNT, indicative of doping. The 2D peak decreases by $\sim 3\text{ cm}^{-1}$ (Fig. 4.4b), which indicates that the type of doping is n-type [33]. Figure 4.5a shows the 2D peak position versus the G peak position of graphene on the SiO_2 substrate (black squares) and on top of the SWCNT (red dots). (It should be noted that in establishing the *doping trajectory* in Fig. 4.5a we took into account the dependence of graphene's 2D peak position on the laser excitation wavelength by downshifting the 2D position data from [33] since they were generated after 532nm laser excitation and this work uses a 633nm laser excitation source.)

The 2D-G position trajectory starts out on the left side of the graph with undoped graphene. For both p- and n- doping the G peak position increases but the 2D position shifts differently for each type of doping resulting in the two branches in Figure 4.5a. Our data superimposed on these doping trajectories supports the conclusion of n-doping of graphene from the m-SWCNT.

Another measure of doping is a decrease of the G peak full width at half maximum (FWHM) [35,37], which we also observe (Fig. 4.4c, Fig. 4.5b). Figure 4.5b shows the FWHM of the G peak plotted versus its position. The dashed doping trajectory, adapted from [33] indicates increased doping levels lead to a stiffer G peak and an increased G peak position. This trend line has been shifted upward to take into account the larger G peak FWHM in CVD graphene, compared to that in exfoliated graphene.

A final indication of doping is a decreased 2D/G intensity ratio, depicted in Figure 4.4d. Combined with the previous trend of increased G peak, another doping trajectory can be set up (Figure 4.5c). The dashed trend line is adapted from data in ref. [33]. It should be noted that G-peak information of graphene on top of the SWCNT was deduced from spectra taken with the half-wave plate, as it is clear from Figure 4.2c it is hard to deduce which peaks belong to graphene and which to SWCNT without it. Due to the introduction of the additional optics the intensity of the G-peak decreases by $\sim 8.5\%$ (as shown in Fig. 4.6) and it can be considered as the lower limit of the actual value of the G peak intensity. This implies that the 2D/G intensity ratio in Figure 4.4d and 4.5c for graphene on top of the SWCNT is an upper limit, which further confirms the doping trend.

Note that the G peak position data taken in Region 3, shown in Figures 4.4 and 4.5 are characterized by a slightly broader distribution than the other distributions. This is likely because the SWCNT G peak and the graphene G peak in Region 3 partially overlap and the deconvolution slightly overestimates the width of the graphene G peak.

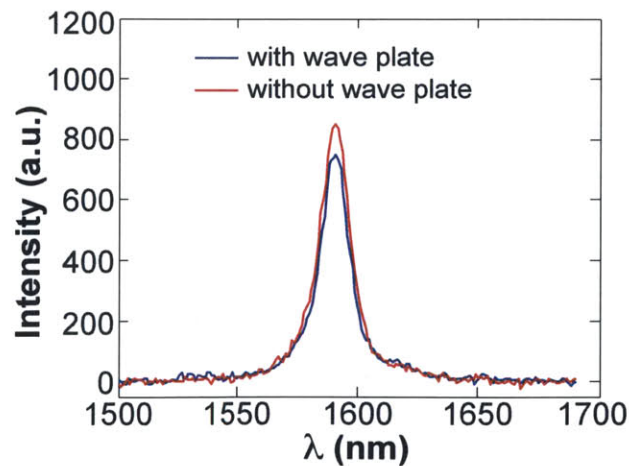


Figure 4.6 Representative intensity loss ($\sim 8.5\%$) of graphene G-peak signal upon insertion of the half wave plate ($\alpha = 90^\circ$).

Comparing the SWCNT Raman signal in Region 1, where the SWCNT is exposed to air, and in Region 3, where it is covered by graphene, also yields some interesting observations. Figure 4.7 shows the influence of the graphene on the RBM and G^- peak position of the m-SWCNT. In contrast to the G^+ peak-position of the m-SWCNT, the G^- position can still be extracted from the Raman signal in Region 2 without the half-wave plate (i.e. the dark blue curve in Figure 4.2c).

Figure 4.7 shows an upshift in both the RBM and the G peak position of the m-SWCNT when it is covered by graphene. It has been shown both theoretically and experimentally that upon doping the RBM and G-peaks of SWCNTs can upshift [38-43]. There is some disagreement in the literature about the exact nature and extent of this doping. Farhat *et al.* claim the RBM upshift is only observed for m-SWCNTs [38], whereas others do not make the distinction between sc-SWCNTs and m-SWCNTs when observing this phenomenon [40,43]. The experimental conditions and nanotube sources are different in each publication. Since Farhat *et al.* also use CVD-grown SWCNTs, their observations may be more relevant to our work.

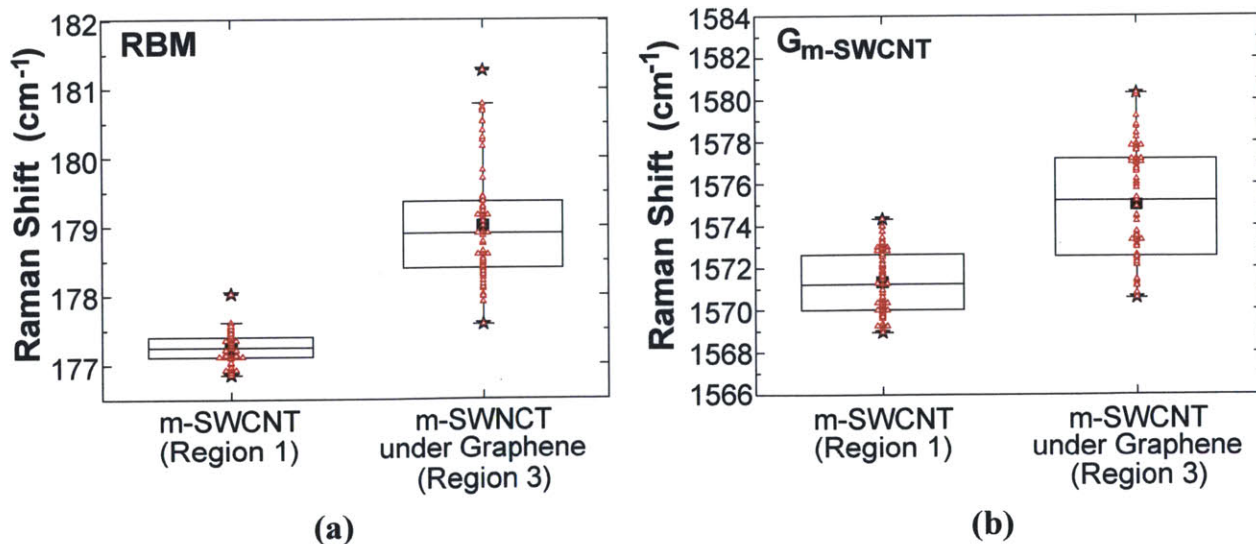


Figure 4.7. Statistical plots showing influence of graphene on the m-SWCNT. Comparison of the RBM **(a)** and the G peak **(b)** positions the m-SWCNT in Region 1 (exposed to air) and Region 3 (underneath the graphene). The lower and higher ends of the boxplots represent the 25 and 75 percentile marks of the distributions respectively, and the middle line is the median value. Minimum and maximum values are represented by black stars, and the average is the black square. The red triangles in Figure 4.7**(a),(b)** represent the complete dataset superimposed on the boxplots. In each case, $p < 0.01$ (see Chapter 4.2.4).

sc-SWCNT/graphene junction: results

A similar junction was created between a semiconducting SWCNT and single layer graphene. The key results are shown in Figure 4.8. Based on the RBM peak position and the shape of the G bands (both shown in the Raman spectrum of the sc-SWCNT in Fig. 4.8a), we assign the SWCNT as semiconducting, specifically as a (18,7) chirality sc-SWCNT with a diameter of $\sim 1.78\text{nm}$.

Figure 4.8b summarizes the doping effect of the sc-SWCNT on the graphene covering it: graphene covering the sc-SWCNT (Region 3) is substantially more doped than graphene far away from the junction (Region 2), as evidenced by the increase of the average G peak position of graphene from 1587.4 cm^{-1} to 1590.2 cm^{-1} .

It should be noted that in this case, it is hard to deduce the type of doping experienced by graphene on top of the sc-SWCNT, since for some datapoints the 2D position of graphene increases in Region 3 vs. in Region 2, whereas for others it decreases. Moreover, the data are all located close to the where the p- and n-branch of the doping trajectories are joined, where the differences observed in 2D peak position for p- vs. n-doping are less pronounced.

The RBM of the sc-SWCNT does not change in a statistically relevant manner when covered by graphene, as is shown in Figure 4.8c. This is consistent with Farhat *et al.*'s results that only the RBM of metallic SWCNTs upshifts upon doping [38]. The sc-SWCNT G peak position does only upshift slightly from 1602.2 cm^{-1} to 1603.2 cm^{-1} (Fig. 4.8d), which is again expected for sc-SWCNTs [39].

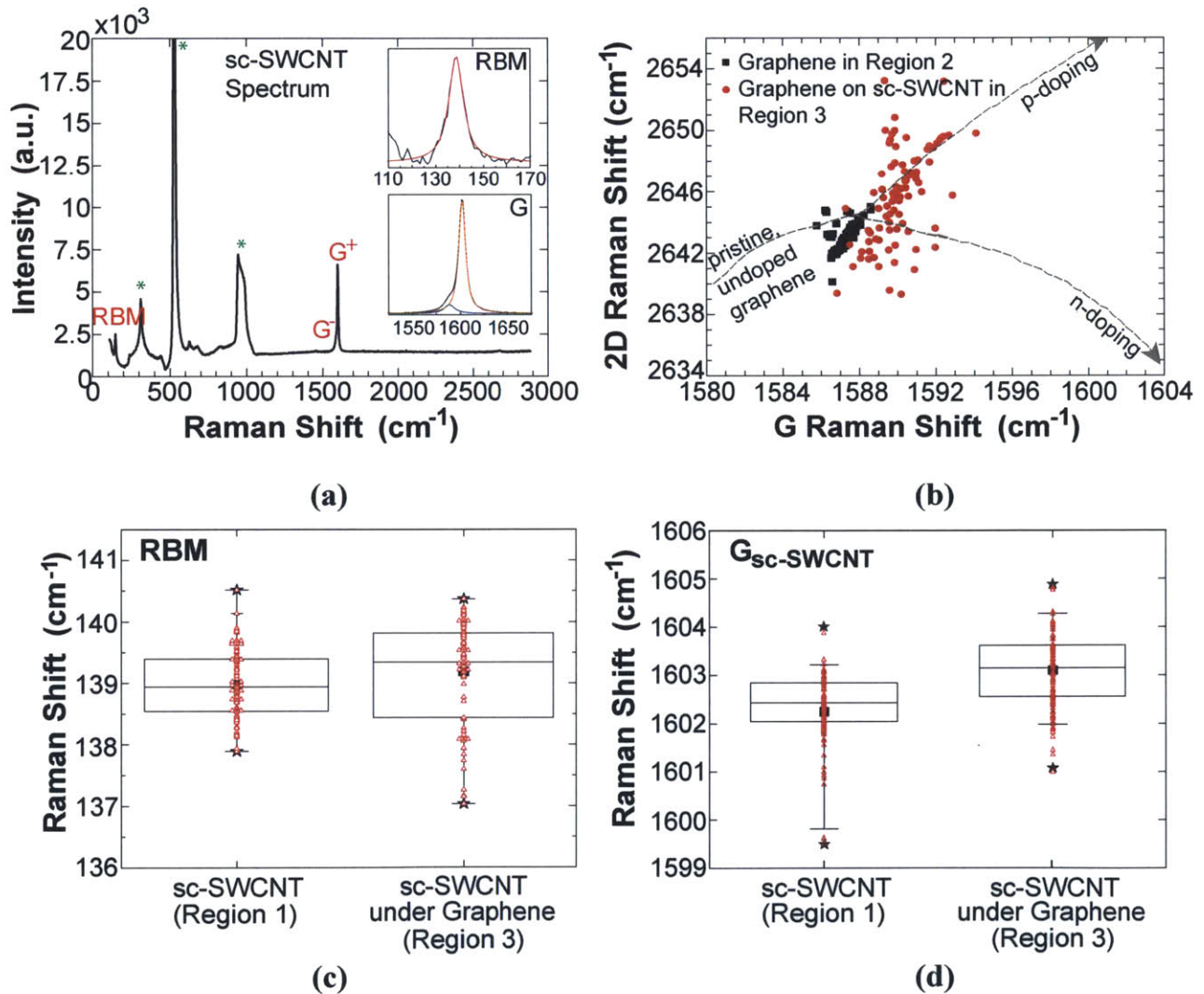


Figure 4.8. Influence of doping at a sc-SWCNT/graphene junction. **(a)** Representative Raman spectrum taken in Region 1 (sc-SWCNT exposed to air). The 2 insets show the RBM and the G peak. **(b)** Effect of sc-SWCNT on the G and 2D-peak position of graphene. Doping trajectories adjusted from ref. [33], with superimposed scatter data of graphene in Region 2 (on the substrate, black squares) and in Region 3 (on top of the

SWCNT, red dots); $p_{G\text{-position,graphene}} < 0.01$; $p_{2D\text{-position,graphene}} < 0.01$ (see Chapter 4.2.4) **(c)**, **(d)** Statistical plots showing influence of graphene on the sc-SWCNT. Comparison of the RBM **(c)** and the G peak **(d)** positions the sc-SWCNT in Region 1 (exposed to air) and Region 3 (underneath the graphene). The lower and higher ends of the boxplots represent the 25 and 75 percentile marks of the distributions respectively, and the middle line is the median value. Minimum and maximum values are represented by black stars, and the average is the black square. The red triangles in Figure 4.8**(c),(d)** represent the complete dataset superimposed on the boxplots. $p_{RBM\text{-position}} = 0.028$ (> 0.01); $p_{G\text{-position,sc-SWCNT}} < 0.01$ (see Chapter 4.2.4).

Discussion

The spectroscopic Raman data indicate that graphene is being n-doped at the junction with the m-SWCNT. Part of these electrons can come directly from the m-SWCNT. When the SWCNT and the graphene are brought in contact, electrons will flow from the material with more electrons (more shallow Fermi energy level E_F compared to vacuum) to the material with fewer electrons (deeper E_F compared to vacuum) to equalize the Fermi levels in the two materials. The theoretical work function of SWCNTs is chirality dependent. For both the m-SWCNT like the one studied here with a diameter of $\sim 1.35\text{nm}$, and the sc-SWCNT with a diameter of $\sim 1.78\text{nm}$ Barone *et al.* have calculated via density functional theory (DFT) that the work function is 4.5 eV, whereas the work function for graphene is determined to be 4.68 eV [44]. The work function is defined as the energy difference between the vacuum energy level and the Fermi energy (E_F) level of the material, which implies a material with a larger work function has a lower lying E_F (in this case graphene). Based on the DFT calculations of the work functions of the materials used in our study, we expect electrons to flow from the m-SWCNT to the graphene, consistent with the doping trends observed in our Raman study. It should be noted that we use CVD-grown graphene that has been exposed to several

processing steps during its growth and transfer, so it is likely that its work function deviates from a pristine graphene crystal in vacuum.

The recorded Raman shifts can inform us about the amount of charge that is transferred between the SWCNT and the CVD graphene. Both Das *et al.* [33] and Farhat *et al.* [38,39] have studied Raman spectra of graphene and SWCNT devices respectively under conditions of electrostatic doping. In the case of the former, Das *et al.* electrochemically gated a graphene monolayer with a polymer top gate (PEO/LiClO₄) and recorded the G-peak position shift as a function of the applied gate voltage V_G . Farhat *et al.* gated a metallic SWCNT with the same top gate (PEO/LiClO₄) and also recorded both G-peak and RBM position shifts as a function of V_G . Below, I calculate the corresponding carrier concentrations that correspond to these shifts in the G peak in order to estimate the respective concentrations observed in SWCNT/graphene junction reported in this work.

The application of a gate voltage results in an electrostatic potential difference between the gate and the graphene (ϕ) as well as a shift in the Fermi level E_F due to the addition of carriers to the graphene.

$$V_G = \phi + \frac{\Delta E_F}{e} \quad (4.1),$$

where e is the unit charge of an electron. ϕ is defined by the electrostatic or geometrical capacitance C_G , whereas the second term is related to the quantum capacitance C_Q of the gated material:

$$V_G = \frac{ne}{C_G} + \frac{2ne}{C_Q} \quad (4.2),$$

where n represents the charge density in the gated material (units of m^{-2} for the 2D graphene and of m^{-1} for the 1D SWCNT). Likewise for a 2D material the units of C_G and C_Q are F/m^2 , whereas for a 1D material the capacitance is normalized per unit length and the units of C_G and C_Q are F/m . The geometrical capacitance (normalized per unit area) for graphene can be written as

$$C_{G,\text{graphene}} = \frac{\epsilon\epsilon_0}{t_d} \quad (4.3),$$

with ϵ the relative dielectric constant of the dielectric, ϵ_0 the permittivity of free space and t_d the thickness of the dielectric. The dielectric constant of the polymer (PEO) is 5 [33,45]. The geometrical length-normalized capacitance C_G between the cylindrical SWCNT and the gate can be written as:

$$C_{G,\text{SWNT}} = \frac{2\pi\epsilon\epsilon_0}{\cosh^{-1}((t_d + r)/r)} \quad (4.4),$$

where r is the SWCNT radius [46]. For polymer top gates the dielectric is formed by the Debye layer that forms at the interface between the gated material and the polymer [33]. Therefore for a polymer top gate:

$$t_d = \left(\frac{2ce^2}{\epsilon\epsilon_0 k_B T} \right)^{-1/2} \quad (4.5),$$

with c is the concentration of the electrolyte, k_B the Boltzmann constant and T the temperature. Typically the exact electrolyte concentration is difficult to estimate, and a Debye length of 2nm is assumed [21,33].

The quantum capacitance for graphene (SWCNT) can be directly derived from the density of states (DOS) of graphene (SWCNT) in the vicinity of the Fermi level [2,47-49]:

$$C_{Q,graphene} = \frac{2e^2\sqrt{n}}{\hbar v_{F,graphene}\sqrt{\pi}} \quad (4.6),$$

$$C_{Q,SWCNT} = \frac{2e^2}{\hbar v_{F,SWCNT}} \quad (4.7),$$

with h and \hbar are the Planck constant and the reduced Planck constant respectively, $v_{F,graphene} = 10^6$ m/s the Fermi velocity for graphene [2] and $v_{F,SWCNT} = 8 \times 10^5$ m/s the Fermi velocity for a m-SWCNT [50]. Note that the factor 2 in the second term of equation (4.2) depends on the definition of C_Q and is related to the spin degeneracy: every state can accommodate two electrons, with opposite spins. Also note that since a 3D bulk metal has a quasi infinite number of available states and thus has a quantum capacitance of ∞ , which implies that the addition of charge carriers barely affects the value of the Fermi level, and the second term in eqn. (4.2) can be omitted.

Combining eqns. (4.1)-(4.7) results in the following relationships between V_G and n for graphene and for a m-SWCNT respectively:

$$\text{for graphene: } V_G = \frac{net_d}{\epsilon\epsilon_0} + \frac{\hbar v_{F,graphene}\sqrt{\pi n}}{e} = An + B\sqrt{n} \quad (4.8),$$

$$\text{for SWCNT: } V_G = \frac{ne \cosh^{-1}((t_d + r)/r)}{2\pi\epsilon\epsilon_0} + \frac{\hbar v_{F,SWCNT}}{e} = (C + D)n \quad (4.9),$$

where A,B,C and D are constants ≥ 0 .

Based on Das *et al.*'s recorded values of G peak shift vs. V_G and the relationship between V_G and n (eqn. (4.8)) we deduce that a peak shift of about 10 cm^{-1} (observed for the m-SWCNT/graphene junction - Fig. 4.4a) requires a gate voltage of 1.2V which corresponds to an added electron concentration $\delta n = 1.12 \times 10^{13} \text{ cm}^{-2}$. The graphene G peak shift from 1587.4 cm^{-1} to 1590.2 cm^{-1} recorded for the sc-SWCNT/graphene junction suggests an added dopant concentration $\delta n = 0.325 \times 10^{13} \text{ cm}^{-2}$. Based on Farhat *et al.*'s recorded peak shifts of the RBM of m-SWCNTs, the shift we observe ($\sim 1.5 \text{ cm}^{-1}$ (Fig. 4.7a)) requires at least a positive or negative gate voltage equal to $|1.5\text{V}|$, which, according to eqn.(4.9) implies a lower bound of the added electron or hole concentration of $\sim |\delta n| = 3.34 \times 10^6 \text{ cm}^{-1}$. It should be noted that for both positive and negative applied gate voltages the observed RBM-shifts of the m-SWCNT eventually saturate. The RBM position upshifts by $\sim 1.5 \text{ cm}^{-1}$ by applying a $|V_G|=1-1.5\text{V}$ but for higher values of $|V_G|$ the RBM peak position no longer changes (e.g. Fig. 5 of ref. [38]). Our observed peak shift is located in this saturated region; hence we can only report a lower limit of added carrier concentration for the SWCNT. Both p- and n-doping of the SWCNT have a similar effect [38,39], but since the graphene is being n-doped (electrons are added) on top of the SWCNT, it is assumed the SWCNT is being p-doped underneath the graphene (deprived of electrons).

Assuming a circular laser spot with a diameter of $1 \mu\text{m}$ (with an area of $\sim 0.785 \mu\text{m}^2$) during our Raman experiments, we can deduce the total amount of charge that is transferred per μm of m-SWCNT. The graphene receives 8.792×10^4 electrons per μm of metallic SWCNT it covers, while the m-SWCNT loses a minimum of 3.34×10^2

electrons per μm . A similar calculation shows graphene receives 2.552×10^4 electrons per μm of sc-SWCNT it covers.

It is plausible that part of the graphene n-doping is caused by the fact that the graphene on top of the SWCNT is no longer in direct contact with the SiO_2 , which is known to p-dope the graphene [51]. Some adsorbants on the SWCNTs itself could potentially also cause additional doping, although the SWCNTs were annealed in air for 350°C for 1.5 hrs to remove amorphous carbon and stored in a vacuum chamber until graphene was put on top. When transferring the graphene to the wafer with SWCNTs the junction is only exposed to deionized water, which then evaporates. Water has been shown to dope graphene [52,53]. Possibly some nanosize water clusters remain trapped between the SWCNT and the graphene, which can locally dope the graphene. This again justifies the need for taking many different spectra in order to get statistically significant results. Water from the air may also adsorb on the topside of the sample. This potentially causes a difference in the doping level of the SWCNT in Region 1 versus the SWCNT in Region 3.

Finally we have examined the possibility that the close interaction between the SWCNT lattice and the monolayer polycrystalline graphene in Region 3 forms a structure resembling turbostratic graphene. Turbostratic graphene is characterized by a very different Raman signature than AB-stacked bilayer graphene or monolayer graphene [54-56]. Compared to pristine graphene both the 2D position, the 2D/G intensity ratio and the G peak width increase. In Region 3 (graphene on top of SWCNT) we only observe a moderate upshift of the 2D peak compared to Region 2, and a decrease of I_{2D}/I_G and a

smaller G peak width. Therefore nothing points in the direction of a turbostratic monolayer/graphene SWCNT interaction.

The amount of SWCNT G band upshift with electrostatic gating is a matter of disagreement in the literature. Farhat *et al.* report an upshift of the G^- peak of an m-SWCNT by $\sim 30\text{cm}^{-1}$ upon the application of a polymer top gate voltage of $|1.5\text{V}|$ (the value of V_G that results in our observed upshift in RBM-peak) [39]; whereas more modest upshifts of the G peak position of a SWCNT upon doping are reported by others [41-43]. In order for the G^- peak to upshift from $\sim 1571\text{ cm}^{-1}$ to 1575 cm^{-1} , as is the case in our data shown in Fig. 4.7b, a $V_G \cong |0.1\text{V}|$ is required, which implies a charge transfer of $0.223 \times 10^2 \mu\text{m}^{-1}$, still within a factor of 15 of the previous analysis. According to Farhat *et al.* the G^- peak upshift we observe seems more typical for the observed upshift of the G^+ peak of a m-SWCNT or of the G-peak of a sc-SWCNT [39].

It should also be clear that all datasets presented show the importance of collecting multiple spectra in each region and comparing the different distributions as a whole. Each distribution shows some spread. This is possibly due to small temperature and humidity fluctuations throughout the experiment and small spatial variations in doping (e.g. residual PMMA on the graphene).

4.3.2. Strain effect investigated by Raman spectroscopy

Radial compressive strain of the SWCNT under the graphene sheet is another physical effect that can shift the RBM and G peak positions of SWCNTs. A recent atomic

force microscopy (AFM) study has shown a reduction of the height of a SWCNT with an original diameter of 1.35nm by nearly 23% when it is covered by a monolayer of graphene oxide (GO) [57].

While the effects of axial compression and strain on the SWCNT Raman signal have been explored [58] [59], the effect of radial compression on the Raman spectrum of a single SWCNT on a substrate has not yet been investigated. There is experimental and computational evidence for an upshift of the Raman peaks of SWCNTs and SWCNT bundles in solution under pressure [60,61]. The case of a single SWCNT compressed by both the substrate underneath it and the graphene on top but free to expand sideways is likely different. Both molecular dynamics (MD) and experimental studies show the effect of axial strain and compression on the Raman peak positions of SWCNTs is opposite: positive axial strain decreases peak positions whereas negative axial strain (compression) increases them [58] [59].

To estimate the amount of strain at equilibrium in our system (a sheet of monolayer graphene covering a (13,7) m-SWCNT on SiO₂/Si substrate), MD calculations were performed at 300K in the canonical (NVT) ensemble using the NAMD molecular dynamics package with CHARMM27 force-field parameters [22,23], as described in Section 4.2. A similar analysis was performed for the (18,7) sc-SWCNT covered by graphene. The simulations were performed similarly to many other MD simulations of graphene and/or SWCNT available in literature [62-64]. A visual representation of the m-SWCNT on top of SiO₂ and graphene-covered SWCNT on top of SiO₂ (generated with the VMD software package [24]) is shown in Figure 4.9a; it is clear the graphene radially compresses the SWCNT. Figure 4.9b shows the distribution of bond lengths in the m-

SWCNT before and after being covered by graphene and key results are summarized in Table 4.1.

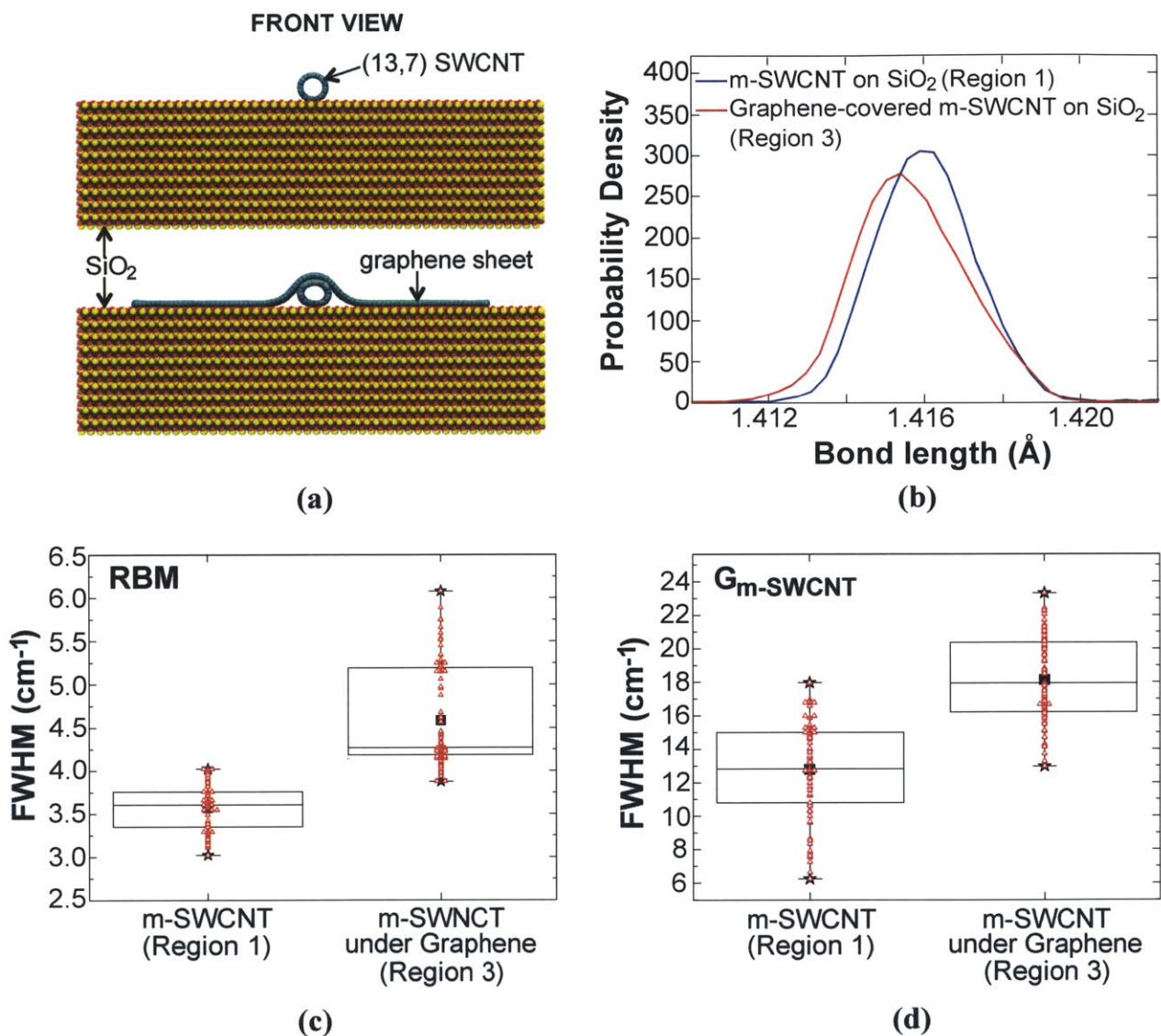


Figure 4.9. Influence of strain on the SWCNT. **(a)** Molecular representation of the system (front view). Upper panel: (13,7) SWCNT on SiO₂; lower panel: (13,7) SWCNT on SiO₂ covered by a graphene sheet. **(b)** Distribution of bond lengths in the (13,7) SWCNT. **(c)** Comparison of FWHM of the m-SWCNT's RBM in Region 1 and Region 3; $p < 0.01$ (see Chapter 4.2.4) **(d)** Comparison of FWHM of the m-SWCNT's G_m-SWCNT peak in Region 1 and Region 3; $p < 0.01$ (see Chapter 4.2.4). The lower and higher ends of the boxplots represent the 25 and 75 percentile marks of the distributions respectively, and the middle line is the median value. Minimum and maximum values are represented by

black stars, and the average is the black square. The red triangles in Figure 4.8 (c),(d) represent the complete dataset superimposed on the boxplots.

	SWCNT on SiO ₂ (Å)	Graphene-covered m-SWCNT on SiO ₂ (Å)	Relative change (%)
Average	1.41589 +/- 0.00004	1.41552 +/- 0.00004	-0.03
Median	1.41600 +/- 0.00004	1.41554 +/- 0.00004	-0.03
FWHM	0.0017 +/- 0.0003	0.0020 +/- 0.0003	14.45

Table 4.1. Key parameters of the bond length distribution of the m-SWCNT in our system (with 95% confidence intervals).

The median of the bond length distribution is correlated to the Raman peak positions of the SWCNT. Yang *et al.* performed calculations for axially strained SWCNTs and showed that for a (10,10) m-SWCNT (with very similar band structure to the (13,7) SWCNT considered here) the peak position (ω) changed with axial strain (ϵ) as:

$$\frac{\partial\omega_{RBM}}{\partial\epsilon} = -0.55 \frac{cm^{-1}}{\%} \quad (4.10),$$

$$\frac{\partial\omega_{G^-}}{\partial\epsilon} = -25.50 \frac{cm^{-1}}{\%} \quad (4.11).$$

It should be noted this linear dependence is only true for small strains ($\sim|\epsilon| < 2\%$) [58].

The Raman peak shifts caused by the graphene compressing the SWCNT can be estimated as:

$$\Delta\omega_{RBM} = \frac{\partial\omega_{RBM}}{\partial\epsilon} \times \Delta\epsilon = -0.55 \frac{cm^{-1}}{\%} \times -0.03\% = 0.0165 cm^{-1} \quad (4.12),$$

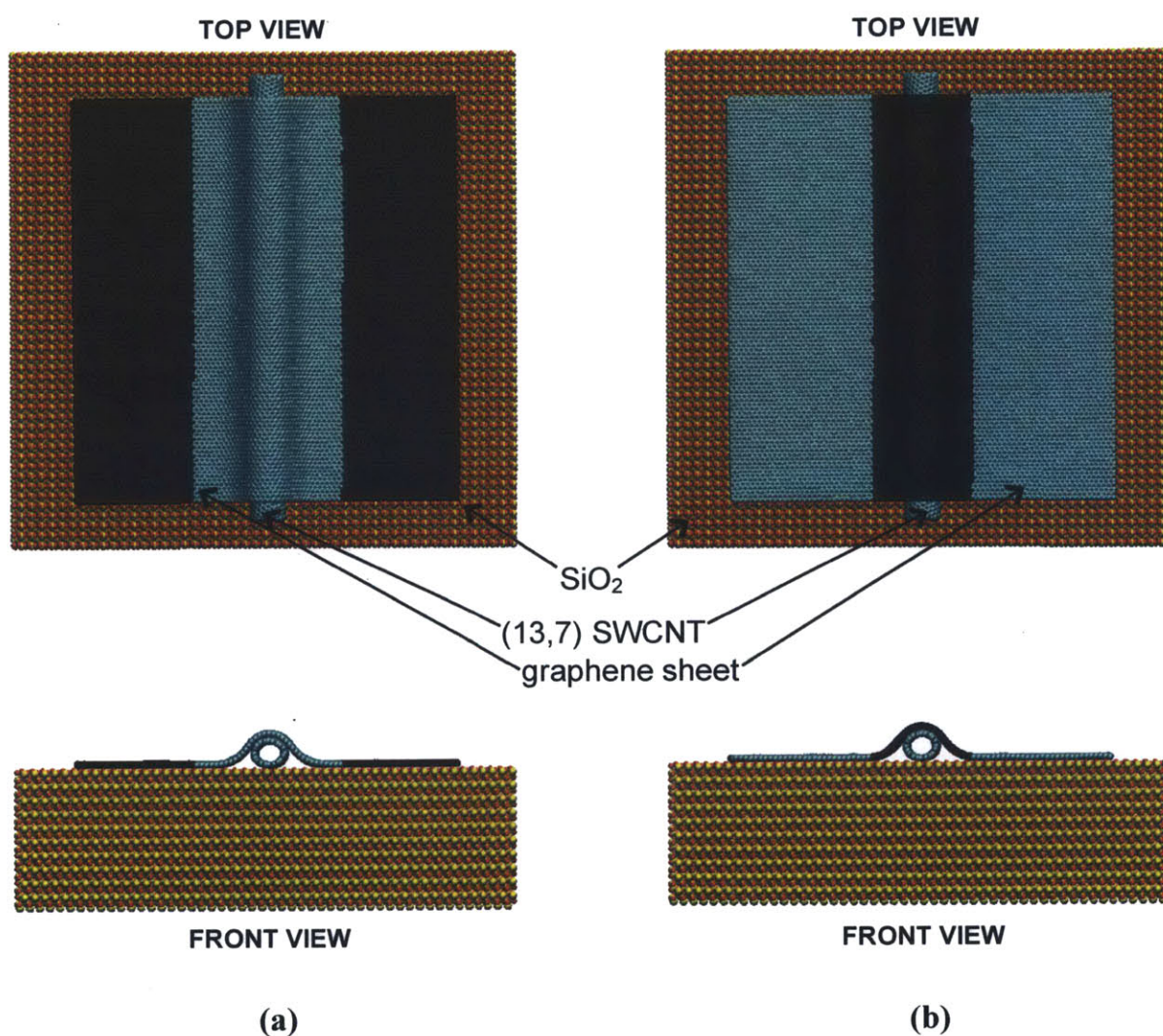
$$\Delta\omega_{G^-} = \frac{\partial\omega_{G^-}}{\partial\varepsilon} \times \Delta\varepsilon = -25.50 \frac{cm^{-1}}{\%} \times -0.03\% = 0.765 cm^{-1} \quad (4.13),$$

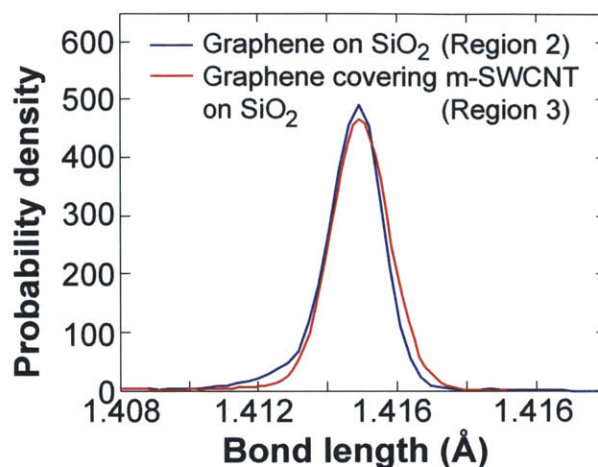
where $\Delta\varepsilon$ is the relative change in the peak position (median value) of the bond length distribution for the SWCNT before and after coverage. From this analysis it is clear the observed (much larger) Raman peak shifts of the SWCNT (Fig. 4.7) can not be explained by strain and are thus due to doping.

Further analysis revealed that although the average SWCNT bond length does not change significantly when graphene covers it, about 58% of all the bonds are compressed (by $\sim -0.1\%$) and 42% are stretched (by $\sim 0.07\%$) compared to the bond lengths of the SWCNT on SiO₂ without graphene covering it. Assuming the positive and negative bond strain have an opposite effect on the peak positions of the SWCNT one can expect to see an inhomogeneous broadening of the RBM and G-peaks of the SWCNT when covered by the graphene. This is confirmed by the Raman data. Figure 4.8c and d show that the FWHM for both the RBM and G⁻ peak of the SWCNT increase by 27.7% (3.6 \pm 0.3 to 4.6 \pm 0.5 cm⁻¹) and 38.5% (13 \pm 1 to 18 \pm 1 cm⁻¹) respectively. The FWHM of the bond length distribution increases by 14.45% when the SWCNT is covered by graphene, indicating that the strain and compression in the graphene-covered SWCNT is largely responsible for the observed inhomogeneous broadening of its Raman peaks. It should be noted that Farhat *et al.* did not notice any significant change of the FWHM of the SWCNT RBM and G-peaks upon doping [38,39].

Graphene straining tends to downshift both its G peak and its 2D peak [65]. Mohiuddin *et al.* observe experimentally that applying less than 0.05% of uniaxial strain to SLG causes a downshift of the 2D peak position of $\sim 3 cm^{-1}$ [65], in agreement with the

trend we observe (Fig. 4.4b). However this is accompanied by a decrease of the G-peak position of $\sim 5\text{cm}^{-1}$, whereas we observe an increase of $\sim 10\text{cm}^{-1}$ (Fig. 4.4a). Our observations of the effect of the m-SWCNT on graphene can thus not be explained by strain. Moreover it would be surprising that graphene would be strained by a feature that is only 1.35nm high; our MD simulations confirm that it is not (Figure 4.10; Table 4.2). The bond length distribution of graphene at the junction and far away from the junction barely changes. Finally, it is interesting to note that the persistence length of graphene at 300K is calculated to be 5.5 nm [66].





(c)

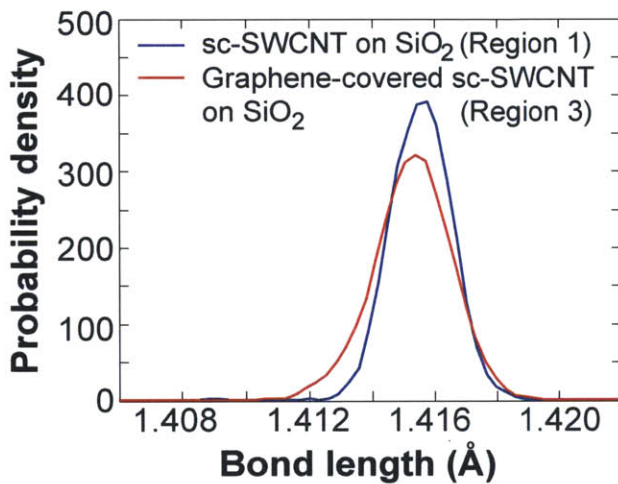
Figure 4.10. Influence of strain on the graphene, caused by the underlying m-SWCNT. (a),(b) Molecular representation of the SWCNT-graphene junction. (a) Graphene that is unaffected by the SWCNT (atoms further than 3nm away from the m-SWCNT) is highlighted in black. (b) Graphene that covers the m-SWCNT (atoms within 1.8nm of the m-SWCNT) is highlighted in black. (c) Distribution of bond lengths of graphene.

	Graphene on top of the SiO ₂ (Å)	Graphene on top of the m-SWCNT (Å)	Relative change (%)
Average	1.41454 +/- 0.00002	1.41484 +/- 0.00002	+0.02
Median	1.41476 +/- 0.00002	1.41492 +/- 0.00002	+0.01
FWHM	0.00112 +/- 0.00015	0.00115 +/- 0.00017	+2.39

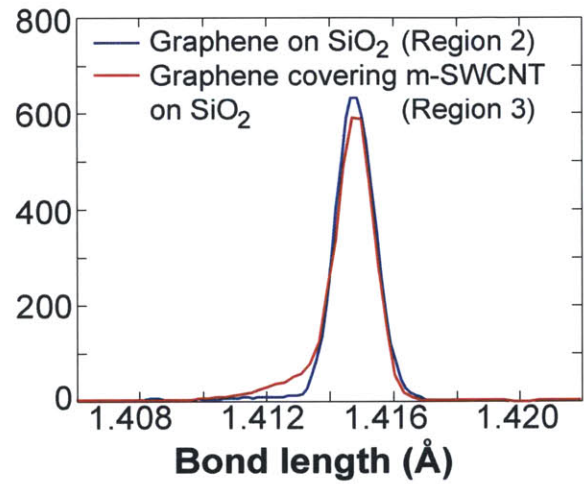
Table 4.2. Key parameters of the bond length distribution of the graphene in our system (with 95% confidence intervals).

In an analogous way the effects of strain at the sc-SWCNT/graphene junction were analyzed. Key results are summarized in Figure 4.11. The results of the MD-simulation (Fig. 4.11a) show that the average bond length of the (18,7) sc-SWCNT only changes by 0.018%, not enough to explain any doping effects.

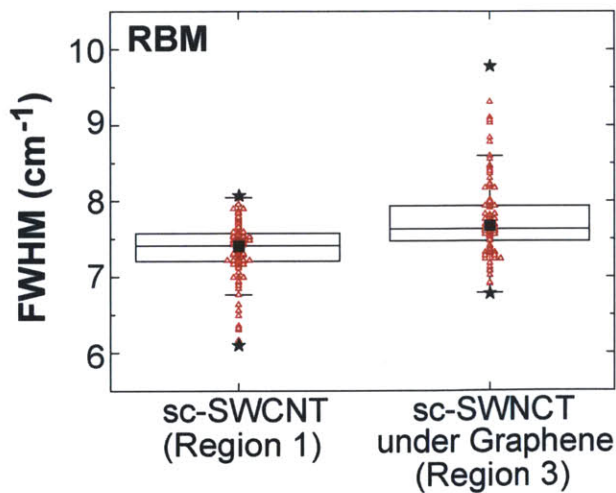
On the other hand, the full-width-half-max of the distribution increases by 23.9% when graphene is covering the sc-SWCNT, again suggesting inhomogeneous broadening of the SWCNT's Raman peaks when covered by graphene (Region 3), which is in effect observed (Fig. 4.11c,d). The MD also shows that graphene's bond lengths are scarcely affected by the presence of this sc-SWCNT with a shift in bond length of 0.004% and a broadening of the bond length distribution of 0.004%.



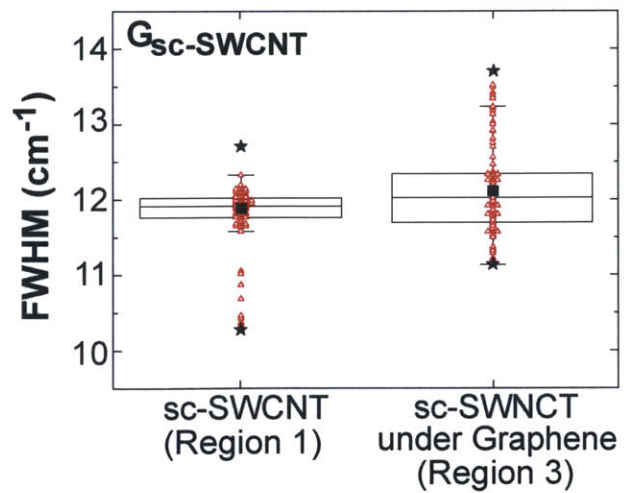
(a)



(b)



(c)



(d)

Figure 4.11. Influence of strain at the sc-SWCNT/graphene junction. **(a)** Distribution of bond lengths in sc-SWCNT in Region 1 (not covered by graphene) and Region 3 (at the junction). **(b)** Distribution of bond lengths in graphene in Region 2 (far away from the junction) and Region 3 (at the junction). **(c)** Comparison of FWHM of the sc-SWCNT's RBM in Region 1 and Region 3; $p < 0.01$ (see Chapter 4.2.4). **(d)** Comparison of FWHM of the sc-SWCNT's G peak in Region 1 and Region 3; $p < 0.01$ (see Chapter 4.2.4). The lower and higher ends of the boxplots represent the 25 and 75 percentile marks of the distributions respectively, and the middle line is the median value. Minimum and maximum values are represented by black stars, and the average is the black square. The red triangles in Figure 4.11 **(c),(d)** represent the complete dataset superimposed on the boxplots.

4.4. Conclusions

We have created a junction between SWCNTs and a single layer of graphene, both synthesized via CVD, and we have explored the electronic interactions between them. Raman spectroscopy in different regions of the sample allows for direct comparison between the spectra of graphene and SWCNT individually with the spectra of the SWCNT and the graphene when graphene covers the SWCNT. The G peak position of the graphene upshifts when it covers the SWCNT, a sign of charge transfer (doping), whereas its 2D peak position downshifts, which indicates it is being doped with electrons (n-type doping). A lower 2D/G intensity ratio confirms the trend. The RBM and G peak positions of the SWCNT increase when it is covered by the graphene, again a sign of charge transfer. Based on this analysis it seems the SWCNT is being more p-doped under the graphene, and thus n-doping the graphene. We calculate that a minimum electron density of $\sim 334 \mu\text{m}^{-1}$ is transferred from the SWCNT to the graphene. For the m-SWCNT/graphene junction, we deduce (based on the analysis of the G-peak upshift of the graphene) that graphene receives $1.12 \times 10^{13} \text{ cm}^{-2}$ electrons at the junction. For the sc-

SWCNT/graphene junction this value $3.25 \times 10^{12} \text{ cm}^{-2}$. The direction and magnitude of this transfer is in line with the work functions of the materials involved. With the help of a molecular dynamics simulation we deduce the effect of strain and radial compression on the Raman peak positions is limited and conclude that the Raman spectroscopic data are evidence that the m-SWCNT is donating electrons to the graphene.

4.5. Ongoing work

It was shown that graphene can be doped with nanometer precision, which allows for several possible applications. Specifically, a m-SWCNT covered with a thin dielectric layer can be used to locally gate graphene, allowing for short-channel transistors. This has been achieved with metallic nanowire/graphene junctions, achieving channel lengths as low as 140nm [67]. This value can be significantly reduced by replacing the nanowire with a m-SWCNT. Moreover, locally gating the graphene means locally changing its Fermi energy. As has been shown in ref. [20] a higher Fermi energy can increase the rate of graphene functionalization. The ability to spatially control and alter graphene's Fermi level and thus its reactivity and surface chemistry is important for biological applications such as microarrays, biosensors and tissue engineering. Graphene surface functionalization will be discussed in more detail in Chapter 5.

In the case of the sc-SWCNT/graphene junction, the potential barrier between both causes a Schottky diode to form at the interface. Upon photo-excitation of the semiconducting SWCNT, the excitons generated in the SWCNT can immediately dissociate at the (semi-)metallic graphene that is directly in contact with the SWCNT. This implies that the excitons don't have to diffuse along the length of the SWCNT

before reaching an electrode where they can dissociate at, which considerably reduces the chances of exciton recombination. In order to achieve this, we plan to create sc-SWCNT/graphene junctions on a transparent (quartz) substrate, and illuminate the sc-SWCNT from below with a laser in the 500-800nm range (the typical range for E_{22} SWCNT excitation, as discussed in Chapter 2.1). While one side of the SWCNTs is covered by a gold electrode, the circuit is closed by the conducting tip of a (home-built) photo-conducting AFM setup, which can be used to scan along the length of the sc-SWCNT/graphene junction and locally detect the generated photocurrent.

4.6. References

- 1 Paulus, G. L. C., Wang, Q. H., Ulissi, Z. W., McNicholas, T. P., Vijayaraghavan, A., Shih, C. J., Jin, Z. & Strano, M. S. Charge transfer at junctions of a single layer of graphene and a metallic single walled carbon nanotube. *Small* doi: 10.1002/sml.201201034 (2012).
- 2 Novoselov, K., Geim, A., Morozov, S., Jiang, D., Grigorieva, M. I. K. I. V., Dubonos, S. & Firsov, A. Two-dimensional gas of massless Dirac fermions in graphene. *Nature* **438**, 197-200 (2005).
- 3 Geim, A. K. & Novoselov, K. S. The rise of graphene. *Nature Materials* **6**, 183-191 (2007).
- 4 Geim, A. K. Graphene: status and prospects. *Science* **324**, 1530-1534 (2009).
- 5 Odom, T. W., Huang, J. L., Kim, P. & Lieber, C. M. Atomic structure and electronic properties of single-walled carbon nanotubes. *Nature* **391**, 62-64 (1998).
- 6 Dresselhaus, M. S., Dresselhaus, G. & Eklund, P. *Science of fullerenes and carbon nanotubes*. (Academic Pr, 1996).
- 7 Saito, R., Dresselhaus, G. & Dresselhaus, M. S. *Physical properties of carbon nanotubes*. Vol. 3 (Imperial College Press London, 1998).
- 8 Yao, Z., Dekker, C. & Avouris, P. Electrical transport through single-wall carbon nanotubes. *Carbon Nanotubes*, 147-171 (2001).
- 9 Cao, H., Yu, Q., Jauregui, L. A., Tian, J., Wu, W., Liu, Z., Jalilian, R., Benjamin, D. K., Jiang, Z. & Bao, J. Electronic transport in chemical vapor deposited graphene synthesized on Cu: Quantum Hall effect and weak localization. *Applied Physics Letters* **96**, 122106-1:3 (2010).
- 10 Charlier, J. C., Blase, X. & Roche, S. Electronic and transport properties of nanotubes. *Reviews of Modern Physics* **79**, 677-732 (2007).
- 11 Neto, A. H. C., Guinea, F., Peres, N., Novoselov, K. & Geim, A. The electronic properties of graphene. *Reviews of Modern Physics* **81**, 109-162 (2009).
- 12 Paulson, S., Helsler, A., Nardelli, M. B., Taylor, R., Falvo, M., Superfine, R. & Washburn, S. Tunable resistance of a carbon nanotube-graphite interface. *Science* **290**, 1742-1744 (2000).
- 13 Pei, T., Xu, H., Zhang, Z., Wang, Z., Liu, Y., Li, Y., Wang, S. & Peng, L. M. Electronic transport in single-walled carbon nanotube/graphene junction. *Applied Physics Letters* **99**, 113102-1:3 (2011).
- 14 Yu, T., Kim, C., Liang, C. W. & Yu, B. Formation of Graphene pn Junction via Complementary Doping. *Electron Device Letters, IEEE* **32**, 1050-1052 (2011).
- 15 Lin, Y. C., Lin, C. Y. & Chiu, P. W. Controllable graphene N-doping with ammonia plasma. *Applied Physics Letters* **96**, 133110-1:3 (2010).
- 16 Liu, H., Liu, Y. & Zhu, D. Chemical doping of graphene. *J. Mater. Chem.* **21**, 3335-3345 (2011).
- 17 Wehling, T., Novoselov, K., Morozov, S., Vdovin, E., Katsnelson, M., Geim, A. & Lichtenstein, A. Molecular doping of graphene. *Nano Letters* **8**, 173-177 (2008).
- 18 Panchakarla, L., Subrahmanyam, K., Saha, S., Govindaraj, A., Krishnamurthy, H., Waghmare, U. & Rao, C. Synthesis, structure, and properties of boron-and nitrogen-doped graphene. *Advanced Materials* **21**, 4726-4730 (2009).
- 19 Gierz, I., Riedl, C., Starke, U., Ast, C. R. & Kern, K. Atomic Hole Doping of Graphene. *Nano Letters* **8**, 4603-4607 (2008).

- 20 Wang, Q. H., Jin, Z., Kim, K. K., Hilmer, A. J., Paulus, G. L. C., Shih, C. J., Ham, M. H., Sanchez-Yamagishi, J. D., Watanabe, K., Taniguchi, T., Kong, J., P., J.-H. & Strano, M. S. Understanding and controlling the substrate effect on graphene electron-transfer chemistry via reactivity imprint lithography. *Nature Chemistry* **4**, 724-732 (2012).
- 21 Lu, C., Fu, Q., Huang, S. & Liu, J. Polymer electrolyte-gated carbon nanotube field-effect transistor. *Nano Letters* **4**, 623-627 (2004).
- 22 Phillips, J. C., Braun, R., Wang, W., Gumbart, J., Tajkhorshid, E., Villa, E., Chipot, C., Skeel, R. D., Kale, L. & Schulten, K. Scalable molecular dynamics with NAMD. *Journal of computational chemistry* **26**, 1781-1802 (2005).
- 23 MacKerell, A. D., Bashford, D., Bellott, Dunbrack, R. L., Evanseck, J. D., Field, M. J., Fischer, S., Gao, J., Guo, H., Ha, S., Joseph-McCarthy, D., Kuchnir, L., Kuczera, K., Lau, F. T. K., Mattos, C., Michnick, S., Ngo, T., Nguyen, D. T., Prodhom, B., Reiher, W. E., Roux, B., Schlenkrich, M., Smith, J. C., Stote, R., Straub, J., Watanabe, M., Wiórkiewicz-Kuczera, J., Yin, D. & Karplus, M. All-Atom Empirical Potential for Molecular Modeling and Dynamics Studies of Proteins. *The Journal of Physical Chemistry B* **102**, 3586-3616 (1998).
- 24 Humphrey, W., Dalke, A. & Schulten, K. VMD: visual molecular dynamics. *Journal of molecular graphics* **14**, 33-38 (1996).
- 25 Dresselhaus, M. S., Dresselhaus, G., Saito, R. & Jorio, A. Raman spectroscopy of carbon nanotubes. *Physics Reports* **409**, 47-99 (2005).
- 26 Araujo, P., Maciel, I., Pesce, P., Pimenta, M., Doorn, S., Qian, H., Hartschuh, A., Steiner, M., Grigorian, L. & Hata, K. Nature of the constant factor in the relation between radial breathing mode frequency and tube diameter for single-wall carbon nanotubes. *Physical Review B* **77**, 241403-1:4 (2008).
- 27 Jorio, A., Araujo, P. T., Doorn, S. K., Maruyama, S., Chacham, H. & Pimenta, M. A. The Kataura plot over broad energy and diameter ranges. *physica status solidi (b)* **243**, 3117-3121 (2006).
- 28 Ferrari, A., Meyer, J., Scardaci, V., Casiraghi, C., Lazzeri, M., Mauri, F., Piscanec, S., Jiang, D., Novoselov, K. & Roth, S. Raman spectrum of graphene and graphene layers. *Physical Review Letters* **97**, 187401-1:4 (2006).
- 29 Ferrari, A. C. Raman spectroscopy of graphene and graphite: Disorder, electron-phonon coupling, doping and nonadiabatic effects. *Solid State Communications* **143**, 47-57 (2007).
- 30 Duesberg, G., Loa, I., Burghard, M., Syassen, K. & Roth, S. Polarized Raman spectroscopy on isolated single-wall carbon nanotubes. *Physical Review Letters* **85**, 5436-5439 (2000).
- 31 Jorio, A., Souza Filho, A., Brar, V., Swan, A., Ünlü, M., Goldberg, B., Righi, A., Hafner, J., Lieber, C. & Saito, R. Polarized resonant Raman study of isolated single-wall carbon nanotubes: Symmetry selection rules, dipolar and multipolar antenna effects. *Physical Review B* **65**, 121402-1:4 (2002).
- 32 Hwang, J., Gommans, H., Ugawa, A., Tashiro, H., Haggemueller, R., Winey, K. I., Fischer, J. E., Tanner, D. & Rinzler, A. Polarized spectroscopy of aligned single-wall carbon nanotubes. *Physical Review B* **62**, 13310-13313 (2000).
- 33 Das, A., Pisana, S., Chakraborty, B., Piscanec, S., Saha, S., Waghmare, U., Novoselov, K., Krishnamurthy, H., Geim, A. & Ferrari, A. Monitoring dopants by Raman scattering in an electrochemically top-gated graphene transistor. *Nature Nanotechnology* **3**, 210-215 (2008).

- 34 Basko, D., Piscanec, S. & Ferrari, A. Electron-electron interactions and doping dependence of the two-phonon Raman intensity in graphene. *Physical Review B* **80**, 233407-1:3 (2009).
- 35 Casiraghi, C., Pisana, S., Novoselov, K., Geim, A. & Ferrari, A. Raman fingerprint of charged impurities in graphene. *Applied Physics Letters* **91**, 233108-1:3 (2007).
- 36 Casiraghi, C. Doping dependence of the Raman peaks intensity of graphene close to the Dirac point. *Physical Review B* **80**, 233407-1:3 (2009).
- 37 Pisana, S., Lazzeri, M., Casiraghi, C., Novoselov, K. S., Geim, A. K., Ferrari, A. C. & Mauri, F. Breakdown of the adiabatic Born-Oppenheimer approximation in graphene. *Nature Materials* **6**, 198-201 (2007).
- 38 Farhat, H., Sasaki, K., Kalbáč, M., Hofmann, M., Saito, R., Dresselhaus, M. S. & Kong, J. Softening of the radial breathing mode in metallic carbon nanotubes. *Physical Review Letters* **102**, 126804-1:4 (2009).
- 39 Farhat, H., Son, H., Samsonidze, G. G., Reich, S., Dresselhaus, M. & Kong, J. Phonon softening in individual metallic carbon nanotubes due to the Kohn anomaly. *Physical Review Letters* **99**, 145506-1:4 (2007).
- 40 Kavan, L., Kalbáč, M., Zukařová, M. & Dunsch, L. Electrochemical doping of chirality-resolved carbon nanotubes. *The Journal of Physical Chemistry B* **109**, 19613-19619 (2005).
- 41 Nguyen, K. T., Gaur, A. & Shim, M. Fano lineshape and phonon softening in single isolated metallic carbon nanotubes. *Physical Review Letters* **98**, 145504-1:4 (2007).
- 42 Hartman, A. Z., Jouzi, M., Barnett, R. L. & Xu, J. M. Theoretical and Experimental Studies of Carbon Nanotube Electromechanical Coupling. *Physical Review Letters* **92**, 236804-1:4 (2004).
- 43 Stoll, M., Rafailov, P., Frenzel, W. & Thomsen, C. Electrochemical and Raman measurements on single-walled carbon nanotubes. *Chemical Physics Letters* **375**, 625-631 (2003).
- 44 Barone, V., Peralta, J. E., Uddin, J. & Scuseria, G. E. Screened exchange hybrid density-functional study of the work function of pristine and doped single-walled carbon nanotubes. *The Journal of chemical physics* **124**, 024709-1:5 (2006).
- 45 Boyd, R. H. The dielectric constant of lamellar semicrystalline polymers. *Journal of Polymer Science: Polymer Physics Edition* **21**, 505-514 (1983).
- 46 Wunnicke, O. Gate capacitance of back-gated nanowire field-effect transistors. *Applied Physics Letters* **89**, 083102-1:3 (2006).
- 47 Xia, J., Chen, F., Li, J. & Tao, N. Measurement of the quantum capacitance of graphene. *Nature Nanotechnology* **4**, 505-509 (2009).
- 48 John, D., Castro, L. & Pulfrey, D. Quantum capacitance in nanoscale device modeling. *Journal of applied physics* **96**, 5180-5184 (2004).
- 49 Burke, P. An RF circuit model for carbon nanotubes. *IEEE Transactions on Nanotechnology* **1** 393-396 (2003).
- 50 McEuen, P. L., Fuhrer, M. S. & Park, H. Single-walled carbon nanotube electronics. *IEEE Transactions on Nanotechnology* **1**, 78-85 (2002).
- 51 Kang, Y. J., Kang, J. & Chang, K. Electronic structure of graphene and doping effect on SiO₂. *Physical Review B* **78**, 115404-1:5 (2008).
- 52 He, K. T., Wood, J. D., Doidge, G. P., Pop, E. & Lyding, J. W. Scanning Tunneling Microscopy Study and Nanomanipulation of Graphene-Coated Water on Mica. *Nano Letters* **12**, 2665-2672 (2012).

- 53 Cao, P., Varghese, J. O., Xu, K. & Heath, J. R. Visualizing local doping effects of individual water clusters on gold (111)-supported graphene. *Nano Letters* **12**, 1459-1463 (2012).
- 54 Kim, K., Coh, S., Tan, L. Z., Regan, W., Yuk, J. M., Chatterjee, E., Crommie, M. F., Cohen, M. L., Louie, S. G. & Zettl, A. Raman Spectroscopy Study of Rotated Double-Layer Graphene: Misorientation-Angle Dependence of Electronic Structure. *Physical Review Letters* **108**, 246103-1:6 (2012).
- 55 Ni, Z., Wang, Y., Yu, T., You, Y. & Shen, Z. Reduction of Fermi velocity in folded graphene observed by resonance Raman spectroscopy. *Physical Review B* **77**, 235403-1:5 (2008).
- 56 Kim, K., Lee, Z., Malone, B. D., Chan, K. T., Alemán, B. n., Regan, W., Gannett, W., Crommie, M. F., Cohen, M. L. & Zettl, A. Multiply folded graphene. *Physical Review B* **83**, 245433-1:8 (2011).
- 57 Zheng, M., Zou, L., Wang, H., Park, C. & Ke, C. Engineering Radial Deformations in Single-Walled Carbon and Boron Nitride Nanotubes Using Ultrathin Nanomembranes. *Acs Nano* **6**, 1814-1822 (2012).
- 58 Yang, W., Wang, R. Z. & Yan, H. Strain-induced Raman-mode shift in single-wall carbon nanotubes: Calculation of force constants from molecular-dynamics simulations. *Physical Review B* **77**, 195440-1:5 (2008).
- 59 Cronin, S., Swan, A., Ünlü, M., Goldberg, B., Dresselhaus, M. & Tinkham, M. Resonant Raman spectroscopy of individual metallic and semiconducting single-wall carbon nanotubes under uniaxial strain. *Physical Review B* **72**, 035425-1:8 (2005).
- 60 Venkateswaran, U., Rao, A., Richter, E., Menon, M., Rinzler, A., Smalley, R. & Eklund, P. Probing the single-wall carbon nanotube bundle: Raman scattering under high pressure. *Physical Review B* **59**, 10928-10934 (1999).
- 61 Loa, I. Raman spectroscopy on carbon nanotubes at high pressure. *Journal of Raman Spectroscopy* **34**, 611-627 (2003).
- 62 Patra, N., Wang, B. & Král, P. Nanodroplet activated and guided folding of graphene nanostructures. *Nano Letters* **9**, 3766-3771 (2009).
- 63 Bellido, E. P. & Seminario, J. M. Molecular dynamics simulations of folding of supported graphene. *The Journal of Physical Chemistry C* **114**, 22472-22477 (2010).
- 64 Patra, N., Song, Y. & Král, P. Self-Assembly of Graphene Nanostructures on Nanotubes. *ACS Nano* **5**, 1798-1804 (2011).
- 65 Mohiuddin, T., Lombardo, A., Nair, R., Bonetti, A., Savini, G., Jalil, R., Bonini, N., Basko, D., Galiotis, C. & Marzari, N. Uniaxial strain in graphene by Raman spectroscopy: G peak splitting, Grüneisen parameters, and sample orientation. *Physical Review B* **79**, 205433-1:8 (2009).
- 66 Neek-Amal, M., Asgari, R. & Rahimi Tabar, M. R. The formation of atomic nanoclusters on garphene sheets. *Nanotechnology* **20**, 135602-1:8 (2009).
- 67 Liao, L., Lin, Y.-C., Bao, M., Cheng, R., Bai, J., Liu, Y., Qu, Y., Wang, K. L., Huang, Y. & Duan, X. High-speed graphene transistors with a self-aligned nanowire gate. *Nature* **467**, 305-308 (2010).

5. Study and manipulation of covalent electron transfer chemistry of graphene with diazonium salts

Some of the work, text and figures presented in this chapter are reprinted or adapted with permission from reference [1,3] (Copyright © 2013, American Chemical Society), and references [2,4].

5.1. Background and motivation

From a chemist's perspective, graphene can be regarded as a very large polycyclic aromatic molecule or as a material that is purely a surface without a bulk contribution. Consequently, chemistries that have been used both with organic molecules and with surfaces have been used as starting points for chemically functionalizing and modifying graphene [5]. While pristine graphene exhibits many desirable properties, chemical modification allows these properties to be tuned and allows graphene to interact with other materials. The motivations for studying the chemical functionalization of graphene include changing the doping levels [6], opening a band gap in the electronic structure [7,8], charge storage [9], chemical and biological sensing [10-12], integration with dielectric layers [13-15], making new composite materials [16], and scale-up of solution-processable graphene [17-19].

Covalent functionalization schemes that directly form bonds to the graphene lattice include oxidation [20], hydrogenation [21,22], fluorination [23], diazonium grafting [18,24-29], and a variety of organic additions [30,31]. These functionalization

schemes tend to be more robust compared to non-covalent ones, but change the graphene electronic properties more strongly due to the disruption of the crystallographic ordering within the graphene lattice. Non-covalent functionalization schemes that preserve the graphene lattice include π - π stacking of physisorbed aromatic molecules [13,15,32], physisorption of surfactants in solution [17,19], and encapsulation in polymer matrices [16]. The π -orbitals in graphene are delocalized throughout the structure such that all conjugated chemical bonds are equivalent. The stability of the extended delocalized π -system ensures the basal plane of graphene is fairly chemically stable. It is therefore not surprising a lot of work on graphene functionalization has been accomplished using highly reactive aryl radicals.

In this Chapter I discuss the covalent functionalization of monolayer graphene with aryl diazonium salts, which react via an electron transfer mechanism. The focus of this work is limited to relatively pristine graphene over graphite or graphene oxide, because free electrons in the latter are already bound in oxygen-containing functionalities that decorate the lattice, and the resulting chemistry is dominated by localized reactivity and defects. Additionally, the focus is limited to electron transfer chemistries because these reactions are sensitive toward differences in Fermi energy (E_F), density of states (DOS), and electrostatic environment. I analyze the effect of reaction conditions (such as degree of functionalization and the effect of the end-group of the diazonium salt) on the Raman signal of graphene as well as on its field effect transistor (FET) performance. Finally I describe charge-transfer curves with a model that takes into account both long-range and short-range scatterers.

5.1.1. Overview of typical experimental conditions

Diazonium salts with different functional groups have been successfully grafted to graphene, e.g. 4-nitrobenzene diazonium tetrafluoroborate (4-NBD) [2,25,27,29,33-36], 4-bromobenzene tetrafluoroborate (4-BBD) [2,26,37], 4-propargyloxybenzene diazonium tetrafluoroborate (4-PBD) [2,38], and 4-tert-butylphenyldiazonium tetrafluoroborate (4-TBD) [18]. In a typical reaction the graphene sample is submerged in 4-25 mM acetonitrile or aqueous solution and is reacted while stirring for 1-16 hours at temperatures between 25 and 45°C. In some cases 0.5-1% of sodium dodecyl sulfate (SDS) is added; the role of the surfactant is to bring the hydrophilic cationic diazonium salts in closer proximity of the hydrophobic graphene [2,25,29,34,36,38]. A higher concentration of the salt, longer reaction times and higher temperatures will increase the degree of reaction.

Covalent attachment can be verified by means of a variety of techniques such as Raman spectroscopy [2,25,26,33,36,37,39,40], scanning tunneling microscopy and spectroscopy (STM/STS) [27], cyclic voltammetry (CV) [35], X-ray photoelectron spectroscopy (XPS) [34][35,37], Fourier transform infrared spectroscopy (FTIR) [35] and attenuated total reflectance infrared spectroscopy (ATR-IR) [38].

5.1.2. Reaction mechanism: theoretical predictions and experimental findings

The most common reaction mechanism of covalent functionalization with aryl diazonium salts is illustrated in Figure 5.1. A delocalized electron is transferred from the graphene to the aryl diazonium cation, which becomes an aryl radical after releasing a

molecule of N_2 . The aryl radical then forms a covalent bond with a carbon atom in the graphene lattice, changing its hybridization to sp^3 and displacing it out of the plane by $\sim 0.7 \text{ \AA}$ [41]. The attachment of a phenyl group results in a delocalized, unpaired electron. Density functional theory (DFT) calculations have shown that a second aryl group preferentially attacks at the para-position of the same graphene ring, i.e. on a different sublattice (see Fig. 5.1). This is known as (1,4)-functionalization [41].

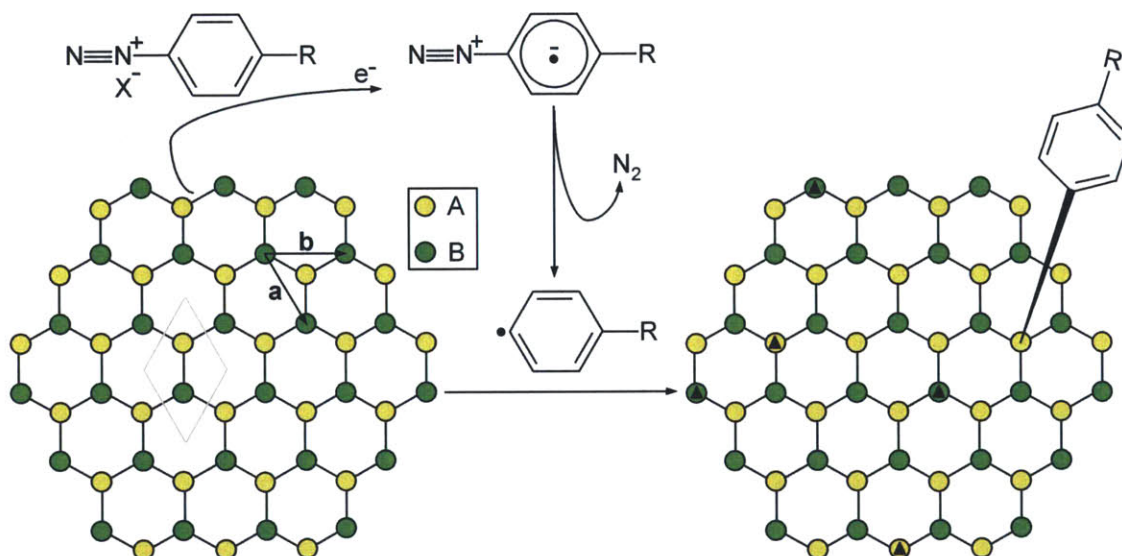


Figure 5.1. Schematic illustration of grafting of a diazonium salt with functional group R and counterion X to the graphene lattice. Commonly X is the tetrafluoroborate ion BF_4^- and R can be a variety of moieties such as a hydrogen atom or a nitro, a bromo, a propargyloxy or a tert-butyl group. Two carbon atoms (in the A and B sublattices) make up the unit cell (grey diamond) of the graphene sheet (with lattice vectors \mathbf{a} and \mathbf{b}). In the typical reaction mechanism for covalent functionalization of graphene, the diazonium salt is reduced by the graphene, releases a molecule of N_2 and becomes an aryl radical, which subsequently attacks the graphene locally. Subsequent thermodynamically favored addition positions are shown with black triangles. Thermodynamically favored lattice positions for further functionalization are marked with black triangles.

Pairwise additions in the A and B sublattices are thermodynamically favorable, and for small adsorbates such as hydrogen atoms, the theoretical maximum coverage is 25% [42]. In graphene there are about 38 carbon atoms/ nm^2 , which implies a theoretical

maximum areal concentration of $\sim 9 \times 10^{14}/\text{cm}^2$. However for phenyl groups, Jiang *et al.* calculate a maximum packing of only 11% coverage ($\sim 4 \times 10^{14}/\text{cm}^2$), attributed to steric hindrance, still in a (1,4)-configuration [41]. These theoretical simulations predicting long-range ordering are based on the thermodynamics of the reaction. However, since the aryl radical is so reactive, the activation energy for the reaction is very low and the reaction is likely dominated by kinetics rather than thermodynamics, preventing any long-range ordering [7]. Quite surprisingly there does exist some experimental evidence of long-range ordering in selected area electron diffraction pattern (SAED) data of the reacted graphene [40], although the observed pattern deviates from the theoretically predicted (1,4)-functionalization. It is very likely that the reaction conditions determine whether one operates in the thermodynamic or the kinetic regime.

Experimentally, different concentrations of covalently bound species have been reported: 25% by using CV [35], 12.5% by SAED [40], 5% by STM/STS [27], 13% and 1.2% by a thermogravimetric analysis coupled to mass spectroscopy (TGA/MS) [18], and 0.3% based on Raman spectroscopy [36]. Rather than concluding these results are contradictory, I argue that the reported values strongly depend on the reaction conditions and the conditions at which the measurements are taken.

Under some reaction conditions, physisorption of aryl molecules is promoted rather than (or in addition to) chemisorption. Englert and coworkers [18] show with TGA/MS that 4-TBD functionalized graphene loses mass in two steps: at $\sim 210^\circ\text{C}$ attributed to the desorption of physisorbed molecules, and at $\sim 480^\circ\text{C}$ due to cleavage of the covalently bound molecules [18]. Hossain *et al.* report STM images of epitaxial graphene functionalized with 4-NBD showing chain-like features, suggestive of aryl

oligomers [27]. It is assumed the physisorbed portion of the oligomers physically inhibits further covalent attachment [27]. Atomic force microscopy (AFM) measurements also suggest multilayer formation [33,40].

The degree of chemi- vs. physisorption strongly depends on the reaction conditions. Farmer *et al.* use milder reactions conditions than most others (1 mM of 4-BBD in a 1:1 mixture of water and methanol for 2 hours at room temperature) and do not observe a significant increase of the D peak in their Raman spectra, but do observe other Raman changes indicative of doping via physisorption [26]. Koehler *et al.* explicitly demonstrate how Raman spectroscopy can distinguish between physi- and chemisorption by exposing SLG to a concentrated 4-NBD solution (ensuring chemisorption) as well as to pure nitrobenzene, which lacks the diazonium group for covalent attachment (thereby ensuring physisorption) [33]. In the first case, they observe a strongly increased value of the D to G integrated peak intensity ratio (I_D/I_G), whereas for the latter case they detect an upshift of the G-peak position and a decrease of the 2D/G intensity ratio (I_{2D}/I_G), both indicative of doping [43]. Under many reaction conditions, a combination of both covalent binding or chemisorption (increased I_D/I_G) and non-covalent doping or physisorption (shifts in the G and 2D peak, as well as an increased I_{2D}/I_G) is present [2,36].

5.1.3. Rate of covalent attachment

The rate-limiting step in the reaction of diazonium salts with graphene is the reduction of the diazonium salt by graphene to form the aryl radical. The reaction rate constant is determined from Gerisher-Marcus theory of electron transfer reactions at

electrodes [44], and has been applied by our group to describe diazonium functionalization of single-walled carbon nanotubes (SWCNTs) [45] and graphene [29,36,39]. The rate is determined by the overlap between the electronic density of states (DOS) of the graphene and the diazonium reactants in solution, as illustrated in Figure 6.2. Electron transfer occurs between any occupied state of the graphene that is matched in energy with an unoccupied state of the diazonium. The electron transfer rate constant, k_{ET} , is:

$$k_{ET} = \nu \int_{E_{redox}}^{E_{F,G}} \varepsilon_{red}(E) DOS_G(E) W_{ox}(\lambda, E) dE \quad (5.1),$$

where

$$W_{ox}(\lambda, E) = \frac{1}{\sqrt{4\pi\lambda kT}} \exp\left(-\frac{(E-(E_{redox}+\lambda))^2}{4\lambda kT}\right) \quad (5.2)$$

is the probability density function of vacant states in the diazonium molecule, ν is the electron-transfer frequency, ε_{red} a proportionality factor and DOS_G the density of states of graphene. λ is the energy difference between the standard potential for the redox couple of the diazonium salt (E_{redox}) and the energy for maximum probability of finding a vacant state in the diazonium, and has a value of 0.5–1 eV [44]. E_F is the Fermi energy (-4.6 eV for undoped graphene) [46], k is the Boltzmann constant and T absolute temperature.

The redox potential for different diazonium salts can be determined via polarography: with respect to vacuum, $E_{redox,4-NBD} = -5.15\text{eV}$ and $E_{redox,4-BBD} = -5.08\text{ eV}$ [45,47]. The redox potential for 4-PBD has not yet been reported, since it is not commercially available, but rather synthesized in our own laboratory. However, its structure is similar to that of the 4-methoxybenzene diazonium salt, with a reported value

of $E_{redox,4-MBD} = -4.87\text{eV}$ [45,47]. Based on Equations (5.1),(5.2) and Figure 5.2 we thus expect a lower reaction rate for 4-PBD compared to 4-NBD and 4-BBD.

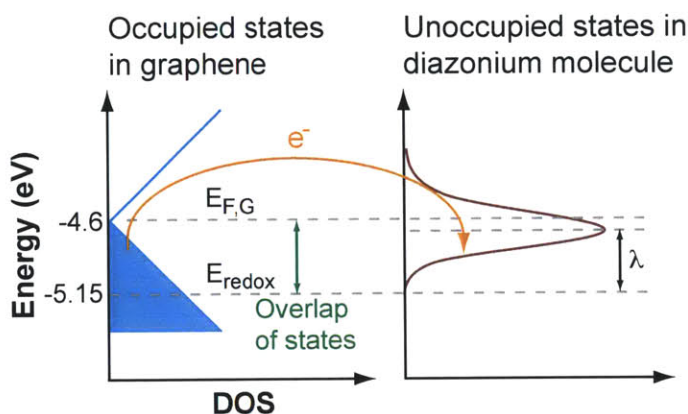


Figure 5.2. Schematic representation of the $DOS(E)$ of graphene and the unoccupied $DOS(E)$ of a typical diazonium salt. Electron transfer can occur at energies when there is overlap between the $DOS(E)$ of graphene and the unoccupied $DOS(E)$ of the diazonium salt. $E_{F,G}$ represents the graphene Fermi energy, E_{redox} is the standard potential of the redox couple of the diazonium salt and λ is the energy between E_{redox} and the energy for maximum probability of finding a vacant state in the diazonium molecule.

Because electron transfer chemistries depend on the Fermi energy of graphene and the density of states of the reagents, the resulting reaction rate depends on the number of graphene layers, edge states, defects, grain boundaries, the underlying substrate and the electrostatic environment. The interested reader is referred to reference [1] in which the effect of the above items on graphene chemistry is reviewed.

5.2. Materials and Methods

5.2.1. Graphene synthesis and transfer

Single layer graphene was synthesized via chemical vapor deposition (following the procedure described in Chapter 4.2.2.) or otherwise obtained directly from a highly-

ordered pyrolytic graphite (HOPG) source via a micromechanical cleavage process described in ref. [48]; the former will be described as CVD graphene, and the latter as exfoliated graphene. In both cases the monolayer graphene is transferred on a SiO₂/Si (300nm of SiO₂) wafer.

5.2.2. Raman spectroscopy and mapping

Raman spectroscopy was performed on a Horiba Jobin Yvon LabRAM HR800 system with a 633nm excitation laser and a 100X objective, following the procedures described in Chapter 4.2.3.

5.2.3. Graphene FET design

Source and drain contact electrodes were deposited onto both sides of a graphene flake on SiO₂/Si substrate using photolithography followed by e-beam evaporation of Ti/Au. Devices were tested at 14K and 10⁻⁷ mbar in a cryogenic probe station (Advanced Research Systems Inc.), using a semiconductor parameter analyzer by Agilent Technologies (model E5270B). Specifically, the source-drain current I_{DS} is measured under a constant source-drain voltage $V_{DS} = 0.1V$ and while sweeping the back-gate voltage V_{BG} from -35 to +35V.

5.2.4. Graphene functionalization

To controllably study the effect of increasing degree of functionalization on the (exfoliated) monolayer graphene Raman signal and its charge transport characteristics, a

new efficient functionalization method was developed [3]. Specifically, the samples are functionalized electrochemically in an acetonitrile solution with 20mM 4-NBD. With the source and drain electrodes of the graphene FET grounded, a positive voltage (V_{RXN}) is applied to the solution for 30s, using a tungsten probe (see Figure 5.3a).

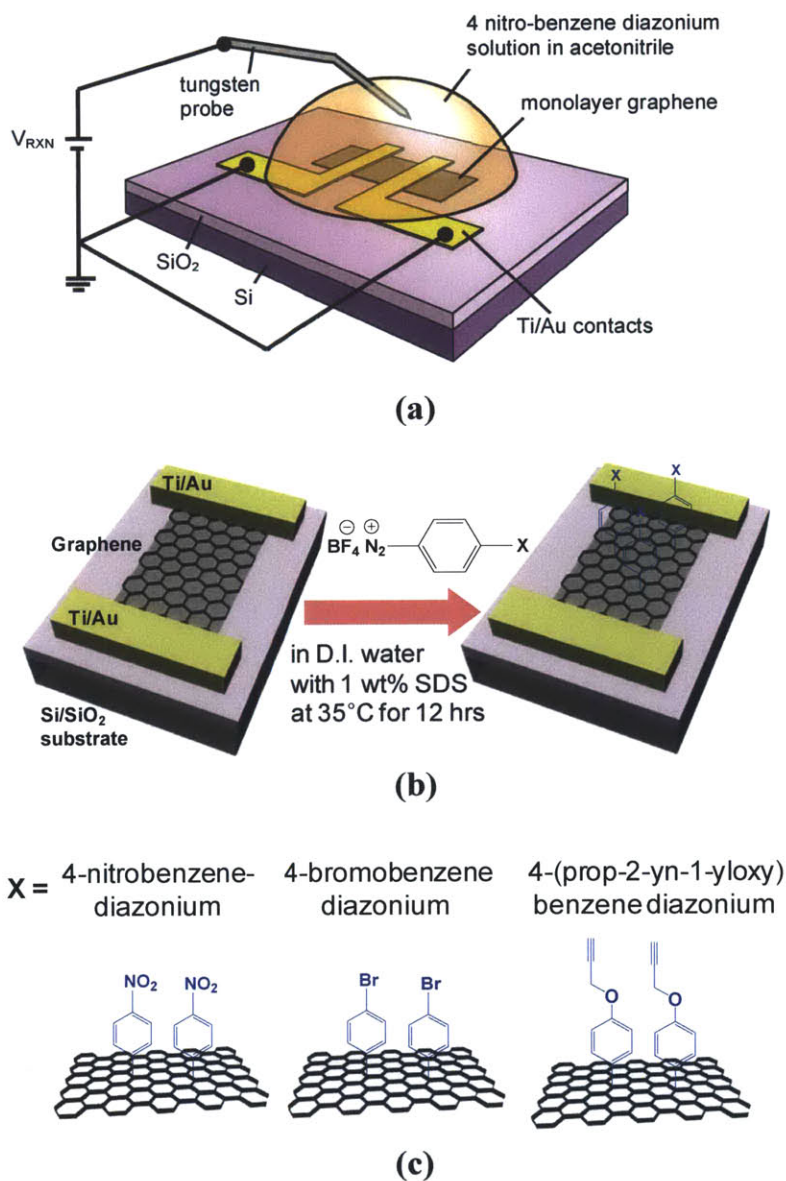


Figure 5.3. Experimental setup. (a) Schematic illustration of electrochemical functionalization of exfoliated monolayer graphene with 4-NBD (b) Schematic illustration of chemical functionalization of CVD monolayer graphene with 4-NBD, 4-BBD or 4-PBD. (c) Three different reaction products after diazonium functionalization.

This creates an electric double layer next to the graphene surface, which raises the graphene Fermi level E_F and thus increases the rate of electron transfer reaction [49]. The positive V_{RXN} also concentrates the diazonium cations within the double layer, increasing the chance of electron transfer from the graphene to them. E_F is raised above the typical value of electron-hole fluctuations in graphene on SiO_2 , implying the substrate effect is negligible [36], as well as a more spatially uniform reaction across the graphene surface. Because the focus lies on investigating the effects of increasing chemisorption, each graphene sample was rinsed with copious amounts of acetonitrile to minimize residual physisorption of the diazonium molecules [26].

To study the effect of different end groups of the diazonium salt on graphene functionalization 4-NBD, 4-BBD and 4-PBD were used, as shown in Figure 5.3. 4-NBD and 4-BBD were purchased from Sigma-Aldrich while 4-PBD was synthesized in our laboratory, following previous protocols [38]. The graphene samples were submerged in a 10 mM aqueous solution of each diazonium salt with 1 wt% sodium dodecyl sulfate (SDS) for 12 hours at 35°C while stirring.

5.3. Results and discussion

5.3.1. Effect of degree of functionalization

Exfoliated monolayer graphene was isolated on Si substrates with a 300 nm SiO_2 capping layer and electrochemically functionalized with 4-NBD at different values of V_{RXN} . Figure 5.4 shows relevant Raman peak parameters for pristine and 4-NBD-functionalized graphene using different values of V_{RXN} .

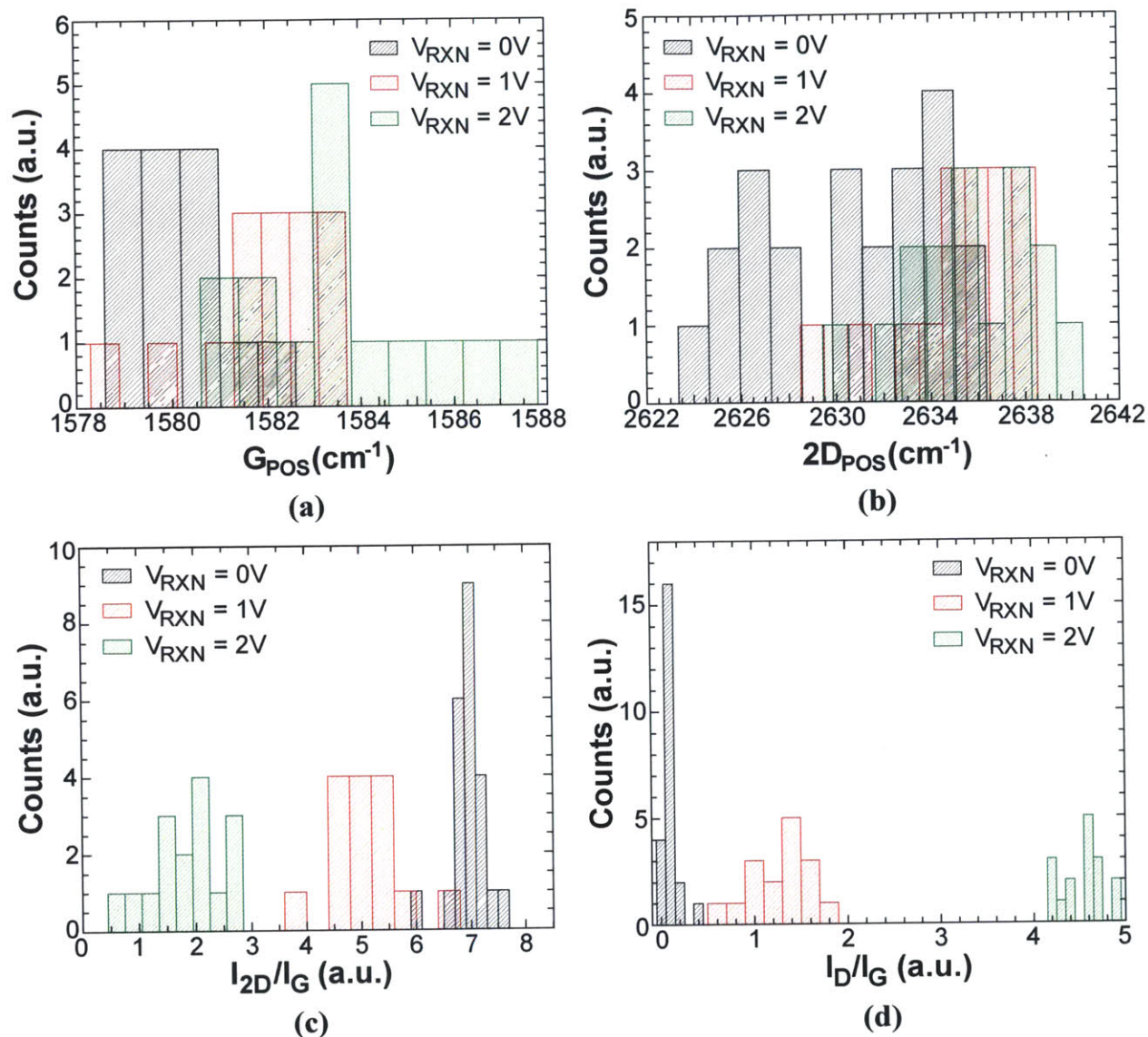


Figure 5.4. Effect of degree of functionalization on graphene Raman peak parameters: **(a)** G peak position, **(b)** 2D peak position, **(c)** 2D/G intensity ratio, **(d)** D/G intensity ratio. For all the distributions compared in this Figure: $p < 0.01$ (see Chapter 4.2.4 for more details).

As expected, increasing V_{RXN} increases the level of covalent modification in graphene, as is evidenced by the increased D/G intensity ratio (Figure 5.4d). The conversion rate achieved at $V_{RXN} = 2V$, characterized by an D/G intensity ratio of 4.6 is the highest to date. Despite rinsing the samples in acetonitrile after reaction to prevent physisorption, the Raman data reveal evidence of increased doping with increasing V_{RXN} :

the G peak and 2D peak positions increase (Figure 5.4a-b), and the 2D/G intensity ratio decreases (Figure 5.4c). The covalent modification in and of itself increases the doping level in graphene, since for each graphed diazonium molecule, graphene loses 2 electrons: one that is used to reduce the diazonium salt (after which the aryl radical is formed), and one that is now shared in the covalent bond with the diazonium molecule after the reaction.

Note that exfoliated graphene (e.g. Figure 5.4) is characterized by much lower G and 2D peak position values than CVD-graphene (e.g Figure 4.5). Synthesized graphene contains a lot of boundaries. Grains of CVD-graphene grown under vacuum conditions following procedures similar to that described in Chapter 4.2.2, are typically sub-micron (average size = 250nm) and two grains intersect with a relative rotation between 0° and 30° [50]. Huang et al. have shown that two grains are typically stitched together through series of pentagons, heptagons and distorted hexagons (e.g Figure 1d in ref. [50]), causing defects and dangling bonds. This implies that many carbon atoms at the grain boundary are sp^3 -rather than sp^2 -hybridized, lowering the charge density in the 2D graphene lattice, which explains the higher Raman peak positions, consistent with p-doping. Note that although exfoliated graphene is more pristine than CVD-graphene, it still has grain boundaries, but the grain sizes are much larger (6-30 μm) [51].

Increasing the degree of covalent modification also strongly affects the charge transport curves in graphene. Figure 5.5a shows a typical graphene charge transport curve. By applying a source-drain voltage V_{DS} , the current through the graphene sheet I_{DS} is measured as a function of the applied gate voltage V_G . Since the current depends on the device geometry, typically the more universal graphene conductivity σ is recorded:

$$\sigma = \frac{I_{DS}}{V_{DS}} \frac{L}{W}, \quad (5.3),$$

where L and W are the graphene channel length and width respectively.

Applying a gate voltage essentially modulates the channel conductivity by altering the total number of added charge carriers n in the channel.

$$V_G = \frac{E_F}{e} + \Phi \quad (5.4),$$

where the E_F is the Fermi level of the graphene, e is the elementary charge of an electron. E_F/e is the contribution of the quantum capacitance C_Q to the gate voltage V_G and Φ represents the contribution of the geometrical capacitance C_G :

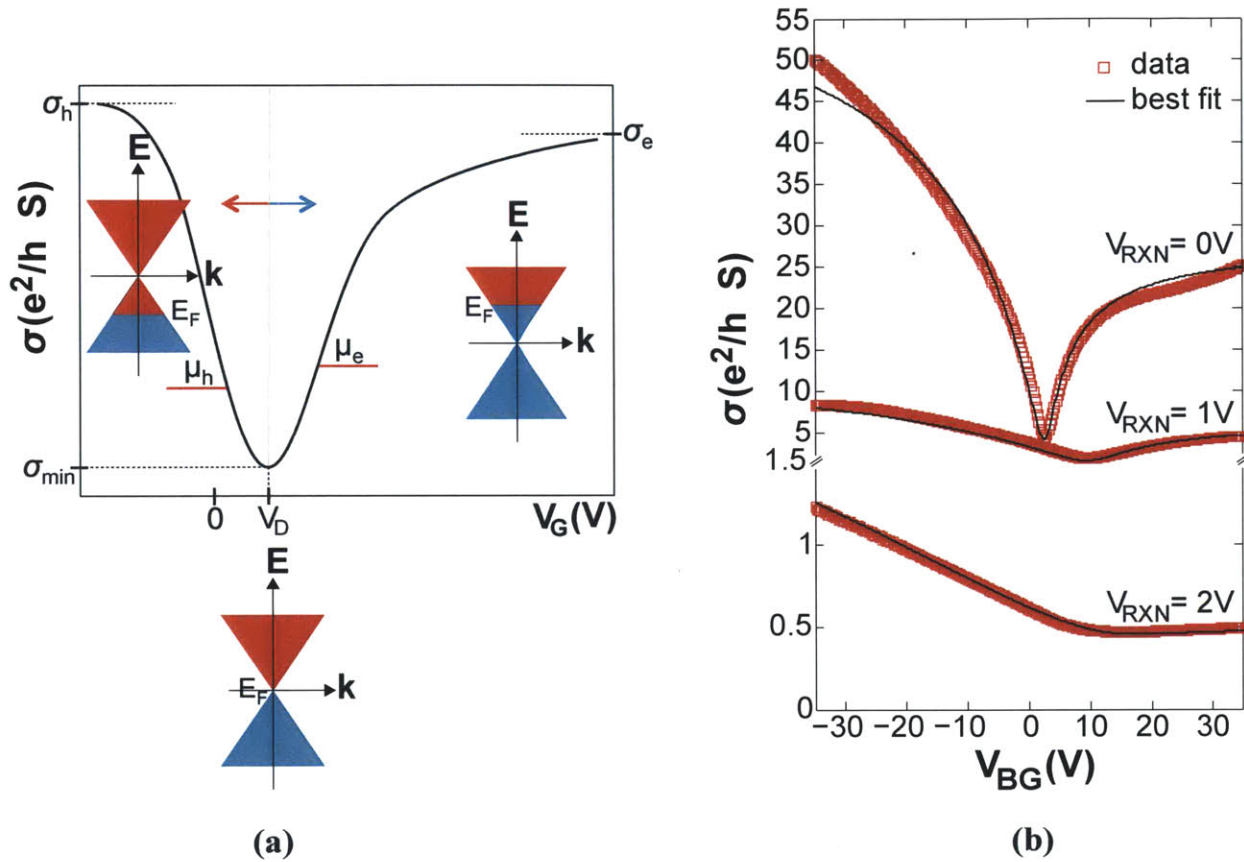
$$\begin{cases} \frac{E_F}{e} = \frac{\hbar |v_F| \sqrt{\pi n}}{e} \\ \Phi = \frac{ne}{C_G} = \frac{net_G}{\epsilon_0 \kappa} \end{cases} \quad (5.5),$$

with \hbar the reduced Planck constant, v_F the Fermi velocity of graphene (1.1×10^6 m/s) [52,53], t_G the thickness of the gate dielectric, ϵ_0 the permittivity of vacuum, and κ the dielectric constants of the dielectric. Inserting (5.5) in (5.4) shows that V_G shows the following dependence on n :

$$V_G = C\sqrt{n} + Dn \quad (5.6),$$

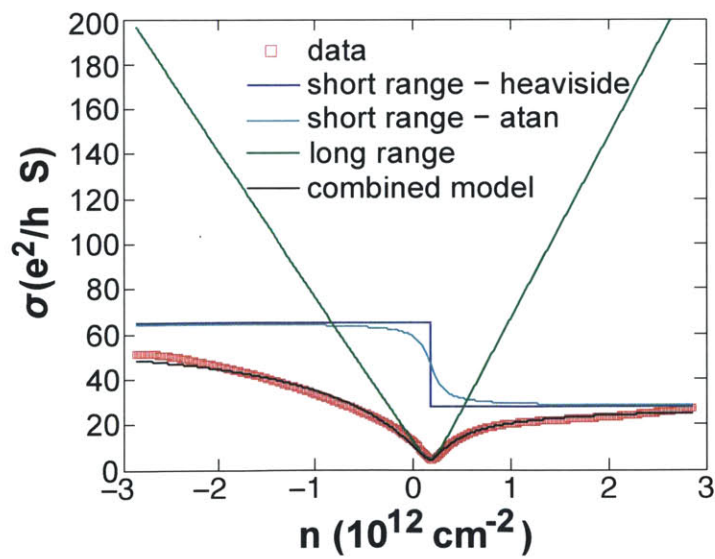
with C and D two constants. For devices where t_G is large (e.g. typically back-gated graphene devices where $t_G \sim 300$ nm) the first term is negligible and $V_G \sim Dn$. However for typical polymer-top-gated devices $t_G \sim 1$ -2 nm [54] (the polymer Debye length) and both terms are equivalent. Note that applying a positive V_G injects electrons into the channel;

therefore we use the convention that positive values of n represent injected electron densities and negative values of n represent injected hole densities.



(a)

(b)



(c)

Figure 5.5. Effect of degree of functionalization on graphene charge transport characteristics. **(a)** Schematic of typical graphene charge transport curve. **(b)** Effect of increasing degree of covalent modification on graphene charge transport curves. **(c)** Breakdown of model describing graphene FET behavior for $V_{RXN}=1V$.

The minimum conductivity σ_{min} is obtained at the Dirac point (otherwise known as the charge-neutrality point), where $V_G=V_D$ and graphene's Fermi level is positioned where the conduction bands meet the valence bands (Figure 5.5a). Although the average carrier density in the channel is zero, charged impurities in the substrate (or superstrate) create charge fluctuations in graphene, which manifest itself as the inhomogeneous electron-hole puddle landscape observed in graphene [55-57] and explains why the conductivity is not zero at the Dirac point.

If graphene is originally hole-doped (p-doped) it is characterized by a positive value of V_D [26], since in order to obtain overall charge-neutrality, electrons needed to be injected into the channel. The opposite is true for electron-doped (n-doped) graphene. At V_G greater (smaller) than V_D , the free carriers in the channel are electrons (holes). Close to the Dirac point the conductivity varies linearly with the carrier density in the channel, but at large values of $|V_G|$ it plateaus (see Figure 5.5a-b). From the slope of linear portions of the charge transport curve the hole mobility μ_h and electron mobility μ_e can be extracted.

Figure 5.5b clearly shows that for increasing degree of covalent modification, (1) the minimum conductivity σ_{min} decreases, (2) the Dirac voltage V_D shifts towards more positive values, (3) the conductivity at high V_G plateaus at lower values σ_h and σ_e , and (4) increasing asymmetry between the hole- and electron- branches of the charge transport curves.

In order to better understand and interpret graphene charge transport curves, we develop a semi-empirical modification to the self-consistent transport theory model first proposed by Das Sarma *et al.* [52]. The model predicts how the conductivity σ scales with the injected carrier concentration n .

The original model states that:

$$\left\{ \begin{array}{l} \sigma(n) = \frac{2e^2}{\hbar n_{imp} G[r_s]} \sqrt{(n + \bar{n})^2 + n^{*2}} \\ G[x] = x^2 \left[\frac{\pi}{4} + 3x - \frac{3\pi x^2}{2} + \frac{x(3x^2 - 2) \arccos[1/x]}{\sqrt{x^2 - 1}} \right] \\ r_s = \frac{e^2}{\hbar v_F 4\pi\epsilon_0 (\kappa_1 + \kappa_2)} \end{array} \right. \quad (5.7),$$

where \hbar is the reduced Planck constant, r_s is the dimensionless constant describing the coupling strength of the dielectrics to graphene [53], and κ_1 and κ_2 the dielectric constants of the substrate (~ 3.9 for SiO_2) and the superstrate (~ 1 for air or vacuum, ~ 5 for PEO/ LiClO_4 [58]) respectively. n is the carrier (electron or hole) density injected into the channel by applying a gate voltage V_G , n_{imp} is the concentration of charged impurities in the vicinity of the graphene (either present in the substrate or created just below or on top of the graphene during the processing or handling of samples) [52] that scatter carrier transport in the graphene, n^* is the residual density of electron-hole puddles in the graphene that screen the electric potential from the gate [52], and \bar{n} is the resulting concentration of carriers in the graphene channel at the Dirac point, so $n_{min} = -(\bar{n})$. Note that the negative sign stems from the fact that in order to reach the charge-neutrality point you need to apply a gate voltage and inject some charge n_{min} to compensate for the charge

that is always present in the channel (\bar{n}). n_{imp} , n^* and \bar{n} are all related to one another: the charged impurities n_{imp} create a spatially inhomogeneous potential distribution in the graphene, which breaks the system up into puddles of electrons and holes with residual density n^* , which is the width of the conductivity ‘plateau’ at the Dirac point. Mathematically these relationships are expressed as:

$$\begin{cases} |\bar{n}| = \frac{n_{imp}^2}{4|n^*|} \\ \frac{n^*}{n_{imp}} = 2r_s^2 C_0^{RPA}(r_s, a = 4d\sqrt{\pi n^*}) \end{cases} \quad (5.8),$$

where C_0^{RPA} is the normalized voltage fluctuation correlation using a Random Phase Approximation (RPA), described in more detail in ref. [52] and d is the average distance of the charged impurities to the graphene. Finally, from (5.7), it is clear that at the Dirac point:

$$\sigma_{\min} = \frac{2n^*}{n_{imp}} G \quad (5.9)$$

There are several limitations to this model in order to use it to fit practical experimental data. First of all, the original model neglects the graphene quantum capacitance effects, which implies it’s only suited to describe graphene FETs characterized by a large dielectric, such that the second term of eqn. (5.4) dominates.

A second limitation of the original model is that it assumes long-range Coulombic scattering dominates the transfer characteristics. These long-range scatterers are caused by physisorption of molecules on top of graphene or by the presence of charged impurities in the substrate. This implies a linear relationship of σ vs. n , or constant

mobility, which clearly is not the case for all devices. While at the lowest carrier densities (close to the charge neutrality point) this is true, at larger densities charge transport has been shown to be dominated by short-range scatterers, caused by e.g. lattice defects [59,60]. At large carrier densities, there are many scatter events of the carriers with the defects in graphene, which strongly reduces the conductivity, deviating from the linear behavior. Even pristine graphene contains lattice defects (mostly in the form of grain boundaries), and the amount of lattice defects is expected to increase dramatically after reaction. It has been shown that for finite carrier density short-range scattering results in a conductivity that is independent of carrier density [61], so the conductivity plateaus at high carrier density are due to chemisorption.

A third limitation of the existing model is that it does not take into account electron-hole conduction asymmetry. The data clearly show that the conductivity for holes (large negative bias) levels off at a different value than the conductivity for electrons (large positive bias). This asymmetry is not only present at large carrier density; it's clear from Figure 5.5b that the electron mobility decreases faster with increasing covalent modification than the hole mobility. Farmer *et al.* have shown that after physisorption of p-doping diazonium molecules on graphene μ_h remains constant but μ_e decreases significantly; similarly, they show that physisorption of n-doping polyethylene imine (PEI) molecules on graphene decreases μ_h but does not affect μ_e [26]. In other words, in p-doped (n-doped) graphene electron (hole) conductance is suppressed. Chemisorption suppresses both electron and hole conduction, although if the reaction also p-dopes (n-dopes) graphene, electron (hole) conduction is suppressed more than hole (electron) conduction [26]. Farmer *et al.* suggest the origin of this asymmetry is

imbalanced electron-hole injection from the graphene underneath the metal contacts (region 1) to the exposed part of the graphene channel (region 2), caused by misalignment of the Fermi level in both regions. Consider the total contact resistance consists of two resistances in series: R_1 signifies the resistance between the metal contact region 1; R_2 is the resistance between region 1 and region 2. In the region 1 the graphene Fermi level is pinned to the metal Fermi level, whereas in region 2 it is affected by physical and chemisorption. Carrier injection from the metal electrodes to the graphene underneath is found to be symmetric. It is also easy to see that upon increasing the covalent functionalization (e.g. by increasing V_{RXN} , Figure 5.5b) in the same device R_1 is not altered, whereas R_2 is.

In our modified model, these three limitations are addressed as follows:

- V_G is ‘translated’ into an injected carrier density n following eqn. (5.6), taking into account both the geometric and the quantum capacitance;
- The presence of short-range scatterers is taken into account by calculating both the long range conductivity σ_{long_range} (first equation in (5.7) – green curve in Figure 5.5c) and the short range conductivity σ_{short_range} (constant with charge density). The total conductivity σ is a serial combination of σ_{long_range} and σ_{short_range} :

$$\sigma = \left(\frac{1}{\sigma_{long_range}} + \frac{1}{\sigma_{short_range}} \right)^{-1} \quad (5.10)$$

- The electron hole conduction asymmetry is taken into account in a semi-empirical manner. For the short-range conductivity it implies assuming a different value of σ_h than σ_e , which switches at Dirac point:

$$\sigma_{short_range} = \sigma_h + (\sigma_e - \sigma_h) \times H(n) \quad (5.11),$$

where H is a Heaviside step function (see dark blue curve in Figure 5.5c). In order to avoid a small discontinuity at the Dirac point caused by the discontinuity in the Heaviside function, it is replaced by an arctangent:

$$\sigma_{short_range} = \left(\frac{\sigma_h + \sigma_e}{2} \right) + \left(\frac{\sigma_e - \sigma_h}{2} \right) \frac{2}{\pi} \arctan \left(\frac{n}{\bar{n}} \right) \quad (5.12),$$

where the argument of arctangent is normalized by \bar{n} to ensure a smooth transition between σ_h to σ_e all the while ensuring the ‘transition’ region is limited to a small range of n -values around \bar{n} , such that the slopes of the conductivity branches are minimally affected by this modification (see light-blue curve in Figure 5.5c).

Because electron-hole conduction asymmetry in the long-range conductivity can be thought of as electrons and holes being scattering differently, it is taken into account empirically by scaling n_{imp} (and because of eqn. (5.8) also \bar{n} and n^*) by a factor f in the electron-conducting regime and $1/f$ in the hole-conducting regime:

$$\left\{ \begin{array}{l} \sigma_{long_range} (n > \bar{n}) = \frac{2e^2}{h f n_{imp} G[r_s]} \sqrt{(n + f\bar{n})^2 + (fn^*)^2} \\ \sigma_{long_range} (n < \bar{n}) = \frac{2e^2}{h \frac{1}{f} n_{imp} G[r_s]} \sqrt{\left(n + \frac{1}{f}\bar{n}\right)^2 + \left(\frac{1}{f}n^*\right)^2} \end{array} \right. \quad (5.13)$$

The model contains 4 fit parameters: σ_h and σ_e (for which initial guesses are made by visually estimating the conductivity plateaus of the data – red squares in Figure 5.5b); n_{imp} (for which an initial guess is made by reading off σ_{min} and \bar{n} from the data and solving eqns. (5.8) and (5.9); and finally f , which is estimated as μ_e / μ_{avg} , with $\mu_{avg} = \frac{\mu_e + \mu_h}{2}$ and where the mobilities are estimated as the maximum slope in each branch of the σ - n plot.

Charge transport characteristics for the same graphene FET device exposed taking at different stages of covalent modification (red squares in Figure 5.5 b) were fitted to this model (black lines in Figure 5.5c). As an example, the different components of the model are plotted for the case of pristine graphene ($V_{RXN} = 0$) in Figure 5.5c.

The results of fitting the model to the charge transport curves obtained for the same device reacted under $V_{RXN} = 0, 1$ and $2V$ (red squares in Figure 5.5b) are shown in Figure 5.5b (black lines).

The model reveals that the density of impurities n_{imp} in the vicinity of graphene increases from $2.65 \times 10^{11} \text{cm}^{-2}$ for pristine graphene, to $2.96 \times 10^{12} \text{cm}^{-2}$ at $V_{RXN} = 1V$, and to $1.17 \times 10^{14} \text{cm}^{-2}$ at $V_{RXN} = 2V$. From eqn. (5.8) it is clear this increase of impurities in the graphene vicinity also increases \bar{n} , which results in a further shift of the minimum towards more positive values. This corresponds to the increasingly positive value of V_D , interpreted as increasing p-doping. As discussed above, for each diazonium molecule that covalently binds to graphene the latter loses two electrons, which is consistent with this

p-doping. Following eqn. (5.8) the increase in \bar{n} also increases n^* , which results in a larger ‘width’ of the conductivity plateau around the Dirac point, and implies the presence of more electron-hole puddles in the graphene. Finally the ratio n^*/n_{imp} decreases from 0.240 for pristine graphene, to 0.098 for medium chemical conversion ($V_{RXN}=1V$) and to 0.024 for the highest levels of chemical conversion ($V_{RXN}=2V$). From eqn. (5.9) one sees this explains the decreasing value of σ_{min} with increasing functionalization observed in the data (Figure 5.5b).

The model reveals a strong decrease of the conductivity plateau at high carrier density with σ_h (σ_e) dropping from 65 (28) e^2/h S for pristine graphene to 15 (6) e^2/h S at $V_{RXN}=1V$, and finally to 6 (10) e^2/h S at $V_{RXN}=2V$. This is consistent with the increasing amount of defect sites (i.e. short range scatterers). Also note the asymmetry between σ_h and σ_e caused by chemisorption, as predicted by Farmer *et al.*

The electron-hole conduction asymmetry caused by physisorption is more noticeable at lower carrier density and the parameter f sheds light on its evolution. Both for pristine graphene and for graphene reacted with $V_{RXN}=1V$ the value of $f \sim 1$, but for $V_{RXN}=2V$, the value of f suddenly drops to 0.27, indicating strongly reduced electron-transport by physisorption (as discussed earlier). Even though precautions were taken to avoid physisorption by rinsing the samples with acetonitrile prior to data collection, Houssain *et al.* have shown that at high degree of chemical conversion multiaromatic oligomers form and adsorb the graphene surface [27]. It is therefore not surprising that samples characterized by a never before observed D/G intensity ratio of 4.6 display this strong asymmetry even close to the Dirac point, captured by a value of f much smaller than 1 (for p-doping). Note for n-doping the value of f would be greater than 1.

5.3.2. Effect of different diazonium end-groups

In order to investigate the effect of using different diazonium salts, Raman data were collected for CVD-graphene reacted with equal concentrations of 4-NBD, 4-BBD and 4-PBD. Histograms of D-peak to G-peak intensity ratio (I_D/I_G), a reflection of the degree of chemisorption, and of the 2D-peak to G-peak intensity ratio (I_{2D}/I_G), a reflection of doping (a combination of chemi- and physisorption) are shown in Figure 5.6. I_D/I_G increases due to covalent functionalization, but the change is the least pronounced for 4-PBD, consistent with Gerisher-Marcus theory, as discussed earlier. Moreover, the propargyloxy-group is larger than the nitro- and bromo-groups (Fig. 6.4d) and thus creates more steric hindrance.

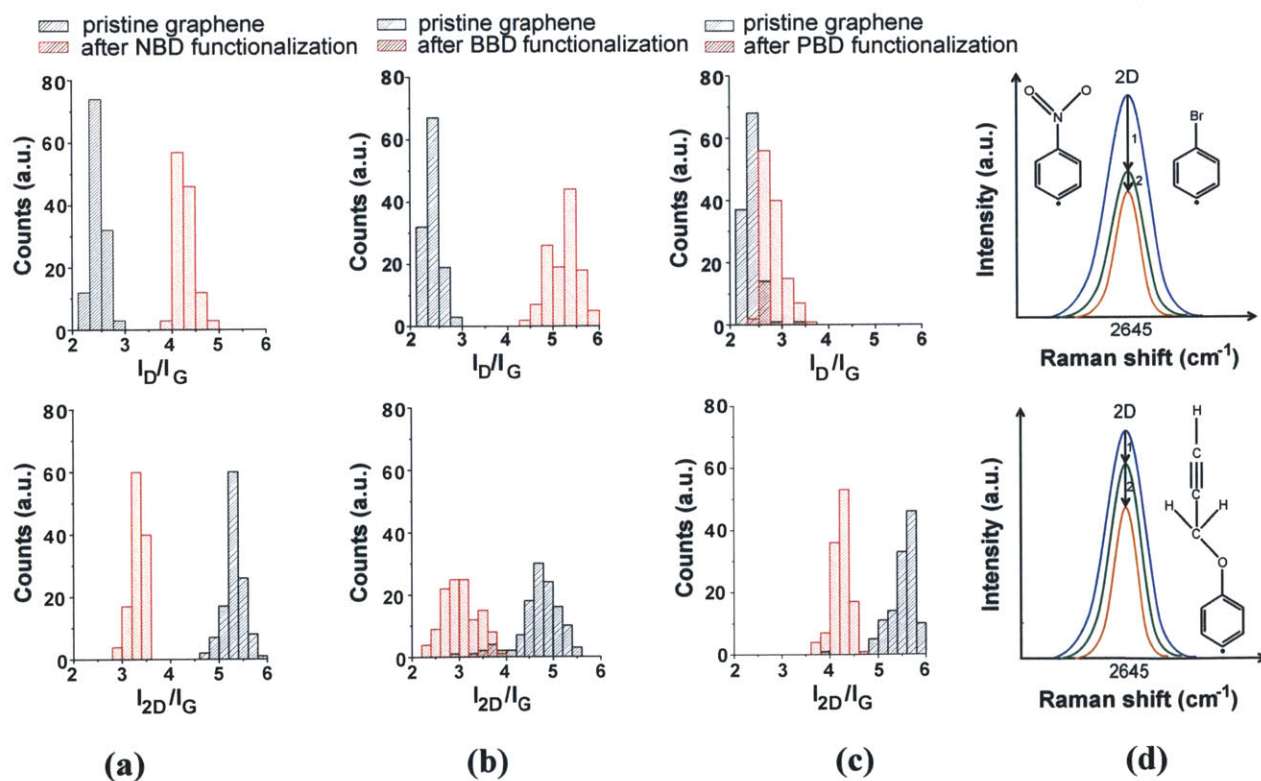


Figure 5.6. Effect of diazonium end-group on functionalized graphene Raman signal. (a)-(c) Effect of different diazonium functional end-groups on Raman spectra of CVD-

grown graphene (black = before reaction; red = after reaction). Reactions conditions: 10 mM aqueous solution with 1 wt% of SDS for 12 h at 35°C. Raman spectroscopy was performed at 633 nm laser excitation. Top panels show I_D/I_G histograms and bottom panels I_{2D}/I_G histograms after functionalization with **(a)** 4-NBD **(b)** 4-BBD and **(c)** 4-PBD. **(d)** Schematic showing the 2D peak intensity decreases due to (1) loss of electrons due to covalent bond formation, and (2) doping due to physisorbed species, and the relative amounts of these for 4-NBD and 4-BBD (top panel) compared to 4-PBD (bottom panel). For all the distributions compared in this figure: $p < 0.01$ (see Chapter 4.2.4 for more details).

Finally, the home-made 4-PBD may be less stable compared to the commercially available 4-NBD and 4-BBD and may thus potentially form more and/or longer oligomers that physisorb onto the graphene and block off reaction sites.

Graphene can be p-doped by the adsorption of electron-withdrawing groups (such as the nitro-group in 4-NBD) to shift E_F below the Dirac point, or n-type doped by electron-donating groups (such as the boro-group and the propargyloxy-group in 4-BBD and 4-PBD respectively) to shift it above [26,62]. The I_{2D}/I_G ratio decreases for both p- and n-doping [43], and here it decreases after all three types of functionalization, with the change being least pronounced for 4-PBD. It should be noted though that the difference in I_{2D}/I_G ratio between 4-PBD and the other two chemistries (4-NBD and 4-BBD) is less pronounced than the difference for the I_D/I_G ratio (Fig. 5.6a-c). We propose two factors that decrease the 2D peak intensity after diazonium functionalization, as illustrated in Figure 5.6d. First, graphene loses 2 electrons as a result of each reduction of a diazonium cation to an aryl radical, and the subsequent covalent attachment of that radical to the graphene lattice. Thus, based on the change of I_D/I_G this factor dominates for 4-NBD and 4-BBD. Second, physisorbed diazonium molecules and oligomers can dope the graphene via surface charge transfer, and based on its structure and the Raman data, we expect this effect dominates for 4-PBD.

Our hypothesis about the additive effects of chemisorption and physisorption on the 2D/G intensity ratio of monolayer graphene has never explicitly been investigated experimentally. However in recent work Cançado and coworkers studied the evolution of the D/G intensity ratio with increasing defect density (caused by Ar⁺ bombarding) [63]. From their Raman data it is clear that for increasing levels of this purely covalent modification of graphene, the 2D/G intensity ratio decreases significantly (see Figure 1 in ref. [63]), which was previously only considered a sign of non-covalent physisorption.

In our laboratory, we compared the D/G and 2D/G intensity ratio for bilayer graphene, before and after reaction [4]. The mechanically exfoliated AB-stacked bilayer graphene sample was functionalized electrochemically in an acetonitrile solution with 20mM 4-BBD and an applied $V_{RXN} = 1.5V$ for 1 minute, similar to the procedure described in Chapter 5.2.4. Likely during the mechanical exfoliation procedure the bilayer flake cracked over its full length, as the optical image in Figure 5.7a shows. This implies that the upper part of the flake was not in contact with the Ti/Pd electrode and hence not subjected to V_{RXN} . One could argue that the upper part of the flake could still undergo *some* covalent modification, but the flake was only immersed in the solution for 1 minute and as discussed in Chapter 5.1.1, typical reaction schemes without an applied V_{RXN} , allow reaction to occur for several hours. Moreover bilayer graphene has been shown to be much less reactive than monolayer graphene [29]. The lack of covalent modification in the upper part of the flake is confirmed by Raman: the D/G intensity ratio in the upper part of the flake is virtually 0 (the same as for the graphene flake prior to the reaction). The bottom part of the graphene flake on the other hand displays a D/G intensity ratio of up to 1.5 (Figure 5.7b). The average 2D/G intensity of the bilayer

graphene flake prior to reaction equals 3.1 [4]. Note this is much lower than for pristine monolayer graphene, as has been shown experimentally [3,64]. The upper part of the flake displays a 2D/G intensity ratio of ~ 2.5 , whereas for the bottom part that value decreases to ~ 1.4 . This dataset proves that physisorption (occurring in the entire flake) is responsible for one part of the decrease of the 2D/G intensity ratio, and chemisorption for another part, confirming our hypothesis presented in Figure 5.6d.

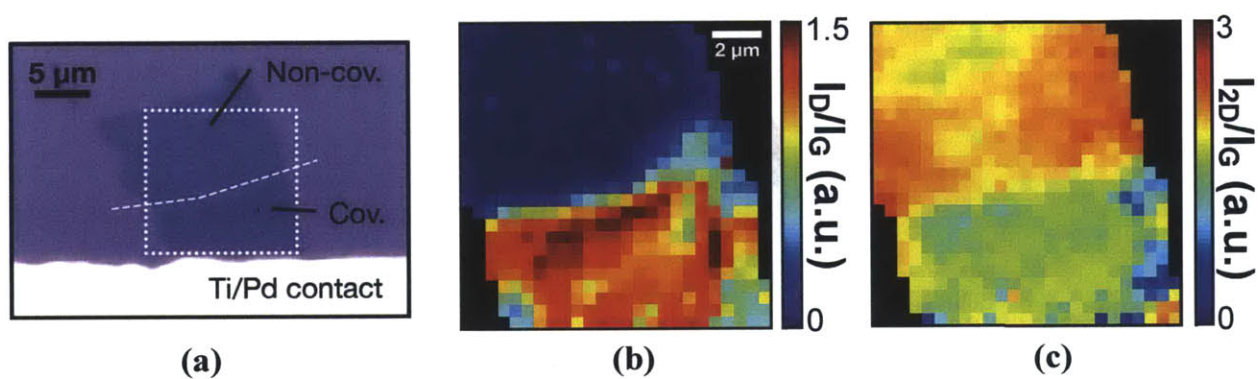


Figure 5.7. Effect of chemi- and physisorption on functionalized bilayer graphene Raman signal. **(a)** Optical image of mechanically exfoliated graphene bilayer flake. The crack down the center of the flake implies that the top half is not subjected to V_{RXN} , whereas the bottom half is. **(b)** D/G intensity ratio for the area in the white box of Figure 5.7a, after reaction. **(c)** 2D/G intensity ratio for the area in the white box of Figure 5.7a, after reaction.

5.3.3. Effect of other reaction conditions

Apart from the degree of functionalization and the type of diazonium salt, other reaction conditions such as temperature and the reaction solvent can also affect graphene's charge-transfer characteristics.

Farmer and coworkers [26] have shown that long-range scatterers (due to physisorption) shift the charge-neutrality point and decrease the mobility of only one type

of carrier: hole-dopants reduce the electron mobility, whereas electron-dopants reduce the hole mobility [26]. Short-range scatterers (i.e. defects, caused by chemisorption) decrease the minimum conductivity and the mobility of both types of charge carriers equally [26]. Depending on the reaction conditions, graphene transistors exposed to diazonium salts can show the effects of both to different degrees: physisorption can be favored over chemisorption (Fig. 5.8a) [34]; both effects can be present in relatively equal degrees (Fig. 5.8b) [25]; or physisorption can be dominant (Fig. 5.8c) [26]. One obvious difference between the different datasets in Figure 5.8 is the reaction solvent. For the reaction in water (acetonitrile) physisorption (chemisorption) dominates. Similar results were obtained for the covalent modification of SWCNTs with diazonium salts [65]. Cyclic voltammetry data has confirmed that under otherwise exactly the same reaction conditions, the electron transfer reaction in acetonitrile has a higher degree of conversion than in water [66]. One possible explanation is that the aprotic acetonitrile with a dipole moment of 3.92 D is better able to solvate the diazonium cations than water, which has a dipole moment of 1.85 D [67]. As discussed earlier, adding SDS to water helps bring the hydrophilic cationic diazonium salts in closer proximity of the hydrophobic graphene [2,25,29,34,36,38], which explains why more chemisorption is observed in Figure 5.8b.

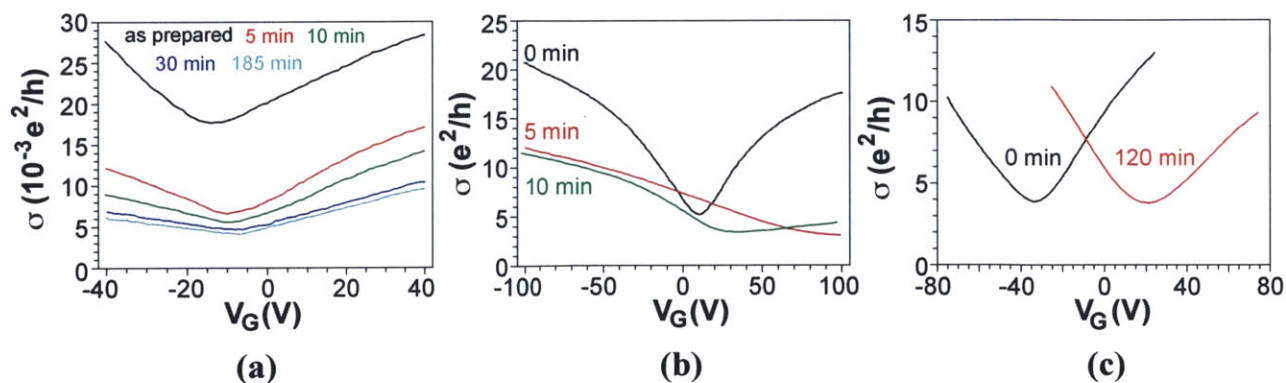


Figure 5.8. Effect of reaction conditions on the charge transport characteristics of graphene FETs. **(a)** 4 mM 4-NBD in acetonitrile at 300 K for 5-185 minutes at 300 K. Adapted from Ref. [34] **(b)** 20 mM 4-NBD in aqueous solution with 1 wt% SDS at 300 K for 5-10 minutes. Adapted from Ref. [25]. **(c)** 1 mM 4-BBD in 1:1 water/methanol mixture at 300 K for 2hrs. Adapted from Ref. [26].

5.4. Conclusions

In this chapter I focused on functionalizing graphene with diazonium salts via an electron transfer reaction. The reaction mechanism is studied both from a theoretical and an experimental perspective: although thermodynamics predict long-range ordering, in reality the process is mostly governed by kinetics, as well as influenced by electron-hole puddles and graphene ripples. Depending on the reaction conditions, the entire range between complete physisorption and complete chemisorption can be achieved, as is evidenced by both Raman spectroscopy and charge transport characteristics of functionalized graphene transistors. We developed a simple model for graphene charge transport that takes into account both the effects of long-range and short-range scatterers.

Controlling the electrical properties of the graphene by chemical doping can lead to great opportunities for developing next-generation electronics and optoelectronics based on graphene. Additionally, the functionalized graphene can be used as biosensors, fillers in polymeric matrices and catalysts in solution. The diazonium chemistry is a versatile, convenient, and powerful tool for selectively modifying and manipulating graphene.

5.5. Ongoing work

Ongoing work is focusing on better understanding and characterizing the diazonium functionalization of bilayer graphene [3,4].

Breaking the translational symmetry of the graphene lattice is believed to open a band gap in graphene [68]. Several theoretical and experimental studies predict the ability of covalent graphene chemistry to open a transport band gap in bilayer graphene [7,21,42,69]. Although in monolayer graphene optical band gaps of several hundreds of meV have been achieved [70], this did not lead to significant enhancement of the on/off ratio of the functionalized graphene transistors. Likely the electronic transport gap is smaller than the optical one, due to interband trapping [71]. For bilayer graphene it was shown that applying a transverse electric field across the bilayer graphene can create a transport band gap [72]. Similarly one could break the symmetry between the two layers by changing the charge density in one of the two layers [73], e.g. by reacting the top layer. This warrants further exploration of covalent modification of bilayer graphene [3,4], and increasing the fundamental understanding of charge transport in functionalized bilayer graphene. This includes extending the model presented in this Chapter to bilayer graphene.

5.6. References

- 1 Paulus, G. L. C., Wang, Q. H. & Strano, M. S. Covalent Electron Transfer Chemistry of Graphene with Diazonium Salts. *Accounts of Chemical Research* **46**, 160-170 (2013).
- 2 Paulus, G. L. C.; Ham, M.H.; Wang, Q.-H.; Hilmer, A.J.; Kim, K.K.; Shih, C.J.; Ulissi, Z.; Kong, J.; Strano, M.S. Substituent Effects for the Control of Covalent Electronic Doping of CVD Graphene *In preparation* (2013).
- 3 Shih, C.-J., Wang, Q. H., Jin, Z., Paulus, G. L., Blankschtein, D., Jarillo-Herrero, P. & Strano, M. S. Disorder Imposed Limits of Mono-and Bilayer Graphene Electronic Modification using Covalent Chemistry. *Nano Letters* **13**, 809-817 (2013).
- 4 Wang, Q. H., Shih, C. J., Paulus, G. L. C. & Strano, M. S. The evolution of physical and electronic structure of bilayer graphene upon chemical functionalization. *In preparation* (2013).
- 5 Loh, K. P., Bao, Q., Ang, P. K. & Yang, J. The chemistry of graphene. *Journal of Materials Chemistry* **20**, 2277-2289 (2010).
- 6 Chen, W., Chen, S., Qi, D. C., Gao, X. Y. & Wee, A. T. S. Surface Transfer p-Type Doping of Epitaxial Graphene. *Journal of the American Chemical Society* **129**, 10418-10422 (2007).
- 7 Niyogi, S., Bekyarova, E., Hong, J., Khizroev, S., Berger, C., de Heer, W. & Haddon, R. C. Covalent Chemistry for Graphene Electronics. *Journal of Physical Chemistry Letters* **2**, 2487-2498 (2011).
- 8 Zhang, H., Bekyarova, E., Huang, J.-W., Zhao, Z., Bao, W., Wang, F., Haddon, R. C. & Lau, C. N. Aryl Functionalization as a Route to Band Gap Engineering in Single Layer Graphene Devices. *Nano Letters* **11**, 4047-4051 (2011).
- 9 Yoo, E., Kim, J., Hosono, E., Zhou, H.-s., Kudo, T. & Honma, I. Large Reversible Li Storage of Graphene Nanosheet Families for Use in Rechargeable Lithium Ion Batteries. *Nano Letters* **8**, 2277-2282 (2008).
- 10 Wehling, T. O., Novoselov, K. S., Morozov, S. V., Vdovin, E. E., Katsnelson, M. I., Geim, A. K. & Lichtenstein, A. I. Molecular Doping of Graphene. *Nano Letters* **8**, 173-177 (2007).
- 11 Schedin, F., Geim, A. K., Morozov, S. V., Hill, E. W., Blake, P., Katsnelson, M. I. & Novoselov, K. S. Detection of individual gas molecules adsorbed on graphene. *Nature Materials* **6**, 652-655 (2007).
- 12 Mohanty, N. & Berry, V. Graphene-based single-bacterium resolution biodevice and DNA transistor: interfacing graphene derivatives with nanoscale and microscale biocomponents. *Nano Letters* **8**, 4469-4476 (2008).
- 13 Alaboson, J. M. P., Wang, Q. H., Emery, J. D., Lipson, A. L., Bedzyk, M. J., Elam, J. W., Pellin, M. J. & Hersam, M. C. Seeding Atomic Layer Deposition of High-k Dielectrics on Epitaxial Graphene with Organic Self-Assembled Monolayers. *Acs Nano* **5**, 5223-5232 (2011).
- 14 Wang, X., Tabakman, S. M. & Dai, H. Atomic Layer Deposition of Metal Oxides on Pristine and Functionalized Graphene. *Journal of the American Chemical Society* **130**, 8152-8153 (2008).
- 15 Wang, Q. H. & Hersam, M. C. Room-temperature molecular-resolution characterization of self-assembled organic monolayers on epitaxial graphene. *Nature Chemistry* **1**, 206-211 (2009).

- 16 Stankovich, S., Dikin, D. A., Dommett, G. H. B., Kohlhaas, K. M., Zimney, E. J., Stach, E. A., Piner, R. D., Nguyen, S. T. & Ruoff, R. S. Graphene-based composite materials. *Nature* **442**, 282-286 (2006).
- 17 Shih, C. J., Vijayaraghavan, A., Krishnan, R., Sharma, R., Han, J. H., Ham, M. H., Jin, Z., Lin, S., Paulus, G. L. C. & Reuel, N. F. Bi-and trilayer graphene solutions. *Nature Nanotechnology* **6**, 439-445 (2011).
- 18 Englert, J. M., Dotzer, C., Yang, G., Schmid, M., Papp, C., Gottfried, J. M., Steinrueck, H.-P., Spiecker, E., Hauke, F. & Hirsch, A. Covalent bulk functionalization of graphene. *Nature Chemistry* **3**, 279-286 (2011).
- 19 Green, A. A. & Hersam, M. C. Solution Phase Production of Graphene with Controlled Thickness via Density Differentiation. *Nano Letters* **9**, 4031-4036 (2009).
- 20 Zhu, Y. W., Murali, S., Cai, W. W., Li, X. S., Suk, J. W., Potts, J. R. & Ruoff, R. S. Graphene and Graphene Oxide: Synthesis, Properties, and Applications. *Advanced Materials* **22**, 3906-3924 (2010).
- 21 Elias, D., Nair, R., Mohiuddin, T., Morozov, S., Blake, P., Halsall, M., Ferrari, A., Boukhvalov, D., Katsnelson, M. & Geim, A. Control of graphene's properties by reversible hydrogenation: evidence for graphane. *Science* **323**, 610-613 (2009).
- 22 Luo, Z., Yu, T., Ni, Z., Lim, S., Hu, H., Shang, J., Liu, L., Shen, Z. & Lin, J. Electronic Structures and Structural Evolution of Hydrogenated Graphene Probed by Raman Spectroscopy. *Journal of Physical Chemistry C* **115**, 1422-1427 (2011).
- 23 Robinson, J. T., Burgess, J. S., Junkermeier, C. E., Badescu, S. C., Reinecke, T. L., Perkins, F. K., Zalalutdniov, M. K., Baldwin, J. W., Culbertson, J. C., Sheehan, P. E. & Snow, E. S. Properties of Fluorinated Graphene Films. *Nano Letters* **10**, 3001-3005 (2010).
- 24 Fan, X., Nouchi, R. & Tanigaki, K. Effect of Charge Puddles and Ripples on the Chemical Reactivity of Single Layer Graphene Supported by SiO₂/Si Substrate. *Journal of Physical Chemistry C* **115**, 12960-12964 (2011).
- 25 Fan, X.-Y., Nouchi, R., Yin, L.-C. & Tanigaki, K. Effects of electron-transfer chemical modification on the electrical characteristics of graphene. *Nanotechnology* **21**, 475208-1:5 (2010).
- 26 Farmer, D. B., Golizadeh-Mojarad, R., Perebeinos, V., Lin, Y.-M., Tulevski, G. S., Tsang, J. C. & Avouris, P. Chemical Doping and Electron-Hole Conduction Asymmetry in Graphene Devices. *Nano Letters* **9**, 388-392 (2009).
- 27 Hossain, M. Z., Walsh, M. A. & Hersam, M. C. Scanning Tunneling Microscopy, Spectroscopy, and Nanolithography of Epitaxial Graphene Chemically Modified with Aryl Moieties. *Journal of the American Chemical Society* **132**, 15399-15403 (2010).
- 28 Lomeda, J. R., Doyle, C. D., Kosynkin, D. V., Hwang, W.-F. & Tour, J. M. Diazonium Functionalization of Surfactant-Wrapped Chemically Converted Graphene Sheets. *Journal of the American Chemical Society* **130**, 16201-16206 (2008).
- 29 Sharma, R., Baik, J. H., Perera, C. J. & Strano, M. S. Anomalously Large Reactivity of Single Graphene Layers and Edges toward Electron Transfer Chemistries. *Nano Letters* **10**, 398-405 (2010).
- 30 Quintana, M., Spyrou, K., Grzelczak, M., Browne, W. R., Rudolf, P. & Prato, M. Functionalization of Graphene via 1,3-Dipolar Cycloaddition. *Acs Nano* **4**, 3527-3533 (2010).
- 31 Sarkar, S., Bekyarova, E. & Haddon, R. C. Chemistry at the Dirac Point: Diels-Alder Reactivity of Graphene. *Accounts of Chemical Research* **45**, 673-682 (2012).

- 32 Wang, Q. H. & Hersam, M. C. Nanofabrication of Heteromolecular Organic Nanostructures on Epitaxial Graphene via Room Temperature Feedback-Controlled Lithography. *Nano Letters* **11**, 589-593 (2011).
- 33 Koehler, F. M., Jacobsen, A., Ensslin, K., Stampfer, C. & Stark, W. J. Selective Chemical Modification of Graphene Surfaces: Distinction Between Single, and Bilayer Graphene. *Small* **6**, 1125-1130 (2010).
- 34 Sinitskii, A., Dimiev, A., Corley, D. A., Fursina, A. A., Kosynkin, D. V. & Tour, J. M. Kinetics of Diazonium Functionalization of Chemically Converted Graphene Nanoribbons. *Acs Nano* **4**, 1949-1954 (2010).
- 35 Bekyarova, E., Itkis, M. E., Ramesh, P., Berger, C., Sprinkle, M., de Heer, W. A. & Haddon, R. C. Chemical Modification of Epitaxial Graphene: Spontaneous Grafting of Aryl Groups. *Journal of the American Chemical Society* **131**, 1336-1337 (2009).
- 36 Wang, Q. H., Jin, Z., Kim, K. K., Hilmer, A. J., Paulus, G. L. C., Shih, C. J., Ham, M. H., Sanchez-Yamagishi, J. D., Watanabe, K., Taniguchi, T., Kong, J., P., J.-H. & Strano, M. S. Understanding and controlling the substrate effect on graphene electron-transfer chemistry via reactivity imprint lithography. *Nature Chemistry* **4**, 724-732 (2012).
- 37 Lim, H., Lee, J. S., Shin, H.-J., Shin, H. S. & Choi, H. C. Spatially Resolved Spontaneous Reactivity of Diazonium Salt on Edge and Basal Plane of Graphene without Surfactant and Its Doping Effect. *Langmuir* **26**, 12278-12284 (2010).
- 38 Jin, Z., McNicholas, T. P., Shih, C.-J., Wang, Q. H., Paulus, G. L. C., Hilmer, A., Shimizu, S. & Strano, M. S. Click Chemistry on Solution-Dispersed Graphene and Monolayer CVD Graphene. *Chemistry of Materials* **23**, 3362-3370 (2011).
- 39 Sharma, R., Nair, N. & Strano, M. S. Structure-Reactivity Relationships for Graphene Nanoribbons. *Journal of Physical Chemistry C* **113**, 14771-14777 (2009).
- 40 Zhu, H., Huang, P., Jing, L., Zuo, T., Zhao, Y. & Gao, X. Microstructure evolution of diazonium functionalized graphene: A potential approach to change graphene electronic structure. *Journal of Materials Chemistry* **22**, 2063-2068 (2012).
- 41 Jiang, D.-E., Sumpter, B. G. & Dai, S. How do aryl groups attach to a graphene sheet? *Journal of Physical Chemistry B* **110**, 23628-23632 (2006).
- 42 Boukhvalov, D. & Katsnelson, M. Tuning the gap in bilayer graphene using chemical functionalization: Density functional calculations. *Physical Review B* **78**, 085413-1:5 (2008).
- 43 Das, A., Pisana, S., Chakraborty, B., Piscanec, S., Saha, S., Waghmare, U., Novoselov, K., Krishnamurthy, H., Geim, A. & Ferrari, A. Monitoring dopants by Raman scattering in an electrochemically top-gated graphene transistor. *Nature Nanotechnology* **3**, 210-215 (2008).
- 44 Bard, A. J. & Faulkner, L. R. *Electrochemical methods: fundamentals and applications*. Vol. 2 (Wiley New York, 1980).
- 45 Nair, N., Kim, W.-J., Usrey, M. L. & Strano, M. S. A structure-reactivity relationship for single walled carbon nanotubes reacting with 4-hydroxybenzene diazonium salt. *Journal of the American Chemical Society* **129**, 3946-3954 (2007).
- 46 Barone, V., Peralta, J. E., Uddin, J. & Scuseria, G. E. Screened exchange hybrid density-functional study of the work function of pristine and doped single-walled carbon nanotubes. *The Journal of chemical physics* **124**, 024709-1:5 (2006).
- 47 Eloffson, R. M. & Gadallah, F. Substituent effects in the polarography of aromatic diazonium salts. *The Journal of Organic Chemistry* **34**, 854-857 (1969).

- 48 Novoselov, K., Jiang, D., Schedin, F., Booth, T., Khotkevich, V., Morozov, S. & Geim, A. Two-dimensional atomic crystals. *Proceedings of the National Academy of Sciences of the United States of America* **102**, 10451-10453 (2005).
- 49 Israelachvili, J. N. *Intermolecular and surface forces: revised third edition*. (Academic press, 2011).
- 50 Huang, P. Y., Ruiz-Vargas, C. S., van der Zande, A. M., Whitney, W. S., Levendorf, M. P., Kevek, J. W., Garg, S., Alden, J. S., Hustedt, C. J. & Zhu, Y. Grains and grain boundaries in single-layer graphene atomic patchwork quilts. *Nature* **469**, 389-392 (2011).
- 51 Park, S., Floresca, H. C., Suh, Y. & Kim, M. J. Electron microscopy analyses of natural and highly oriented pyrolytic graphites and the mechanically exfoliated graphenes produced from them. *Carbon* **48**, 797-804 (2010).
- 52 Adam, S., Hwang, E. H., Galitski, V. M. & Das Sarma, S. A self-consistent theory for graphene transport. *Proceedings of the National Academy of Sciences of the United States of America* **104**, 18392-18397 (2007).
- 53 Chen, F., Xia, J. L., Ferry, D. K. & Tao, N. J. Dielectric Screening Enhanced Performance in Graphene FET. *Nano Letters* **9**, 2571-2574 (2009).
- 54 Lu, C., Fu, Q., Huang, S. & Liu, J. Polymer electrolyte-gated carbon nanotube field-effect transistor. *Nano Letters* **4**, 623-627 (2004).
- 55 Zhang, Y., Brar, V. W., Girit, C., Zettl, A. & Crommie, M. F. Origin of spatial charge inhomogeneity in graphene. *Nature Physics* **5**, 722-726 (2009).
- 56 Martin, J., Akerman, N., Ulbricht, G., Lohmann, T., Smet, J., Von Klitzing, K. & Yacoby, A. Observation of electron-hole puddles in graphene using a scanning single-electron transistor. *Nature Physics* **4**, 144-148 (2007).
- 57 Xue, J., Sanchez-Yamagishi, J., Bulmash, D., Jacquod, P., Deshpande, A., Watanabe, K., Taniguchi, T., Jarillo-Herrero, P. & LeRoy, B. J. Scanning tunnelling microscopy and spectroscopy of ultra-flat graphene on hexagonal boron nitride. *Nature Materials* **10**, 282-285 (2011).
- 58 Boyd, R. H. The dielectric constant of lamellar semicrystalline polymers. *Journal of Polymer Science: Polymer Physics Edition* **21**, 505-514 (1983).
- 59 Hwang, E., Adam, S. & Das Sarma, S. Carrier transport in two-dimensional graphene layers. *Physical Review Letters* **98**, 186806-1:4 (2007).
- 60 Nomura, K. & MacDonald, A. H. Quantum Hall ferromagnetism in graphene. *Physical Review Letters* **96**, 256602-1:4 (2006).
- 61 Tsuneya, A. Screening effect and impurity scattering in monolayer graphene. *Journal of the Physical Society of Japan* **75**, 074716-1:7 (2006).
- 62 Liu, H., Liu, Y. & Zhu, D. Chemical doping of graphene. *Journal of Materials Chemistry* **21**, 3335-3345 (2011).
- 63 Cançado, L. G., Jorio, A., Ferreira, E. M., Stavale, F., Achete, C., Capaz, R., Moutinho, M., Lombardo, A., Kulmala, T. & Ferrari, A. Quantifying defects in graphene via Raman spectroscopy at different excitation energies. *Nano Letters* **11**, 3190-3196 (2011).
- 64 Malard, L., Nilsson, J., Elias, D., Brant, J., Plentz, F., Alves, E., Neto, A. C. & Pimenta, M. Probing the electronic structure of bilayer graphene by Raman scattering. *Physical Review B* **76**, 201401-1:4 (2007).
- 65 Bahr, J. L., Yang, J., Kosynkin, D. V., Bronikowski, M. J., Smalley, R. E. & Tour, J. M. Functionalization of carbon nanotubes by electrochemical reduction of aryl diazonium salts: a bucky paper electrode. *Journal of the American Chemical Society* **123**, 6536-6542 (2001).

- 66 Brooksby, P. A. & Downard, A. J. Electrochemical and atomic force microscopy study of carbon surface modification via diazonium reduction in aqueous and acetonitrile solutions. *Langmuir* **20**, 5038-5045 (2004).
- 67 Clayden, G., Warren, W., Greeves, N. & Wothers, P. (Oxford University Press).
- 68 Mañes, J. L., Guinea, F. & Vozmediano, M. a. A. Existence and topological stability of Fermi points in multilayered graphene. *Physical Review B* **75**, 155424-1:6 (2007).
- 69 Ryu, S., Han, M. Y., Maultzsch, J., Heinz, T. F., Kim, P., Steigerwald, M. L. & Brus, L. E. Reversible basal plane hydrogenation of graphene. *Nano Letters* **8**, 4597-4602 (2008).
- 70 Niyogi, S., Bekyarova, E., Itkis, M. E., Zhang, H., Shepperd, K., Hicks, J., Sprinkle, M., Berger, C., Lau, C. N. & Deheer, W. A. Spectroscopy of covalently functionalized graphene. *Nano Letters* **10**, 4061-4066 (2010).
- 71 Szafranek, B. N., Schall, D., Otto, M., Neumaier, D. & Kurz, H. Electrical observation of a tunable band gap in bilayer graphene nanoribbons at room temperature. *Applied Physics Letters* **96**, 112103-1:3 (2010).
- 72 Zhang, Y., Tang, T.-T., Girit, C., Hao, Z., Martin, M. C., Zettl, A., Crommie, M. F., Shen, Y. R. & Wang, F. Direct observation of a widely tunable bandgap in bilayer graphene. *Nature* **459**, 820-823 (2009).
- 73 Gava, P., Lazzeri, M., Saitta, A. M. & Mauri, F. Ab initio study of gap opening and screening effects in gated bilayer graphene. *Physical Review B* **79**, 165431-1:13 (2009).

6. Study and manipulation of graphene-cell doping interactions

Some of the work, text and figures presented in this chapter are reprinted or adapted with permission from reference [1].

6.1. Background and motivation

There is a pressing need for tools capable of both single cell and population-based analysis of metabolic activity. Cancer cells typically have a higher metabolism than regular cells [2,3], causing a stronger acidification of their environment. pH can thus be seen as a proxy for cellular metabolism. Similarly there is a need to make both single-cell and population-based assessments of drug toxicity by monitoring the pH of the cells to which the drugs are administered [4], and to monitor the growth of biofilms, which is also strongly pH-dependent [5].

Currently there are two issues in accurately monitoring (sub)cellular pH. Typical pH sensors require an entire population of 10^4 - 10^6 cells to accurately measure pH or metabolism [3,6-8]. In principle, pH-activated fluorescent probes can be used for single-cell pH-measurements [3]; however here the issue is that the probes are discrete on/off switches at one particular pH and therefore are unable to report actual pH values. The work presented in this Chapter will show that graphene can address both issues.

Due to single layer graphene's large contact area and high surface-to-volume ratio, it has significant potential as a sensor, particularly for biological applications.

Graphene oxide and chemically modified graphene have shown the ability to detect the presence of ssDNA, aptamers, proteins, bacteria and viruses by quenching fluorescence of dyes attached to a part of the analyte by means of fluorescent resonant energy transfer (FRET) [9]. Fabrication of graphene and graphene-based field effect transistor (FET) devices and electrochemical sensors has allowed the detection of DNA, proteins, bacteria, enzymes, small molecules (e.g. hydrogen peroxide, dopamine, glucose), biomacromolecules (e.g. hemoglobin) and different acids and bases [9]. For graphene FET devices, the detection mechanism is based on a change in graphene charge carrier mobility, minimum conductivity and charge neutrality point, caused by charge donation or extraction by the analyte (i.e. doping) [10]. However, these types of devices typically have active graphene areas of $\sim 100 \mu\text{m}^2$ and are implemented such that the sensor response is averaged over the entire graphene surface. Alternatively, emerging topics of interest in biological analysis include single cell interrogation [11-13], subcellular mapping of biochemical signaling [14,15], and understanding phenotypic diversity within a cell population [16-18].

Raman spectroscopy has shown to be a reliable, fast, and non-destructive technique to measure the degree of doping in graphene [19-23]. Graphene is very sensitive to chemical dopants, and even small shifts in its Fermi level result in distinctive changes in its Raman spectrum [20,24]. We assert that a graphene lattice can be conceptualized as an array of independently addressable optical sensors, practically limited in size only by extrinsic factors (i.e. the diffraction limit, near field resolution). This offers the potential for spatial and temporal monitoring of the doping state of graphene locally, and the possibility of single-molecule detection, in contrast to bulk

conductivity measurements in graphene devices. Furthermore, because graphene can be synthesized by chemical vapor deposition (CVD) methods into large macroscopic areas [25,26], the high-sensitivity graphene-based sensor can extend over large detection areas.

A significant advantage of graphene as a biosensor is its potential to display a continuum of independent and aligned sensors at a specific interface. In this Chapter, I demonstrate a nanoscale version (with respect to the volumetric detection limit) of a micro-physiometer – a device that measures cellular metabolic activity from the local acidification rate. Graphene can function as an array of independent pH sensors enabling subcellular and spatiotemporal detection of single biological cells. Raman spectroscopy explores the spatial chemical sensitivity of graphene and show that aqueous protons (H^+) p-dope it – in agreement with established doping trajectories. The experiments reveal graphene displays two distinct pKa values (2.9 and 14.2). The cell physiometer is able to detect the metabolic footprint of isolated, living cells adhered to the graphene surface, differentiating immunoglobulin (IgG) producing human embryonic kidney (HEK) cells from non-IgG-producing control cells. Graphene also allows single cell counting in a population for mapping phenotypic diversity, variances in metabolic rate, and cellular adhesion. This work motivates the application of graphene as a unique biosensor array for cellular and sub-cellular interrogation.

6.2. Materials and methods

6.2.1. Graphene synthesis and transfer

Single layer graphene was synthesized and transferred on a SiO₂/Si (300nm of SiO₂) wafer, following the procedure described in Chapter 4.2.2.

6.2.2. Raman spectroscopy and mapping

Raman spectroscopy was performed on a Horiba Jobin Yvon LabRAM HR800 system with a 633nm excitation laser, following the procedure described in Chapter 4.2.3.

The 100X objective was used to probe bare graphene (exposed to air). In order to limit evaporation whenever graphene was exposed to a liquid, a glass microscope cover slip was used. The thickness of the glass cover slip (~0.25mm) and of the liquid layer increased the total distance between the graphene layer and the objective, requiring the use of the 50X objective (with a working distance of 0.38 mm instead of 0.21 mm for the 100X objective). The diffraction limited spot size (in nm) can be calculated with the following equation:

$$spot\ size = \frac{1.22\ \lambda}{NA} \quad (6.1),$$

with λ the wavelength of the laser excitation and NA the numerical aperture of the objective. When using the 100X objective ($NA=0.9$) the minimum spot size is $\sim 0.86\ \mu\text{m}$ in diameter, whereas it is $\sim 1.03\ \mu\text{m}$ for the 50X objective ($NA=0.75$). Therefore when constructing a Raman map, it was ensured the distance between two points of the map is at least $1\ \mu\text{m}$ to avoid overlap. A 5 second exposure time was used.

A description of the pristine graphene Raman signal can be found in Chapter 4.3.1. The graphene D, G and 2D peaks were fit to Lorentzians after which values of the

peak position, full width half maximum (FWHM), and total intensity (total area under the Lorentzian) were extracted and compared.

6.2.3. Cell line generation

A stable cell line expressing a murine IgG2a (TA99) [27] and green fluorescent protein (GFP) was established using a modified lentiviral transduction process previously described [28]. Briefly, pLB2-CMV-GFP-TA99, a polycistronic expression vector using 2A skip peptides was cloned by overlap extension PCR [29]. This resulted in a promoter/expression cassette of CMV-GFP-F2A-TA99 Light Chain-T2A-TA99 Heavy Chain in the lentiviral expression vector pLB2 [30]. Lentiviral particles were generated by transfecting HEK-293F cells (Invitrogen) with the plasmids pLB2-CMV-GFP-TA99, pCMV-dR8.91 [31], and pCMV-VSV-G [32] at a mass ratio of 2:1:1 using PEI. Fresh media was exchanged after 24 hours. Lentivirus containing supernatant was harvested 48 hours later and supplemented with protamine sulfate at 5 $\mu\text{g}/\text{mL}$. HEK-293F cells (Invitrogen) were transduced by resuspension in freshly harvested viral supernatant. 24 hours later, the HEK-293F cells were transduced a second time. GFP positive, and therefore IgG expressing, cells were purified using flow fluorescence activated cell sorting at the Koch Institute Flow Cytometry Core. Untransduced HEK-293F cells were used as non-expressing controls. It should be noted that unlike the IgG antibody the GFP is not excreted by the cells and thus does not have an active doping effect on graphene.

6.2.4. Cell passaging

The cells are typically passaged after 2 days of growth in a petri dish in the incubator. The spent medium is removed from the dish, after which the dish is rinsed with sterile phosphate buffered saline (PBS), which is then removed again. Subsequently, we diluted as received trypsin (cellgro #25-053-CI) by 5X to a final trypsin concentration of 0.05wt% in PBS. 1ml of this solution is added to the petri dish to loosen the cells. After ~ 30s 9ml medium is added to dilute and deactivate the trypsin and the entire contents of the petri dish are pipetted into a falcon tube and centrifuged at 1000 rpm for 5 minutes. Afterwards, the supernatant (medium + trypsin) is removed and the cells are re-suspended in 5 ml fresh medium. Because our extended Raman mappings the cells spend several hours outside of the incubator. In order to prolong the lifetime of the cells outside of the incubator, we chose to use L-15 medium (with pH buffer pair $\text{KH}_2\text{PO}_4/\text{Na}_2\text{HPO}_4$) because it does not require CO_2 to maintain a stable pH, as does Dulbecco's modified eagle's medium (with buffer pair $\text{H}_2\text{CO}_3/\text{NaHCO}_3$).

6.2.5. IgG expression and purification

Purified TA99 (murine IgG2a) was generated by culturing HEK-GFP-TA99 in suspension for 8-10 days in Freestyle-293 media (Invitrogen). Each cell produces on average 1pg IgG2a per day. After harvest, the culture was clarified by centrifugation and the supernatant was passed through a 0.2 μm filter. The filtered supernatant was then passed over a Protein A column (Genscript) to capture the IgG. Eluted IgG was buffer exchanged into PBS using 10 kDa dialysis cartridges (Slide-A-Lyzer, Thermo Scientific) over 48 hours. Finally, the IgG was concentrated by centrifugal ultrafiltration using 10 kDa membrane filters (Amicon, Millipore). The final IgG concentration is ~1.5 mg/ml.

6.2.6. UV-VIS spectroscopy

UV-VIS spectroscopy was performed on a Shimadzu UV-3101PC UV-VIS-NIR Scanning Spectrophotometer system using a deuterium arc lamp as the excitation source from 190-360 nm and a tungsten excitation source from 360-2500 nm. The photodetector is a visible photomultiplier tube in the considered wavelength range (200-800 nm).

6.2.7. Statistics

For the comparison of distributions of datasets in this Chapter, the same statistics was applied that was described in Chapter 4.2.4.

6.3. Results and discussion

6.3.1. Graphene pH response investigated by Raman spectroscopy

Large area ($\sim 1\text{cm}^2$) monolayer graphene was synthesized via chemical vapor deposition and transferred onto Si substrates with a 300 nm SiO_2 capping layer. Six different graphene samples were exposed to unbuffered, aqueous solutions of varying initial pH (with pH values 0, 2, 4.5, 7.4, 12 and 14) with simultaneous micro-Raman spectroscopic mapping, as shown in Figure 6.1a. Figure 6.1b shows characteristic Raman spectra of pristine graphene in air (blue curve) and for graphene exposed to extremely alkaline (red curve) and acidic (blue curve) conditions. Pristine graphene is characterized by a small D peak near $1300\text{-}1350\text{ cm}^{-1}$, a G peak near 1580 cm^{-1} and a 2D peak between 2600 and 2700 cm^{-1} , depending on the laser excitation source [22,33]. These three

primary peaks are associated with various phonon modes in graphene, and are sensitive to the electronic and structural properties of graphene [19,20,22,33,34].

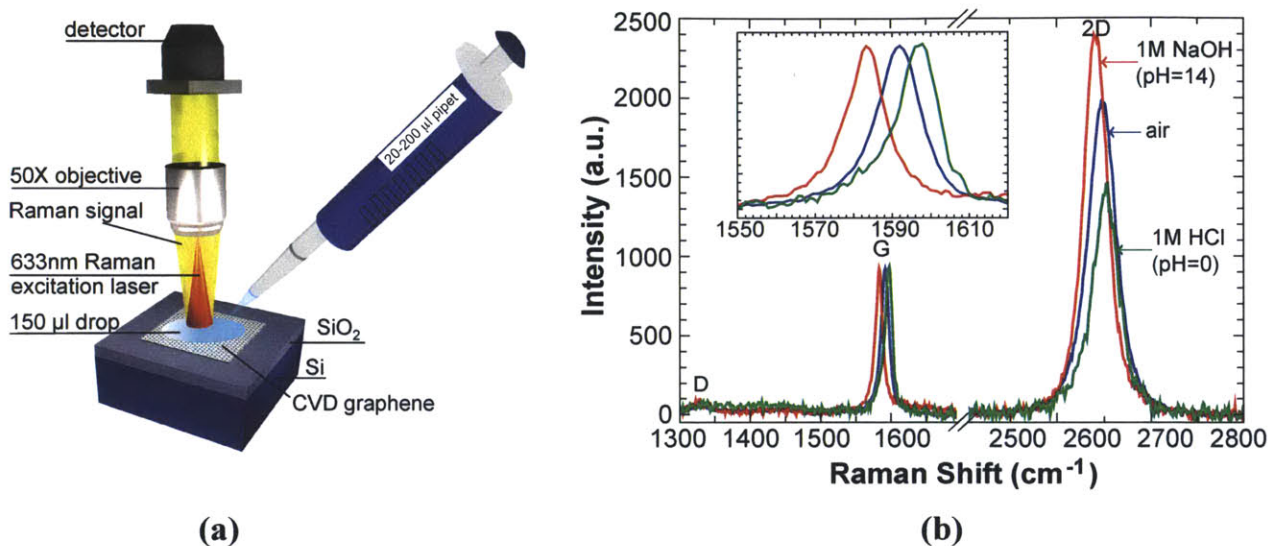
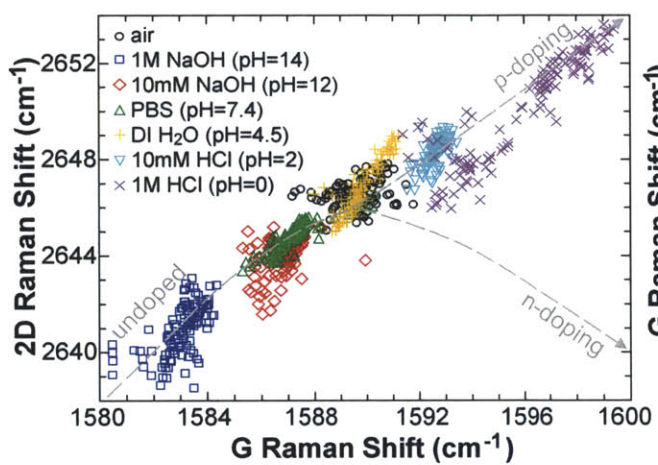
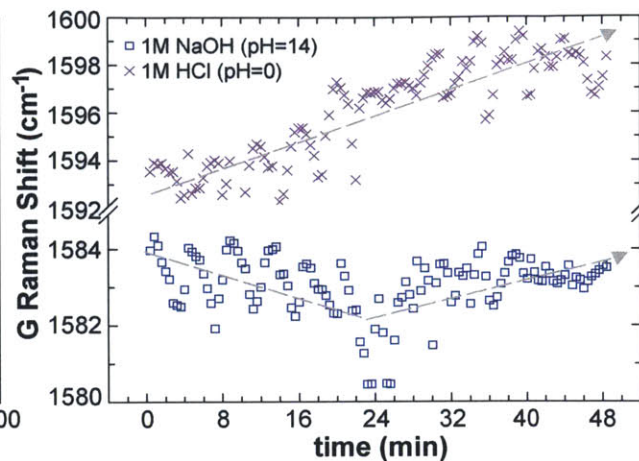


Figure 6.1. Experimental setup. **(a)** Schematic of experimental setup (not to scale). A 150 μl drop of unbuffered solution with a specific pH is deposited onto a monolayer of CVD graphene supported by a SiO_2/Si wafer. A cover slip (not shown) is put on top to slow down evaporation of the solution. 121 spatially distinct Raman spectra of graphene were collected both before and after it was exposed to the solution. **(b)** Characteristic Raman spectra of bare graphene in air (blue), graphene exposed to 1M NaOH (red) and graphene exposed to 1M HCl (green), showing the 3 main graphene peaks (D, G, 2D). All spectra are normalized to G peak height; inset zooms in on the G peak region. Exposure of graphene to alkaline solution decreases its peak positions, whereas contact with an acidic solution increases its peak positions.

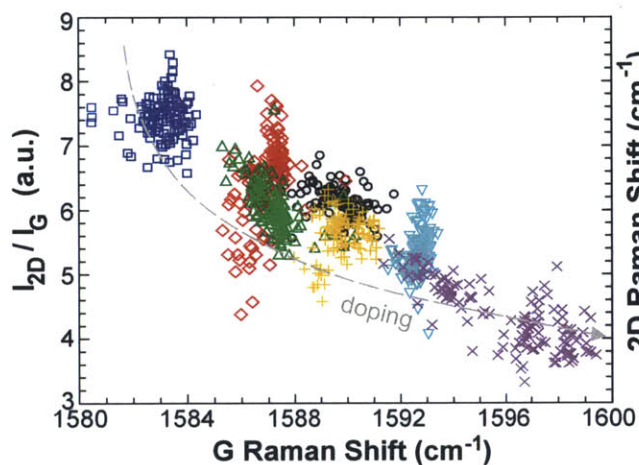
The spectra in Figure 6.1b all show a very small D peak (indicating largely defect-free graphene) and clear differences in the G peak position, 2D peak position and 2D/G intensity ratio, corresponding to differences in the degree of doping (i.e. excess charge carriers in graphene) [19,20,22,33,34]. For each sample, 121 (11 x 11) spatially distinct Raman spectra at $2\mu\text{m}$ pitch were collected.



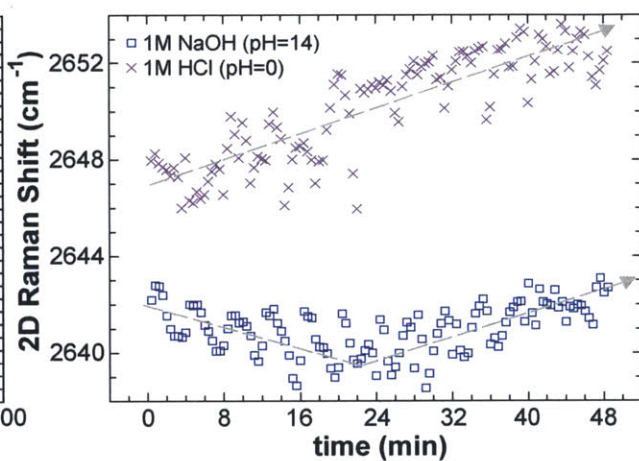
(a)



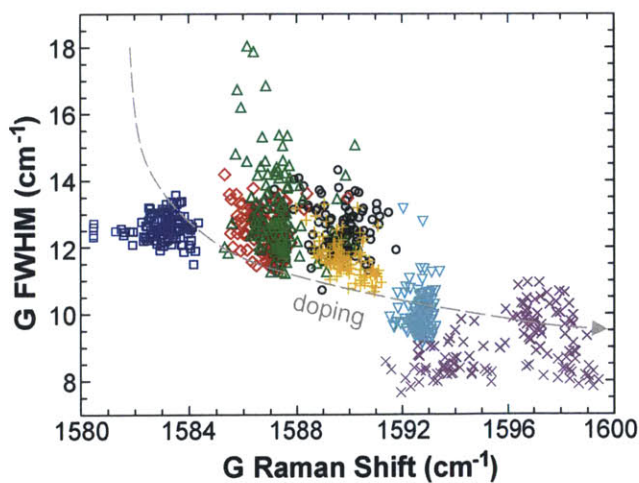
(d)



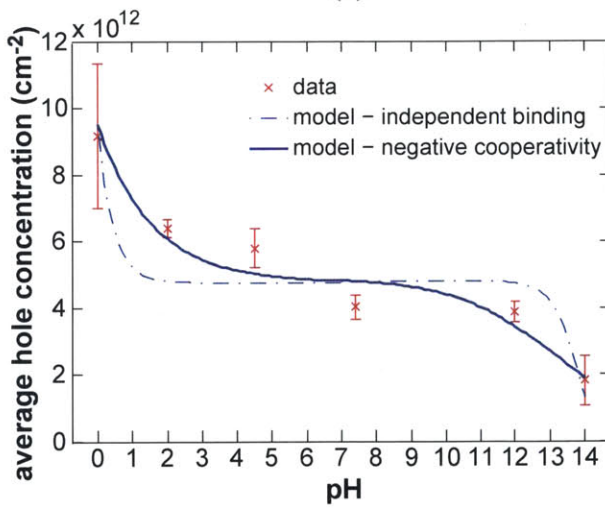
(b)



(e)



(c)



(f)

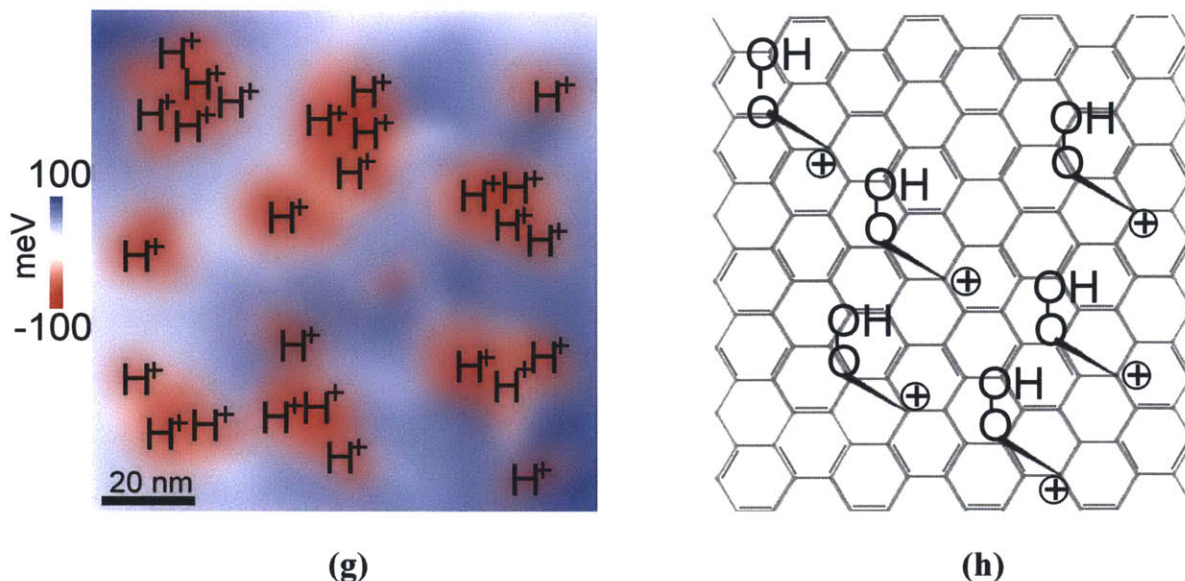


Figure 6.2. pH dependence of graphene Raman signal. Scatter plots of Raman 2D peak position vs. G peak position (a), 2D to G intensity ratio vs. G peak position (b) and G peak width vs. G peak position (c) for graphene exposed to air (black dots) and solutions of different pH. Dashed lines are doping trajectories that serve as a guide to the eye and are adapted from ref. [20]. The trend lines in (a) are shifted downwards to account for the dependence of the 2D peak position on the excitation wavelength (a 532nm laser was used in ref. [20], as opposed to a 633nm laser in this work). Temporal evolution of G peak position (d) and 2D peak position (e) of graphene samples exposed to 1M HCl (purple crosses) and 1M NaOH (blue squares). Trendlines are linear regressions that serve as a guide to the eye (f) Average hole concentration in graphene as a function of the pH of the solution in contact with graphene (red crosses). Dashed line represents independent binding events, whereas solid line represents negative cooperativity (with Hill coefficient $n=0.28$). In the acidic regime the pre-hole doped graphene becomes increasingly p-doped with decreasing pH, and it has a pKa value of 2.9. In the alkaline regime the OH⁻ ions compensate for (part) of the pre-existing hole-doping in graphene, which reveals a second pKa value of graphene of 14.2. The two pKa values indicate two types of binding sites for H⁺ to graphene, each with a different strength: H⁺ physisorbing to negative puddles in graphene (g) and H⁺ forming a covalent -OOH bound in the presence of oxygen (h).

Figure 6.2 shows scatter plots of the 2D peak position ($2D_{POS}$) (Fig. 6.2a), the 2D/G intensity ratio (I_{2D}/I_G) (Fig. 6.2b) and the G peak full width at half maximum (G_{FWHM}) (Fig. 6.2c) versus G peak position (G_{POS}); where the peak parameters were

determined by Lorentzian fitting. Dashed lines represent doping trajectories based on data in ref. [20], in which Das *et al.* monitored the graphene Raman signature of electrostatically gated graphene as a function of the gate voltage V_G . Applied gate voltages that are higher (lower) than the Dirac voltage V_D (at which the number of excess charge carriers is zero, i.e. no doping) inject additional electrons (holes) into the graphene. G_{POS} increases with either kind of excess charge carrier, whereas $2D_{POS}$ changes differently depending on the type of charge carrier: it increases for p-doping (additional holes) and decreases for n-doping (additional electrons) [19,20,24]. In previous work our group has shown that carriers injected or withdrawn by different substrates produce Raman peak dispersions that adhere to these trajectories [21,23]. Other signs of increased doping are a decreased I_{2D}/I_G and a decreased G_{FWHM} [19,20,22,33,34].

The scatter plots of the doping-dependent Raman parameters show that graphene on SiO₂ exposed to air (black dots) is somewhat p-doped, conform with literature results showing charge-transfer curves characterized by a positive Dirac voltage V_D [19,34,35]. The additional holes can come both from the oxygen in the air, as well as from charged impurities in the SiO₂ substrate, evidenced by the fact that both suspended graphene [36] and graphene in vacuum [35] display values of G_{POS} as low as 1580 cm⁻¹ and Dirac voltages closer to 0, indicative of virtually undoped graphene. Additionally, the data in Figure 6.2 indicate that when graphene is exposed to increasingly acidic solutions (deionized (DI) water, 10 mM HCl, 1M HCl), it becomes increasingly doped, specifically hole-doped. Due to the absence of organic buffers and competing adsorbates this reversible p-doping can unambiguously be assigned to the adsorption of protonated

hydrogen ions. Protons adsorbed to the graphene surface form a charge transfer complex with an electron in the graphene, thereby localizing this electron resulting in its p-doping.

For alkaline solutions one would expect the negatively charged hydroxide ions to increasingly n-dope the graphene. Experimentally we observe that with increasing pH, graphene becomes more and more undoped, as evidenced by the low G_{POS} and $2D_{POS}$ (Fig. 6.2a), high I_{2D}/I_G (Fig. 6.2b) and G_{FWHM} (Fig. 6.2c). The n-doping effect of the hydroxide ions appears to offset the initial p-doping in graphene. At first glance, even 1M NaOH does not appear strongly alkaline enough to create a net negative excess charge in graphene. Eventually, for even higher concentrations of NaOH, we do expect the graphene $2D_{POS}$ vs. G_{POS} scatter data to move up the doping trajectory again, and then eventually move down the n-doping branch, characterized by a high G_{POS} but low $2D_{POS}$. Similarly we expect that graphene that starts out more undoped (e.g. suspended graphene) exposed to a 1M NaOH solution would present a net n-doping.

There is a significant spread in the values of G_{POS} and $2D_{POS}$ of graphene exposed to 1M HCl (purple crosses in Fig. 6.2a). Allowing the water to evaporate from the solution over the course of the experiment (~50 min) increases the concentration of aqueous H^+ beyond the starting pH, causing the graphene to become more strongly p-doped over time. Indeed, in a plot of the G peak and 2D peak position data as a function of the time at which they are collected, a linear trend arises (purple crosses in Fig. 6.2d,e). Logically one would expect a similar spread in the peak positions of graphene exposed to extremely alkaline solutions (e.g. blue squares in Fig. 6.2a). At first glance this is not the case; however plotting the peak positions vs. collection time (Fig. 6.2d,e) suggests otherwise. During the first half of the experiment G_{POS} and $2D_{POS}$ decrease,

reaching minimum values of $\sim 1580 \text{ cm}^{-1}$ and 2639 cm^{-1} respectively. This represents the point where the hydroxide ions have fully compensated the initial p-doping in graphene. As time progresses, and more water evaporates from the solution, G_{POS} and $2D_{POS}$ increase again (i.e. the data disperse upward along the doping trajectory) and graphene has a net excess of negative carriers. The average dopant concentration in graphene for each condition shown in Figure 6.2a is plotted as a function of pH in Figure 6.2f. The data are also included in Table 6.1, which summarizes the doping effects different chemical environments have on graphene.

Of interest is the H^+ equilibrium demonstrated by graphene, a fundamental material property, in the form of the acid dissociation constant (K_a) or constants. From the empirical data, two regimes can be distinguished: the acidic regime ($\text{pH} < 7$) and the alkaline regime ($\text{pH} > 7$). In the former, graphene becomes more p-doped with increasing H^+ concentration. Thus:



$$\text{with } \theta_{free} + \theta_{P,H^+} = \theta_{tot,P} \quad (6.3),$$

where θ_{free} is the concentration of available (free) ‘sites’ on graphene for p-doping, θ_{P,H^+} are the ‘sites’ that are p-doped by H^+ and $\theta_{tot,P}$ the total concentration of graphene sites available for p-doping by H^+ . The total graphene carbon atom density is $3.8 \times 10^{15} \text{ cm}^{-2}$. Of this, a portion ($\theta_{initial,P}$) is already hole-doped by the substrate and/or oxygen as discussed earlier. This implies $\theta_{tot,P} = 3.8 \times 10^{15} \text{ cm}^{-2} - \theta_{initial,P}$.

Rearranging these equations gives the concentration of p-doped sites of graphene:

$$\theta_p = \theta_{tot,P} \frac{K_{a,1} [H^+]}{1 + K_{a,1} [H^+]} + \theta_{initial,P} = \theta_{tot,P} \frac{K_{a,1} 10^{-pH}}{1 + K_{a,1} 10^{-pH}} + \theta_{initial,P} \quad (6.4).$$

The last step in eqn. (6.4) assumes that the bulk concentration of aqueous H^+ does not decrease significantly as the graphene becomes p-doped. This is easily justified by comparing the highest amount of excess holes present on the $\sim 1\text{cm}^2$ graphene sample ($\sim 9 \times 10^{12}$ at 1M HCl, see Table 6.1) to the total amount of H^+ present in solution: 150 μL of 1M HCl contains $1 \frac{\text{mol}}{\text{L}} \times N_{AV} \frac{\#}{\text{mol}} \times 150 \mu\text{L} = 9.03 \times 10^{19}$ hydrogen ions, meaning only 0.00001% of these p-dope graphene. It is interesting to note that at this highest doping concentration, 0.25% of all carbon atoms in the graphene lattice are p-doped.

In the alkaline regime ($\text{pH} > 7$) the data show the hydroxide ions (OH^-) ‘neutralizes’ the initially present hole-doping in graphene; thus:



$$\text{with } \theta_{free} + \theta_p = \theta_{initial,P} \quad (6.6),$$

where K_b is the ‘neutralization’ dissociation constant.

Solving for the hole concentration in the alkaline regime leads to:

$$\theta_p = \frac{\theta_{initial,P}}{1 + K_{b,2} [\text{OH}^-]} \quad (6.7).$$

As in the acidic regime we can assume that $[\text{OH}^-] \approx 10^{-pOH}$ with $pOH = 14 - pH$. Moreover it should be noted that

$$\begin{aligned}
K_{a,1} &= 10^{-pKa_1}, \\
K_{b,1} &= 10^{-pKb_2} \quad \text{and} \\
pKb_2 + pKa_2 &= 14 \quad \text{such that } pKa_2 = 14 - pKb_2
\end{aligned} \tag{6.8}$$

Fitting the combined model (eqn. (6.4),(6.7) and (6.8)) to the data (dashed line in Fig.6.2f) results in a value of $pKa_1 = 2.9$, $pKa_2 = 14.2$ and $\theta_{initial,P} = 4.85 \times 10^{12} \text{ cm}^{-2}$. Note that the latter value is close to the experimentally hole concentration in pristine graphene on SiO₂ exposed to air ($= 5.2 \times 10^{12} \text{ cm}^{-2}$, Table 6.1). The Hill coefficient n , originally developed to describe protein-ligand binding [37,38], accounts for cooperativity and modifies eqns. (6.4) and (6.7) as follows:

$$\theta_P = \theta_{tot,P} \frac{K_{a,1} [H^+]^{n_1}}{1 + K_{a,1} [H^+]^{n_1}} + \theta_{initial,P} \tag{6.9},$$

$$\theta_P = \frac{\theta_{initial,P}}{1 + K_{b,2} [OH^-]^{n_2}} \tag{6.10}.$$

A Hill coefficient <1 (negative cooperativity) implies that when one ‘ligand’ (in this case H⁺ or OH⁻) binds to graphene, the affinity for another binding event with that ‘ligand’ decreases. Similarly Hill coefficients >1 (positive cooperativity) indicate binding affinity increases with the number of binding events. Finally a Hill coefficient of 1 signifies each binding event occurs independently (dashed line in Fig.6.2f). The solid line in Fig. 6.2f yields $n_1 = n_2 = 0.28$, indicating negative cooperativity, with the other parameter values remaining the same. Based on this fit the maximum sensitivity in the acid (basic) regime equals $-2.98 \times 10^{12} \text{ cm}^{-2}/\text{pH}$ ($-7.90 \times 10^{11} \text{ cm}^{-2}/\text{pH}$).

The fact that, in the pH range explored in these experiments, graphene displays two pKa 's, implies it has two types of binding sites for H^+ , a weaker and a stronger one, represented by pKa_1 and pKa_2 respectively. Charged impurities in the graphene substrate (in this case SiO_2) have been shown to cause spatial electron-density inhomogeneities (i.e. electron and hole puddles) in graphene itself [39,40]. One explanation is that the weaker type of binding is positive hydrogen ions physisorbing to the negative charge puddles in graphene. This is shown schematically in the lower left inset of Figure 6.2f, where blue (red) areas represent the positive (negative) charge puddles in graphene, with protons adsorbing the negative ones. The schematic puddle landscape drawn in Figure 6.2f is based on spectroscopic tunneling microscope (STM) imaging of graphene puddles on SiO_2 [41]. The resulting electrostatic screening associated with ion adsorption anticipates negative cooperativity as found above. The second pKa_2 may be associated with a hydroperoxide group (-OOH) covalently bound to graphene in the presence of oxygen and H^+ , leaving the graphene p-doped (schematically shown in upper right inset of Figure 6.2f). Although the presence of this structure in graphene has not yet been investigated to date, it is known to be present on and p-dope their 1D equivalent, single walled carbon nanotubes (SWCNTs) [42].

Finally it is interesting to note that the graphene pH dependence, probed via Raman spectroscopy in this work, displays seemingly opposite trends compared to those reported using electrostatic gating of a graphene field effect transistor (FET) exposed to solutions with different pH values [43-45]. In FET experiments, a shift of the Dirac voltage V_D towards more positive values with increasing pH has been interpreted as increased p-doping in several studies [43-45]. In contrast, our Raman results clearly

indicate increased p-doping with decreasing pH. FET experiments for determining the pH response of graphene are complicated by several factors. First, contrary to our approach, a FET is operated with an applied bias voltage and thus does not investigate an equilibrium carrier population. Second, application of a gate voltage results in a transverse electric field that can either attract or repel ionic charges away from the graphene surface, altering ionic adsorption. And third, buffered pH solutions are used in all literature describing pH dependence using graphene FETs. These buffers (e.g. phthalate) contain groups that can themselves dope graphene.

6.3.2. Graphene as an array of addressable pH sensors: a single cell physiometer

One marker for cellular metabolism is the cellular acidification rate, forming the basis for established methods such as the cytosensor micro-physiometer, but these techniques require typically 10^4 - 10^6 cells [6,8]. Decreasing the sensor size to micron- and nano-meter dimension has the potential to extend this analysis of single cells. Metabolically active cells excrete acidic products, which cause the pH in their immediate surroundings to decrease [6,8]. Next, the possibility of spatially mapping the sub-cellular acidification rate of a single biological cell placed on a graphene substrate, was investigated. Graphene can be considered a micro-array of sensor units, with the size of these units determined by the optical diffraction limit of the objective lens used in the Raman spectroscopy system. For example, when using a 50X objective with NA=0.75 the diffraction limited spot size of the excitation laser on the graphene is $\sim 1.03\mu\text{m}$, implying a minimum sensor size of $0.84\mu\text{m}^2$. A typical cell with a ~ 20 - $40\mu\text{m}$ length

scale would cover multiple sensors which can all be individually probed via Raman spectroscopy (Fig. 6.3a).

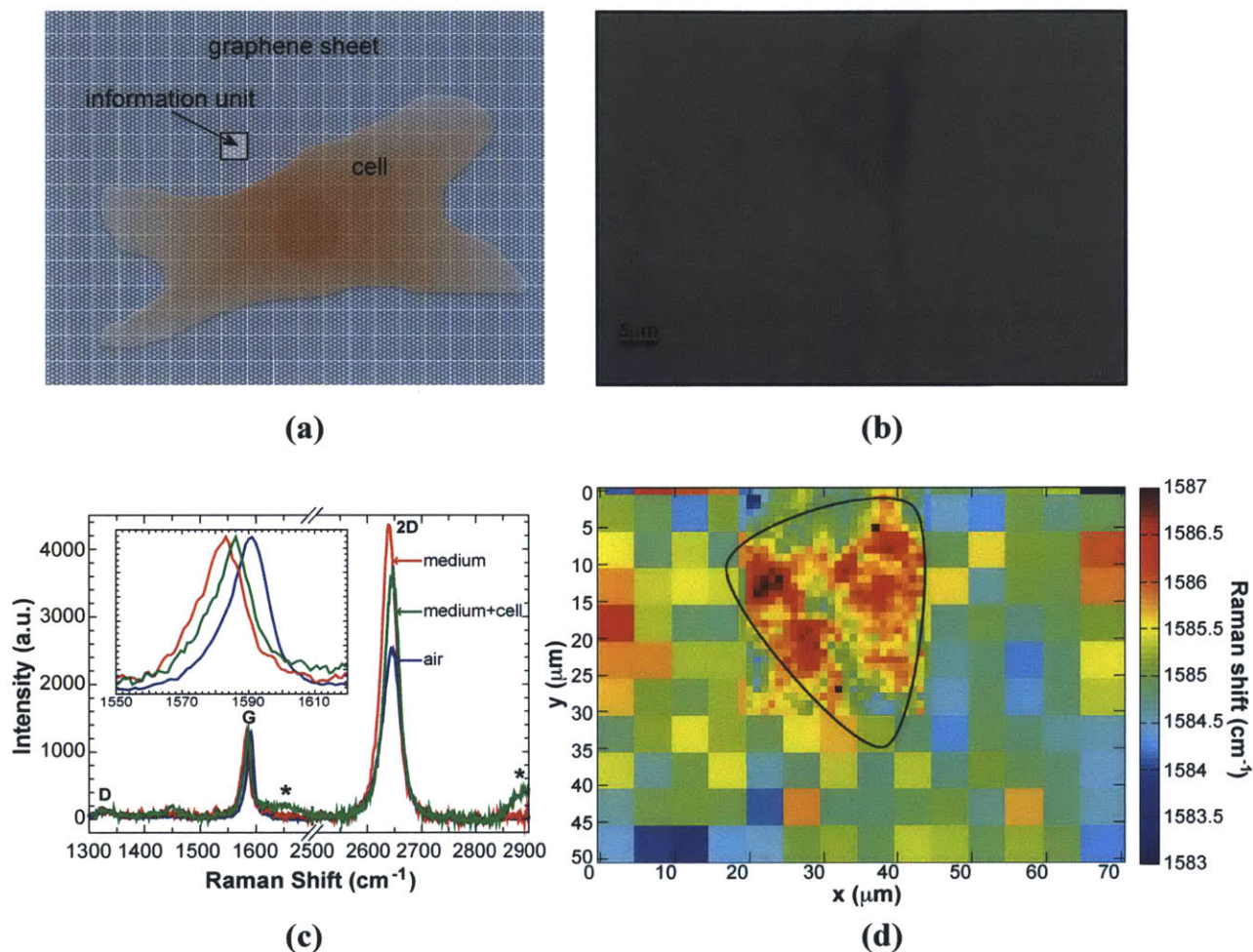


Figure 6.3. Graphene, a tool for subcellular mapping of cellular metabolism. **(a)** Schematic of graphene as a micro-array of information units, with each unit acting as a micro-sensor. Each unit can be probed via Raman spectroscopy and reveal information about the doping state of graphene. Cell placed on graphene is expected to leave a ‘footprint’ on the graphene which can be detected via Raman spectroscopy. Graphene lattice not drawn to scale. **(b)** optical micrograph of IgG-producing HEK-293F cell well-adhered to graphene. **(c)** Characteristic individual Raman spectra of graphene exposed to air (blue), exposed to growth medium (green), under the cell (red) showing the 3 main graphene peaks (D,G,2D). All spectra are normalized with respect to G peak height. Inset zooms in on the G peak region. Stars denote additional peaks observed in graphene covered by the cell. **(d)** Spatial Raman footprint of the cell shown optically in **(b)**, by probing the graphene G peak position: higher values are found under the cell, indicative of more doping.

Transducing human embryonic kidney (HEK-293F) cells with lentiviral vectors created a stable cell line expressing a murine IgG2a antibody (TA99). After passaging, the cells were re-suspended and diluted in L-15 medium. An aliquot of 150 μ l of this solution was deposited onto a monolayer of graphene supported by a SiO₂/Si wafer. A coverslip was put on to prevent evaporation and after 3 hours of incubation (allowing the cells to adhere to the graphene) the sample was examined with optical microscopy and Raman spectroscopy. More details on the experimental procedures can be found in Chapter 6.2.

Figure 6.3b shows an optical image of a typical well-adhered IgG-producing cell, after 3 hrs of incubation on the graphene. Figure 6.3c shows representative Raman spectra of bare graphene exposed to air (blue), and of graphene covered in cellular growth medium (green) and underneath the cell (red). Having verified that the graphene underneath the cell exhibits a different Raman signal from that exposed to just medium, we recorded the spatial Raman footprint of an entire cell. To avoid evaporation of the growth medium, a rapid, spatial map of the G_{POS} was performed for each cell, because this feature displays the most pronounced changes to pH and other adsorbates (inset Fig. 6.3c). We find that other peak parameters, such as the $2D_{POS}$, the G_{FWHM} and the I_{2D}/I_G also show doping-dependent changes, but require an extended spectral window (1500 cm⁻¹-2800 cm⁻¹ for both G and 2D peak vs. 1500 cm⁻¹-1675 cm⁻¹ for just the G peak) in this configuration, increasing the scan time. Figure 6.3d shows the G peak position of the cell and surrounding medium shown in Figure 6.3b. We used the maximal spatial resolution (1 μ m steps) underneath and in the immediate surroundings of the cell but relaxed the

resolution (to $5\mu\text{m}$ steps) further away from the cell. The shape of the cell is remarkably well preserved in the spatial plot of G peak position (Fig. 6.3d).

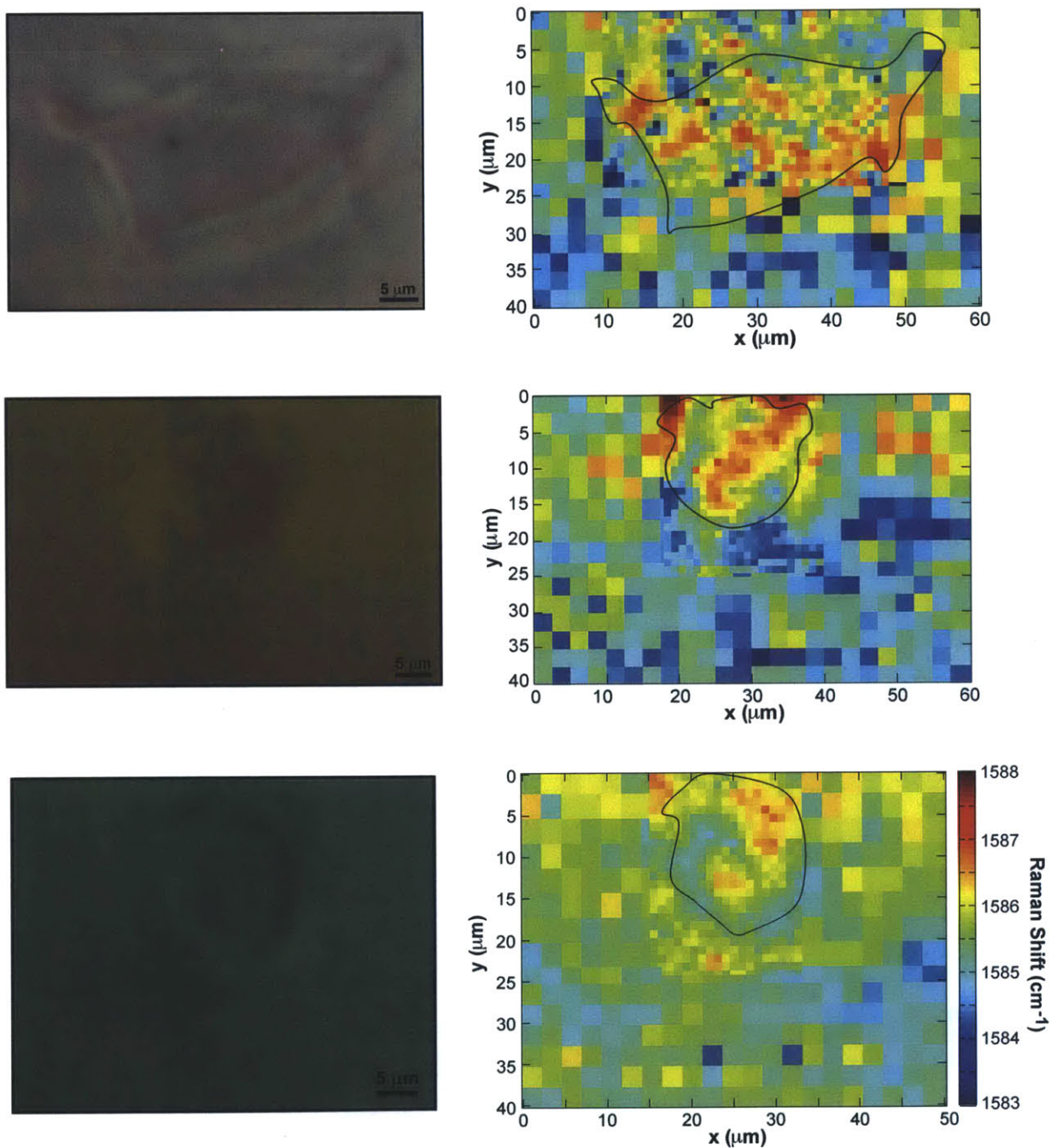


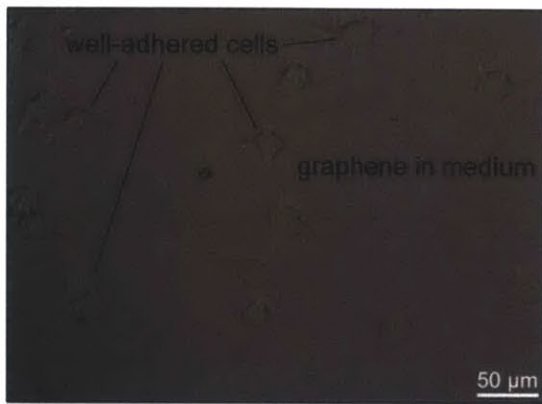
Figure 6.4. Additional examples of Raman footprints for different cells. Left panels show optical images of the cell, right panels the corresponding spatial map of the G peak position (scale is identical for all and shown on the bottom right). The top panel shows a

control cell that was allowed to adhere to graphene for 3 hours in the incubator prior to data collection. A control cell is a non-IgG producing HEK-293F cell (see Chapter 6.2). Middle panel shows an IgG-producing cell that is less adhered (spent 30 minutes in the incubator prior to data collection). Bottom panel shows a less-adhered control cell.

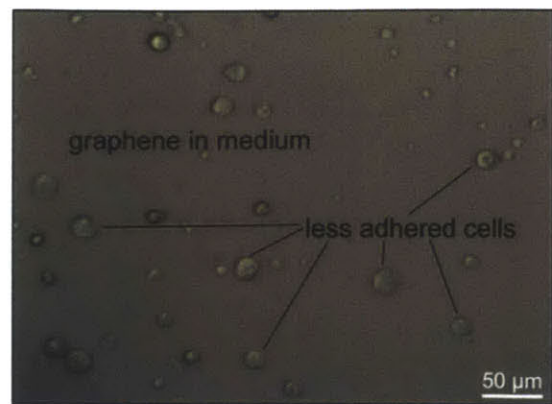
We note that spatial inhomogeneity in these maps is likely not only caused by the cell and the cell medium but also by the graphene itself and the SiO₂ substrate, both of which have documented inhomogeneity from variations in doping and electron/hole puddles in the graphene [21,23,39]. Central to this present study, however, is the observation that underneath and immediately around the cell the graphene exhibits higher values of G_{POS} compared to further away from the cell, indicating the cell is selectively p-doping the graphene within its immediate footprint [19,20,22,33,34]. In light of our earlier findings, we assign these observations to the cellular efflux of acidic products whose protons p-dope the graphene.

Similar spatial footprints have been collected for less-adhered IgG-producing cells (after 30 minutes of incubation), as well as for both well- and less- adhered control (non IgG-producing) cells. Optical images and Raman footprints are shown in Figure 6.4. In suspension, the HEK293 cells are round. When fully adhered to a surface, they are spread, flat and spindle-shaped. The cells that were only allowed to spend 30 minutes in the incubator prior to data collection are still round, indicating they are not fully adhered yet. Figure 6.4 indicates that the doping effect is more pronounced for the more strongly adhered cells as well as for IgG-producing cells compared to non-IgG producing control cells.

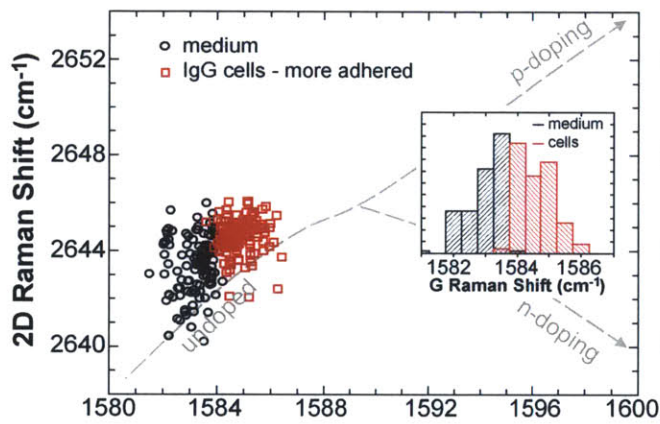
6.3.3. Graphene as a cytometer based on cell-induced graphene doping



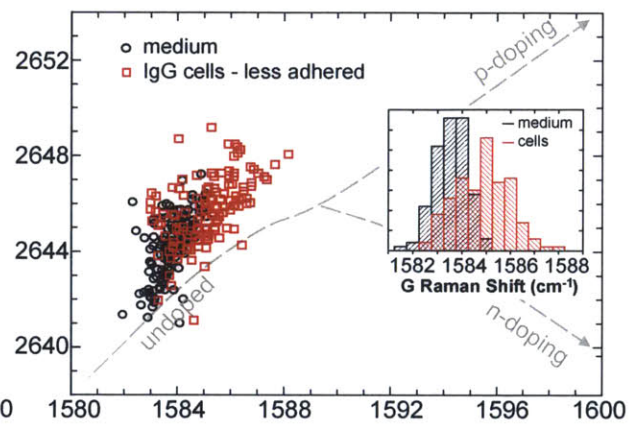
(a)



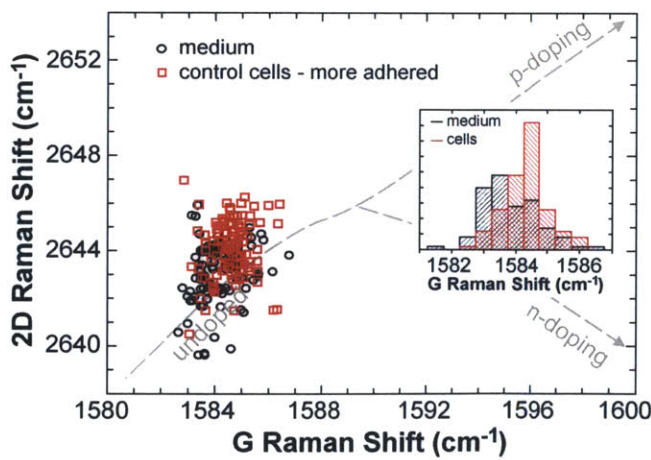
(b)



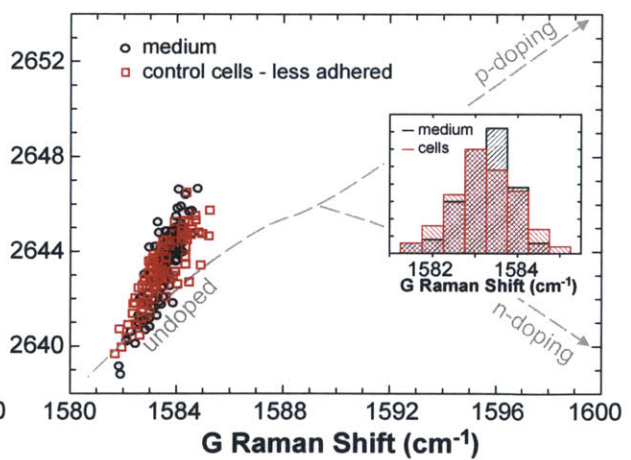
(c)



(d)



(e)



(f)

Figure 6.5. Graphene, a tool for mapping phenotypic diversity in cell populations. Optical micrograph of well-adhered cells (allowed to adhere to graphene for 3 hours in the incubator prior to data collection) in growth medium on graphene (a) and of less adhered cells (spent only 30 minutes in the incubator prior to data collection) in medium

on graphene **(b)**. Scatter plots of 2D peak position vs. G peak position of graphene covered in medium (black dots) and 100 distinct cells (red squares) for IgG-producing cells **((c),(d))** and non-IgG-producing control cells **((e),(f))**. Left panels **((a),(c),(e))** represent well-adhered cells (3 hrs of incubation prior to data collection); right panels **((b),(d),(f))** represent less-adhered cells (30 min of incubation prior to data collection). Dashed lines represent trend lines adapted from ref.[20] The trend lines are shifted downwards to account for the dependence of the 2D peak position on the excitation wavelength (a 532nm laser was used in ref.[20], as opposed to a 633nm laser in this work). Scales and axes are identical for all panels. Insets in **(c),(d),(e)** and **(f)** are histograms of the G peak position of graphene in medium (black) and under the cells (red). $p_{G\text{-position}} < 0.01$ for datasets in panel **(c-e)**, indicating the distributions are significantly different ; $p_{G\text{-position}} = 0.09$ for datasets in panel **(f)** indicating the distributions are not significantly different (see Chapter 4.2.4. for more details).

An alternative way to utilize graphene as a pH sensor array is to reduce the spatial resolution but dramatically increase the throughput by measuring the average local acidification under each single cell in a population. Such an experiment can profile hundreds of cells and again compare the results to established doping trajectories to yield information about the ensemble. This approach also allows us to verify that the data observed for single cells extends to representative populations.

Specifically we collected Raman spectra underneath 100 individual cells for all 4 cases: well-adhered IgG-producing cells, less-adhered IgG-producing cells, well-adhered control cells and less-adhered control cells. For each sample size of 100 cells we collected one full Raman spectrum in the center of each cell. Figure 6.5a and b are optical micrographs displaying typical cell densities used in these experiments, for both the IgG-producing cells and the control cells respectively. Figure 6.5c-f shows scatter plots of $2D_{POS}$ vs. G_{POS} , for cells (red squares) and for growth medium far away from the cell (black dots). The insets display histograms of the G peak positions of the graphene sampled underneath the cells (red) and of the graphene covered in growth medium (black). The growth medium was sampled in various locations on the graphene, but

always at least 100 micron away from a cell to minimize the presence of products excreted by the cells. Scatter plots showing I_{2D}/I_G and G_{FWHM} versus G_{POS} are shown in Fig. 6.6 and 6.7.

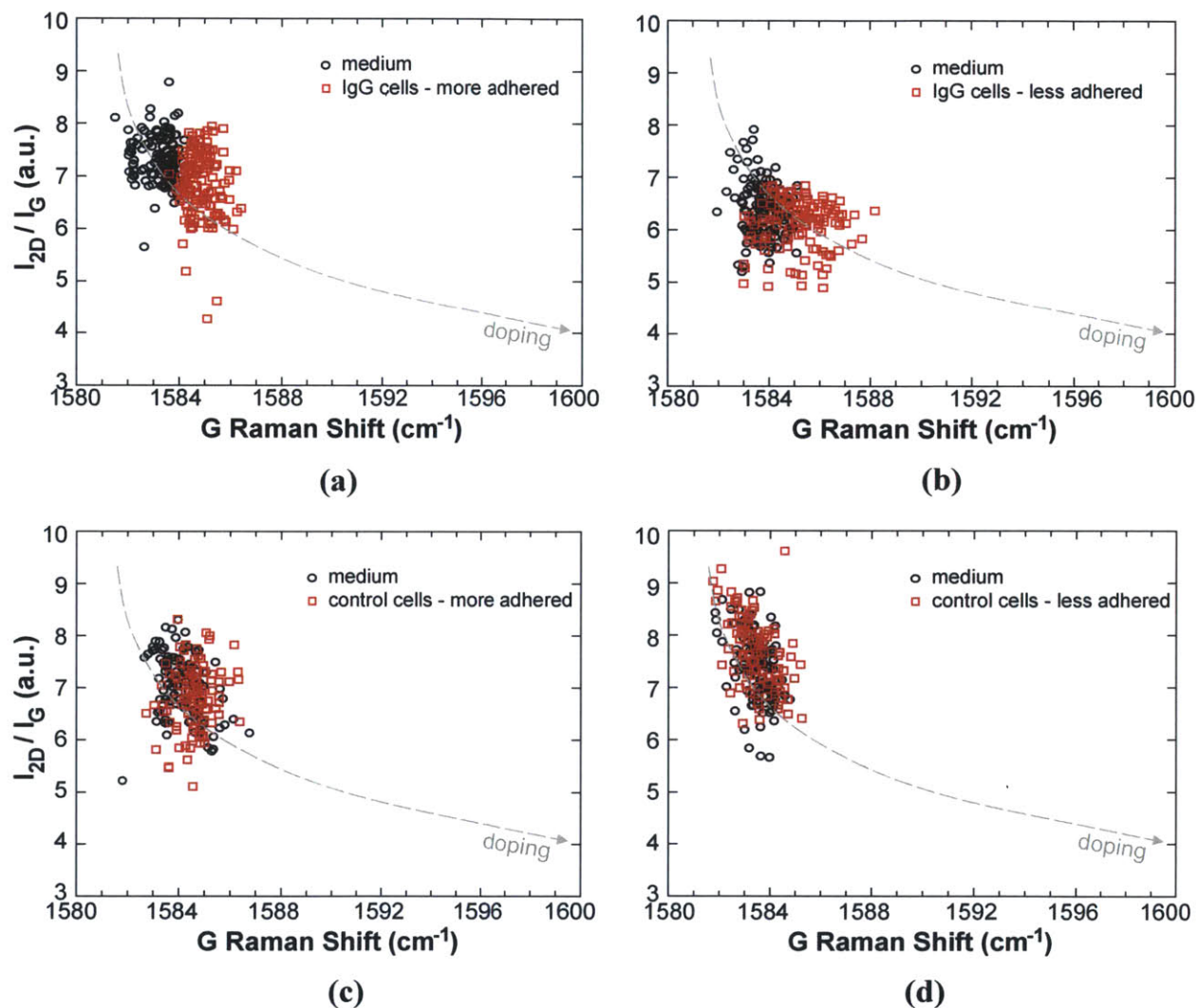


Figure 6.6. Scatter plots of 2D peak position vs. G peak position of graphene covered in growth medium (black dots) and cells (red squares) for IgG-producing cells (top panels) and non-IgG-producing control cells (bottom panels). Left panels show data for well-adhered cells (3 hrs of incubation prior to data collection); right panels represent data for less-adhered cells (30 min of incubation prior to data collection). Dashed lines represent trend lines adapted from ref.[20] The trend lines are shifted downwards to account for the dependence of the 2D peak position on the excitation wavelength (a 532nm laser was used in ref.[20], as opposed to a 633nm laser in this work). Scales are identical for all panels.

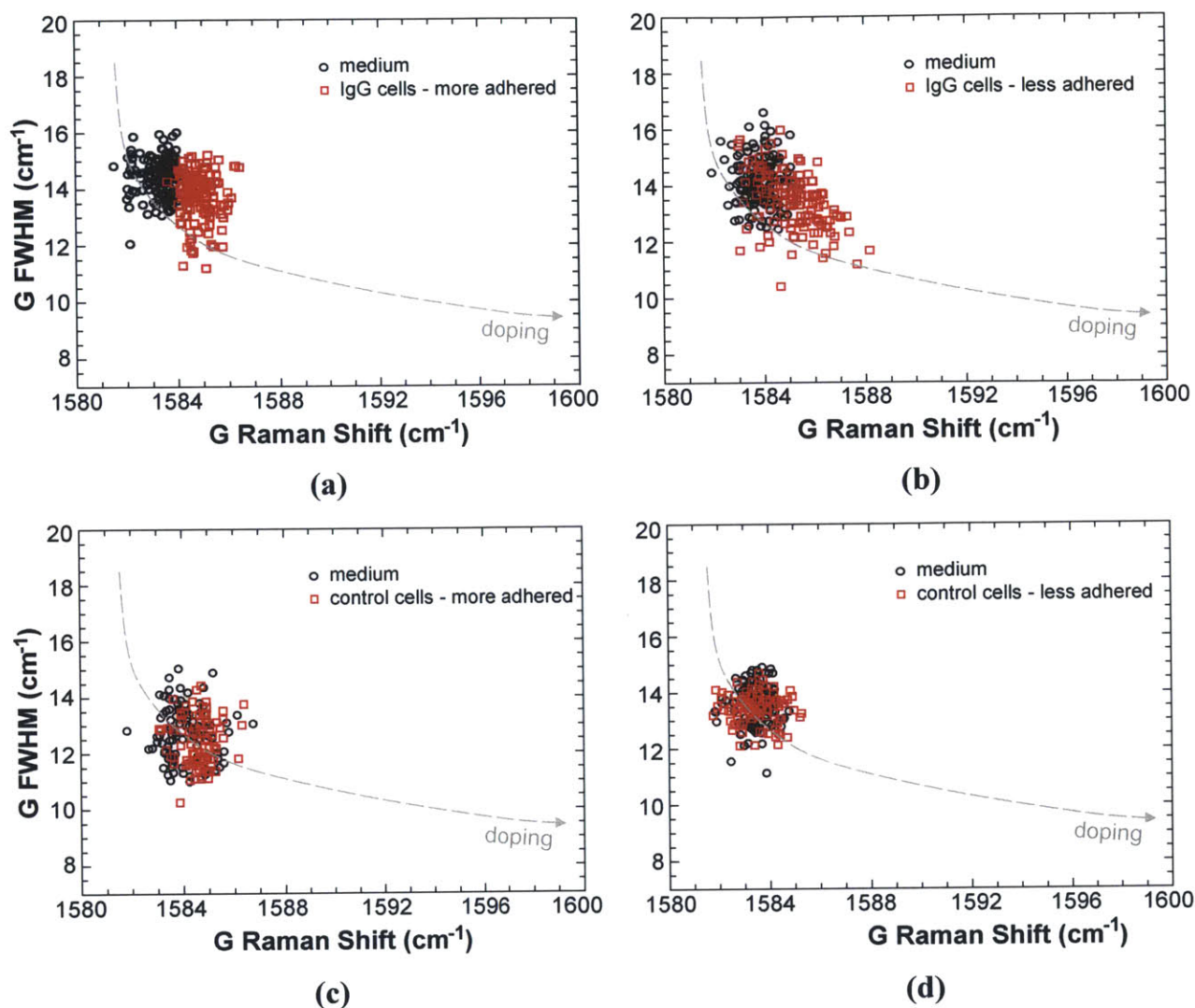


Figure 6.7. Scatter plots of 2D peak position vs. G peak position of graphene covered in growth medium (black dots) and cells (red squares) for IgG-producing cells (top panels) and non-IgG-producing control cells (bottom panels). Left panels show data for well-adhered cells (3 hrs of incubation prior to data collection); right panels represent data for less-adhered cells (30 min of incubation prior to data collection). Dashed lines represent trend lines adapted from ref.[20]. The trend lines are shifted downwards to account for the dependence of the 2D peak position on the excitation wavelength (a 532nm laser was used in ref.[20], as opposed to a 633nm laser in this work). Scales are identical for all panels.

The data in Figures 6.5-6.7 confirm all the trends we uncovered based on the single cell Raman footprints in Figure 6.3 and 6.4:

- Graphene exposed to cell medium is virtually undoped; introducing cells then upshifts the peak positions of graphene locally, indicative of p-doping.
- Increased cell adhesion causes stronger graphene doping (compare left panels (c) and (e) in Figure 6.5 to right panels (d) and (f)). The stronger contact between the cells and the graphene likely allows for more trapping of proton efflux at the graphene surface and a lower local pH.
- IgG-producing cells dope graphene more strongly than non-IgG producing control cells (compare top panels (c) and (d) to bottom panels (e) and (f) in Figure 6.5).

6.3.4. A graphene cell physiometer as a tool to measure cellular metabolic rate

The fact that IgG-producing cells dope graphene to a greater extent than the non-IgG producing cells is consistent with the former having a higher proton efflux rate. The IgG-producing cells have been genetically manipulated to produce an additional antibody in comparison to the control cells (see Chapter 6.2); this additional task requires more energy from the cells, increasing their metabolism, and hence the excretion of acidic products [6,8]. The difference between the measured graphene hole concentration underneath the cell and far away from the cell can be shown to be linearly proportional with the cell's steady state proton production rate (and thus, its metabolic rate):

This is a steady-state (SS) problem involving spherical symmetry (assuming spherical cells). The appropriate equation could be derived from the general vector equation, but we can instead use a simpler approach, based on Fick's law of diffusion (for SS):

$$J = -D \frac{\delta C}{\delta r} \quad (6.11).$$

In the steady state, we assume that a constant rate of generated protons is diffusing out of the cell. Therefore, for any radius, r :

$$J = \frac{Q}{4\pi r^2} \quad (6.12).$$

Thus:

$$\frac{Q}{4\pi r^2} = -D \frac{\delta C}{\delta r} \quad (6.13).$$

Or,

$$Q = -4\pi r^2 D \frac{\delta C}{\delta r} = \text{constant} \quad (6.14).$$

Rearranging and integrating this expression with semi-infinite boundary conditions:

$$\int_C^{C_{med}} dC = \frac{-Q}{4\pi D} \int_r^\infty \frac{1}{r^2} dr \quad (6.15)$$

$$C_{med} - C = \frac{Q}{4\pi D} \left[\frac{1}{r} \right]_r^\infty = \frac{Q}{4\pi D} \left(\frac{1}{\infty} - \frac{1}{r} \right) = -\frac{Q}{4\pi D r} \quad (6.16).$$

So

$$C = C_{med} + \frac{Q}{4\pi D r} \quad (6.17).$$

At cell radius r_0 (assume $\sim 10 \mu\text{m}$) $C = C_{cell}$

$$C_{cell} = C_{med} + \frac{Q}{4\pi D r_0} \quad (6.18).$$

Thus:

$$Q = 4\pi D r_0 (C_{cell} - C_{med}) \quad (6.19).$$

The proton measurements described in the main manuscript are surface concentrations, not bulk concentrations. These can be linked by an adsorption constant. At equilibrium we can state that

$$K = \frac{k_{on}}{k_{off}} = \frac{\Gamma}{(\Gamma_{max} - \Gamma) C_{bulk}} \quad (6.20),$$

where K is the equilibrium adsorption constant, k_{on} is the adsorption rate constant and k_{off} the desorption rate constant, Γ is the surface concentration (in $\#/cm^2$), Γ_{max} is the maximum surface concentration and C_{bulk} is the bulk concentration (in $\#/cm^3$).

Rearranging this leads to

$$\Gamma = \frac{K C_{bulk} \Gamma_{max}}{(1 + K C_{bulk})} \quad (6.21).$$

In the present case $\Gamma \ll \Gamma_{max}$, as the largest obtained surface concentration (at pH=0) equals $9.15 \times 10^{12} cm^{-2}$, whereas the maximal surface concentration equals $3.8 \times 10^{15} cm^{-2}$, i.e., the total carbon atom density of graphene. Thus eqn. (6.20) becomes:

$$K = \frac{\Gamma}{\Gamma_{max} C_{bulk}} \quad (6.22).$$

Rearranging:

$$\Gamma = K C_{bulk} \Gamma_{max} \quad (6.23).$$

Combining eqn. (6.19) with (6.13) relates the cellular proton production rate Q (related to its metabolic activity) to the proton surface concentration Γ :

$$Q = \frac{4\pi D r_0}{K \Gamma_{max}} (\Gamma_{cell} - \Gamma_{med}) \quad (6.24),$$

where $\frac{4\pi D r_0}{K \Gamma_{max}}$ is a constant.

This implies that Q is linearly proportional to the difference in proton surface concentration under the cell and in the medium. These quantities were indirectly measured as the G peak position can translated into a surface hole concentration[20]:

For IgG producing, well-adhered, based on the statistical analysis of the 100 cells (Fig. 6.5):

$$|\Gamma_{cell} - \Gamma_{med}| = 1.28 \times 10^{12} \text{ cm}^{-2}$$

For non-IgG producing, well-adhered, based on the statistical analysis of the 100 cells (Fig. 6.5):

$$|\Gamma_{cell} - \Gamma_{med}| = 0.32 \times 10^{12} \text{ cm}^{-2}.$$

Compared to well-adhered control cells, the IgG producing well-adhered cells have a proton production rate (and thus metabolism) that is four times higher.

To further substantiate our claim that the metabolic rate is the main factor that distinguishes the Raman signal of IgG- from non-IgG-producing cells, we examined whether IgG itself (excreted by the genetically manipulated IgG-producing cells) p- or n-dopes graphene upon adsorption. IgG produced by the HEK-293F cells was collected and concentrated to 1.5 mg/ml in phosphate buffered saline (PBS). As we have shown

that PBS has a significant effect on the Raman spectrum of graphene (Fig. 6.2) the PBS was exchanged for medium by centrifuge filtration to best mimic the conditions of our experiment. The filter tubes (Amicon, Millipore) had a membrane with a MWCO (molecular weight cut off) value of 3000 Da. The IgG is ~150kDa, and will thus definitely be retained by the membrane. We added 800 μ l of L-15 growth medium to 200 μ l of PBS containing 0.3mg IgG. This solution is centrifuged five consecutive times for 15 minutes at 4000 rpm. After each of the first four centrifugations the filtrate (~400 μ l) is removed and an equivalent volume of new L-15 medium is added to the residue. In order to get a high enough concentration of IgG in the final product, we added only 100 μ l of fresh growth medium prior to the fifth centrifugation, which resulted in a final residue of 300 μ l.

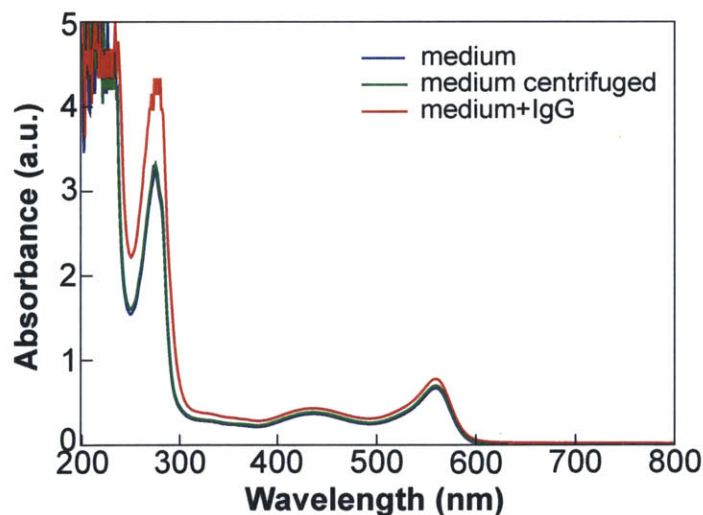


Figure 6.8. Absorption spectra of growth medium (blue), growth medium that has been centrifuged (green), and medium+IgG (red).

Most proteins absorb strongly at 280nm [46]; comparison of UV-VIS absorbance of pure medium (blue curve in Fig. 6.8) and the medium+IgG solution after filtration (red

curve in Fig. 6.8) shows a clear increase in absorbance at 280 nm. In order to determine whether this increase is caused by the presence of IgG or by an up-concentration of proteins in the growth medium after five centrifuge filtration cycles we performed a control experiment in which L-15 growth medium was centrifuge-filtered under the exact same conditions described above.

UV-VIS spectroscopy of this sample shows almost no increase of absorbance at 280 nm (green curve in Fig. 6.8) compared to the absorbance of pure medium (blue curve in Fig. 6.8), indicating the increase in absorbance for the medium+IgG case is predominantly caused by IgG. IgG has a protein extinction coefficient of 14 (i.e. $A_{280\text{nm}}^{1\%} = 14$, where $A_{280\text{nm}}^{1\%}$ is the absorbance at 280 nm for a 1% (1g/100ml) solution measured in a 1cm path length)[47]; therefore $A_{280\text{nm}}^{1\text{mg/ml}} = 1.4$. The increase in absorbance at 280 nm between the centrifuged medium and the medium+IgG solution was 1.386, implying the total concentration of IgG in medium was 0.99 mg/ml (=1.386/1.4), indicating we have recuperated ~ 0.297mg of IgG (i.e. it was a 99% successful buffer exchange).

Raman maps (consisting of 121 spatially distinct points) were collected for graphene in air, graphene exposed to growth medium and graphene exposed to the IgG in growth medium (Fig. 6.9). All 3 datasets were collected in the same 20x20 μm area on the same sample of graphene. Exposure of the graphene to medium decreases the amount of excess charge carriers in graphene (red squares) compared to when graphene is exposed to air (blue dots), with the data points shifting towards the undoped end of the doping trajectories. The L-15 growth medium contains n-doping amino acids that can counteract the initial p-doping in graphene, rendering it overall more undoped. Moreover it is likely

that medium partially shields the graphene from the p-doping oxygen in the air. Interestingly the average G-peak position of graphene exposed to medium ($\sim 1587 \text{ cm}^{-1}$) is significantly higher than that measured in the earlier experiments ($\sim 1584 \text{ cm}^{-1}$ e.g. in Fig. 6.5).

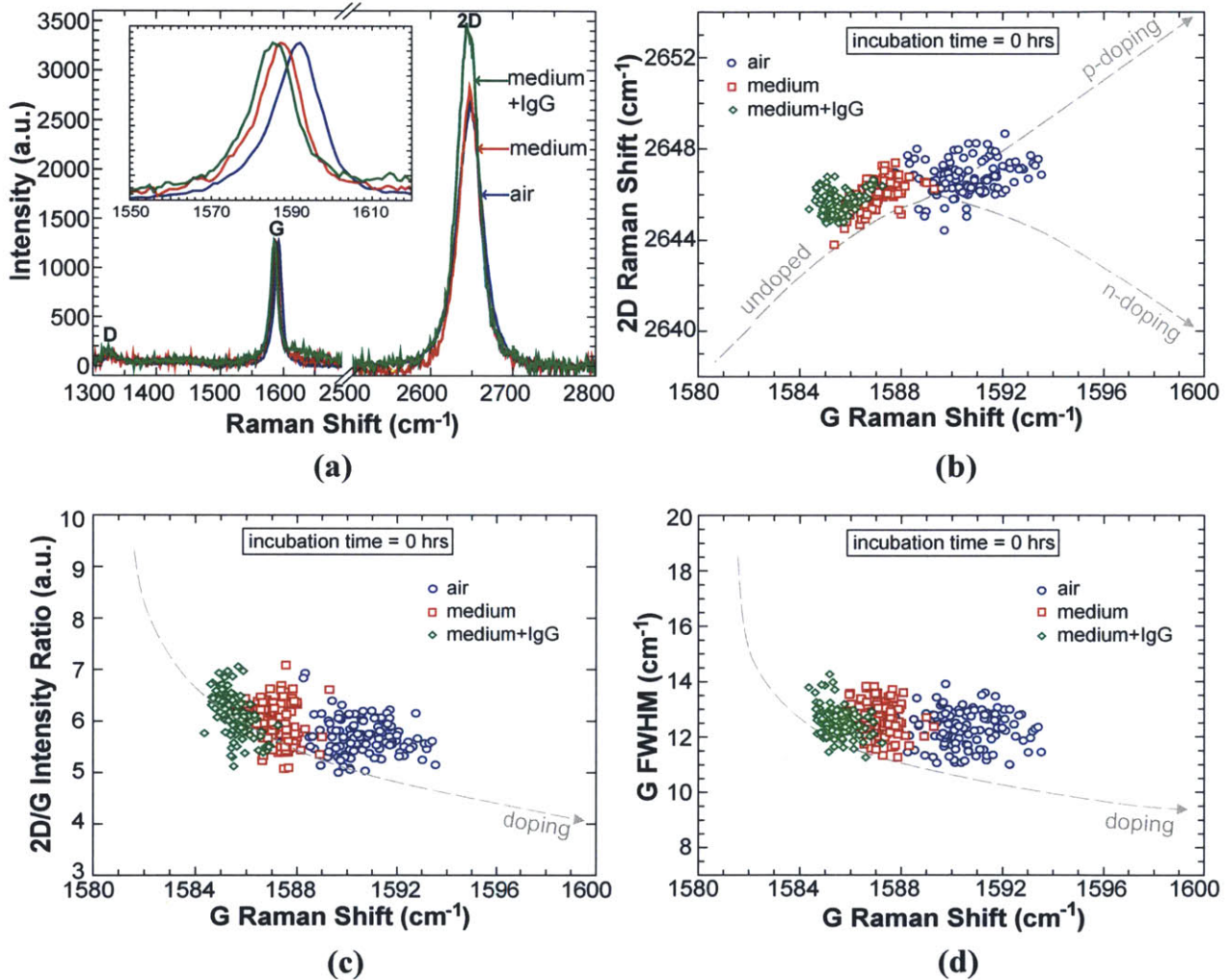


Figure 6.9 Raman data of graphene exposed to air (blue), growth medium (red) and both growth medium and IgG (green), without incubation. **(a)** Characteristic Raman spectra showing the D, G and 2D peaks of graphene; inset zooms in on the G peak. **(b)** $2D_{POS}$ - G_{POS} doping trajectory. **(c)** $I_{2D/G}$ - G_{POS} doping trajectory. **(d)** G_{FWHM} - G_{POS} doping trajectory. Dashed lines are a guide to the eye adapted from ref.[20]. The trend lines in (a) are shifted downwards to account for the dependence of the 2D peak position on the excitation wavelength (a 532nm laser was used in ref.[20], as opposed to a 633nm laser in this work). For all distributions compared in this figure: $p_{G\text{-position}} < 0.01$ (see Chapter 4.2.4 for more details).

The main difference between both sets of measurements is that the graphene exposed to growth medium in Fig. 6.5 had spent 0.5-3 hours in the incubator prior to Raman mapping. In effect, incubation of the medium-covered graphene samples was shown to downshift the G and 2D peaks (Fig. 6.10). Since the incubator is a CO₂-rich environment it is plausible that CO₂ replaces the oxygen, thereby removing the p-dopant.

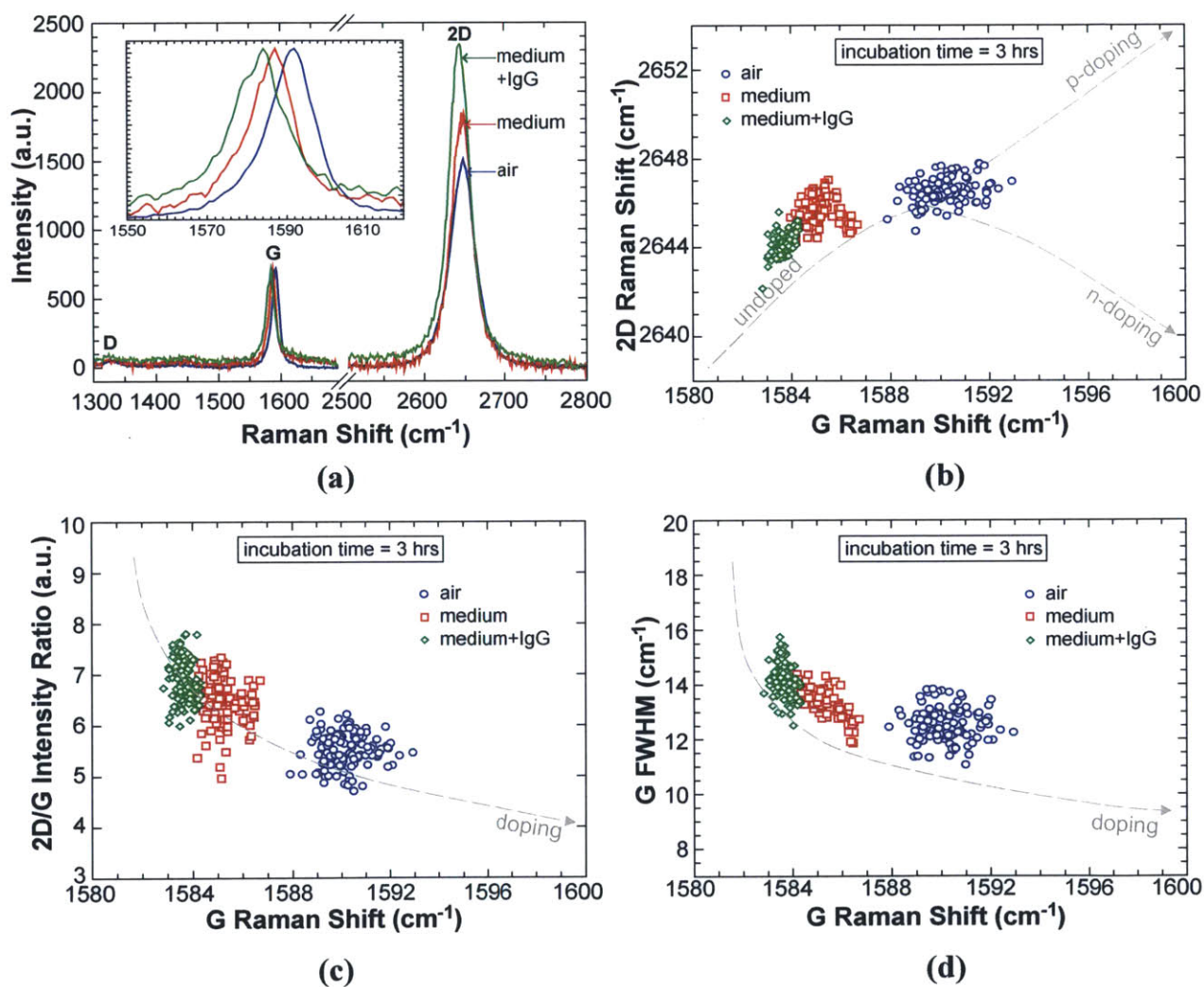


Figure 6.10. Raman data of graphene exposed to air (blue), growth medium (red) and both growth medium and IgG (green), after incubation. (a) Characteristic Raman spectra showing the D, G and 2D peaks of graphene; inset zooms in on the G peak. (b) 2D_{POS}-G_{POS} doping trajectory. (c) 2D/G doping trajectory. (d) G_{FWHM}-G_{POS} doping trajectory. For all distributions compared in this figure: $p_{G\text{-position}} < 0.01$ (see Chapter 4.2.4 for more details).

It is clear that adding IgG to the growth medium (green diamonds in Fig. 6.9 and 6.10) further decreases the average doping in graphene, likely due to the presence of n-doping moieties in the protein that make the originally p-doped graphene even more neutral. The doping effects these chemical environments have on graphene are added to Table 6.1.

Chemical Environment	Average hole-doping in graphene ($\times 10^{12} \text{cm}^{-2}$)	Change compared to graphene in air ($\times 10^{12} \text{cm}^{-2}$)	dopant type
Air	5.20	0	p
1M NaOH	1.80	-3.40	n
10mM NaOH	3.86	-1.33	n
PBS	4.01	-1.19	n
DI water	5.78	+0.58	p
10mM HCl	6.39	+1.19	p
1M HCl	9.16	+3.96	p
Medium	4.03	-1.17	n
Medium	3.23	-1.97	n
+ Incubation			
Medium+IgG	3.35	-1.84	n
Medium+IgG	2.20	-3.00	n
+ Incubation			

Table 6.1. Summary of doping effects of different chemical environments on graphene. Based on the monitoring of graphene Raman G and 2D peak positions while electrostatically gating graphene (thereby at each gate voltage V_G injecting a known amount of excess charge carriers into the graphene) a universal relationship between both has been established[20]. Applying this relationship the total average degree of hole-doping is determined for each dopant, as well as the deviation in doping from bare graphene in air, on a Si/SiO₂ wafer.

The result of this control experiment allows us to exclude IgG as an alternatively responsible agent for the observed doping differences between the control cells and the IgG-producing cells, and supports our conclusions. Additionally, it opens the door to

monitor the presence of a variety of other chemical analytes with graphene, based on the sensitivity of its Raman signal to excess charge carriers presented by such analytes. The response to IgG is particularly noteworthy, since antibody structure is largely conserved [48], and the extension of this technique to antigen detection is highly compelling.

6.4. Conclusions

A nanoscale version of a micro-physiometer – a device that measures cellular metabolic activity from the local acidification rate, was demonstrated. Graphene can function as an array of independent pH sensors enabling subcellular and spatiotemporal detection of single biological cells. Raman spectroscopy shows that aqueous protons (H^+) p-dope graphene – in agreement with established doping trajectories, and that graphene displays two distinct pKa values (2.9 and 14.2). The cell physiometer allows micron spatial resolution of cellular acidification, differentiating immunoglobulin (IgG) producing human embryonic kidney (HEK) cells from non-IgG-producing control cells. Graphene also allows single cell counting in a population for mapping phenotypic diversity, variances in metabolic rate, and cellular adhesion. This work motivates the application of graphene as a unique biosensor array for cellular and sub-cellular interrogation.

6.5. Ongoing work

There is a pressing need for tools capable of single cell analysis of metabolic activity. Cancer cells typically have a glycolytic rate up to 200 times higher than non-

cancerous cells [2,3], leading to a stronger acidification of their environment. The proposed graphene physiometer could gauge the metabolic activity of such cells, correlate this with tumor malignancy [49], and ultimately derive options for personalized medical treatments. Single-cell or population-based assessments of drug toxicity using pH changes of the cells are also compelling [50]. Graphene has advantages for monitoring biofilm growth, which is strongly pH-dependent [5].

Ongoing and future work will explore these applications as well as focus on increasing the sensor sensitivity. We have set up a collaboration with Dr. Jeon Woong Kang and Dr. Ramachandra Dasari of the Laser Biomedical Research Center in MIT's spectroscopy lab, allowing us to use their home-built high signal/noise ratio confocal Raman setup that can simultaneously collect Rayleigh scattering (used to construct confocal reflectance images of the cells). An objective with a high numerical aperture and high near-infrared (nIR) transmission, a sensitive detector with a high quantum-efficiency in the nIR and galvanometers to direct the Raman laser excitation (8mW at the sample) on the sample improve both spatial resolution and collection speed. An exposure time of 0.5 seconds is sufficient to achieve strong Raman signals. For example, to collect a map of Raman spectra in a $45\mu\text{m} \times 45\mu\text{m}$ area, with $1.5\mu\text{m}$ step size, ~ 7 minutes are required, which is ~ 30 times faster than when using the Horiba Jobin Yvon LabRAM HR800 setup. The home-built instrument is described in more detail in reference [51]. The only downside is that the spectral range of this Raman spectrometer is limited to 1840 cm^{-1} , which means only the graphene Raman D and G peaks can be monitored.

Additionally we aim to explore the detection of different analytes, such as catecholamines, an important group of neurotransmitters and neuromodulators, of which

the most important examples are epinephrine, norepinephrine and dopamine. A lot of research efforts focus on spatially and temporally detecting exocytosis of these molecules across the membrane of single cells [52-58]. Ultimately, we wish to study dopamine uptake and release in fully differentiated healthy mammalian neural cell network.

Preliminary work is done using neuroendocrine, dopaminergic rat pheochromocytoma (PC12) cells, a clone cell line that shares a lot of properties of sympathetic ganglion neurons and is often used to study properties of the latter, since the primary mammalian neurons stop proliferation once matured, making them hard to work with in a laboratory setting [53]. Like sympathetic ganglion neurons, the catecholamines in PC12 cells contain mostly dopamine, a small amount of norepinephrine, and no detectable level of epinephrine [53]. When these cells are exposed to a solution with a high concentration of K^+ , the latter depolarizes the cell membrane and allows a Ca^{2+} influx, which in turn causes the exocytosis of vesicles of catecholamines [52,53,56,58]. Current methods for detecting exocytosed dopamine include amperometric detection with a carbon fiber electrode [53], cyclic voltammetry [59], patch clamp [60], capillary electrophoresis [61], electrochemical cytometry [52], and field effect transistors [56]. Currently, the spatial and resolutions for chemical measurements are $\sim 100 \mu m$; this is where our Raman sensing technique displays a clear advantage. Passaging the PC12 cells happens following the procedure described in Chapter 6.2.4., with two exceptions. Firstly, the PC12 neural progenitor cells are much less prone to adhere to a substrate than the HEK293 tissue cells, alleviating the need to use trypsin when passaging them. Secondly, RPMI-1640 medium with 10% horse serum and 5% bovine serum is used to culture the cells (standard for this cell line [62]), instead of L-15 or Dulbecco medium.

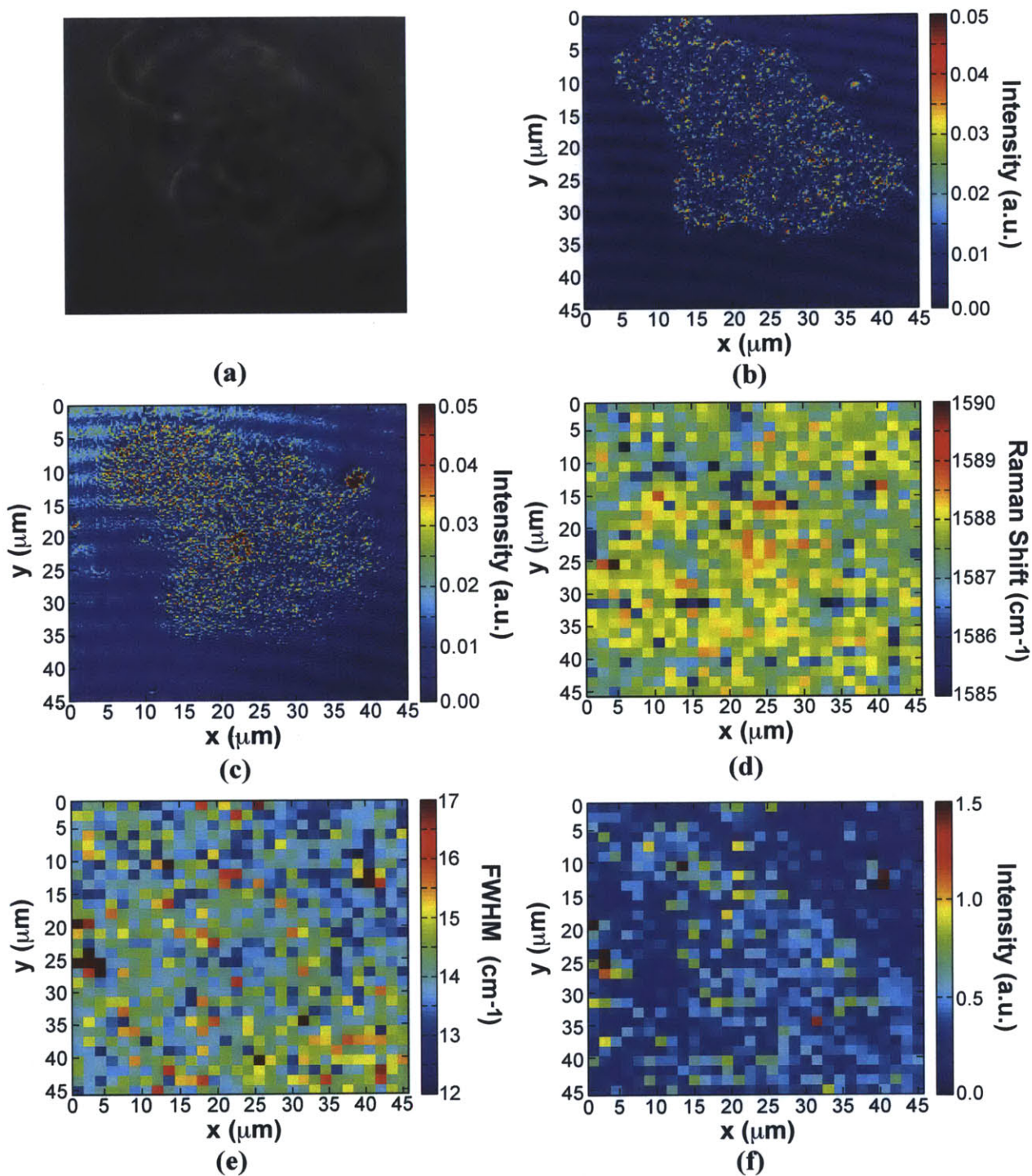


Figure 6.11. Effect of non-stimulated neural progenitor cells on the graphene Raman signal. **(a)** Optical micrograph of a cluster of PC12 cells on graphene (45 μm x 45 μm). **(b)** Rayleigh scattering (i.e. confocal reflectance) map of the area shown in (a), in the central focal plane of the cell cluster. **(c)** Rayleigh scattering map of the area shown in (a), in the graphene focal plane, showing the part of the cell cluster that is well-adhered to the graphene. **(d-f)** Spatial map of Raman G peak position (d), G peak FWHM (e), and D to G intensity ratio (f) of the graphene shown in (a).

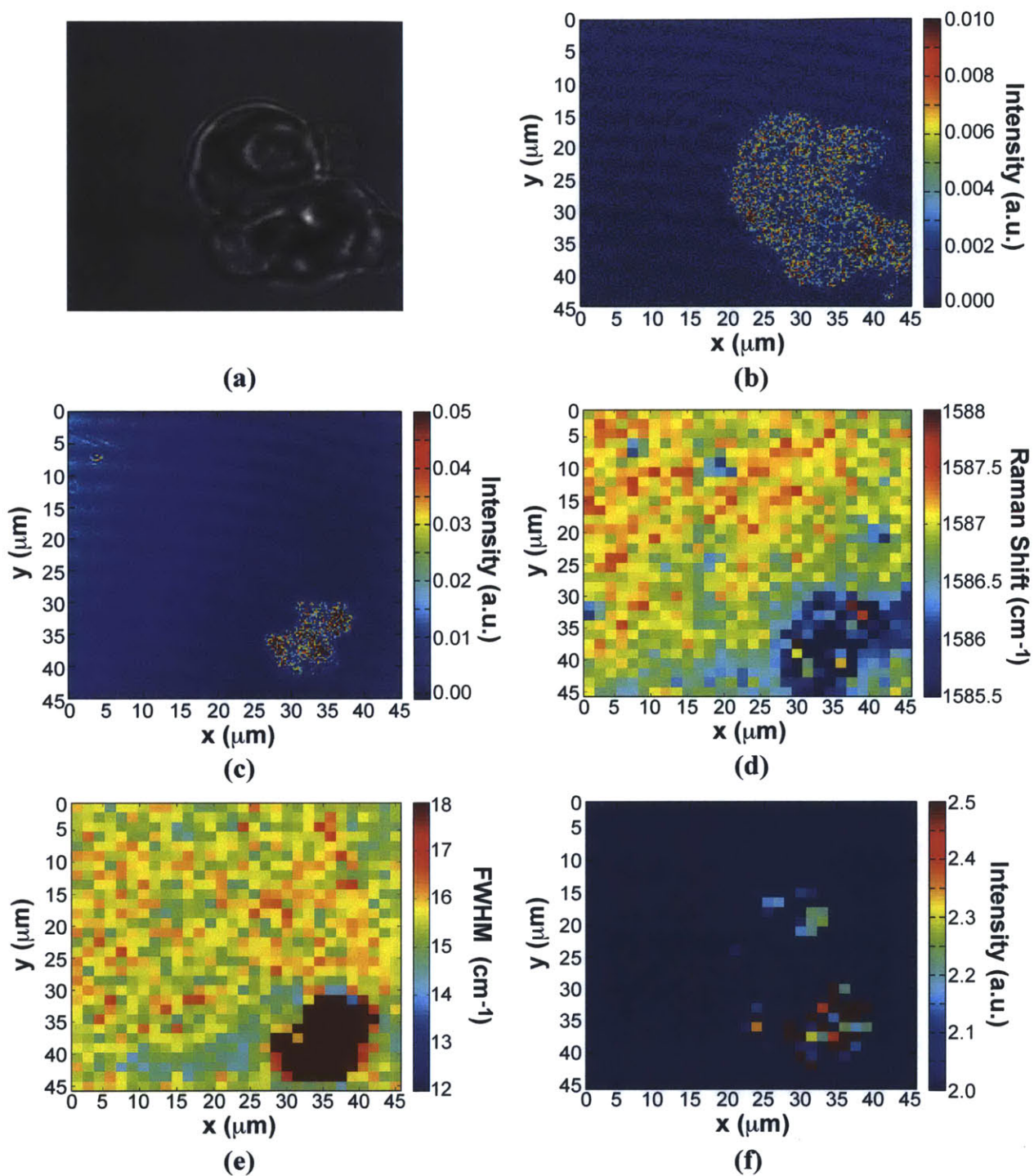


Figure 6.12. Effect of stimulated neural progenitor cells on the graphene Raman signal. **(a)** Optical micrograph of a cluster of PC12 cells on graphene ($45\mu\text{m} \times 45\mu\text{m}$). **(b)** Rayleigh scattering (i.e. confocal reflectance) map of the area shown in (a), in the central focal plane of the cell cluster. **(c)** Rayleigh scattering map of the area shown in (a), in the graphene focal plane, showing the part of the cell cluster that is well-adhered to the graphene. **(d-f)** Spatial map of Raman G peak position (d), G peak FWHM (e), and D to G intensity ratio (f) of the graphene shown in (a).

Figure 6.11 shows that non-stimulated PC12 cells do not leave a significant Raman footprint on the graphene it covers. Note that since neural progenitor cells are typically less adherent than tissue cells, they tend to cluster together more (due to a stronger affinity for one another than for a substrate) and have a relatively round shape. In many ways the cells behave like the less-adhered control cells of Chapter 6.3.3.; it is thus not surprising the cells do not display a metabolic footprint in the graphene Raman signal (see also Figure 6.5f).

Figure 6.12 shows the effect of a potassium-evoked calcium-dependent dopamine secretion on the graphene Raman signal. 50 μ l of 120 mM aqueous KCl solution was added to the already present 150 μ l of medium containing cells on the graphene surface. Figure 6.12a-b show the outline of the cell cluster in the cluster's focal plane, and Figure 6.12c is a confocal reflectance map of the cell cluster collected in the graphene focal plane. Comparing Figure 6.12c to 6.12b shows only the bottom part of the cell cluster is well adhered to the graphene surface. Upon stimulation, the Raman signal of the graphene that is in close contact with the cells displays a lower G peak position (Fig. 6.12d), an increased G peak width (Fig. 6.12e) and an increased D to G intensity ratio (Fig. 6.12f). The decrease in G peak position and increase in its width is indicative of neutralization of the pre-hole doped graphene (similarly observed for exposure of graphene to IgG – see Fig. 6.9-6.10 and to -OH groups – see Fig. 6.2). This is expected given the electron-rich aromatic ring, the -OH groups and the amine group that make up the dopamine molecule. The G peak width increase is very significant; it can also signify an increased concentration of lattice defects [63], which is consistent with the observation

of the increased D to G intensity ratio [63] (which does not occur for graphene exposed to IgG).

Overall, Figure 6.12 indicates that dopamine not only changes the charge density of graphene by doping it but also covalently interacts with it. This is not surprising given the knowledge that dopamine is an extremely reactive molecule that can oxidize to form free radicals and reactive quinones [64]. It should be noted that the Raman data in Figure 6.12 were collected about one minute after cellular stimulation. Collecting the dataset took ~7 minutes. A second dataset was collected 10 minutes after stimulation and the results were quasi identical, indicating that (1) the effect of dopamine on the graphene is irreversible and/or (2), the dopamine released by the cell is ‘trapped’ between the cell and the graphene and can not diffuse out of this small pocket. Likely a combination of both explains the data. The covalent modification of the lattice (resulting in the increased D to G intensity ratio and increased G peak width) is typically irreversible, while physisorption (resulting in the decreased G peak position) can be reversible.

From Figure 6.12 it is clear that adhesion once more plays an important role: only the part of the graphene to which the cells are closely adhered displays a significant change in its Raman signal upon stimulation. Likely the dopamine released from the other cells in the cluster diffuses quickly in the medium, and is thereby significantly diluted to such an extent that it barely affects the graphene Raman signal. Increased adhesion could be achieved by coating the graphene with poly-L-lysine prior to depositing cells on it [65]. Moreover, using fully differentiated neurons (with dendrites and axons) rather than the round progenitor cells will likely also eliminate the adhesion issue. Future efforts will explore these options.

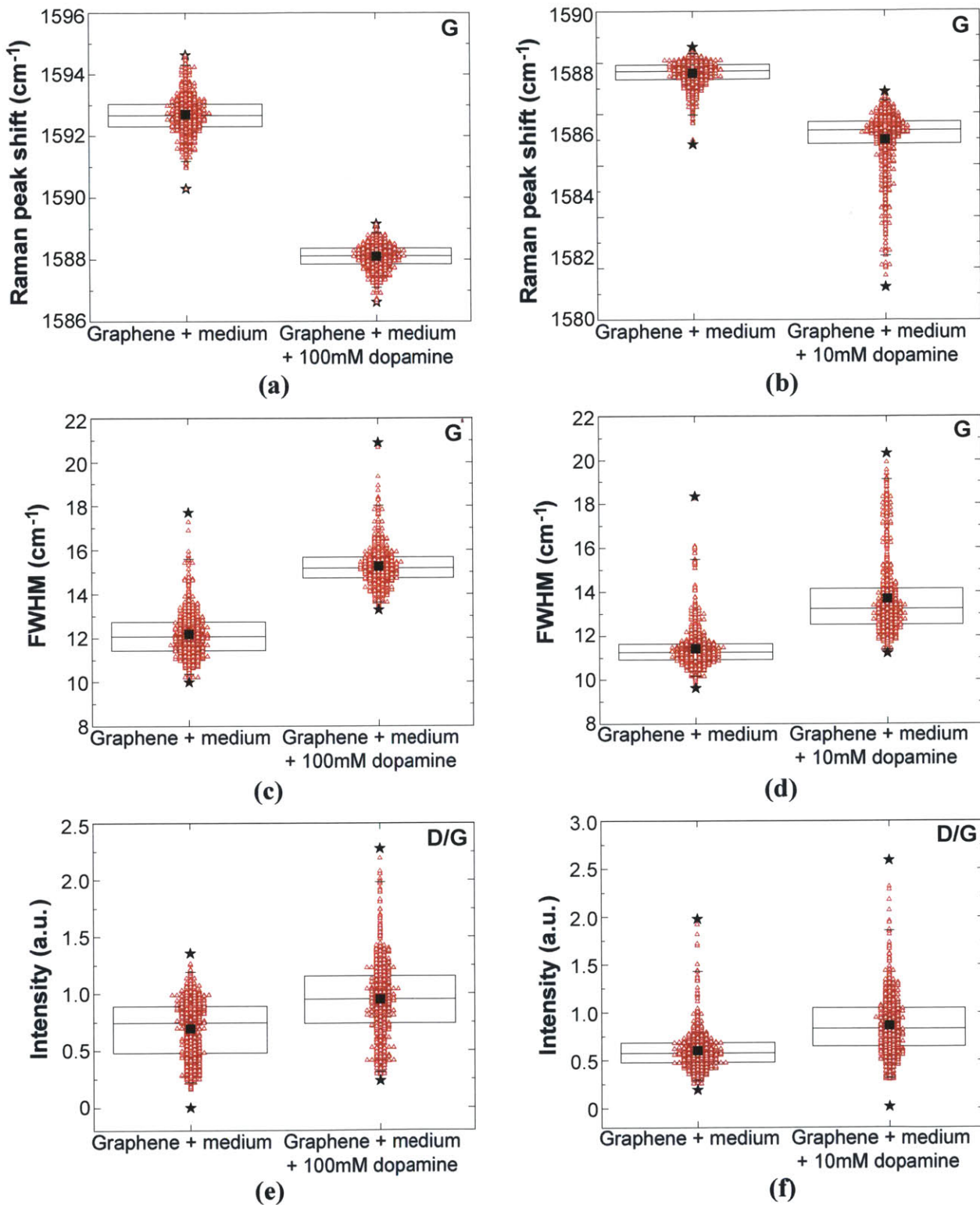


Figure 6.13. Raman data of graphene exposed to medium vs. medium containing dopamine. **(a-b)** Effect of dopamine on the graphene G peak position. **(c-d)** Effect of dopamine on the graphene G peak width. **(e-f)** Effect of dopamine on the graphene D to G intensity ratio. The lower and higher end of the boxplots represent the 25 and 75

percentile mark respectively; whereas the middle line is the median value of the distribution. Minimum and maximum values are represented by black stars, and the average is the black square. The red triangles represent the complete dataset, superimposed on the boxplots. Panels (a),(c) and (e) show the Raman effect of 100mM dopamine, whereas panels (b),(d) and (f) reveal the effect of 10mM dopamine. For all distributions compared in this figure: $p < 0.01$ (see also Chapter 4.2.4. for more details).

To verify that the observed effects in Figure 6.12 are caused by dopamine, graphene control samples were exposed to different concentrations of dopamine. For each scenario, 900 Raman spectra were collected in a $45\mu\text{m} \times 45\mu\text{m}$ area. The main results are incorporated in Figure 6.13. The left (right) panels show the effect on the graphene Raman signal of adding 100 (10) mM dopamine to the medium. Similarly to what was observed for the graphene covered by stimulated cells, the G peak position decreases, the G peak width increases and the D to G intensity ratio increases. Figure 6.13 also indicates the importance of making relative comparisons rather than absolute statements about the values of Raman peak parameters. Everything depends on the starting doping and defect state of the graphene sample, which can differ between different growths, but also between different samples (e.g. one substrate may be cleaner than another).

When graphene is exposed to 100mM of dopamine the average G peak position decreases by $\sim 4.5 \text{ cm}^{-1}$, the peak width increases by $\sim 3.1 \text{ cm}^{-1}$ and the D to G intensity ratio increases from ~ 0.7 to 0.95. For graphene exposed to 10mM of dopamine the dopamine the average G peak position decreases by $\sim 2.6 \text{ cm}^{-1}$, the peak width increases by $\sim 2.3 \text{ cm}^{-1}$ and the D to G intensity ratio increases from ~ 0.6 to 0.85. The observed Raman changes for graphene covered by a stimulated cell (Figure 6.12d-f) fall in this 10-100mM range. Amperometric measurements of stimulated PC12 cells have revealed that $\sim 190 \text{ zmol}$ catecholamines (i.e. 114300 molecules) are released per vesicle, which yields an average vesicular transmitter concentration of 0.11M [53], supporting our findings.

6.5. References

- 1 Paulus, G. L. C., Lee, K.Y., Reuel, N.F., Wang, Q.H.; Grassbaugh B.R., Kruss S., Nelson, J.T., Landry, M.P., Zhang, J., Mu, B., Kang, J.W., Dasari, R.R., Opel, C.F.; Wittrup, K.D. & Strano, M.S. A graphene-based physiometer array for the analysis of single biological cells. *Nature Chemistry* **out for review** (2013).
- 2 Warburg, O. On the origin of cancer cells. *Science* **123**, 309-314 (1956).
- 3 Urano, Y., Asanuma, D., Hama, Y., Koyama, Y., Barrett, T., Kamiya, M., Nagano, T., Watanabe, T., Hasegawa, A. & Choyke, P. L. Selective molecular imaging of viable cancer cells with pH-activatable fluorescence probes. *Nature medicine* **15**, 104-109 (2008).
- 4 Nelson, S. D. Metabolic activation and drug toxicity. *Journal of medicinal chemistry* **25**, 753-765 (1982).
- 5 Dunne, W. M. Bacterial adhesion: seen any good biofilms lately? *Clinical microbiology reviews* **15**, 155-166 (2002).
- 6 Hafner, F. Cytosensor® Microphysiometer: technology and recent applications. *Biosensors and Bioelectronics* **15**, 149-158 (2000).
- 7 Mosmann, T. Rapid colorimetric assay for cellular growth and survival: application to proliferation and cytotoxicity assays. *Journal of Immunological methods* **65**, 55-63 (1983).
- 8 Owicki, J. C. & Wallace Parce, J. Biosensors based on the energy metabolism of living cells: the physical chemistry and cell biology of extracellular acidification. *Biosensors and Bioelectronics* **7**, 255-272 (1992).
- 9 Feng, L. & Liu, Z. Graphene in biomedicine: opportunities and challenges. *Nanomedicine* **6**, 317-324 (2011).
- 10 Chen, J. H., Jang, C., Adam, S., Fuhrer, M., Williams, E. & Ishigami, M. Charged-impurity scattering in graphene. *Nature Physics* **4**, 377-381 (2008).
- 11 Wheeler, A. R., Throdset, W. R., Whelan, R. J., Leach, A. M., Zare, R. N., Liao, Y. H., Farrell, K., Manger, I. D. & Daridon, A. Microfluidic device for single-cell analysis. *Analytical chemistry* **75**, 3581-3586 (2003).
- 12 Cornelison, D. & Wold, B. J. Single-cell analysis of regulatory gene expression in quiescent and activated mouse skeletal muscle satellite cells. *Developmental biology* **191**, 270-283 (1997).
- 13 Reiter, M., Kirchner, B., Müller, H., Holzhauer, C., Mann, W. & Pfaffl, M. Quantification noise in single cell experiments. *Nucleic Acids Research* **39**, e124-e124 (2011).
- 14 Jin, H., Heller, D. A., Kalbacova, M., Kim, J. H., Zhang, J., Boghossian, A. A., Maheshri, N. & Strano, M. S. Detection of single-molecule H₂O₂ signalling from epidermal growth factor receptor using fluorescent single-walled carbon nanotubes. *Nature Nanotechnology* **5**, 302-309 (2010).
- 15 Jin, H., Heller, D. A., Kim, J. H. & Strano, M. S. Stochastic analysis of stepwise fluorescence quenching reactions on single-walled carbon nanotubes: single molecule sensors. *Nano letters* **8**, 4299-4304 (2008).
- 16 Varadarajan, N., Julg, B., Yamanaka, Y. J., Chen, H., Ogunniyi, A. O., McAndrew, E., Porter, L. C., Piechocka-Trocha, A., Hill, B. J. & Douek, D. C. A high-throughput

- single-cell analysis of human CD8⁺ T cell functions reveals discordance for cytokine secretion and cytolysis. *The Journal of clinical investigation* **121**, 4322-4331 (2011).
- 17 Gupta, P. B., Fillmore, C. M., Jiang, G., Shapira, S. D., Tao, K., Kuperwasser, C. & Lander, E. S. Stochastic state transitions give rise to phenotypic equilibrium in populations of cancer cells. *Cell* **146**, 633-644 (2011).
- 18 Kou, P. M. & Babensee, J. E. Macrophage and dendritic cell phenotypic diversity in the context of biomaterials. *Journal of Biomedical Materials Research Part A* **96**, 239-260 (2011).
- 19 Casiraghi, C. Doping dependence of the Raman peaks intensity of graphene close to the Dirac point. *Physical Review B* **80**, 233407-1:3 (2009).
- 20 Das, A., Pisana, S., Chakraborty, B., Piscanec, S., Saha, S., Waghmare, U., Novoselov, K., Krishnamurthy, H., Geim, A. & Ferrari, A. Monitoring dopants by Raman scattering in an electrochemically top-gated graphene transistor. *Nature Nanotechnology* **3**, 210-215 (2008).
- 21 Wang, Q. H., Jin, Z., Kim, K. K., Hilmer, A. J., Paulus, G. L. C., Shih, C. J., Ham, M. H., Sanchez-Yamagishi, J. D., Watanabe, K., Taniguchi, T., Kong, J., P., J.-H. & Strano, M. S. Understanding and controlling the substrate effect on graphene electron-transfer chemistry via reactivity imprint lithography. *Nature Chemistry* **4**, 724-732 (2012).
- 22 Ferrari, A. C. Raman spectroscopy of graphene and graphite: Disorder, electron-phonon coupling, doping and nonadiabatic effects. *Solid State Communications* **143**, 47-57 (2007).
- 23 Paulus, G. L. C., Wang, Q. H., Ulissi, Z. W., McNicholas, T. P., Vijayaraghavan, A., Shih, C. J., Jin, Z. & Strano, M. S. Charge transfer at junctions of a single layer of graphene and a metallic single walled carbon nanotube. *Small* doi:10.1002/smll.201201034 (2012).
- 24 Basko, D., Piscanec, S. & Ferrari, A. Electron-electron interactions and doping dependence of the two-phonon Raman intensity in graphene. *Physical Review B* **80**, 165413-1:10 (2009).
- 25 Li, X., Cai, W., An, J., Kim, S., Nah, J., Yang, D., Piner, R., Velamakanni, A., Jung, I. & Tutuc, E. Large-area synthesis of high-quality and uniform graphene films on copper foils. *Science* **324**, 1312-1314 (2009).
- 26 Bae, S., Kim, H., Lee, Y., Xu, X., Park, J. S., Zheng, Y., Balakrishnan, J., Lei, T., Kim, H. R. & Song, Y. I. Roll-to-roll production of 30-inch graphene films for transparent electrodes. *Nature Nanotechnology* **5**, 574-578 (2010).
- 27 Thomson, T. M., Mattes, M. J., Roux, L., Old, L. J. & Lloyd, K. O. Pigmentation-associated glycoprotein of human melanomas and melanocytes: definition with a mouse monoclonal antibody. *Journal of investigative dermatology* **85**, 169-174 (1985).
- 28 Kuroda, H., Kutner, R. H., Bazan, N. G. & Reiser, J. Simplified lentivirus vector production in protein-free media using polyethylenimine-mediated transfection. *Journal of virological methods* **157**, 113-121 (2009).
- 29 Hu, T., Fu, Q., Chen, P., Zhang, K. & Guo, D. Generation of a stable mammalian cell line for simultaneous expression of multiple genes by using 2A peptide-based lentiviral vector. *Biotechnology letters* **31**, 353-359 (2009).
- 30 Stern, P., Astrof, S., Erkeland, S. J., Schustak, J., Sharp, P. A. & Hynes, R. O. A system for Cre-regulated RNA interference in vivo. *Proceedings of the National Academy of Sciences* **105**, 13895-13900 (2008).

- 31 Zufferey, R., Nagy, D., Mandel, R. J., Naldini, L. & Trono, D. Multiply attenuated lentiviral vector achieves efficient gene delivery in vivo. *Nature biotechnology* **15**, 871-875 (1997).
- 32 Dull, T., Zufferey, R., Kelly, M., Mandel, R., Nguyen, M., Trono, D. & Naldini, L. A third-generation lentivirus vector with a conditional packaging system. *Journal of virology* **72**, 8463-8471 (1998).
- 33 Ferrari, A., Meyer, J., Scardaci, V., Casiraghi, C., Lazzeri, M., Mauri, F., Piscanec, S., Jiang, D., Novoselov, K. & Roth, S. Raman spectrum of graphene and graphene layers. *Physical Review Letters* **97**, 187401 (2006).
- 34 Casiraghi, C., Pisana, S., Novoselov, K., Geim, A. & Ferrari, A. Raman fingerprint of charged impurities in graphene. *Applied Physics Letters* **91**, 233108-1:3 (2007).
- 35 Guo, B., Liu, Q., Chen, E., Zhu, H., Fang, L. & Gong, J. R. Controllable N-doping of graphene. *Nano letters* **10**, 4975-4980 (2010).
- 36 Berciaud, S., Ryu, S., Brus, L. E. & Heinz, T. F. Probing the intrinsic properties of exfoliated graphene: Raman spectroscopy of free-standing monolayers. *Nano letters* **9**, 346-352 (2008).
- 37 Hill, A. The possible effects of the aggregation of the molecules of haemoglobin on its dissociation curves. *Journal of physiology* **40**, 4-7 (1910).
- 38 Heck, H. A. Statistical theory of cooperative binding to proteins. Hill equation and the binding potential. *Journal of the American Chemical Society* **93**, 23-29 (1971).
- 39 Zhang, Y., Brar, V. W., Girit, C., Zettl, A. & Crommie, M. F. Origin of spatial charge inhomogeneity in graphene. *Nature Physics* **5**, 722-726 (2009).
- 40 Martin, J., Akerman, N., Ulbricht, G., Lohmann, T., Smet, J., Von Klitzing, K. & Yacoby, A. Observation of electron-hole puddles in graphene using a scanning single-electron transistor. *Nature Physics* **4**, 144-148 (2007).
- 41 Xue, J., Sanchez-Yamagishi, J., Bulmash, D., Jacquod, P., Deshpande, A., Watanabe, K., Taniguchi, T., Jarillo-Herrero, P. & LeRoy, B. J. Scanning tunnelling microscopy and spectroscopy of ultra-flat graphene on hexagonal boron nitride. *Nature Materials* **10**, 282-285 (2011).
- 42 Dukovic, G., White, B. E., Zhou, Z., Wang, F., Jockusch, S., Steigerwald, M. L., Heinz, T. F., Friesner, R. A., Turro, N. J. & Brus, L. E. Reversible surface oxidation and efficient luminescence quenching in semiconductor single-wall carbon nanotubes. *Journal of the American Chemical Society* **126**, 15269-15276 (2004).
- 43 Yang, F. & Forrest, S. R. Photocurrent generation in nanostructured organic solar cells. *Acs Nano* **2**, 1022-1032 (2008).
- 44 Ohno, Y., Maehashi, K., Yamashiro, Y. & Matsumoto, K. Electrolyte-gated graphene field-effect transistors for detecting pH and protein adsorption. *Nano letters* **9**, 3318-3322 (2009).
- 45 Lei, N., Li, P., Xue, W. & Xu, J. Simple graphene chemiresistors as pH sensors: fabrication and characterization. *Measurement Science and Technology* **22**, 107002-1:6 (2011).
- 46 Scopes, R. K. *Protein purification: principles and practice*. (Springer, 1993).
- 47 Ross, D. & Jirgensons, B. The far ultraviolet optical rotatory dispersion, circular dichroism, and absorption spectra of a myeloma immunoglobulin, immunoglobulin G. *Journal of Biological Chemistry* **243**, 2829-2836 (1968).
- 48 Wang, W., Singh, S., Zeng, D. L., King, K. & Nema, S. Antibody structure, instability, and formulation. *Journal of pharmaceutical sciences* **96**, 1-26 (2006).
- 49 Bickis, I. & Henderson, I. Biochemical studies of human tumors. I. Estimation of tumor malignancy from metabolic measurements in vitro. *Cancer* **19**, 89-102 (1966).

- 50 Ekwall, B. Toxicity to HeLa cells of 205 drugs as determined by the metabolic inhibition test supplemented by microscopy. *Toxicology* **17**, 273-295 (1980).
- 51 Kang, J. W., Lue, N., Kong, C.-R., Barman, I., Dingari, N. C., Goldfless, S. J., Niles, J. C., Dasari, R. R. & Feld, M. S. Combined confocal Raman and quantitative phase microscopy system for biomedical diagnosis. *Biomedical optics express* **2**, 2484-2492 (2011).
- 52 Mellander, L., Cans, A. Å. & Ewing, A. G. Electrochemical probes for detection and analysis of exocytosis and vesicles. *ChemPhysChem* **11**, 2756-2763 (2010).
- 53 Chen, T. K., Luo, G. & Ewing, A. G. Amperometric monitoring of stimulated catecholamine release from rat pheochromocytoma (PC12) cells at the zeptomole level. *Analytical chemistry* **66**, 3031-3035 (1994).
- 54 Heien, M. L., Khan, A. S., Ariansen, J. L., Cheer, J. F., Phillips, P. E., Wassum, K. M. & Wightman, R. M. Real-time measurement of dopamine fluctuations after cocaine in the brain of behaving rats. *Proceedings of the National Academy of Sciences of the United States of America* **102**, 10023-10028 (2005).
- 55 Phillips, P. E., Stuber, G. D., Heien, M. L., Wightman, R. M. & Carelli, R. M. Subsecond dopamine release promotes cocaine seeking. *Nature* **422**, 614-618 (2003).
- 56 He, Q., Sudibya, H. G., Yin, Z., Wu, S., Li, H., Boey, F., Huang, W., Chen, P. & Zhang, H. Centimeter-long and large-scale micropatterns of reduced graphene oxide films: fabrication and sensing applications. *ACS nano* **4**, 3201-3208 (2010).
- 57 Alivisatos, A. P., Andrews, A. M., Boyden, E. S., Chun, M., Church, G. M., Deisseroth, K., Donoghue, J. P., Fraser, S. E., Lippincott-Schwartz, J. & Looger, L. L. Nanotools for Neuroscience and Brain Activity Mapping. *ACS nano* **7**, 1850-1866 (2013).
- 58 Koike, T. & Takashima, A. Cell Cycle-Dependent Modulation of Biosynthesis and Stimulus-Evoked Release of Catecholamines in PC12 Pheochromocytoma Cells. *Journal of neurochemistry* **46**, 1493-1500 (1986).
- 59 Livett, B., Boksa, P., Dean, D., Mizobe, F. & Lindenbaum, M. Use of isolated chromaffin cells to study basic release mechanisms. *Journal of the autonomic nervous system* **7**, 59-86 (1983).
- 60 Staal, R. G., Mosharov, E. V. & Sulzer, D. Dopamine neurons release transmitter via a flickering fusion pore. *Nature neuroscience* **7**, 341-346 (2004).
- 61 Chen, G., Gavin, P. F., Luo, G. & Ewing, A. G. Observation and quantitation of exocytosis from the cell body of a fully developed neuron in Planorbis corneus. *The Journal of neuroscience* **15**, 7747-7755 (1995).
- 62 Li, R., Kong, Y. & Ladish, S. Nerve growth factor-induced neurite formation of PC12 cells is independent of endogenous cellular gangliosides. *Glycobiology* **8**, 597-603 (1998).
- 63 Cançado, L.G., Jorio, A., Martins Ferreira E.H., Stavale, F., Achete, C.A., Capaz, R.B., Moutinho, M.V.O., Lombardo, A., Kulmala, T.S. & Ferrari, A.C. Quantifying defects in graphene via raman spectroscopy at different excitation energies. *Nano Letters* **11**, 3190-3196 (2011).
- 64 Cadet, J.L. & Brannock, C. Invited Review: Free radicals and the pathobiology of brain dopamine systems. *Neurochemistry International* **32**, 117-131 (1997).
- 65 Li, N., Zhang, X., Song, Q., Su, R., Zhang, Q., Kong, T., Liu, L., Jin, G., Tang, M., Cheng, G. The promotion of neurite sprouting and outgrowth of mouse hippocampal cells in culture by graphene substrates. *Biomaterials* **32**, 9374-9382 (2011).

7. Conclusions and outlook

This thesis was aimed at understanding the processes by which charges are transferred at the interface of carbon nanomaterials, specifically graphene and single walled carbon nanotubes (SWCNTs). Figure 7.1 summarizes the different types of interactions studied in this work. We then discussed how these interactions can be used to our advantage in various applications in the fields of photovoltaics, electronics, and biosensing and developed proof-of-concept demonstrations thereof.

Chapter 1 introduces low dimensional materials (LDMs), characterized by at least one dimension that is on the order of the wavelength of the electron wave function. This quantum confinement brings about a transition from a continuous to a discontinuous density of states (DOS), which causes the LDMs to have different properties than their bulk counterparts. We focus on carbon LDMs, specifically graphene and SWCNTs, the protagonists of this work. Graphene is a conductive two-dimensional sheet of sp^2 -bonded carbon atoms, organized in a hexagonal crystal lattice. Conceptually, a SWCNT is a sheet of graphene rolled up into a seamless hollow cylinder with nanoscale diameter. Depending on the direction in which the sheet is rolled, SWCNTs can be metallic or semi-conducting. Both materials display exceptional electronic, optical, thermal and mechanical properties.

Next we discuss the concept of excitons (Coulombically bound electron-hole pairs) since they are central in the parts of this thesis that focus on semiconducting materials (Chapter 2 and 3). Specifically, we argue that since they are localized neutral particles,

they can be described with the same population balances, mass transfer and chemical kinetics approaches that chemical engineers know well and practice extensively.

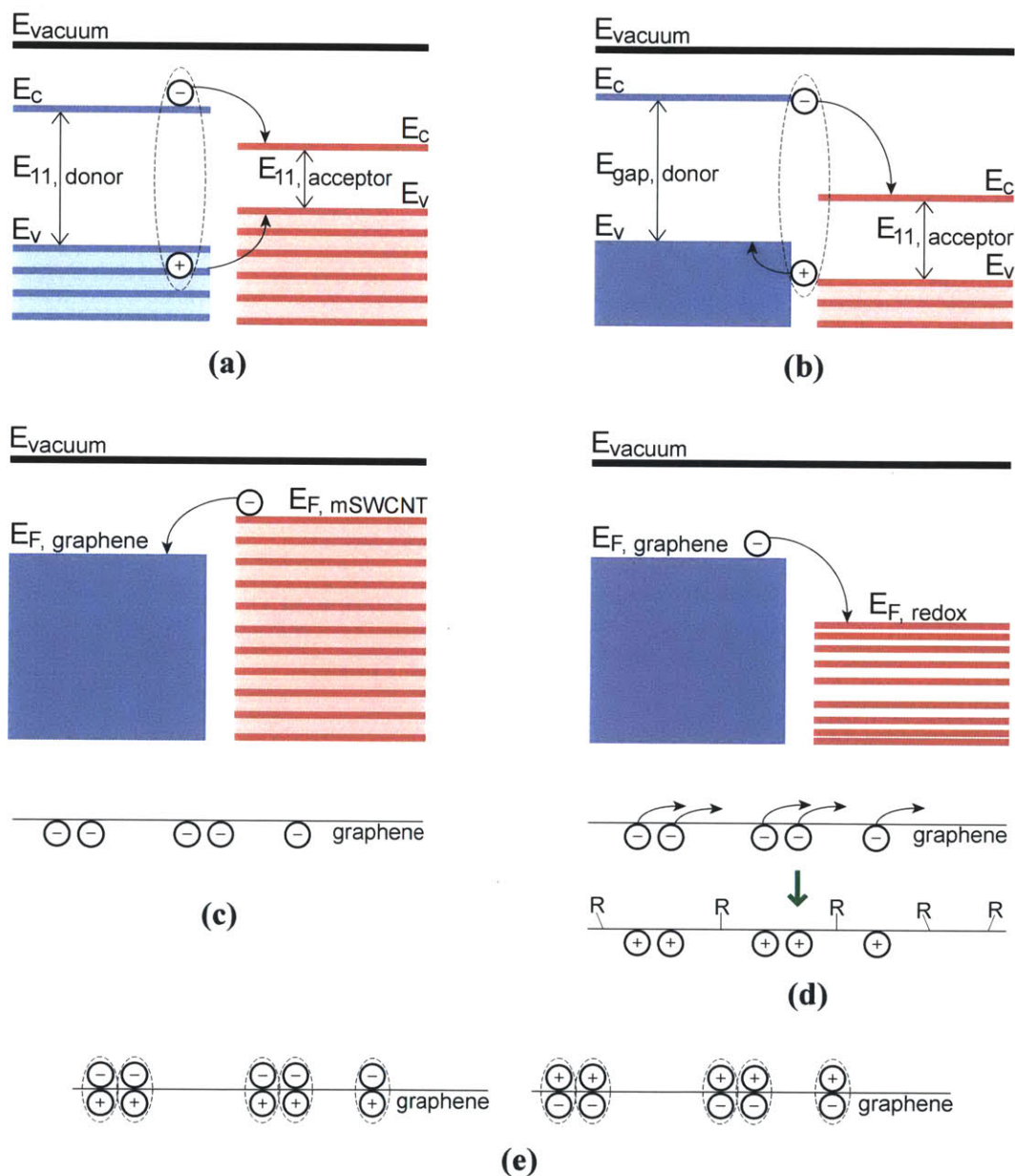


Figure 7.1. Overview of the different mechanisms for charge transfer at the interface of carbon nanotubes and graphene. For (a)-(d) the relative position of the energy levels of the materials involved is the driving force for the observed interactions. For (e) electrostatic attraction governs the mechanism. **(a)** Excitons are transferred from a larger band gap semi-conducting SWCNT (blue) to a smaller band gap one (red). The interface forms a type I heterojunction (Chapter 2). **(b)** Excitons are split at the interface between

P3HT (blue) and semiconducting SWCNTs (red); this interface is a type II heterojunction (Chapter 3). **(c)** Upon contact of a metallic SWCNT (red) and graphene (blue), electrons are transferred from the former to the latter to align their Fermi levels, leaving the graphene n-doped (Chapter 4). **(d)** Upper panel: electrons are transferred from graphene (blue) to unoccupied states of a diazonium molecule (red). Lower panels: After delocalized electrons are used to reduce the diazonium molecules, an aryl radical is formed which subsequently locally reacts with a carbon atom in the graphene lattice, changing its hybridization from sp^2 to sp^3 (Chapter 5). **(e)** Left panel: negatively charged species (or species with a high electron density) physisorb onto hole puddles in the graphene lattice, thereby immobilizing the charges in the graphene and n-doping it. Right panel: positively charged species physisorb onto electron puddles in the graphene lattice, thereby immobilizing the charges in the graphene and p-doping it (Chapter 6).

Chapter 2 discusses how energy is transferred from large band gap semiconducting SWCNTs to small band gap semiconducting SWCNTs via exciton energy transfer. At their interface a type I heterojunction is formed (Figure 7.1a). Note that the band structure of the SWCNTs is characterized by Van Hove singularities (VHS), discrete energy levels with plenty of available states, shown schematically by the thick lines in Fig. 7.1a. Unlike for a molecule (e.g. diazonium molecule in Fig. 7.1d) there are still (some) states present at the energy levels between the VHS, represented in Fig. 7.1a by the lighter background.

A deterministic model that takes into account exciton generation, first order exciton decay (radiatively and non-radiatively), second order exciton decay (via Auger recombination) and exciton energy transfer shows that the rate constant of the latter is two to three orders of magnitude greater than that of the other processes. Based on this knowledge we designed an antenna that consists of a core of small band gap semiconducting SWCNTs surrounded by a shell of larger band gap semiconducting SWCNTs. When light is incident on the antenna structure, all of its energy is funneled to the center of the antenna in the form of excitons. The excitons finally radiatively

recombine in the center of the optical concentrator at the E_{11} emission wavelength of the smallest band gap SWCNTs in the core.

Ongoing and future work focuses on using this concept to design efficient photovoltaics. In order to achieve this the core of the antenna needs to be a material that is able to dissociate the excitons reaching the core into free charge carriers (e.g. [6,6]-phenyl-C61-butyric acid methyl ester, i.e. PCBM). Additionally both the core and the shell need to be connected to electrodes so current can be extracted. Similarly a planar equivalent of the antenna can be designed. The number of shells can be increased as long as each shell is constructed out of semiconducting SWCNTs with a band gap larger than the SWCNTs in the layer beneath it. Since a lot of work has been done on the separation of different SWCNT chiralities, this option is becoming a reality. The fact that many layers of different SWCNT chirality can be used will allow for broad band absorption of the (sun)light, and given the efficiency of the EET process, the generated excitons will be transferred to the core faster than they would otherwise recombine.

In Chapter 3 we have discussed organic photovoltaics with poly(3-hexylthiophene) (P3HT) as the electron donor and semiconducting SWCNTs as the electron acceptors. The interface between both materials forms a type II heterojunction (Figure 7.1b), which means that when an exciton reaches it, it is efficiently dissociated into a free hole (which is subsequently transported through the P3HT to the anode) and a free electron (which is carried to the cathode by the SWCNTs). In principle a SWCNT-based photovoltaic should outperform a PCBM-based one, since SWCNTs are characterized by an electron mobility that is ~ 5 orders of magnitude larger than PCBM. However P3HT/PCBM bulk heterojunction (BHJ) photovoltaics have a much higher efficiency than P3HT/SWCNT

BHJs. We showed that the efficiency of the P3HT/SWCNT photovoltaic is ~30 times higher in a planar configuration compared to when it is used in a bulk heterojunction where both materials are intimately mixed. We argued that clustering of SWCNTs in BHJs is the responsible factor for this observation. If a metallic SWCNT is part of a SWCNT cluster it can quench all excitons reaching it. Moreover, the cluster might not make direct contact with the cathode electrode, implying the circuit is broken.

We also noticed that when changing the thickness of the P3HT layer in the PHJ configuration, a maximum solar cell efficiency was obtained for a P3HT thickness of ~60 nm. We noticed the same trend for a P3HT/PCBM solar cell described in literature. This is odd since it is expected that a maximum efficiency in PHJ photovoltaics is obtained for a polymer thickness of ~10 nm, the exciton diffusion length. The logic is that every exciton that is generated at a distance further away from the type II heterojunction would recombine before ever reaching it. A Kinetic Monte Carlo (KMC) simulation that tracks exciton generation and transport in the photovoltaic reveals that in the case of the P3HT/SWCNT photovoltaic the shifted maximum efficiency is caused by the fact that excitons can also dissociate in the bulk of the P3HT, not just at the junction. The chance of this happening is inversely proportional to the P3HT thickness: up to 60% of the excitons dissociate when 10 nm of P3HT is used, whereas only 15% for 100 nm of P3HT. The excitons that dissociate in the bulk cannot contribute to the current, making thinner devices less efficient.

In part due to the different exciton generation profile in the P3HT/PCBM device (due to the presence of the reflective cathode underneath the active layers of the photovoltaic) this bulk exciton dissociation is not sufficient to describe the shifted

maximum for this device. The main reason is the diffusion of mobile PCBM molecules into the P3HT layer upon device annealing.

It is clear that planar heterojunctions are not just governed by the exciton diffusion length of the donor material, as was previously thought, but that optical interference effects, bulk exciton dissociation, and diffusion of small molecules into the bulk of the polymer affect the device performance.

Ongoing and future work will focus on increasing the efficiency of the P3HT/SWCNT photovoltaics. Firstly, an increased SWCNT density (without forming clusters) will increase the amount of current that can be collected. Secondly, an analysis revealed that the relatively low fill factor of our SWCNT-based photovoltaics was caused by a large series resistance. The resistance can be lowered by using a more conductive, flexible and transparent electrode instead of indium tin oxide (ITO), and by abandoning sputtering as a method to form that electrode on top of the active layer of the device.

In Chapter 4 a fundamentally new junction between SWCNTs and graphene was created; an ideal one-dimensional/two-dimensional carbon interface. Our interest was to examine the degree of charge transfer (i.e. doping) between both materials. The ability to controllably dope graphene and change its workfunction on small scales is key to its implementation in for example (opto-)electronic and biosensor devices. Raman spectroscopy was used to probe the graphene/SWCNT sample. A comparison of the Raman peak parameters such as G and 2D peak position, G peak width and the 2D/G intensity ratio of graphene at the junction with those of graphene far away from the junction revealed that graphene receives $\sim 1.12 \times 10^{13}$ electrons per cm^2 from a metallic SWCNT it covers and $\sim 0.325 \times 10^{13}$ electrons per cm^2 from a semiconducting SWCNT.

This is in agreement with the higher Fermi level of the SWCNTs compared to that of graphene, which provides the driving force for the observed doping (Figure 7.1c). Similarly, the Raman peak shifts observed in the SWCNTs are also indicative of doping. However, peak shifts can also be caused by strain. A molecular dynamics simulation revealed that although the SWCNTs were radially compressed by the graphene sheet, this resulted in an elongation of $\sim 50\%$ of all SWCNT bonds and an equivalent but opposite reduction of the other SWCNT bonds. This in turn causes no Raman peak shifts, but rather an inhomogeneous broadening of the SWCNT peaks, which is consistent with our experimental observations.

In this Chapter the need to collect many Raman spectra (~ 100) to analyze the doping level of graphene (or SWCNT) in a statistically relevant manner became obvious. Spatial inhomogeneities are omnipresent in the sample substrate, as well as in the chemically synthesized graphene and SWCNTs themselves. Similarly, the fact that temperature fluctuations can alter the Raman peak positions indicates proper calibration of the Raman system before and after data collection is crucial.

Ongoing and future work will focus on developing applications for this platform. The semiconducting SWCNT/graphene junction can function as a nanoscale photo-detector. When light is incident on the SWCNTs, the excitons generated therein can be dissociated into free charge carriers at the interface with the graphene, since at this interface a Schottky barrier is formed. An application for the metallic SWCNT/graphene junction is the formation of a short-channel transistor. Moreover, locally gating the graphene implies locally changing its Fermi energy. As discussed more in detail in Chapter 5, a lower lying Fermi energy (with respect to vacuum) of graphene causes

increased functionalization of the lattice. The ability to spatially control graphene's reactivity and thus surface chemistry is important for biological applications such as multiplex microarrays and biosensors.

In Chapter 5 the covalent modification of graphene with diazonium salts is discussed. Chemically functionalizing graphene allows graphene to interact with other molecules, which can be important to make new composite materials or perform chemical and biological sensing. Moreover it is a longstanding goal of the field to introduce a band gap in graphene to increase its performance as a transistor; it has been shown both experimentally and theoretically this can be achieved by covalently modifying the graphene lattice, for example with diazonium salts.

The reaction with graphene occurs in two steps. In solution diazonium salts are dissolved. The diazonium cation is reduced by a delocalized electron of the graphene (middle panel Figure 7.1d), then releases a molecule of N_2 and becomes an aryl radical. This radical then binds to the graphene by attacking the graphene lattice and changing the hybridization of the attacked carbon atom from sp^2 to sp^3 . This effectively immobilizes an electron of the graphene lattice in the newly formed bond (lower panel Figure 7.1d). The rate of reaction depends on the overlap between the filled energy levels of graphene and unoccupied states of the diazonium molecule (upper panel Figure 7.1d). In many ways the process is similar to the one described in Figure 7.1c, except graphene is now being p-doped (i.e. loses electrons) instead of n-doped (i.e. gains electrons).

We studied the effect of increasing levels of functionalization on the properties of graphene. High levels of covalent modification increase the Raman D/G intensity ratio, a sign of lattice defects. The graphene lattice loses two electrons for every diazonium

molecule it binds (Figure 7.1.d), and this p-doping is reflected by increased G and 2D peak positions and a decreased 2D/G intensity ratio. Moreover, some of the diazonium molecules will physisorb onto the graphene lattice rather than chemisorb, which also increases the doping level. We created graphene field effect transistors (FETs) and showed that with increasing functionalization the minimum conductivity decreases, the Dirac voltage increases, the conductivity plateaus at high carrier density decrease and the asymmetry between hole and electron conduction increases. All these effects were quantitatively described in a model of graphene charge transport. Contrary to earlier models, our model takes into account both long-range Coulombic scatterers (reflecting physisorption) as well as short-range scatterers (representing chemisorption). Moreover, our model incorporates the electron-hole conduction asymmetry that is caused by an imbalanced electron-hole injection at the contacts. We find that the density of impurities in the vicinity of graphene increases from about $2.65 \times 10^{11} \text{cm}^{-2}$ for pristine graphene (D/G intensity ratio ~ 0) to $1.17 \times 10^{14} \text{cm}^{-2}$ for heavily functionalized graphene (D/G intensity ratio ~ 4.6). The model also reveals that the conductivity at large carrier density decreases by about one order of magnitude for highly functionalized graphene (D/G ~ 4.6) due to the presence of short-range scatterers. Finally the model taught us that electron-hole asymmetry near the Dirac point increases mainly at very high levels of covalent modification.

We also studied the effect of using diazonium salts with different end groups. The end group affects the Fermi (or redox) level of the diazonium molecule and consequently, the reaction rate and the eventual degree of covalent modification. When the diazonium salt physisorbs on the graphene rather than reacting with it, the end group can determine

the type of doping graphene experiences (n- versus p-doping). Moreover, some diazonium salts are less stable in solution and thus more prone to forming long oligomers, which increase the degree of physisorption vs. chemisorption.

Ongoing and future work will focus on better understanding and characterizing the diazonium functionalization of bilayer graphene. Despite promising theoretical studies and experimentally observed optical band gaps of several hundred meVs in monolayer graphene, the electronic band gap is much smaller due to interband trapping. In bilayer graphene, simply breaking the symmetry between the two layers should be able to create a substantial electronic band gap. Future work will thus focus on expanding the charge transport model to be able to describe graphene bilayer FET behavior quantitatively.

Chapter 6 shows how graphene doping (mostly via physisorption) can be considered as the basic principle of a fundamentally new type of biosensor with (sub-) cellular resolution. Since each location of graphene that is probed via Raman spectroscopy reports back on its local environment, graphene can be thought of a continuous array of aligned and independent sensor units, with the size of these units determined by the spot size of the Raman excitation laser (in our case $\sim 1\mu\text{m}^2$). The ability of charged species (or species with a high electron density) to adsorb to graphene is attributed to the presence of electron-hole charge puddles in the otherwise largely neutral sheet, which are the result of charged impurities in the substrate and are $\sim 20\text{nm}$ in size (for graphene supported by SiO_2). Due to electrostatic interactions charged species will adsorb onto puddles of opposite charge in the graphene lattice, thereby immobilizing the charges in the puddles (Figure 7.1e).

We determined the graphene Raman signal displays a strong pH sensitivity. Since metabolically active cells acidify their environment, pH can be considered as a proxy for cellular metabolism. We placed different types of cells on the graphene lattice. Since the cells typically have a diameter of 20-40 μm they cover multiple sensor units and sub-cellular detection of their excreted protons is possible. A simple model that takes into account proton generation, diffusion and adsorption relates the observed shifts of the Raman G peak positions to a metabolic activity of the cells. We find that human embryonic kidney cells that were genetically engineered to perform additional tasks have a metabolic activity that is 4 times higher than the same cells that were not genetically manipulated. We also find that increasing the interaction between the cells and graphene (by increasing cellular adhesion) allows the differences in metabolic activity to be observed more clearly.

Ongoing and future work focuses on increasing the spatial and temporal resolution of our sensor, as well as developing different applications. It is known that the glycolytic rate of cancer cells can be up to 200 times that of healthy cells. Thus in principle, our sensor can be used to inform us about the degree of tumor malignancy based on proton excretion. Additionally we explore the detection of different analytes, such as catecholamines, an important group of neurotransmitters and neuromodulators that help regulate heartbeat, blood pressure and the body's stress response. Spatial and temporal monitoring of dopamine uptake and release is an important goal of the field we aim to contribute to with our graphene Raman-based biosensor.